Study of the influence of structural properties on the fluid-structure interaction of artificial vocal folds

Mohammad Ahmad

▶ **To cite this version:**

Mohammad Ahmad. Study of the influence of structural properties on the fluid-structure interaction of artificial vocal folds. Mechanics of materials [physics.class-ph]. Université Grenoble Alpes [2020-..], 2023. English. NNT : 2023GRALI013 . tel-04109733

HAL Id: tel-04109733
https://theses.hal.science/tel-04109733

Submitted on 30 May 2023

HAL is a multi-disciplinary open access archive for the deposit and dissemination of scientific research documents, whether they are published or not. The documents may come from teaching and research institutions in France or abroad, or from public or private research centers.

L'archive ouverte pluridisciplinaire **HAL**, est destinée au dépôt et à la diffusion de documents scientifiques de niveau recherche, publiés ou non, émanant des établissements d'enseignement et de recherche français ou étrangers, des laboratoires publics ou privés.

THÈSE

Pour obtenir le grade de

DOCTEUR DE L'UNIVERSITÉ GRENOBLE ALPES

École doctorale : I-MEP2 - Ingénierie - Matériaux, Mécanique, Environnement, Energétique, Procédés, Production
Spécialité : MEP : Mécanique des fluides Energétique, Procédés
Unité de recherche : Laboratoire des Ecoulements Géophysiques et Industriels

Etude de l'influence des propriétés structurelles sur l'interaction fluide-structure des cordes vocales artificielles

Study of the influence of structural properties on the fluid-structure interaction of artificial vocal folds

Présentée par :

Mohammad AHMAD AMEEN AHMAD

Direction de thèse :

Annemie VAN HIRTUM DIRECTRICE DE RECHERCHE, Université Grenoble Alpes	Directrice de thèse
Xavier PELORSON DIRECTEUR DE RECHERCHE, CNRS	Co-encadrant de thèse

Rapporteurs :

Jorge C. LUCERO
PROFESSEUR, Universidade de Brasilia
Anna BARNEY
PROFESSEUR, University of Southampton

Thèse soutenue publiquement le **28 février 2023**, devant le jury composé de :

Annemie VAN HIRTUM DIRECTRICE DE RECHERCHE, CNRS délégation Alpes	Directrice de thèse
Jorge C. LUCERO PROFESSEUR, Universidade de Brasilia	Rapporteur
Carlo DRIOLI PROFESSEUR ASSISTANT, Università degli Studi di Udine	Examinateur
Ana I. FERNANDEZ PROFESSEUR, Universitat de Barcelona	Examinatrice
Henda DJERIDI PROFESSEUR DES UNIVERSITES, Grenoble INP	Présidente
Anna BARNEY PROFESSEUR, University of Southampton	Rapporteure

Invités :

Xavier PELORSON
Directeur de Recherche, CNRS Grenoble

Acknowledgements

An important saying of the prophet Mohammad is: *"He who does not thank people has not thanked Allah"*. My doctoral degree does not belong to me alone. Therefore, I would like to extend my heartfelt gratitude to the following remarkable individuals and groups who have contributed to my journey and made this memorable opportunity possible:

First and foremost, I must express my deepest appreciation to Annemie. Your unwavering support, invaluable guidance, and patience throughout this rollercoaster ride have been nothing short of extraordinary. I'm convinced you have some kind of magical power (or, of course, incredible technical knowledge and emotional maturity) to decipher my incoherent findings and transform them into respectable research.

To Xavier, thank you for your expertise, encouragement, and the occasional reality check. Your keen insights and witty remarks were always more than welcome. It was an honour working with you.

I would like to extend my thanks to the esteemed members of my PhD defence jury. Your insightful questions and constructive feedback have pushed me to refine my work further and broaden my scientific perspective. Thank you Anna for your kindness for accepting being a reporter on a such short notice. Thank you Jorge for the brief yet valuable time we worked together. To Inés and Carlo, thank you for taking the time and effort to be there at LEGI. Your presence added a touch of excitement to an otherwise stressful experience. A special shout-out goes to the president of the jury and EDT team head, Henda. Thank you for your generous spirit that is obvious to everyone interacting with you.

I must acknowledge Anne, who paved the way for me. Your insights and shared experiences have been invaluable in shaping my research journey. Your legacy lives on.

A heartfelt thank you goes out to Cristina and Antonin, my internship students who joined me on this wild ride. Your dedication, hard work, and creative problem-solving skills have not only lightened the load but also made the experimental room a livelier place. I hope you've learned as much from me as I have from you.

To my dear LEGI friends, you have been the wind beneath my wings throughout this entire endeavour. To Raphael, thank you for the time we shared together, and we have yet to play some Fifa. To Al Oualid, thank you for all the time we shared and all the moments we discussed and had fun speaking in darija. A special mention to Benjamin. Your expertise in both research and football planning has been awe-inspiring. Shoutout to Yann and Quentin, my tennis teachers and partners. And let's not forget the lab's meme lord, Ivan. Your memes provided much-needed comic relief during the darkest hours of lab life. You have a talent for turning any normal lab

event into a hilarious visual masterpiece. Shout out to Umair, Helder, Mathieu, Luis, Cruz, Arman, Amin, Neda, Arash, Karla, Oliver, Thibault, Alban, Christophe, Felix, Alexandre, Jacobo, Maxime, Sara, Amélie, Maria-Rita, Sevan, Pablo, Christophe, Miguel, and Christian.

To all the researchers and personnel at LEGI, you've created an environment where scientific rigour coexists with laughter, camaraderie, and shared moments of joy. Thank you for making LEGI feel like a second home. A special thanks to Chantal, responsible of EFM master, for being a great mentor as well as a great researcher.

A heartfelt shout-out to all my friends in the beautiful city of Grenoble, especially those from the legendary residence, Le Rabot. You've turned my stay into an unforgettable experience, filled with late-night discussions, laughter, and occasional mischief. Le Rabot truly deserves its title as the best university residence in France, thanks to all of you. Shout out to Abdelrahman, Aymen, Ahmad, Mehdi, Hamza, Cimo, Fadil, Alhasana, Mahmoud, Ghina, Xavier, the other three team members of the fantastic four team; Lucie, Anna, Romain, and last but not least, Aida.

A special thanks goes out to my Egyptian friends and my football buddies. You were the ones who kept me sane during those gruelling times, reminding me that life existed beyond the lab walls. Our friendly matches and fierce competitions provided the much-needed adrenaline rush to balance out the hours spent working. Whether we won or lost, the camaraderie we shared on the pitch will forever remain a cherished part of my PhD experience. Shoutout to Salah, Sabry, Adham, Mostafa, Abdelrahman, Adham, Nour, and Hadi. Special thanks to Halim, who was always a great listener and motivator, and Omar, with whom I presented my first defence practice.

I cannot forget to express my gratitude to Jessica, the kinesitherapist who became my frequent companion due to my numerous sports-related mishaps. I may have been a regular visitor, but you always managed to greet me with a smile, as if my never-ending parade of injuries was the highlight of your day. Thank you for your professional care and for transforming my many mishaps into hilarious anecdotes.

To my friends in Egypt, especially my dear friend Moaz, thank you for being a constant source of positivity and encouragement. No matter how challenging things got, you always managed to see the bright side and remind me of the bigger picture. Your unwavering belief in my abilities and your infectious optimism lifted my spirits and helped me conquer the toughest hurdles. You are a true beacon of light, and I'm incredibly grateful to have you in my corner. Shout out to Abdo, Mostafa, Mshmsh, Omar, Menna, Taban, Mr. K, Maged, Gemi, Amr, Badry, and Khaled.

A very special thanks to my supervisors, Antoine, Shaltout, and El Shafei, who believed in me and encouraged me to start this journey. I hope I can make you proud.

Last but certainly not least, the most important thanks goes to my family. To my parents,

who have been my pillars of support throughout this entire journey (and my entire life), thank you for your unwavering belief in me, even when I doubted myself. Your love has fuelled my determination and kept me going. I am eternally grateful for your guidance, encouragement, and the countless pep talks that always managed to bring me back from the brink of despair. I hope to always be by your side.

To my brother and sisters, Hossam, Hend, and Somaya, thank you for being my best friends, confidants, and partners in crime. Your constant stream of hilarious anecdotes provided the perfect escape from the pressures of academia. I'm grateful for the countless laughs, the shared adventures, and the unconditional love that has sustained me throughout this entire journey. Wish you the best, always.

In conclusion, this achievement is not solely mine. It is a collective triumph, made possible by the unwavering support, guidance, and humour of so many incredible individuals. I am truly blessed to have such an extraordinary network of people in my life. As I embark on the next chapter, I carry with me the lessons, memories, and connections forged during my PhD. Thank you all from the bottom of my heart for being a part of this incredible journey.

Contents

List of Figures

List of Tables

Nomenclature

Acronyms

VF	vocal fold
FS	fluid-structure
FSI	fluid-structure interaction
1L, 2L, 3L, 4L	one-layer, two-layer, three-layer, four-layer
M5, MRI, EPI	labels of three silicone VF replicas
T, T(-)	silicone Thinner
E, (-)E	silicone Ecoflex
D, (-)D	silicone Dragonskin
TE	mixture of silicone Thinner and Ecoflex
TD	mixture of silicone Thinner and Dragonskin
WAM	weighted arithmetic mean
WHM	weighted harmonic mean
MP	mechanical press
PL	precision loading
In	inclusion
On	onset
Off	offset
pp	peak to peak

Physical quantities

P	pressure	Pa
ρ	density	$\mathrm{kg.m^{-3}}$
$\mathscr{V}$	volume	$\mathrm{m^3}$

m	mass	g

Geometry Parameters

$\mathscr{A}$	cross-section area	mm^2
$\mathscr{A}^*$	cross-section area based on volume conservation	mm^2
$\mathscr{A}^q$	cross-section area based on a quadratic fit	mm^2
$\mathscr{A}_0$	initial area	mm^2
$\mathscr{H}_{(j,j+1)}$	height stacking dimension ratio between adjacent layers	[–]
$\mathscr{L}_{(j,j+1)}$	length stacking dimension ratio between adjacent layers	[–]
l_t	replica layer thickness	mm
l_{eq}	equivalent layer thickness	mm

Measurement Parameters

$\mathscr{F}$	uni-axial force	N
σ	stress	Pa
ε	deformation strain	[–]
$\mathscr{E}$	Young's modulus	kPa
$\mathscr{E}_{eff}$	effective Young's modulus	kPa
P_u	upstream pressure	Pa
P_{On}	threshold pressure	Pa
f_0	fundamental frequency	Pa
z_r	displacement of the top surface of the replica	Pa

Spatial Parameters

x	left - right axis
y	posterior - anterior axis
z	inferior - superior axis

Miscellaneous

$\perp$	serial stacking
$\parallel$	parallel stacking
$\perp\parallel$	combined serial and parallel stacking
$o_{(j,j+1)}$	stacking orientation between adjacent layers
$\mathscr{M}$	mass mixing ratio
n	total number of layers in a composite
R	coefficient of determination
$\widehat{x}$	indicates modelled value of parameter x
ref	superscript indicating reference values obtained from literature

CHAPTER 1

Introduction

1.1 Context of the study

The vocal apparatus is a sophisticated system that enables the production of voice sounds. This system is comprised of numerous sections of the human body, with three key components: an airflow system (the lungs and trachea), a vibration source (the vocal folds in the larynx), and a group of resonators in the vocal tract (different cavities between the vocal folds and the lips and nostrils).

The human larynx, situated between the trachea and the vocal tract, is a complex organ with major functions such as airway protection and speech sound production [1]. For phonation or voiced speech sound production, the presence of two apposed vocal folds (VF) within the larynx, depicted in Fig. 2.1, is crucial. The fluid-structure interaction between airflow coming from the lungs and the deformable multi-layer (ML) VF tissues on each side of the glottal constriction can result in sustained VF auto-oscillation which is the major sound source for voiced speech [1, 2]. This oscillation will modulate airflow and generate an acoustic wave that travels through the vocal tract. The vocal tract, which is articulated by a number of muscles, modifies the spectrum of the acoustic wave to produce a voiced sound (vowels, sonorous consonants) that is ultimately emitted from the lips. As a consequence, the role of normal (healthy) and abnormal (pathological) VF structural properties on the fluid-structure interaction underlying VF auto-oscillation and sound production is an ongoing and multi-disciplinary research subject [1, 3–11].

Mechanical VF replicas for which the structural properties can be altered are thus of major benefit for physical studies since systematic, and preferably controlled, structural changes allow to mimic not only the normal elasticity regulating function of the vocal ligament and vocalis muscle but also to explore the influence of structural abnormalities, either within a single VF or related to left-right asymmetries, on VF auto-oscillation [15–18].

The aim of this thesis is to consider and validate an analytical model for the effective elasticity of ML silicone composites from its layers properties, *i.e.* Young's modulus $\mathscr{E}_{eff}$ and geometry. A validated analytical model predicting $\mathscr{E}_{eff}$ of ML moldings is of interest for the (*a-priori*) mechanical characterisation, and the design of ML VF representations, for normal as well as for abnormal VF structures. Indeed, in the long term, such a model is of particular interest

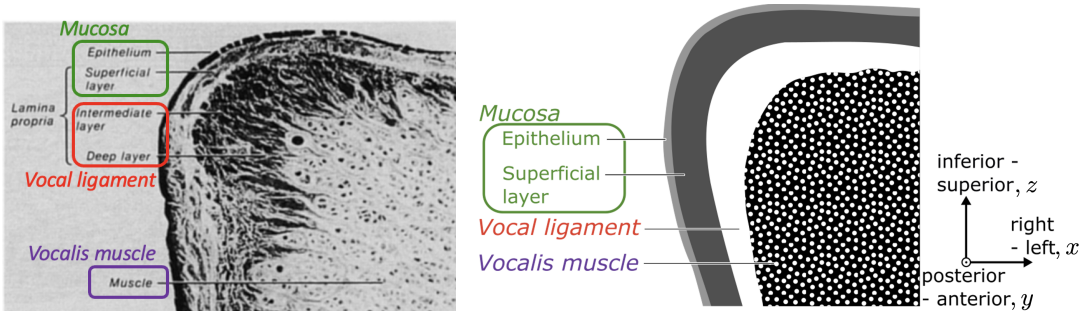

(a) *ex-vivo* observation (b) a multi-layer representation

Figure 1.1: Illustration of the (micro-)anatomical structure of a left human VF in the medio-frontal plane [1]: a) coronal section (adapted from [12]), b) example of a simplified multi-layer representation [13, 14].

for physical studies (using deformable silicone-based molded replicas) involving a systematic elasticity variation mimicking either intra- and inter-speaker diversity (voice type, morphology, aging *etc.* [9]) or a structural pathology (scar, nodule, carcinoma, cyst *etc.* [1]).

1.2 Objective and organisation of the thesis

In the context of physical investigations on vocal folds auto-oscillation, this thesis aims to make four main contributions.

Firstly, to consider and validate an analytical model for the effective Young's modulus $\mathscr{E}_{eff}$ of ML silicone composites from its layers properties, *i.e.* $\mathscr{E}_{eff}$ and geometry. Additionally, The model is to be extended to account for an arbitrary-shaped inclusion of any size embedded somewhere within a single or multiple layers.

Secondly, extending the characterisation of the stress-strain behaviour of such ML silicone composites to account for the non-linear strain range with two-parameter relationships. It is then of interest to show that the parameters can be *a priori* modelled as a constant or as a linear function of the effective low-strain Young's modulus. In addition, analytical expressions of the linear high-strain Young's modulus and the linear high-strain onset, again as a function of the effective low-strain Young's modulus, are formulated as well.

Thirdly, apply the validated models to silicone replicas based ML specimens for estimating their low-strain and high-strain moduli, as well as quantifying the stress-strain behaviour of a pressurised latex tube replica.

And finally, an experimental study of the influence of a structural inclusion on the fluid-

structure interaction underlying the VFs auto-oscillation is realised. Therefore, the objective is to quantify at first the structural properties of the normal and the abnormal designed VFs replicas in order to investigate its influence on the vibration.

CHAPTER 2

The vocal folds apparatus

2.1 Human voice production

Vocal communication plays the most important role in social interactions [19]. Speech, which is a unique attribute of humans, is our primary mode of communication and voice can be considered the most used musical instrument [20]. Physically, the production of speech involves two operations, which are known as the source-filter decomposition of speech [21]. Firstly, generating an acoustic wave either by the quasi-periodic vibration of the vocal folds (VFs) that modulates airflow in voiced speech or by turbulent airflow constricted by the vocal tract in unvoiced speech, e.g., fricatives. Secondly, filtering of the generated signals by the amplification or attenuation of different frequencies in the vocal tract.

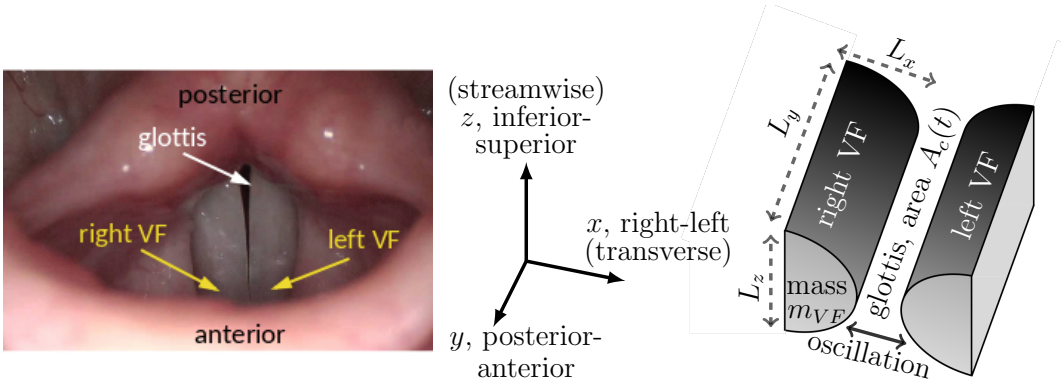

(a) *in-vivo* observation (b) schematic overview

Figure 2.1: Illustration of the larynx during VF auto-oscillation or phonation: a) *in-vivo* videostroboscopic observation (top view) (adapted from [1]), b) schematic overview of the time-varying glottal constriction area $A_c(t)$ and main VF characteristics (dimensions L_x, L_y, L_z and mass m_{VF}).

The generation of voiced speech in the larynx by the fluid-structure interaction induced vibrations of the VFs is called phonation [22]. Although they act as a protector of the lungs from the aspiration of food through the trachea, VFs play a primary function in the production of speech.

The physical process of phonation is governed by the principles of fluid-structure interactions, where the characteristics of the VFs and the airflow can significantly alter the output voice. Although healthy VFs already produce complex voice signals, any presence of VFs pathology can considerably enhance the complexity and the nonlinear behaviour of the dynamics of phonation [22].

2.2 Deformable mechanical VF replicas

Given the complexity of a human VF, physical studies of the VF auto-oscillation commonly rely on deformable mechanical VF replicas which simplify the anatomical VF structure and functionality in order to ensure the reproducibility, quantifiability, controllability and thus interpretability of findings [8, 23–31]. A first type of deformable VF replicas consists of silicone molded VF replicas. These replicas focus on maintaining, up to some degree, the anatomical ML structure so that each layer has an appropriate, but constant elasticity. At first, a two-layer (2L) VF approximation was made consisting of a soft outer layer, representing the vocal fold mucosa covering a stiffer muscle-like layer [28]. This 2L approach was mainly motivated by the mucosal wave theory or body-cover theory of normal VF vibration, which situates vibration within the mucosal layers only [32, 33]. Recent studies consider more complex ML approximations in order to represent the micro-anatomical structure of a normal VF in more detail [8, 16, 17, 29]. Nevertheless, whereas elasticity values of each VF layer are reported in literature [3, 4, 6, 7, 34–36], the rigidity of a human VF is not constant as one of the functions of the vocal ligament and vocalis muscle is to vary its stiffness. Therefore, a second type of deformable VF replica consists of pressurised latex tubes. These VF replicas intend to mimic the elasticity regulating function of the vocal ligament and vocalis muscle and not its ML structure [27, 30, 31].

Physical studies using these deformable mechanical VF replicas have shown that both VF replica types allow to reproduce sustained VF auto-oscillation following a fluid-structure interaction [8, 16, 27, 28, 30, 37]. Nevertheless, observed major flow and vibration properties, such as the auto-oscillation frequency and required minimum upstream pressure (phonation onset threshold) *etc*., differ between replicas [17]. These differences are partly due to elasticity differences as explicitly shown for pressurised latex tube replicas (second type) [18, 30].

Silicone molded VF replicas (M5, MRI and EPI) of the first type, mimicking the ML representation of the (micro-)anatomical VF structure, are detailed in Section 2.2.1. A pressurised latex tube VF replica (PLT) of the second type, mimicking the elasticity regulating VF function, is outlined in Section 2.2.2. An overview of right-left length L_x, posterior-anterior length L_y, inferior-superior length L_z, VF volume $_{VF}$ and mass m_{VF} is given in Table 2.1. As a reference, typical values observed for a human male adult are indicated as well [3, 10, 38].

Table 2.1: Overall geometrically based VF properties: right-left length L_x, posterior-anterior length L_y, inferior-superior length L_z, volume $_{VF}$ and mass m_{VF}.

	L_x [mm]	L_y [mm]	L_z [mm]	$_{VF}$ [mm^3]	m_{VF} [g]
M5	7.9	17.0	10.7	1025	0.96
MRI	13.1	18.0	10.0	1707	1.57
EPI	8.5	17.0	10.2	1079	1.01
PLT*	11.0	42.0	12.0	3531	3.71
human†	7-8	15-25	4-8	610-830	0.61-0.82

* values at $P_{PLT} = 0$ Pa

† male adult [3, 10, 11, 38] and soft tissue density 1.03 g/cm^3 [9, 39]

2.2.1 Anatomical ML VF representation: silicone replicas M5, MRI and EPI

Silicone VF replicas mimic the ML (micro-)anatomical VF structure as an overlap of silicone molding layers with constant elasticity following the methodology outlined in [8, 16, 17, 29, 40]. Fig. 2.2 illustrates three molded deformable ML silicone VF replicas labelled M5, MRI and EPI. The layer thicknesses l_t and overall dimensions L_x and L_z are indicated (in mm). The M5 replica is a two-layer (2L) reference model following the body-cover theory of phonation representing thus the vocalis muscle and superficial layer, respectively [26]. The MRI replica

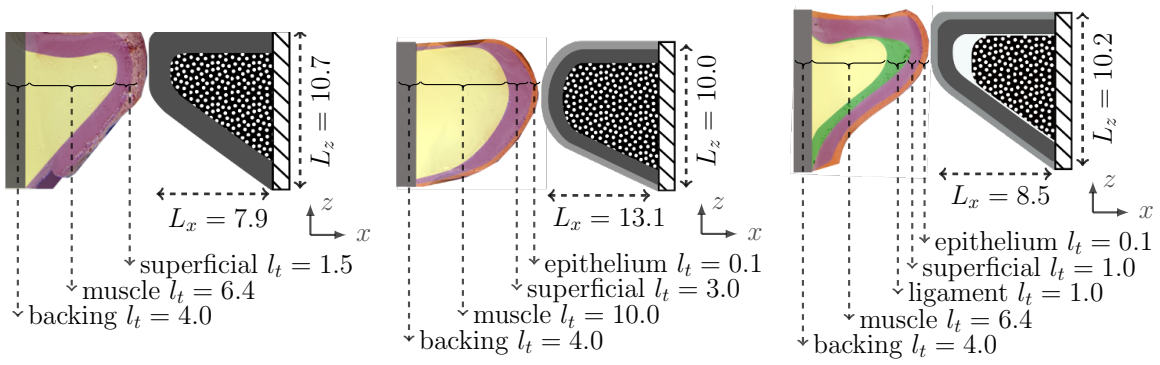

(a) M5 (b) MRI (c) EPI

Figure 2.2: Coronal section (dimensions in mm) of a molded silicone VF replica indicating thickness l_t of each layer (right VF) and its schematic ML representation with overall dimensions L_x and L_z (left VF): a) two-layer M5, b) three-layer MRI and c) four-layer EPI. For visualisation, each layer is molded (right VF) with a different colour.

Table 2.2: Layer properties for a male adult [3, 4, 6, 7, 34–36] and silicone VF replicas (M5*, MRI†, EPI‡ [14, 17, 40]): Young's modulus $\mathscr{E}$, layer thickness l_t, mixture (Mix) TE (Thinner-Ecoflex) or TD (Thinner-Dragonskin), mass mixing ratio $\mathscr{M}$, normalised layer thicknesses l_t/L_x and normalised volumes $/_{VF}$.

Layer	Male adult $\mathscr{E}$ [kPa]	Male adult l_t [mm]	Silicone VF replicas $\mathscr{E}^{\star\star}$ [kPa]	Mix	$\mathscr{M}$ [-]	l_t/L_x [%]	$/_{VF}$ [%]
Muscle	8-29	6.0	$14.4^\star$ $4.0^\dagger$ $23.4^\ddagger$	TE	$2{:}2^\star$ $4{:}2^\dagger$ $1{:}2^\ddagger$	$81.0^\star$ $76.3^\dagger$ $75.2^\ddagger$	$50.0^\star$ $68.5^\dagger$ $38.1^\ddagger$
Ligament	10-45	0.8	$4.0^\ddagger$	TE	$4{:}2^\ddagger$	$11.8^\ddagger$	$7.6^\ddagger$
Superficial	2-9	0.6	$4.0^\star$ $2.2^{\dagger,\ddagger}$	TE	$4{:}2^\star$ $8{:}2^{\dagger,\ddagger}$	$19.0^\star$ $22.9^\dagger$ $11.8^\ddagger$	$50.0^\star$ $27.5^\dagger$ $50.3^\ddagger$
Epithelium$^\circ$	40-60	0.1	$64.7^{\dagger,\ddagger}$	TD	$1{:}2^{\dagger,\ddagger}$	$0.8^\dagger$ $1.2^\ddagger$	$4.0^{\dagger,\ddagger}$

* M5: muscle and superficial
† MRI: muscle, superficial and epithelium
‡ EPI: muscle, ligament, superficial and epithelium
** $\mathscr{E}$ measured from uni-axial tensile test with precision loading [14]
$^\circ$ also used for backing layer

has a three-layer (3L) structure by adding a third thin surface layer representing the epithelium to the 2L structure of the M5 replica [16, 29]. The EPI replica is a four-layer (4L) structure obtained by inserting an extremely soft deep layer, representing the ligament, between the muscle and the superficial layer of the 3L structure of the MRI replica [8]. Each VF is mounted on a stiff backing layer.

Briefly, each molding layer consists of a different mixture of silicone Thinner and Ecoflex (TE, silicone Thinner and two-part A&B Ecoflex 00-30, Smooth-On, Inc., Easton, PA) or silicone Thinner and Dragonskin (TD, two-part A& fast B Dragon Skin 10, Smooth-On, Inc., Easton, PA). The mass mixing ratio $\mathscr{M} = r_T : r_{E(D)}$ for each TE (or TD) mixture expresses the relative mass of silicone thinner to Ecoflex (or Dragonskin). The relative mass portion of silicone thinner r_T is varied between 1 and 8 whereas the relative mass portion of two-part Ecoflex (or Dragonskin) is held constant to $r_{E(D)} = 2$ (1 part A and 1 part B). Layer properties are given in Table 2.2 [13, 14, 17]. Measured (uni-axial tensile test [14]) low-strain Young's moduli $\mathscr{E}$ for TE or TD mixtures of the molding layers (up to 65 kPa) are consistent with values (up to 60 kPa) reported for VF's of male adults [3, 4, 6–8, 41]. Note that the Young's modulus $\mathscr{E}$ of the molded ligament layer is underestimated as no tension is accounted for in the deep layer. In general, both the Young's modulus $\mathscr{E}$ as well as the density of TE mixtures decreases as the mixing ratio $\mathscr{M}$ (and hence r_T) increases [14].

2.2.2 Elasticity regulation function: PLT replica

A VF replica with variable elasticity is obtained by representing each VF as a pressurised latex tube (PLT) [13, 15, 31]. Each VF consists of a latex tube (diameter 11 mm, thickness 0.2 mm, low-strain Young's modulus 1.8 MPa and density 1635 kg·m^{-3} [40]) enveloping a hollow rigid metal support (diameter 12 mm, posterior-anterior length 42 mm) as depicted in Fig. 2.3(a). The latex tube is pressurised by filling it with distilled water at room temperature (temperature 22 ± 2 C°, density $\rho_L = 998$ kg·m^{-3}, dynamic viscosity coefficient $\mu_L = 1.0 \times 10^{-3}$ Pa·s). The water inlet (internal diameter 4 mm) is connected to a water column whose height determines the internal pressure P_{PLT} within each latex tube. Overall PLT VF properties L_x, L_y, L_z, $_{VF}$ and m_{VF} at $P_{PLT} = 0$ Pa are given in Table 2.1. The elasticity of the PLT VF replica varies with the imposed P_{PLT} and thus with the height of the water column [42]. Concretely, in this work P_{PLT} is varied between 450 Pa and 6500 Pa (with steps of at most 500 Pa) corresponding to a water column range of about 60 cmH_2O.

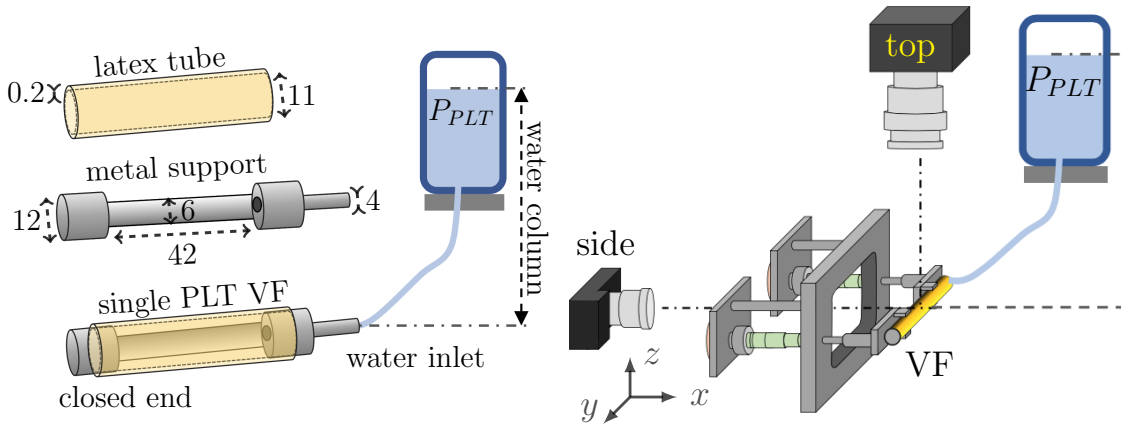

(a) single PLT VF

(b) right VF positioning and view angles

Figure 2.3: Overview pressurised latex tube (PLT) VF replica (dimensions in mm): a) single PLT VF, b) spatial positioning of right VF and camera view angles (side and top).

The PLT VF is then positioned in a rigid frame, as depicted in Fig. 2.3(b), in the same way as during fluid-structure interaction experiments [13, 15, 31]. The metal support part of the PLT VF is fixed whereas the unconstrained deformable portion faces the medio-sagittal plane as schematically shown in Fig. 2.3(b). The frame allows simultaneous observation of the VF along the sagittal plane (side view angle in Fig. 2.3(b), Nikon AF-S Nikkor 18-70 mm, shutter time 2 ms, aperture 4.3 mm, 0.037 mm/px) and along the transverse plane (top view angle in Fig. 2.3(b), Motion Blitz Eosens Cube 7, shutter time 726 μs, aperture 11 mm, ≤ 0.049 mm/px).

CHAPTER 3

Low-strain effective Young's modulus model and validation for multi layered silicone specimens

---

Based on:

Ahmad, M., Bouvet, A., Pelorson, X., & Van Hirtum, A. (2021). Modeling and validation of the elasticity parameters of multi-layer specimens pertinent to silicone vocal fold replicas. International Journal of Mechanical Sciences, 208, 106685.

Ahmad, M., Pelorson, X., Fernández, I. A., Guasch, O., & Van Hirtum, A. (2022). Low-strain effective Young's modulus model and validation for multi-layer vocal fold-based silicone specimens with inclusions. Journal of Applied Physics, 131(5), 054701.

3.1 Introduction

Physical studies [16, 17] have shown that deformable mechanical VF replicas allow one to reproduce sustained VF auto-oscillation. Nevertheless, major flow and vibration properties, such as their auto-oscillation frequency and required minimum upstream pressure (phonation onset threshold), vary between replicas. These differences are partly attributed to the elasticity of the replicas, which depend on the adopted VF representation and the layer molding. Despite its role in the fluid-structure interaction, and hence on observed feature values and physical model validation, the effective elasticity of silicone VF replicas is rarely considered, instead the elasticity of the individual molding layers is mentioned.

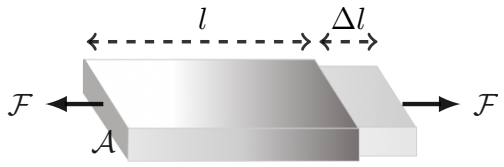

Figure 3.1: Elastic material with cross-section $\mathscr{A}$, length l and elongation Δl following an uni-axial force $\mathscr{F}$.

Each molding layer composition within the silicone VF replicas is assumed to be an elastic and isotropic solid material consisting of a single constituent or of a mixture of multiple constituents. The layers elasticity is then characterised by Young's modulus $\mathscr{E}$ for a single constituent (or component) and by effective Young's modulus $\mathscr{E}_{eff}$ for a mixture of constituents (or components). Considering a material portion with length l and cross-section $\mathscr{A}$ depicted in Fig. 3.1, Young's modulus $\mathscr{E}_{(eff)}$ relates stress σ,

$$\sigma = \frac{\mathscr{F}}{\mathscr{A}}, \tag{3.1}$$

exerted by an uni-axial force $\mathscr{F}$, to its relative linear deformation strain ε,

$$\varepsilon = \frac{\Delta l}{l}, \tag{3.2}$$

expressing a linear stress-strain relationship

$$\mathscr{E}_{(eff)} = \frac{\sigma}{\varepsilon}, \tag{3.3}$$

with $\Delta l \geq 0$ denoting the elongation along the force $\mathscr{F}$ direction.

The aim of this work is to consider and validate an analytical model for the effective Young's modulus $\mathscr{E}_{eff}$ of ML silicone composites from its layers properties, *i.e.* $\mathscr{E}_{eff}$ and geometry.

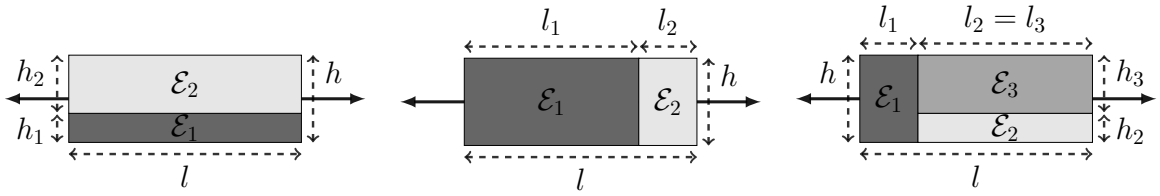

(a) parallel, $\|$ (b) serial, $\perp$ (c) combined, $\perp\|$

Figure 3.2: Layer stacking about the force direction (full arrows) in ML composites with the stacking orientation $o_{j,j+1} \in \{\perp, \|\}$ of adjacent layers: a) 2L parallel ($\|$) with $o_{(1,2)} = \|$, b) 2L serial ($\perp$) with $o_{(1,2)} = \perp$, c) 3L combined ($\perp\|$) with $o_{(1,2)} = \perp$ and $o_{(2,3)} = \|$.

The model is also extended to account for an arbitrary-shaped inclusion of any size embedded somewhere within a single or multiple layers.

3.2 Analytical model of the effective linear Young's modulus

ML composites are considered which consist of n elastic, isotropic and perfectly bounded layers, which are themselves composed of one or more constituents. The linear stress-strain behaviour of a ML composite is then described in the same way as for each individual layer by attributing an effective Young's modulus $\mathscr{E}_{eff}$ describing the linear stress-strain behaviour for an equivalent homogeneous elastic composite. It follows that Eq. (3.3) holds for each layer and for the equivalent homogeneous ML composite. An analytical model is sought predicting $\mathscr{E}_{eff}$ for the equivalent homogeneous composite for which adjacent layers are stacked either parallel ($\|$) or serial ($\perp$) with respect to the force or stress direction. Stacking orientations between adjacent layers are denoted $o_{(j,j+1)} \in \{\perp, \|\}$ with $j = 1 \ldots n-1$. The stacking orientation is assumed to remain similar during all deformation stages. Thus, besides parallel (Fig. 3.2(a)) or serial (Fig. 3.2(b)) stacked composites, both stacking orientations ($\|$ and $\perp$) can be combined to describe more complex ML composites (combined, $\perp\|$) as illustrated in Fig. 3.2(c). Each layer $i = 1 \ldots n$ is characterised by its length l_i (parallel to the force direction), height h_i (transverse to the force direction) and Young's modulus $\mathscr{E}_i$. The effective Young's modulus $\mathscr{E}_{eff}$ for parallel or serial stacked layers is then modelled applying the theory of linear elasticity (Eq. (3.3)) to each layer and to the equivalent homogeneous composite.

For n parallel stacked layers the force is distributed over the layers ($\mathscr{F} = \sum_{i=1}^{n} \mathscr{F}_i$) so that the strain ε in the equivalent homogeneous composite and the strain $\varepsilon_{i=1\ldots n}$ in each layer is constant, *i.e.* $\varepsilon_{i=1\ldots n} = \varepsilon$. The effective Young's modulus of the equivalent homogeneous composite with transverse height $h = \sum_{i=1}^{n} h_i$ is then modelled using the Voigt hypothesis [43] of homogeneous

deformation as

$$\mathscr{E}_{eff}^{\parallel} = \frac{\sum_{i=1}^{n} h_i \cdot \mathscr{E}_i}{\sum_{i=1}^{n} h_i}. \tag{3.4}$$

Thus, $\mathscr{E}_{eff}^{\parallel}$ is computed as the weighted arithmetic mean (WAM) of the layers Young's moduli $\mathscr{E}_i$. The arithmetic mean is weighted with transverse layer heights h_i, which amounts to applying the rule of mixtures.

For n serial stacked layers the stress σ in the equivalent homogeneous composite and the stress $\sigma_{i=1\ldots n}$ in each layer is constant, *i.e.* $\sigma_{i=1\ldots n} = \sigma$. The effective Young's modulus of the equivalent homogeneous composite with parallel length $l = \sum_{i=1}^{n} l_i$ is then modelled using the Reuss hypothesis [44] of homogeneous stress as

$$\mathscr{E}_{eff}^{\perp} = \frac{\sum_{i=1}^{n} l_i}{\sum_{i=1}^{n} \left(\frac{l_i}{\mathscr{E}_i} \right)}. \tag{3.5}$$

Thus, $\mathscr{E}_{eff}^{\perp}$ is obtained as the harmonic mean of the layers Young's moduli $\mathscr{E}_i$ weighted with their parallel lengths l_i. It is noted that applying the rule of mixtures would results in the weighted arithmetic mean of $\mathscr{E}_i$ instead of the weighted harmonic mean (WHM) expressed in Eq. (3.5).

Both Eq. (3.4) and Eq. (3.5) result in $\mathscr{E}_{eff}^{\perp,\parallel} = \mathscr{E}_1$ when $n = 1$. Eq. (3.4) and Eq. (3.5) do not account for the stacking order so that modelled $\mathscr{E}_{eff}^{\parallel}$ and $\mathscr{E}_{eff}^{\perp}$ remain unaffected when layers are permuted or splitted as long as the overall composition and orientation of the stack is maintained. It is well established that WAM values are larger than WHM values. Therefore, layers with large $\mathscr{E}_i$ tend to mask layers with lower Y_i for modelled $\mathscr{E}_{eff}^{\parallel}$ (WAM in Eq. (3.4)) whereas this is less the case for modelled $\mathscr{E}_{eff}^{\perp}$ (WHM in Eq. (3.5)).

The equivalent Young's modulus $\mathscr{E}_{eff}^{\perp\parallel}$ of more complex ML composites with combined ($\perp\parallel$) stacking, composed of both serial and parallel layers as illustrated in Fig. 3.2(c), is modelled using a two-step approach. Firstly, Eq. (3.4) is used to homogenise parallel stacked layers. Secondly, Eq. (3.5) is applied to the resulting stack of serial layers. As WAM (Eq. (3.4)) and WHM (Eq. (3.5)) value layers with large $\mathscr{E}_i$ differently, the layer order might affect the model value of $\mathscr{E}_{eff}^{\perp\parallel}$, which is not the case for ML composites consisting of serial or parallel layers only.

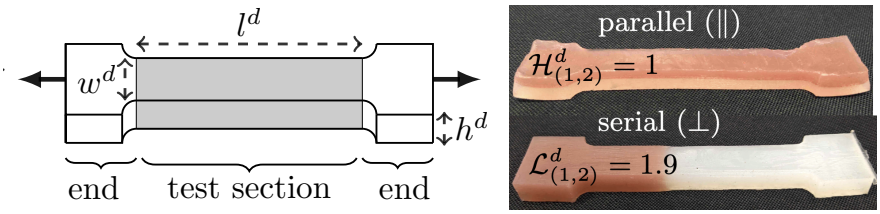

(a) design (b) 2L moldings

Figure 3.3: Bone-shaped specimens: a) design (superscript d) for uni-axial stress testing (black arrows), end terminations for clamping and the test section (shaded) with $l^d = 80$ mm, $h^d = 10$ mm and $w^d = 15$ mm, b) molded parallel (∥) and serial (⊥) 2L composites (colours) for stacking dimension ratios $\mathcal{H}^d_{(1,2)} = h_1/h_2$ and $\mathcal{L}^d_{(1,2)} = l_1/l_2$.

3.3 Design of specimens without inclusion

3.3.1 Model analysis and selected designs of specimens without inclusion

In this section the $\mathcal{E}_{eff}$ model approach outlined in Section 3.2 is analysed for bone-shaped ML composites with two or three layers stacked parallel (Eq. (3.4), WAM), serial (Eq. (3.5), WHM) or combined (Eq. (3.4) followed by Eq. (3.5), WAM followed by WHM). The model analysis is then used to select and motivate the designs of bone-shaped specimen suitable to validate the model approach outlined in Section 3.2 against experimental values obtained from uni-axial stress testing outlined in Section 3.5. Design values are indicated with superscript d. Model analysis is then assessed for bone-shaped specimen designs containing a test section with dimensions $l^d = 80$ mm, $h^d = 10$ mm, $w^d = 15$ mm and volume $\mathcal{V}^d = 12$ cm^3 as depicted in Fig. 3.3(a). Layers are indicated with indexes $i = 1 \ldots n$ and $j = 1 \ldots n-1$. The layer width is held constant so that $w^d_i = w^d$ for all designs layers regardless of the stacking orientation. The geometrical specimen designs are then characterised from the height dimension ratio $\mathcal{H}^d$ and the length dimension ratio $\mathcal{L}^d$ between adjacent stacked layers:

$$\mathcal{H}^d_{(j,j+1)} = \frac{h^d_j}{h^d_{j+1}}, \tag{3.6a}$$

$$\mathcal{L}^d_{(j,j+1)} = \frac{l^d_j}{l^d_{j+1}}. \tag{3.6b}$$

For two adjacent parallel stacked layers ($o_{(j,j+1)} = \parallel$ and $l^d_j = l^d_{j+1}$), the layers geometry is characterised by the height stacking dimension ratio $\mathcal{H}^d_{(j,j+1)}$ since $\mathcal{L}^d_{(j,j+1)} = 1$ is constant. Similarly, for two adjacent serial stacked layers ($o_{(j,j+1)} = \perp$ and $h^d_j = h^d_{j+1}$), the layers geometry is characterised by the length stacking dimension ratio $\mathcal{L}^d_{(j,j+1)}$ as $\mathcal{H}^d_{(j,j+1)} = 1$ is constant. Consequently,

Table 3.1: 1L specimen design: label, mixture, mixing ratio $\mathscr{M}$, reference $\mathscr{E}_{eff}^{ref}$ [17, 40].

Specimen	mixture	ratio $\mathscr{M}$	$\mathscr{E}_{eff}^{ref}$ [kPa]
I_1	TD	1:2	52.0
I_2	TE	2:2	10.4
I_3	TE	4:2	4.9

the stacking geometry of ML specimens is fully defined by the series of stacking dimension ratios $\nabla^d_{(j,j+1)} \in \{\mathscr{H}^d_{(j,j+1)}, \mathscr{L}^d_{(j,j+1)}\}$ associated with the stacking orientation between adjacent layers $o_{(j,j+1)}$. It follows that for ML composites composed solely with either parallel or serial stacked layers, the series reduces to $\nabla^d_{(j,j+1)} = \mathscr{H}^d_{(j,j+1)}$ or $\nabla^d_{(j,j+1)} = \mathscr{L}^d_{(j,j+1)}$, respectively. Moreover, the design of ML composite specimens must satisfy $0.1 \leq \nabla^d_{(j,j+1)} \leq 6.4$ in order to match the order of magnitude associated with the ratio of adjacent layer thicknesses for the silicone VF replicas outlined in Section 2.2. The specimen designs composition is characterised from the composition ratio between the Young's moduli of adjacent layers as:

$$\mathscr{B}^d_{(j,j+1)} = \frac{\left(\mathscr{E}^d_{eff}\right)_j}{\left(\mathscr{E}^d_{eff}\right)_{j+1}}. \tag{3.7}$$

Each layer must contain one of the mixtures pertinent to silicone VF replicas described in Section 2.2. Therefore, model analysis of $\mathscr{E}^d_{eff}$ is assessed for $0.2 \leq \mathscr{B}_{(j,j+1)} \leq 5$ within the range pertinent for silicone VF replicas. In the following, first (Section 3.3.1.1) three single layer compositions are detailed resulting in three one-layer (1L, $n = 1$) specimen designs, next (Section 3.3.1.2) model analysis motivates the designs of six two-layer (2L, $n = 2$) specimen and finally (in Section 3.3.1.3) the designs of seven three-layer (3L, $n = 3$) specimens is justified.

3.3.1.1 1L specimen design

One-layer specimens, labelled I, are designed in order to address the reproducibility of TD and TE mixtures compared to reference values $\mathscr{E}_{eff}^{ref}$ in [17, 40] as literature values (Table 2.2) of $\mathscr{E}_{eff}$ for similar moldings vary considerable, *e.g.* 67% for ES $\mathscr{M} = 4:2$ as $\mathscr{E}_{eff}^{ref} = 4.9$ kPa in [17, 40] compared to $\mathscr{E}_{eff} = 1.6$ kPa in [8]. Single layer design dimensions of a 1L specimen match the dimensions of the test section, *i.e.* $l_1^d = l^d$, $h_1^d = h^d$ and $w_1^d = w^d$. An overview of 1L specimen designs is given in Table 3.1. The three 1L specimens, and hence their layer mixtures, are selected for three reasons: 1) there frequent use in ML silicone replicas (Table 2.2), 2) known reference $\mathscr{E}_{eff}^{ref}$ from [17, 40] and 3) the resulting $\mathscr{E}_{eff}^{ref}$-range ($4.9 \leq \mathscr{E}_{eff}^{ref} \leq 52$ kPa) overlaps most of the $\mathscr{E}$-range associated with anatomical VF layers ($\mathscr{E} \leq 60$ kPa, Table 2.2).

Table 3.2: 2L specimen design: label, stacking orientation $o_{(1,2)}$, layer composition, stacking composition ratio $\mathscr{B}^{ref}_{(1,2)}$, stacking dimension ratio $\mathscr{H}^{d}_{(1,2)}$ or $\mathscr{L}^{d}_{(1,2)}$, modelled $\mathscr{E}^{\cdot,d}_{eff}$.

Specimen	$o_{(1,2)}$	composition		$\mathscr{B}^{ref}_{(1,2)}$	$\mathscr{H}^{d}_{(1,2)}$, $\mathscr{L}^{d}_{(1,2)}$	model $\mathscr{E}^{\cdot,d}_{eff}$
		layer 1	layer 2			
$II_{1,\parallel}$	$\parallel$	as I_2	as I_3	2.1	$\mathscr{H}^{d}=5.0$	9.5 kPa
$II_{2,\parallel}$	$\parallel$	as I_2	as I_3	2.1	$\mathscr{H}^{d}=1.0$	7.7 kPa
$II_{3,\parallel}$	$\parallel$	as I_1	as I_2	5.0	$\mathscr{H}^{d}=1.0$	31.2 kPa
$II_{1,\perp}$	$\perp$	as I_2	as I_3	2.1	$\mathscr{L}^{d}=5.0$	8.8 kPa
$II_{2,\perp}$	$\perp$	as I_2	as I_3	2.1	$\mathscr{L}^{d}=1.0$	6.7 kPa
$II_{3,\perp}$	$\perp$	as I_1	as I_2	5.0	$\mathscr{L}^{d}=1.0$	17.3 kPa

Indeed, reported $\mathscr{E}^{ref}_{eff}$ in Table 3.1 represent values reported for the muscle (I_2), superficial (I_3) and epithelium (I_1) layer of a human VF in Table 2.2.

These three mixtures are then used in the model analysis and resulting designs of the 2L and 3L composite specimens outlined hereafter. The layer mixtures (and associated $\mathscr{E}^{d}_{eff}=\mathscr{E}^{ref}_{eff}$ in Table 3.1) for these ML specimens are indicated referring to the corresponding 1L specimen, *i.e.* as I_1, as I_2 or as I_3.

3.3.1.2 2L specimen design

Two-layer composite specimens, labelled II, consist of two parallel ($o_{(1,2)}=\parallel$ in Fig. 3.2(a)) or two serial ($o_{(1,2)}=\perp$ in Fig. 3.2(b)) stacked layers. The geometrical design is fully characterised considering the stacking dimension ratio between both layers given as $\nabla^{d}_{(1,2)}=\mathscr{H}^{d}_{(1,2)}$ for parallel ($\parallel$) stacking and $\nabla^{d}_{(1,2)}=\mathscr{L}^{d}_{(1,2)}$ for serial ($\perp$) stacking. This is illustrated for colour-molded specimens in Fig. 3.3(b). An overview of the 2L specimen designs and its characteristics is given in Table 3.2.

Modelled curves for $\mathscr{E}^{\parallel,d}_{eff}$ (from Eq. (3.4)) and for $\mathscr{E}^{\perp,d}_{eff}$ (from Eq. (3.5)) as a function of their stacking dimension ratio are plotted in Fig. 3.4(a) and Fig. 3.4(b), respectively. Modelled values for three different 2L composition ratios $\mathscr{B}^{ref}_{(1,2)}$ are shown, *i.e.* $\mathscr{B}^{ref}_{(1,2)}=2.1$ for mixtures (as I_2, as I_3), $\mathscr{B}^{ref}_{(1,2)}=5$ for mixtures (as I_1, as I_2) and $\mathscr{B}^{ref}_{(1,2)}=10.6$ for mixtures (as I_1, as I_3). As a reference, $\mathscr{E}^{ref}_{eff}$ for 1L specimens are indicated (horizontal dashed lines annotated $I_{1,2,3}$). The shown stacking dimension ratio ranges ($0<\mathscr{H}^{d}_{(1,2)}\leq 700$ and $0<\mathscr{L}^{d}_{(1,2)}\leq 90$) are adapted

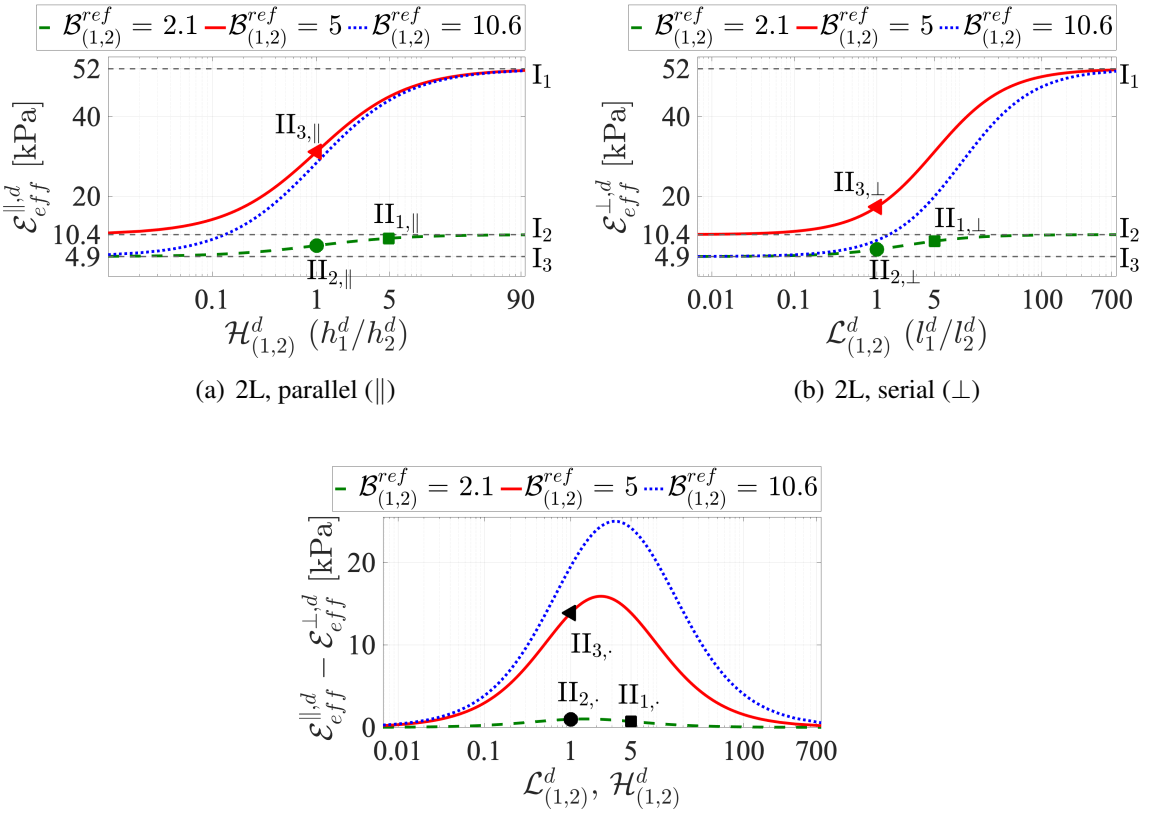

(a) 2L, parallel ($\parallel$)

(b) 2L, serial ($\perp$)

(c) 2L, WAM ($\parallel$) minus WHM ($\perp$)

Figure 3.4: Modelled $\mathscr{E}^{\cdot,d}_{eff}$ for 2L stacking for different $\mathscr{B}^{ref}_{(1,2)}$ as a function of dimension ratio. 2L specimen design values (symbols) are annotated ($\mathrm{II}_{\cdot,\parallel}$ or $\mathrm{II}_{\cdot,\perp}$): a) $\mathscr{H}^d_{(1,2)}$ for parallel ($\parallel$), b) $\mathscr{L}^d_{(1,2)}$ for serial ($\perp$). Horizontal dashed lines indicate $\mathscr{E}^{ref}_{eff}$ of individual layers ($\mathrm{I}_\cdot$), c) averaging (WAM ($\parallel$) or WHM ($\perp$)) induced difference $\mathscr{E}^{\parallel,d}_{eff} - \mathscr{E}^{\perp,d}_{eff}$.

so that modelled $\mathscr{E}^{\cdot,d}_{eff}$ vary in the range between single layer values $(\mathscr{E}^{ref}_{eff})_{i=2}$ and $(\mathscr{E}^{ref}_{eff})_{i=1}$. For similar dimension ratios ($\mathscr{L}^{d}_{(1,2)} = \mathscr{H}^{d}_{(1,2)}$) and composition ratios $\mathscr{B}^{ref}_{(1,2)}$, modelled $\mathscr{E}^{\cdot,d}_{eff}$ values for serial and for parallel stacking differ only due to the applied averaging, *i.e.* arithmetic (WAM) for parallel stacking in Eq. (3.4) and harmonic (WHM) for serial stacking in Eq. (3.5). The resulting inter-model difference, $\mathscr{E}^{\parallel,d}_{eff} - \mathscr{E}^{\perp,d}_{eff} \geq 0$, due to the stacking orientation is plotted in Fig. 3.4(c). The curves exhibit a maximum for dimension ratios in the range of interest ($0.1 \leq \nabla^{d}_{(j,j+1)} \leq 6.4$) and tend to zero for very small or very large ratios for which $\mathscr{E}^{\cdot,d}_{eff} \approx (\mathscr{E}^{ref}_{eff})_2$ and $\mathscr{E}^{\cdot,d}_{eff} \approx (\mathscr{E}^{ref}_{eff})_1$, respectively. The difference increases with composition ratio $\mathscr{B}^{ref}_{(1,2)}$ reflecting the increasing impact of layers with large $\mathscr{E}^{ref}_{eff}$ to modelled $\mathscr{E}^{\parallel,d}_{eff}$ values. This is also seen from Fig. 3.4(a) and Fig. 3.4(b), *e.g.* comparing dimension ratios at which $\mathscr{E}^{\cdot,d}_{eff}$ increases from its lowest value $(\mathscr{E}^{ref}_{eff})_{i=2}$.

Modelled curves show that stacking dimension ratios $\nabla^{d}_{(1,2)} = \{1, 5\}$ are suitable for 2L specimen design as modelled $\mathscr{E}^{\cdot,d}_{eff}$ differ between both stacking orientations $o_{(1,2)} \in \{\parallel, \perp\}$, vary with dimension ratio $\nabla^{d}_{(j,j+1)}$ and differ from layer values $(\mathscr{E}^{ref}_{eff})_i$ for all $\mathscr{B}^{ref}_{(1,2)}$. Model curves for $\mathscr{B}^{ref}_{(1,2)} \in \{2.1, 5.0\}$ (dashed and full curve in Fig. 3.4) enclose the curve for $\mathscr{B}^{ref}_{(1,2)} = 10.6$ (dotted curve in Fig. 3.4) so that the influence of the stacking composition on $\mathscr{E}^{d}_{eff}$ is larger considering $\mathscr{B}^{ref}_{(1,2)} \in \{2.1, 5.0\}$ for 2L specimen design. The 2L specimens are thus designed so that for each stacking orientation $o_{(1,2)} \in \{\parallel, \perp\}$ the influence of stacking composition $\mathscr{B}^{ref}_{(1,2)} \in \{2.1, 5.0\}$ ($\mathrm{II}_{2,\cdot}$ versus $\mathrm{II}_{3,\cdot}$) and stacking dimension ratio $\nabla^{d}_{(1,2)} \in \{1, 5\}$ ($\mathrm{II}_{1,\cdot}$ versus $\mathrm{II}_{2,\cdot}$) on the modelled $\mathscr{E}^{\cdot,d}_{eff}$ can be evaluated. The influence of stacking orientation $o_{(1,2)}$ on modelled $\mathscr{E}^{\cdot,d}_{eff}$ can be assessed as well ($\mathrm{II}_{\cdot,\parallel}$ versus $\mathrm{II}_{\cdot,\perp}$). Modelled values $\mathscr{E}^{\cdot,d}_{eff}$ for 2L specimen designs are reported in Table 3.2 and indicated (symbols annotated with the specimen label $\mathrm{II}_{\cdot,\cdot}$) in Fig. 3.4.

3.3.1.3 3L specimen design

Three-layer composite specimens, labelled III, consist of three layers with 2 or 3 different mixtures. Adjacent layers are stacked either parallel or serial so that $o_{(1,2)}, o_{(2,3)} \in \{\parallel, \perp\}$. Dimension ratios are chosen within the range of interest $0.1 \leq \nabla^{d}_{(1,2)}, \nabla^{d}_{(2,3)} \leq 6.4$. The 3L composition is characterised by composition ratios $\mathscr{B}^{ref}_{(1,2)}$ and $\mathscr{B}^{ref}_{(2,3)}$. An overview of the 3L specimen designs is given in Table 3.3.

Table 3.3: 3L specimen design: label, stacking orientation o, layer composition, stacking composition ratios $\mathscr{B}^{ref}$, stacking dimension ratio $\nabla^d \in \{\mathscr{H}^d, \mathscr{L}^d\}$, modelled $\mathscr{E}^{\cdot,d}_{eff}$.

Specimen	$o_{(j,j+1)}$		layer i composition			$\mathscr{B}^{ref}_{(j,j+1)}$		$\mathscr{H}^d_{(j,j+1)}, \mathscr{L}^d_{(j,j+1)}$		model
	(1,2)	(2,3)	1	2	3	(1,2)	(2,3)	(1,2)	(2,3)	$\mathscr{E}^{\cdot,d}_{eff}$
$III_{1,\perp}$	$\perp$	$\perp$	as I_2	as I_3	as I_2	2.1	0.47	$\mathscr{L}^d = 0.50$	$\mathscr{L}^d = 2.0$	6.7 kPa
$III_{2,\perp}$	$\perp$	$\perp$	as I_1	as I_2	as I_1	5.0	0.2	$\mathscr{L}^d = 0.50$	$\mathscr{L}^d = 2.0$	17.3 kPa
$III_{3,\perp}$	$\perp$	$\perp$						$\mathscr{L}^d = 0.66$	$\mathscr{L}^d = 1.0$	8.5 kPa
$III_{4,\perp}$	$\perp$	$\perp$						$\mathscr{L}^d = 4.2$	$\mathscr{L}^d = 1.0$	16.2 kPa
$III_{1,\parallel}$	$\parallel$	$\parallel$	as I_1	as I_2	as I_3	5.0	2.1	$\mathscr{H}^d = 0.50$	$\mathscr{H}^d = 1.0$	16.5 kPa
$III_{1,\perp\parallel}$	$\perp$	$\parallel$						$\mathscr{L}^d = 0.14$	$\mathscr{H}^d = 1.5$	8.7 kPa
$III_{2,\perp\parallel}$	$\perp$	$\parallel$						$\mathscr{L}^d = 2.1$	$\mathscr{H}^d = 1.5$	14.4 kPa

Two 3L composite specimens ($III_{1,\perp}$ and $III_{2,\perp}$) with serial stacking ($o_{(j,j+1)} = \perp$) are designed in order to evaluate the model property that layer splitting and layer permutation do not affect modelled $\mathscr{E}^{\perp,d}_{eff}$. These specimens have the same overall composition as 2L specimens $II_{2,\perp}$ and $II_{3,\perp}$ respectively, so that modelled $\mathscr{E}^{\perp,d}_{eff} \in \{6.7, 17.3\}$ kPa in Table 3.3 and Table 3.2 match. Both 3L specimens are obtained by permuting half of the first layer ($i = 1$) of the 2L specimens to form a third layer ($i = 3$) on top of the second layer ($i = 2$) so that the dimension ratio $\mathscr{L}^d_{1,2} = 0.5$ of the resulting 3L specimens amounts to half of the 2L specimens value and $\mathscr{L}^d_{2,3} = \left(\mathscr{L}^d_{1,2}\right)^{-1}$. It follows that $(\mathscr{E}^{ref}_{eff})_1 = (\mathscr{E}^{ref}_{eff})_3$ so that $\mathscr{B}^{ref}_{(1,2)} = \left(\mathscr{B}^{ref}_{(2,3)}\right)^{-1}$ with $\mathscr{B}^{ref}_{(1,2)} \in \{2.1, 5\}$ as for the 2L specimens in Table 3.2. Serial ($\perp$, WHM in Eq. (3.5)) and not parallel ($\parallel$, WAM in Eq. (3.4)) stacked specimens are considered as modelled $\mathscr{E}^{\perp,d}_{eff}$ are less affected by layers with large $\mathscr{E}^{ref}_{eff}$ than modelled $\mathscr{E}^{\parallel,d}_{eff}$, so that the potential influence of layer permutation in a parallel stack is more likely to go unnoticed.

Different stacking orientations ($o_{(1,2)}, o_{(2,3)} \in \{\parallel, \perp\}$) and dimension ratios ($\nabla^d_{(1,2)}$ and $\nabla^d_{(2,3)}$) are considered for the design of five 3L composite specimens ($III_{3,\perp}$, $III_{4,\perp}$, $III_{1,\parallel}$, $III_{1,\perp\parallel}$ and $III_{2,\perp\parallel}$) with three different layer mixtures. The same mixtures (as I_1 in layer $i = 1$, as I_2 in layer $i = 2$, as I_3 in layer $i = 3$) are considered, so that $\left(\mathscr{E}^{ref}_{eff}\right)_{i=1} > \left(\mathscr{E}^{ref}_{eff}\right)_{i=2} > \left(\mathscr{E}^{ref}_{eff}\right)_{i=3}$ result in constant composition ratios $\mathscr{B}^{ref}_{(1,2)} = 5$ from mixtures (as I_1, as I_2) and $\mathscr{B}^{ref}_{(2,3)} = 2.1$ from mixtures (as I_2, as I_3). The specimens are stacked either parallel ($o_{(1,2)}, o_{(2,3)} = \parallel$, $\nabla^d_{(j,j+1)} = \mathscr{H}^d_{(j,j+1)}$), serial ($o_{(1,2)}, o_{(2,3)} = \perp$, $\nabla^d_{(j,j+1)} = \mathscr{L}^d_{(j,j+1)}$) or combined ($o_{(1,2)} = \perp$, $o_{(2,3)} = \parallel$, $\nabla^d_{(1,2)} = \mathscr{L}^d_{(1,2)}$, $\nabla^d_{(2,3)} = \mathscr{H}^d_{(2,3)}$) as schematically illustrated in Fig. 3.2(c).

Modelled curves for $\mathscr{E}^{\parallel,d}_{eff}$ (from Eq. (3.4)), $\mathscr{E}^{\perp,d}_{eff}$ (from Eq. (3.5)) and $\mathscr{E}^{\parallel\perp,d}_{eff}$ (from Eq. (3.4)

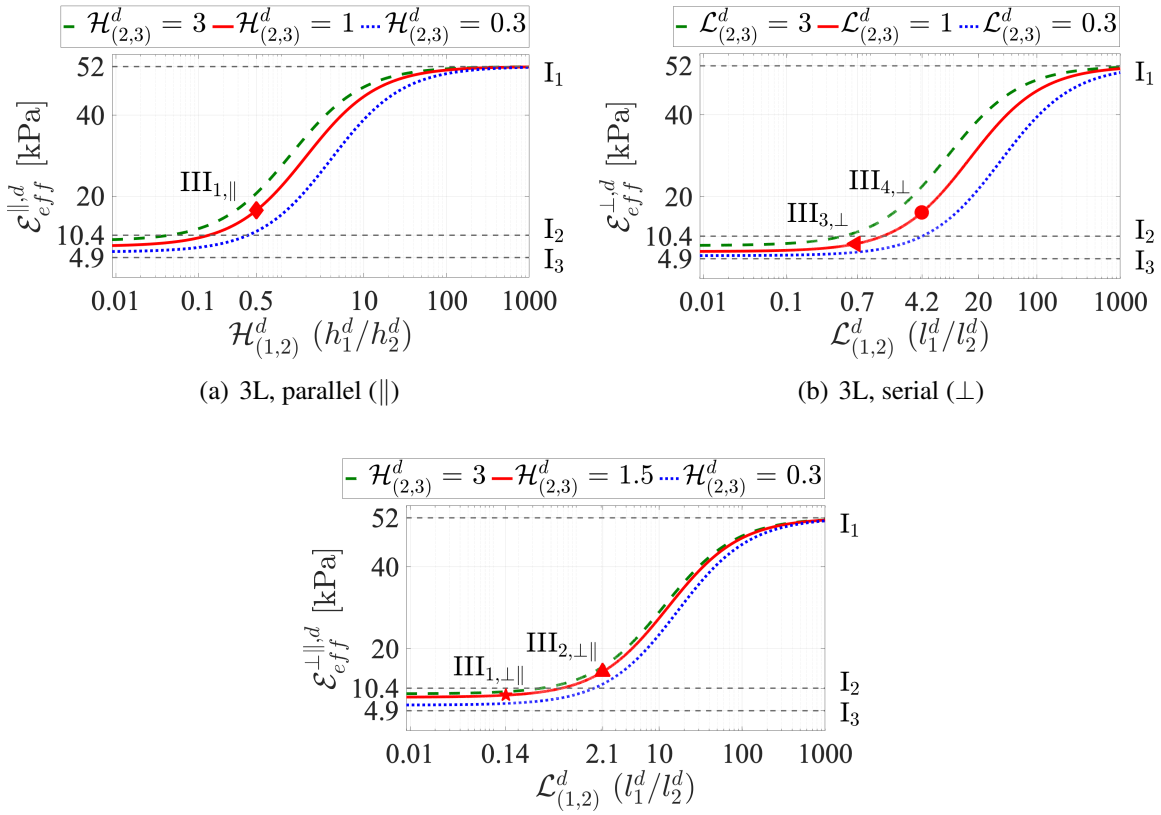

(a) 3L, parallel (∥)

(b) 3L, serial (⊥)

(c) 3L, combined (⊥∥)

Figure 3.5: Modelled $\mathscr{E}^{\cdot,d}_{eff}$ for 3L stacking with $\mathscr{B}^{ref}_{(1,2)} = 5$ and $\mathscr{B}^{ref}_{(2,3)} = 2.1$ as a function of dimension ratio $\nabla^d_{(1,2)}$ for three different dimension ratios $\nabla^d_{(2,3)}$. 3L specimen design values (symbols) are annotated (III$_{\cdot,\parallel}$, III$_{\cdot,\perp}$ or III$_{\cdot,\perp\parallel}$): a) parallel, $o_{(j,j+1)} = \parallel$ and $\nabla^d_{(j,j+1)} = \mathscr{H}^d_{(j,j+1)}$, b) serial, $o_{(j,j+1)} = \perp$ and $\nabla^d_{(j,j+1)} = \mathscr{L}^d_{(j,j+1)}$ and c) combined $o_{(1,2)} = \perp$ and $o_{(2,3)} = \parallel$ so that $\nabla^d_{(1,2)} = \mathscr{L}^d_{(1,2)}$ and $\nabla^d_{(2,3)} = \mathscr{H}^d_{(2,3)}$. Horizontal dashed lines indicate $\mathscr{E}^{ref}_{eff}$ of individual layers (I$_\cdot$).

followed by Eq. (3.5)) as a function of dimension ratio $\nabla^d_{(1,2)}$ are plotted in Fig. 3.5(a), Fig. 3.5(b) and Fig. 3.5(c), respectively. Modelled values for three different dimension ratios $0.3 \leq \nabla^d_{(2,3)} \leq 3$ are shown. As a reference, $\mathscr{E}^{ref}_{eff}$ for 1L specimens are indicated (horizontal dashed lines annotated $\mathrm{I}_{1,2,3}$). The shown stacking dimension ratio range ($0 < \nabla^d_{(1,2)} \leq 1000$) is adapted so that modelled $\mathscr{E}^{\cdot,d}_{eff}$ vary within the range spanned between the smallest $\left(\mathscr{E}^{ref}_{eff}\right)_{i=3}$ and largest $\left(\mathscr{E}^{ref}_{eff}\right)_{i=1}$ single layer values. For large dimension ratios $\nabla^d_{1,2}$ modelled $\mathscr{E}^{\cdot,d}_{eff}$ approximate the largest single layer value $\left(\mathscr{E}^{ref}_{eff}\right)_{i=1}$ so that $\mathscr{E}^{\cdot,d}_{eff} \approx \left(\mathscr{E}^{ref}_{eff}\right)_{i=1}$. However, for small dimension ratios $\nabla^d_{1,2}$, the 3L specimen behaves as a 2L specimen composed of layers $i = 2$ and $i = 3$ so that modelled values depend on $\nabla^d_{(2,3)}$ (and implied orientation $o_{(2,3)}$). Concretely, modelled values for small $\nabla^d_{1,2}$ vary in the range $\left(\mathscr{E}^{ref}_{eff}\right)_{i=3} < \mathscr{E}^{\cdot,d}_{eff} < \left(\mathscr{E}^{ref}_{eff}\right)_{i=2}$ as $\mathscr{E}^{\cdot,d}_{eff}$ increases towards $\left(\mathscr{E}^{ref}_{eff}\right)_2$ with $\nabla^d_{(2,3)}$.

The layer stacking orientation influences the weighted average accounted for in the model for parallel ($\|$, WAM), serial ($\perp$, WHM) or combined ($\perp\|$, WAM followed by WHM) stacked 3L specimen designs. The influence of stacking orientations on modelled values is evaluated considering inter-model differences for similar dimension ratios (and composition ratios as these are held constant) so that inter-model discrepancies are solely due to the applied averaging: $\mathscr{E}^{\|,d}_{eff} - \mathscr{E}^{\perp,d}_{eff} > 0$ in Fig. 3.6(a), $\mathscr{E}^{\|,d}_{eff} - \mathscr{E}^{\perp\|,d}_{eff} > 0$ in Fig. 3.6(b) and $\mathscr{E}^{\perp\|,d}_{eff} - \mathscr{E}^{\perp,d}_{eff} > 0$ in Fig. 3.6(c). All plotted curves exhibit a maximum for dimension ratios $0.1 < \nabla^d_{(1,2)} < 11$ which is within or near the range of interest ($0.1 < \nabla^d_{(1,2)} \leq 6.4$). As for small dimension ratios $\nabla^d_{(1,2)}$ each 3L specimen conducts itself as a 2L specimen characterised by $\nabla^d_{(2,3)}$, plotted inter-model differences in this range are governed by $\nabla^d_{(2,3)}$. Therefore, 3L specimens with combined stacking ($\perp\|$) perform as 2L specimens with parallel stacking ($\|$) so that in this range: 1) inter-model differences obtained comparing either "$\|$ versus $\perp$" or "$(\perp)$ $\|$ versus $\perp$" are similar (so for small $\nabla^d_{(1,2)}$ Fig. 3.6(c) zooms in on Fig. 3.6(a)) and 2) inter-model comparison "$\|$ versus $(\perp)$ $\|$" (Fig. 3.6(b)) reduces to comparing $\|$ with itself yielding negligible inter-model differences regardless of $\nabla^d_{(2,3)}$. For very large $\nabla^d_{(1,2)}$ the influence of stacking orientation is small as for all stacking conditions $\mathscr{E}^{\cdot,d}_{eff}$ approximates single layer value I_1. Within the range of interest $0.1 < \nabla^d_{(1,2)} < 6.4$, inter-model differences mostly increase with $\nabla^d_{(1,2)}$. Inter-model differences between serial ($\perp$) and combined ($\perp\|$) stacking (Fig. 3.6(c)) remain limited to less than 2 kPa whereas inter-model comparisons involving parallel ($\|$) stacking (Fig. 3.6(a) and Fig. 3.6(b)) amounts to larger (by a factor ≈ 10) inter-model differences up to 23 kPa. This illustrates again the impact of a layer with large $\mathscr{E}^{ref}_{eff}$, such as layer $i = 1$ (by a factor 5 or more), when it is accounted for using WAM averages associated with parallel stacking ($o_{(1,2)} = \|$) instead of WHM averages associated with serial or combined stacking ($o_{(1,2)} = \perp$).

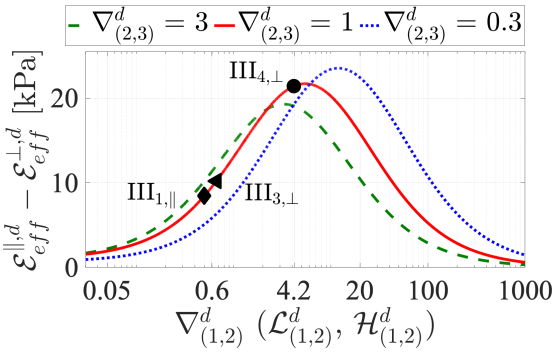

(a) 3L, $\parallel$ versus $\perp$

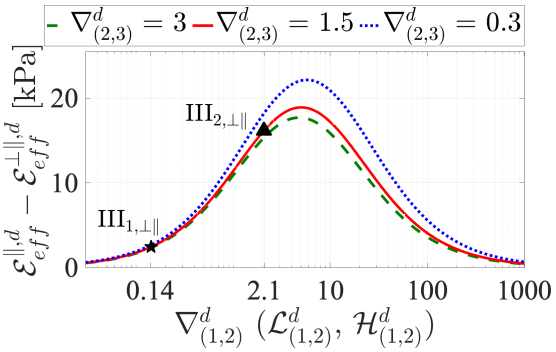

(b) 3L, $\parallel$ versus $\perp\parallel$

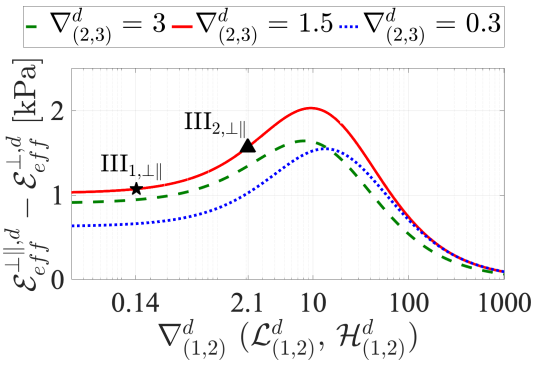

(c) 3L, $\perp\parallel$ versus $\perp$

Figure 3.6: Differences in modelled $\mathscr{E}^{\cdot,d}_{eff}$ due to 3L layer stacking (parallel ($\parallel$), serial ($\perp$) or combined ($\perp\parallel$)) with $\mathscr{B}^{ref}_{(1,2)} = 5$ and $\mathscr{B}^{ref}_{(1,2)} = 2.1$ as a function of dimension ratio $\nabla^d_{(1,2)}$ for three different dimension ratios $\nabla^d_{(2,3)}$. 3L specimen design values (symbols) are annotated ($\mathrm{III}_{\cdot,\parallel}$, $\mathrm{III}_{\cdot,\perp}$ or $\mathrm{III}_{\cdot,\perp\parallel}$): a) $\mathscr{E}^{\parallel,d}_{eff} - \mathscr{E}^{\perp,d}_{eff}$, b) $\mathscr{E}^{\parallel,d}_{eff} - \mathscr{E}^{\perp\parallel,d}_{eff}$, c) $\mathscr{E}^{\perp\parallel,d}_{eff} - \mathscr{E}^{\perp,d}_{eff}$.

Table 3.4: Molded 2L and 3L specimens: stacking dimension ratio $\nabla^s \in \{\mathscr{H}^s, \mathscr{L}^s\}$, modelled $\mathscr{E}^{\cdot,s-ref}_{eff}$, relative model discrepancy $\xi_{\mathscr{E}_{eff}}$ between $\mathscr{E}^{s-ref}_{eff}$ and $\mathscr{E}^{d}_{eff}$ associated with molded and designed specimen dimensions, respectively.

2L specimen				3L specimen				
Label	$\mathscr{H}^s$, $\mathscr{L}^s$	model		Label	$\mathscr{H}^s_{(j,j+1)}$, $\mathscr{L}^s_{(j,j+1)}$		model	
	(1,2)	$\mathscr{E}^{\parallel,\perp,s-ref}_{eff}$	$\xi_{\mathscr{E}_{eff}}$		(1,2)	(2,3)	$\mathscr{E}^{\cdot,s-ref}_{eff}$	$\xi_{\mathscr{E}_{eff}}$
$II_{1,\parallel}$	$\mathscr{H}^s = 2.3$	8.8 kPa	-7.4%	$III_{1,\perp}$	$\mathscr{L}^s = 0.56$	$\mathscr{L}^s = 1.8$	6.8 kPa	1.5%
$II_{2,\parallel}$	$\mathscr{H}^s = 1.2$	7.9 kPa	2.6%	$III_{2,\perp}$	$\mathscr{L}^s = 0.45$	$\mathscr{L}^s = 2.0$	17.1 kPa	- 1.2%
$II_{3,\parallel}$	$\mathscr{H}^s = 1.0$	31.6 kPa	1.3%	$III_{3,\perp}$	$\mathscr{L}^s = 0.68$	$\mathscr{L}^s = 0.91$	8.3 kPa	- 2.4%
$II_{1,\perp}$	$\mathscr{L}^s = 6.6$	9.1 kPa	3.4%	$III_{4,\perp}$	$\mathscr{L}^s = 4.2$	$\mathscr{L}^s = 1.1$	16.8 kPa	3.7%
$II_{2,\perp}$	$\mathscr{L}^s = 1.0$	6.7 kPa	0.0%	$III_{1,\parallel}$	$\mathscr{H}^s = 0.51$	$\mathscr{H}^s = 0.74$	15.3 kPa	-7.3%
$II_{3,\perp}$	$\mathscr{L}^s = 0.93$	16.9 kPa	-2.3%	$III_{1,\perp\parallel}$	$\mathscr{L}^s = 0.11$	$\mathscr{H}^s = 1.3$	8.4 kPa	-3.4%
				$III_{2,\perp\parallel}$	$\mathscr{L}^s = 2.1$	$\mathscr{H}^s = 1.3$	14.2 kPa	-1.4%

Curves in Fig. 3.5 and in Fig. 3.6 show that dimension ratios $\nabla^d_{(2,3)}$ near unity ($\nabla^d_{(2,3)} \in \{1, 1.5\}$) are suitable for 3L specimen designs. These ratios are then associated with both smaller ($0.1 < \nabla^d_{(1,2)} < 1$) and larger ($1 < \nabla^d_{(1,2)} < 6.4$) design dimension ratios $\nabla^d_{(1,2)}$ since modelled $\mathscr{E}^{\cdot,d}_{eff}$ curves for larger $\nabla^d_{(1,2)}$ are more sensitive to the stacking orientation combination ($\parallel$, $\perp$ or $\perp\parallel$) and to the exact value of $\nabla^d_{(1,2)}$. The 3L specimens (Table 3.3) with constant composition ratios $\mathscr{B}^{ref} \in \{5, 2.1\}$ are thus designed with the aim of assessing the influence of geometrical design parameters as the stacking orientation on modelled $\mathscr{E}^{\cdot,d}_{eff}$ ("$III_{1,\parallel}$ versus $III_{3,\perp}$" and "$III_{1,\parallel}$ versus $III_{1,\perp\parallel}$") and the influence of $\nabla^d_{(1,2)}$ for different stacking combinations ("$III_{3,\perp}$ versus $III_{4,\perp}$" and "$III_{1,\perp\parallel}$ versus $III_{2,\perp\parallel}$").

3.3.2 From designed to molded ML specimen: $\mathscr{E}^d_{eff}$ versus $\mathscr{E}^{s-ref}_{eff}$

Designed specimens are molded with a bone-shaped horizontal or vertical mold (volume 23.7 cm^3 and 3D printed, Stratasys ABS-P430, accuracy 0.33 mm) for parallel ($\parallel$) and serial ($\perp$) stacked layers respectively, following the mixture procedure outlined in [17, 40]. All together, selected ML specimen designs contain 13 layers with parallel orientation and 24 layers with serial orientation. As specimens are molded layer by layer, the thickness of each molded layer along the molding direction is measured with a laser transceiver (Panasonic HL-G112-A-C5, wavelength 655 nm, accuracy 8 μm). Measured layer dimensions are indicated with superscript s. The dimensional accuracy of each molded layer is obtained as the difference between the

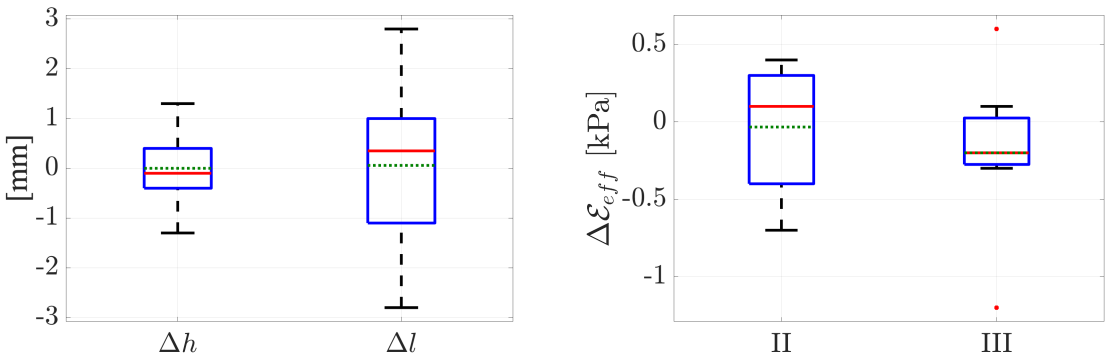

(a) Δh, Δl [mm] (b) $\Delta\mathscr{E}_{eff}$ [kPa]

Figure 3.7: Boxplots with median (full line), mean (dotted line), interquartile range between the first and third quartile (box), extrema (whiskers) of molding accuracies (molded minus design values) of: a) parallel (Δh) and serial (Δl) stacked layer dimensions, b) modelled $\Delta\mathscr{E}_{eff}$ for 2L (II) and 3L (III) specimens.

measured and designed dimension denoted Δh and Δl for a parallel and serial layer orientation, respectively. The repartition of dimensional molding accuracies -2.8 mm $\leq \Delta h, \Delta l \leq 2.8$ mm is represented by a boxplot in Fig. 3.7(a). Overall, accuracies are characterised by their mean plus minus their standard deviation as $\Delta h = 0.00 \pm 0.65$ mm and $\Delta l = 0.12 \pm 1.46$ mm, so that Δh and Δl are distributed around a small mean value near 0 mm. The overall dimensional molding accuracy from both Δh and Δl yields ± 1.5 mm.

Dimension ratios $\mathscr{H}^s$ and $\mathscr{L}^s$ of molded specimens (superscript s) are given in Table 3.4. Modelled $\mathscr{E}_{eff}^{s-ref}$ values of molded specimens are obtained using for each layer the measured specimen dimensions and reference values $\mathscr{E}_{eff}^{ref}$ given in Table 3.1. The relative molding accuracy $\xi_{\mathscr{E}_{eff}}$ for 2L and 3L specimens expresses then the relative model discrepancy of the Young's modulus due to layer molding dimension accuracy as $\xi_{\mathscr{E}_{eff}} = \Delta\mathscr{E}_{eff}/\mathscr{E}_{eff}^{d}$ with molding accuracy $\Delta\mathscr{E}_{eff} = \mathscr{E}_{eff}^{s-ref} - \mathscr{E}_{eff}^{d}$, where $\mathscr{E}_{eff}^{d}$ indicates as before the Young's modulus associated with the design dimensions of the specimen. The repartition of molding accuracies -1.2 kPa $\leq \Delta\mathscr{E}_{eff} \leq 0.6$ kPa is shown for 2L (II) and 3L (III) specimens by a boxplot in Fig. 3.7(b). Overall, $\Delta\mathscr{E}_{eff}$ is characterised by their mean plus minus their standard deviation as $\Delta\mathscr{E}_{eff}^{\mathrm{II}} = -0.03 \pm 0.43$ kPa for 2L specimens and $\Delta\mathscr{E}_{eff}^{\mathrm{III}} = -0.43 \pm 0.81$ kPa for 3L specimens. Thus, $\Delta\mathscr{E}_{eff}$ of the molded 2L specimens are distributed around a small mean value near 0 kPa as ± 0.5 kPa whereas $\Delta\mathscr{E}_{eff}$ of the molded 3L specimens are distributed around a negative mean value (-0.20 kPa) as -0.20 ± 0.56 kPa. From the relative accuracies $\xi_{\mathscr{E}_{eff}}$ in Table 3.4 is seen that for all 2L specimens $|\xi_{\mathscr{E}_{eff}}| \leq 7.5\%$ and for all 3L specimens $|\xi_{\mathscr{E}_{eff}}| \leq 7.4\%$. The absolute difference between modelled $\mathscr{E}_{eff}^{d}$ for designed specimens and $\mathscr{E}_{eff}^{s-ref}$ for molded specimens

remains limited to $|\Delta\mathscr{E}_{eff}| \leq 1.2$ kPa. Thus molded specimens are suitable to validate the model and to assess potential influences on modelled $\mathscr{E}_{eff}$ such as stacking orientation, dimension ratio or composition ratio.

3.4 Design of specimens with inclusion

3.4.1 Molded specimens with inclusion

Silicone mixtures, mixing ratios $\mathscr{M}$ and measured $\mathscr{E}$ commonly used to represent the muscle (Mu), superficial (Su) and epithelium (Ep) layer in ML silicone vocal fold replicas are given in Table 3.5 [8, 14, 16, 17, 29, 45–48]. The measured Young's modulus $\mathscr{E}$ of molded layers varies between 4 kPa and 65 kPa, which corresponds to the range associated with anatomical layers in a normal adult male human vocal fold [3, 4, 6, 7, 34–36].

Specimens are obtained from a three-layer reference specimen (labelled $A_{0.0}$) to which a

Table 3.5: Molded layer properties: mixture (Mix) TE (Thinner-Ecoflex) or TD (Thinner-Dragonskin), mass mixing ratio $\mathscr{M}$, measured Young's modulus $\mathscr{E}$, ratio between $\mathscr{E}$ and the value of the inclusion $\mathscr{E}^{In}$.

Molded layer	Mix	$\mathscr{M}$ [-]	$\mathscr{E}$ [kPa]	$\mathscr{E}^{In}/\mathscr{E}$ [-]
Muscle (Mu)	TE	1:2	23	13.0
Superficial (Su)	TE	4:2	4	74.5
Epithelium (Ep)	TD	1:2	65	4.6
Inclusion (In)	TD	0:2	298*	1.0

* $\mathscr{E}$ of the inclusion material is denoted $\mathscr{E}^{In}$.

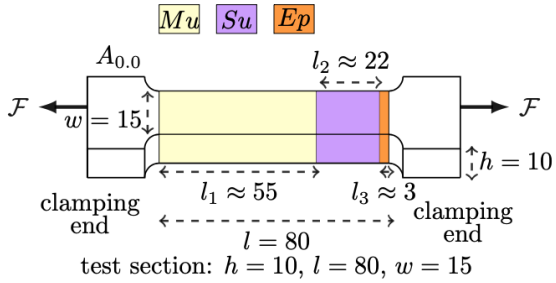

Figure 3.8: Molded bone-shaped three-layer reference specimen $A_{0.0}$ with serial stacking ($\perp$) without inclusion (dimensions in mm). The force $\mathscr{F}$ direction during uni-axial tension testing is shown (black arrows).

silicone inclusion (In) is inserted with constant elasticity $\mathscr{E}^{In}$ given in Table 3.5. The reference specimen without inclusion is depicted in Fig. 3.8. It consists of three serial ($\perp$) stacked layers with a composition similar to the muscle, superficial and epithelium layer indicated in Table 3.5. The length l_i of each layer $i = 1 \ldots n$ in the force ($\mathscr{F}$) direction, with $n = 3$ serial stacked layers, is set so that the volume ratios for the muscle, the superficial and the epithelium layer with respect to the test section's volume match the volume ratios of a three-layer silicone vocal fold replica (MRI-replica [16, 17, 47, 48]), *i.e.* 69% (Mu, $i = 1$), 27% (Su, $i = 2$) and 4% (Ep, $i = 3$) respectively. Varying the size, the position or the orientation of the inclusions allows us to extent the model validation to more complex ML composites. From the ratio $\mathscr{E}^{In}/\mathscr{E}$ in Table 3.5 is seen that $\mathscr{E}^{In}$ is about 4.5 up to 75 times greater than $\mathscr{E}$ associated with the layers in $A_{0.0}$. The presence of a stiffer portion somewhere within the vocal fold structure is commonly reported in case of a vocal fold abnormality or pathology [1, 49–51]. Fig. 3.9 schematically illustrates the different positions of beam-shaped inclusions with varying height h_{in} and length l_{in} inserted (striped region) in the test section of the reference specimen $A_{0.0}$ with serial layer stacking ($\perp$) depicted in Fig. 3.8. All inclusions have constant width $w_{in} = 15$ mm, which matches the width of the test section ($w_{in} = w$ with $w = 15$ mm) as illustrated for two specimens with inclusions in Fig. 3.10. Thus, the inclusion size is fully characterised by its height h_{in} and its length l_{in} and its position is fully defined by the side views provided in Fig. 3.9. Six different ML composite specimen types – A, B, C, D, E and F – are considered based on the position and size of the inclusion. Concretely, the size, in terms of height h_{in} and length l_{in}, of experimentally assessed inclusions is summarised in Table 3.6:

(A) specimens $A_{h_{in}/h}$ (Fig. 3.9(a)) are obtained for 5 inclusions with constant length $l_{in} = l_2$ and varying height $0.1 \leq h_{in}/h \leq 1$ placed at the side of the superficial layer (Su, $i = 2$) of $A_{0.0}$. In general, these specimens have four layers ($n = 4$) with combined stacking ($\perp\|$) as the inclusion in the superficial layer results in two adjacent layers with parallel stacking. This is illustrated for $A_{0.3}$ ($h_{in}/h = 0.3$) in Fig. 3.10(a). In the extreme case, that the inclusion replaces the superficial layer ($h_{in}/h = 1.0$), a three-layer ($n = 3$) specimen $A_{1.0}$ with serial stacking ($\perp$) is obtained as illustrated in Fig. 3.10(b).

(B) specimens $B_{h_{in}/h}$ (Fig. 3.9(b)) are obtained for 3 of the 5 inclusions with constant length $l_{in} = l_2$ and varying height $0.1 \leq h_{in}/h \leq 0.6$ considered in type A, but now translated (in the transverse direction) to the centre of the superficial layer (Su, $i = 2$) in $A_{0.0}$. Comparing the elasticity of $A_{h_{in}/h}$ and $B_{h_{in}/h}$ allows to assess the influence of the transverse inclusion position (side versus centre) within the superficial layer of $A_{0.0}$. These specimens are composed of five layers ($n = 5$) with combined stacking ($\perp\|$) as the inclusion in the superficial layer results in three adjacent parallel stacked layers.

(C) specimen $C_{h_{in}/h}$ (Fig. 3.9(c)) is obtained using the inclusion with constant length $l_{in} = l_2$ and height $h_{in}/h = 0.8$ positioned in both the superficial and the muscle layer of $A_{0.0}$. This specimen can be considered as a seven-layer ($n = 7$) specimen with combined stacking

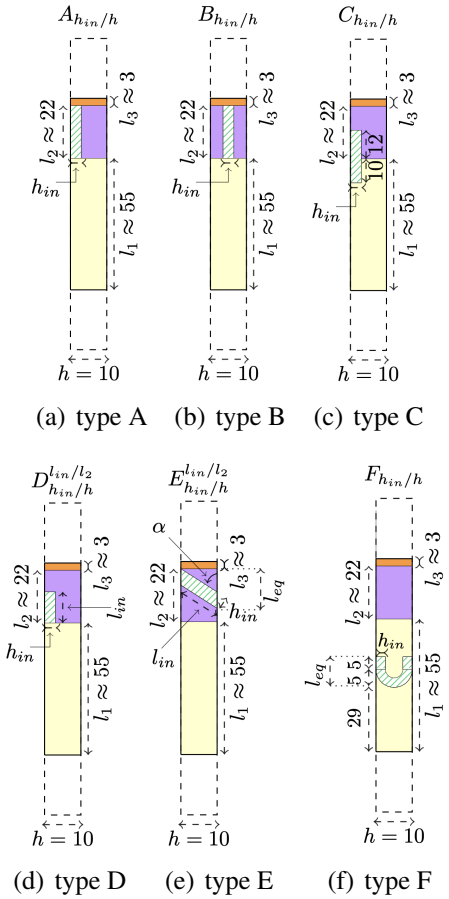

(a) type A (b) type B (c) type C

(d) type D (e) type E (f) type F

Figure 3.9: Side view of molded ML composite types with inclusions (striped region) of size h_{in}, l_{in} and constant width $w_{in} = 15$ mm (dimensions in mm). In a,b,c,f) $l_{in} = l_2$. In d,e) $l_{in} < l_2$. The clamping ends are dashed.

($\perp\|$) as the inclusion has parallel stacking with respect to the adjacent portions of the superficial layer and the muscle layer.

(D) specimens $D^{l_{in}/l_2}_{h_{in}/h}$ (Fig. 3.9(d)) are obtained for 5 inclusions with varying length $0.2 \leq l_{in}/l_2 \leq 0.6$ and varying height $0.3 \leq h_{in}/h \leq 0.8$ placed at the side of the superficial layer and at the interface with the muscle layer. These specimens are considered to have five layers ($n = 5$) with combined stacking ($\perp\|$) as the inclusion has a parallel stacking with respect to the adjacent portion of the superficial layer with the same height. Thus, the inclusion length is reduced so that comparing type A and type D allows one to assess the influence of the inclusion length.

(E) specimen $E^{l_{in}/l_2}_{h_{in}/h}$ (Fig. 3.9(e)) is obtained by inclining the inclusion with angle α ($\alpha = 46°$ is experimentally assessed). The inclined inclusion is placed in the superficial layer at the

interface with the epithelium layer. Due to the inclination, the stacking in the superficial layer is arbitrary (Arb) and it is neither serial ($\perp$) nor parallel ($\parallel$) with respect to the adjacent superficial layer portion. The equivalent length l_{eq} of the inclusion corresponds to its length in the force direction and $l_{eq} < l_{in}$ due to the inclination.

(F) specimen $F_{h_{in}/h}$ (Fig. 3.9(f)) is obtained by bending the inclusion with length $l_{in} = l_2$ and placing it in the muscle layer. As for type E, the stacking orientation within the muscle layer is arbitrary (Arb) since the bent portion of the inclusion is stacked neither serial ($\perp$) nor parallel ($\parallel$) with respect to the adjacent muscle layer portion. Again, the equivalent length l_{eq} of the inclusion corresponds to its length in the force direction and $l_{eq} < l_{in}$ due to the bending.

A total of 15 silicone specimens are molded following the mixture procedure outlined in [14, 40]. The size and position of the inclusion and the resulting ML specimen type (Fig. 3.9) and associated layer stacking – serial ($\perp$), combined ($\perp\parallel$) or arbitrary (Arb) – is summarised in Table 3.6. Firstly, inclusions are molded using horizontal 3D-printed specimen molds (Stratasys ABS-P430, accuracy 0.33 mm), which are filled with the inclusion silicone mixture indicated in Table 3.5 up to each inclusion's height h_{in} whereas their width is determined by the width of the mold so that $w_{in} = 15$ mm. The molded inclusion sheets are then cut to match the desired inclusion length l_{in}. Next, vertical 3D-printed specimen molds are used to build the ML specimens layer-by-layer with the appropriate silicone mixture detailed in Table 3.5. Inclusions are inserted during the molding process so that they are fully embedded. The length of each molded layer is measured with a laser transceiver (Panasonic HL-G112-A-C5, wavelength 655 nm, accuracy 8 μm) whereas the inclination angle is derived from the spatial position of the inclined mold (accuracy 0.1 mm) using trigonometry. The overall molding accuracy for all 45 molded layers with lengths $l_1 \approx 55$ mm (muscle), $l_2 \approx 22$ mm (superficial) and $l_3 \approx 3$ mm (epithelium) results in a mean and a standard deviation of 0.1 ± 0.8 mm, which is within the molding accuracy of

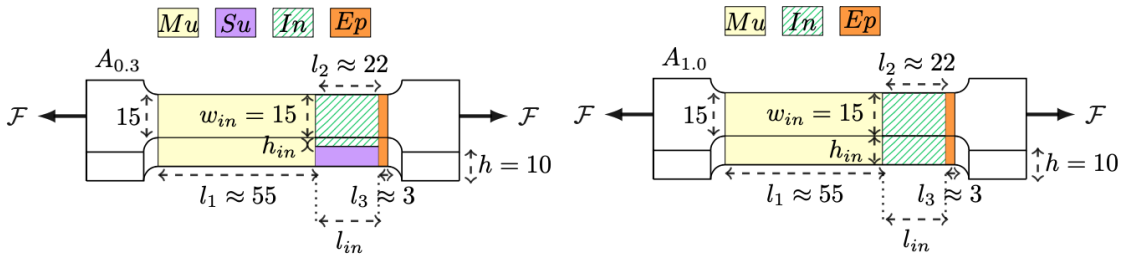

(a) $A_{0.3}$ (b) $A_{1.0}$

Figure 3.10: Molded ML bone-shaped specimens (dimensions in mm) with inclusion (In) inserted in the superficial (Su) layer of the reference specimen $A_{0.0}$ depicted in Fig. 3.8: a) four-layer specimen $A_{0.3}$ with combined stacking ($\perp\parallel$), b) three-layer specimen $A_{1.0}$ with serial stacking ($\perp$). The force $\mathcal{F}$ direction during uni-axial tension testing is shown (black arrows).

Table 3.6: Inclusions geometry (constant width $w_{in} = 15$ mm): h_{in} , l_{in}, ratios h_{in}/h and l_{in}/l_2 with $h \approx 10$ mm and $l_2 \approx 22$ mm. ML molded specimens with these inclusions and their layer stacking: serial ($\perp$), combined ($\perp\|$) and arbitrary (Arb). Reference specimen $A_{0.0}$ corresponds to $h_{in}/h = 0$.

Inclusion geometry		Dimension ratios		Specimens & stacking			
h_{in} [mm]	l_{in} [mm]	h_{in}/h [-]	l_{in}/l_2 [-]	($\perp$)	($\perp\|$)		Arb
0.0	–	0.0	0.0	$A_{0.0}$			
1.3	22.0	0.1	1.0		$A_{0.1}$	$B_{0.1}$	
2.6	22.0	0.3	1.0		$A_{0.3}$	$B_{0.3}$	$F_{0.3}$
5.8	22.0	0.6	1.0		$A_{0.6}$	$B_{0.6}$	
7.8	22.0	0.8	1.0		$A_{0.8}$	$C_{0.8}$	
10.0	22.0	1.0	1.0	$A_{1.0}$			
2.6	5.0	0.3	0.2		$D_{0.3}^{0.2}$		
7.8	5.0	0.8	0.2		$D_{0.8}^{0.2}$		
4.6	13.4	0.5	0.6		$D_{0.5}^{0.6}$		$E_{0.5}^{0.6}$

± 1.5 mm previously reported in Section 3.3.2.

3.4.2 Serial, parallel and combined layer stacking effective Young's modulus $\widehat{\mathscr{E}}_{eff}$ model

For the composite specimens in Table 3.6 and in Fig. 3.9 with serial ($\perp$) or combined ($\perp\|$) stacked layers – *i.e.* of type A (Fig. 3.9(a)), type B (Fig. 3.9(b)), type C (Fig. 3.9(c)) or type D (Fig. 3.9(d)) – the effective Young's modulus $\widehat{\mathscr{E}}_{eff}$ is modelled considering an equivalent homogeneous composite as outlined in Section 3.2 for serial, parallel or combined stacked layers.

Inclusions associated with type A, type B, type C and type D in Fig. 3.9 result in serial ($\perp$) or combined ($\perp\|$) stacked layers as summarised in Table 3.6. The effective Young's modulus $\widehat{\mathscr{E}}_{eff}$ of the molded specimens from these types are thus modelled as $\widehat{\mathscr{E}}_{eff} = \widehat{\mathscr{E}}_{eff}^{\perp}$ or $\widehat{\mathscr{E}}_{eff} = \widehat{\mathscr{E}}_{eff}^{\perp\|}$. Following this model approach, shifting the same inclusion from the side to the center of the superficial layer does not affect the model outcome. Thus $\widehat{\mathscr{E}}_{eff}$ for type A and type B specimens containing an inclusion with the same height ratio h_{in}/h have equal value. Indeed as $\mathscr{E}_i$ are similar, modelled $\widehat{\mathscr{E}}_{eff}$ depend solely on the height ratio $0 \leq h_{in}/h \leq 1$ and length ratio $0 \leq l_{in}/l_2 \leq 1$ of the inclusion and not on its position. The influence of h_{in}/h and l_{in}/l_2 on $\widehat{\mathscr{E}}_{eff}$ is illustrated in Fig. 3.11. Model values for molded specimens are indicated (symbols). Extending the size of the inclusion in the superficial layer increases modelled $\widehat{\mathscr{E}}_{eff}$ from $\widehat{\mathscr{E}}_{eff} = 10$ kPa for the reference specimen $A_{0.0}$ without inclusion up to about $\widehat{\mathscr{E}}_{eff} = 33$ kPa for specimen $A_{1.0}$,

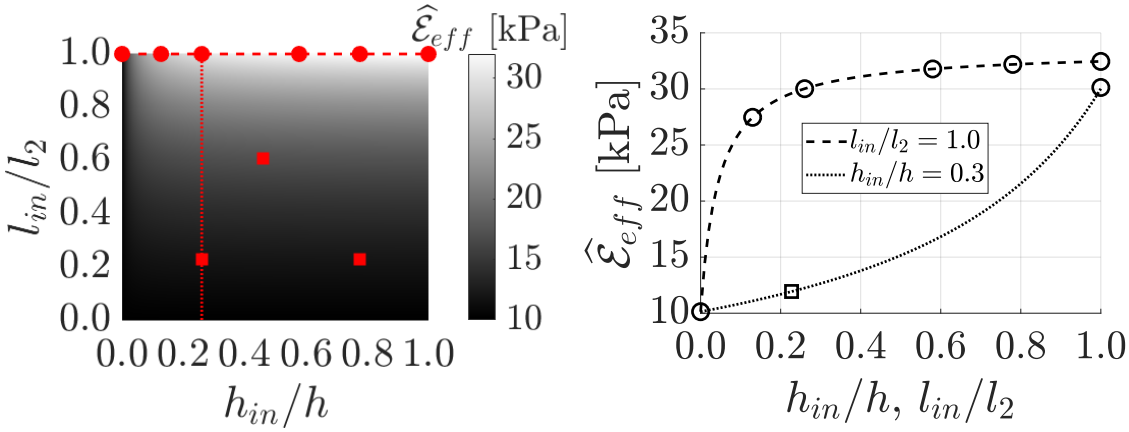

(a) varied l_{in}/l_2 and h_{in}/h

(b) constant l_{in}/l_2 or h_{in}/h

Figure 3.11: Influence of the height ratio $0 \leq h_{in}/h \leq 1$ and length ratio $0 \leq l_{in}/l_2 \leq 1$ of an inclusion in the superficial layer on modelled $\widehat{\mathscr{E}}_{eff}$. Values for molded specimens (◯, □) are shown: a) specimens type A (or B) (◯) and type D (□), constant length ratio $l_{in}/l_2 = 1.0$ (horizontal dashed line) and constant height ratio $h_{in}/h = 0.3$ (dashed vertical line), b) detail for these constant length and height ratios.

for which the inclusion occupies the entire superficial layer. Nevertheless, Fig. 3.11(a) shows that $\widehat{\mathscr{E}}_{eff}$ increases more rapidly with l_{in}/l_2 than with h_{in}/h. In particular, this is the case for $h_{in}/h \geq 0.2$. This is due to the arithmetic mean associated with parallel stacked layers in Eq. (3.4), which tends to mask low $\mathscr{E}_i$ in favour of the large $\mathscr{E}_i$ of the inclusion (Table 3.5) which is not the case for the harmonic mean associated with serial stacking in Eq. (3.5). Therefore, it is mainly the length ratio l_{in}/l_2 of the inclusion in the superficial layer what affects the mean value $\widehat{\mathscr{E}}^{\parallel}_{eff}$ of the equivalent homogenised superficial layer and hence $\widehat{\mathscr{E}}_{eff}$ of the homogenised specimen. This is further illustrated for $l_{in}/l_2 = 1$ in Fig. 3.11(b) as an increase of h_{in}/h from 0.1 to 1 only increases $\widehat{\mathscr{E}}_{eff}$ 27%, from 26 kPa up to 33 kPa, whereas for constant $h_{in}/h > 0.2$ ($h_{in}/h = 0.3$ is plotted) an increase of l_{in}/l_2 from 0.1 to 1 increases $\widehat{\mathscr{E}}_{eff}$ with about 270% from 11 kPa up to 30 kPa. Thus the most notable variation of $\widehat{\mathscr{E}}_{eff}$ for the molded specimens plotted in Fig. 3.11(a) is predicted to occur for specimens with different inclusion lengths $l_{in}/l_2 \in \{0.0, 0.2, 0.6, 1\}$ associated with $\widehat{\mathscr{E}}_{eff} \in \{10, 12, 17, 30\}$ kPa.

3.4.3 Arbitrary layer stacking $\widehat{\mathscr{E}}_{eff}$ model

Specimens of type E with an inclined inclusion ($\alpha > 0°$) in the superficial layer (Fig. 3.9(e)) or of type F with a bent inclusion in the muscle layer (Fig. 3.9(f)) are not serial or parallel stacked with respect to adjacent layers. Instead, their stacking is arbitrary (Arb). However, using

the model outlined in Section 3.2 for serial, parallel and combined stacking, two approaches are proposed to model the effective Young's modulus $\widehat{\mathscr{E}}_{eff}$ for arbitrary stacked layers either based on spatial discretisation along the force direction (Section 3.4.3.1) or on geometrical approximation (Section 3.4.3.2). A comparison of modelled values with both approaches for molded specimens with arbitrary stacking $E_{0.5}^{0.6}$ and $F_{0.3}$ is provided in Section 3.4.3.3.

3.4.3.1 Discretisation

The model approach outlined in Section 3.2 is extended to arbitrary stacking by discretising the specimen portion containing the inclusion with equivalent length l_{eq} into multiple shorter layers with discretisation step length l_j. The inclusion within each discretised layer is then approximated by a rectangle with height h_j set either to height h_j^U of the largest rectangle enveloped within the inclusion or to height h_j^O of the smallest rectangle enveloping the inclusion in that discretised layer as schematically depicted in Fig. 3.12 for specimens of type E and type F. Consequently, each discretised layer with rectangular inclusion approximation is represented as parallel stacked layers so that $\widehat{\mathscr{E}}_{eff,j}$ of each homogenised discretised layer is modelled using Eq. (3.4). The sought $\widehat{\mathscr{E}}_{eff,j}$ of each discretised layer with length l_j is thus underestimated (U) as $\widehat{\mathscr{E}}_{j,U} = \widehat{\mathscr{E}}_{eff}^{\parallel}$ using height h_j^U or overestimated (O) as $\widehat{\mathscr{E}}_{j,O} = \widehat{\mathscr{E}}_{eff}^{\parallel}$ using height h_j^O. Following this discretisation, the equivalent homogenised specimen portion with inclusion and therefore the

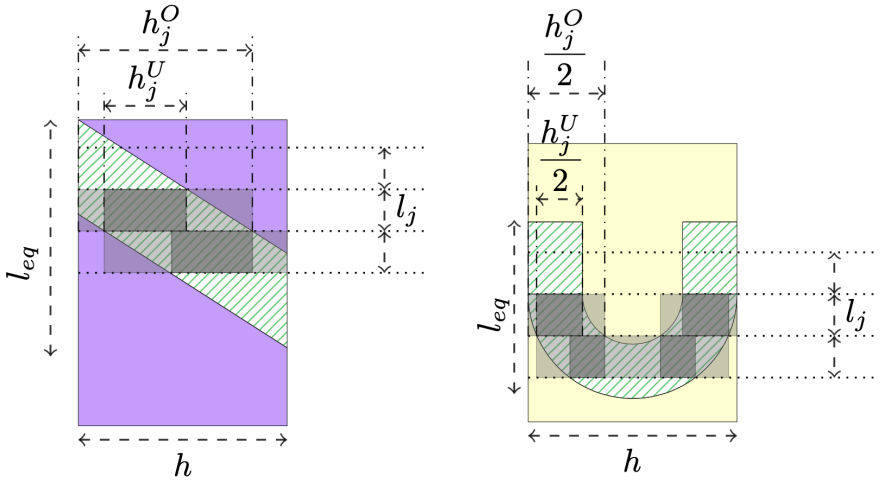

(a) type E, specimen $E_{0.5}^{0.6}$ (b) type F, specimen $F_{0.3}$

Figure 3.12: Illustration of discretisation along the force direction (step length l_j) for inclusions (striped region) with arbitrary stacking: a) type E (specimen $E_{0.5}^{0.6}$), b) type F (specimen $F_{0.3}$). Rectangular inclusion portion approximations with height h_j^O (light gray shade) and h_j^U (dark gray shade) overestimating (O) and underestimating (U) the inclusion, respectively.

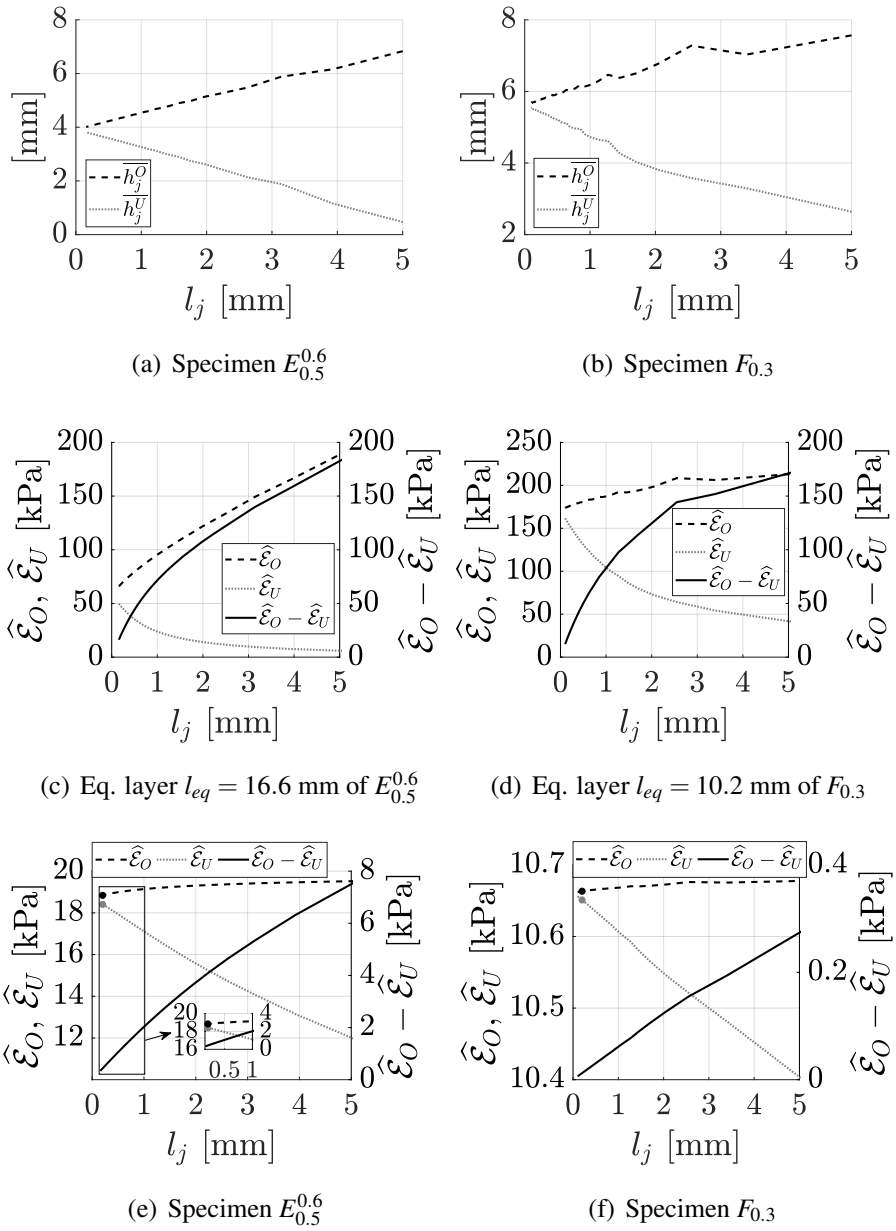

(a) Specimen $E_{0.5}^{0.6}$ (b) Specimen $F_{0.3}$

(c) Eq. layer $l_{eq} = 16.6$ mm of $E_{0.5}^{0.6}$ (d) Eq. layer $l_{eq} = 10.2$ mm of $F_{0.3}$

(e) Specimen $E_{0.5}^{0.6}$ (f) Specimen $F_{0.3}$

Figure 3.13: Effect of discretisation step length l_j for molded ML specimens $E_{0.5}^{0.6}$ and $F_{0.3}$ on a,b) mean rectangle heights $\overline{h_j^O}(l_j)$ and $\overline{h_j^U}(l_j)$, c,d) modelled effective Young's modulus $\widehat{\mathscr{E}}_O(l_j, h_j^O)$ and $\widehat{\mathscr{E}}_U(l_j, h_j^U)$ and the difference $\widehat{\mathscr{E}}_O - \widehat{\mathscr{E}}_U$ for the homogenised specimen portion with inclusion of length l_{eq}, e,f) modelled effective Young's modulus $\widehat{\mathscr{E}}_O(l_j, h_j^O)$ and $\widehat{\mathscr{E}}_U(l_j, h_j^U)$ and the difference $\widehat{\mathscr{E}}_O - \widehat{\mathscr{E}}_U$ for the homogenised specimen. Values of $\widehat{\mathscr{E}}_{O,U}$ for $l_j = 0.2$ mm are indicated (•).

equivalent homogenised specimen consists of a stack of serial layers, so that $\widehat{\mathscr{E}}_{eff}$ is modelled

using Eq. (3.5) resulting in overestimation $\widehat{\mathscr{E}}_O = \widehat{\mathscr{E}}_{eff}^{\perp}$ for $\widehat{\mathscr{E}}_{j,O}$ or in underestimation $\widehat{\mathscr{E}}_U = \widehat{\mathscr{E}}_{eff}^{\perp}$ for $\widehat{\mathscr{E}}_{j,U}$. The overall difference $\widehat{\mathscr{E}}_O - \widehat{\mathscr{E}}_U \geq 0$ for the equivalent homogenised specimen portion with inclusion of length l_{eq} (Fig. 3.13(c) and Fig. 3.13(d)) as well as for the equivalent homogenised specimen (Fig. 3.13(e) and Fig. 3.13(f)) decreases with discretisation step length l_j. Consequently, the sought model value $\widehat{\mathscr{E}}_{eff}$ of the homogenised specimen is found for small enough discretisation step length l_j. The influence of the discretisation step length l_j is illustrated in Fig. 3.13 for molded specimen $E_{0.5}^{0.6}$ containing an inclined inclusion with $l_{eq} = 15.7$ mm (type E in Fig. 3.9(f)) and for molded specimen $F_{0.3}$ containing a bent inclusion with $l_{eq} = 10.2$ mm (type F in Fig. 3.9(e)). For these specimens, $\widehat{\mathscr{E}}_{eff}$ of both the equivalent homogeneous inclusion layer (with length l_{eq}) and of the specimen is approximated when the discretisation step length $l_j \leq 0.2$ mm as $\widehat{\mathscr{E}}_O - \widehat{\mathscr{E}}_U \leq 0.5$ kPa for both homogenised specimens. For $l_j = 0.2$ mm, the discretisation of l_{eq} corresponds to splitting l_{eq} into 78 ($E_{0.5}^{0.6}$) and 51 ($F_{0.3}$) equi-length layers. It is seen from Fig. 3.13(a) and Fig. 3.13(b) that also the mean of rectangle heights for all discretised layers $\overline{h_j^O}$ and $\overline{h_j^U}$ converges as l_j decreases.

3.4.3.2 Geometrical approximation

Besides the discretisation approach outlined in Section 3.4.3.1, the quasi-analytical model approach outlined in Section 3.2 can be applied when the inclusion of height h_{in} and length l_{in} with arbitrary stacking can be treated as an equivalent beam-shaped inclusion of length l_{eq} and height h_{eq} with serial, parallel or combined layer stacking. The length l_{eq} corresponds to the equivalent length of the inclusion in the force direction as illustrated for type E and type F specimens in Fig. 3.9 and in Fig. 3.12. The height h_{eq} of the equivalent inclusion is obtained when imposing area conservation and exploiting the model property that neither serial (Eq. (3.5)) or parallel (Eq. (3.4)) layer stacks depend on the stack order so that layers in both stacks can be split or permuted. The area conservation condition is defined as $h_{in}l_{in} = h_{eq}l_{eq}$ so that

$$h_{eq} = \frac{h_{in}l_{in}}{l_{eq}}. \tag{3.8}$$

The dimensions of the equivalent inclusions h_{eq} and l_{eq} can then be expressed in terms of geometrical parameters such as inclusion dimensions h_{in} and l_{in}.

For specimens of type E, such as $E_{0.5}^{0.6}$ containing an inclined inclusion as depicted in Fig. 3.9(e), l_{eq} and h_{eq} are expressed as:

$$\begin{aligned} l_{eq} &= \frac{h_{in} + h\cos(\alpha)}{\sin(\alpha)}, \\ h_{eq} &= \frac{l_{in}h_{in}\sin(\alpha)}{h_{in} + h\cos(\alpha)}. \end{aligned} \tag{3.9}$$

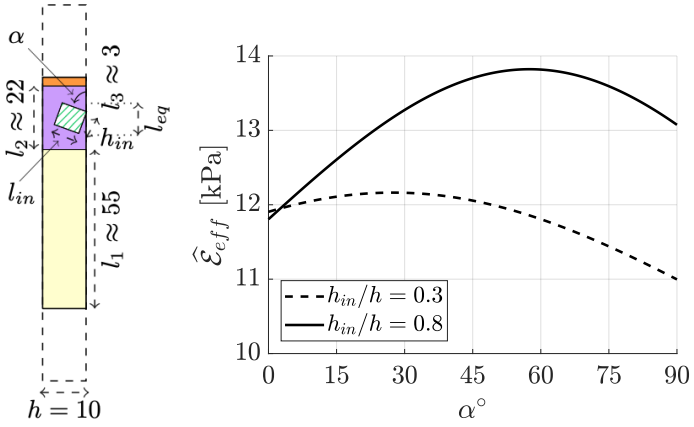

Figure 3.14: Modelled $\widehat{\mathscr{E}}_{eff}$ as a function of inclination angle α ($0° \leq \alpha \leq 90°$) for specimens with an embedded inclusion of diagonal $\sqrt{l_{in}^2 + h_{in}^2} \leq h$ as schematically depicted (left). Curves $\widehat{\mathscr{E}}_{eff}(\alpha)$ are plotted for $l_{in}/l_2 = 0.2$ and either $h_{in}/h = 0.3$ (dashed line) or $h_{in}/h = 0.8$ (full line).

For specimens of type F, such as $F_{0.3}$ containing a bent inclusion as depicted in Fig. 3.9(f), l_{eq} and h_{eq} are given as:

$$\begin{aligned} l_{eq} &= \frac{l_{in} + h}{2} - \frac{\pi(h - h_{in})}{4}, \\ h_{eq} &= \frac{4 h_{in} l_{in}}{2 l_{in} + \pi h_{in} - (\pi - 2) h}. \end{aligned} \tag{3.10}$$

Analytical expressions of the geometry of equivalent inclusions, such as Eq. (3.9) and Eq. (3.10), are of interest when considering the influence of geometrical inclusion parameters on $\widehat{\mathscr{E}}_{eff}$. As an additional example (not molded), expressions of the equivalent length l_{eq} and height h_{eq} of an inclusion with inclination angle α fully embedded in the superficial layer, *i.e.* with a diagonal shorter than the total specimen height h so that $\sqrt{l_{in}^2 + h_{in}^2} \leq h$ as schematically depicted in Fig. 3.14, are,

$$\begin{aligned} l_{eq} &= l_{in} \cos(\alpha) + h_{in} \sin(\alpha), \\ h_{eq} &= \frac{l_{in} h_{in}}{l_{in} \cos(\alpha) + h_{in} \sin(\alpha)}. \end{aligned} \tag{3.11}$$

Modelled $\widehat{\mathscr{E}}_{eff}$ for two fully embedded inclined inclusions from Table 3.6, with length $l_{in} =$ 5.0 mm (or $l_{in}/l_2 = 0.2$) and height $h_{in} \in \{2.6\text{ mm}, 7.8\text{ mm}\}$ (or $h_{in}/h \in \{0.3, 0.8\}$), as a function of inclination angle $0° \leq \alpha \leq 90°$ are plotted in Fig. 3.14. Although the overall tendency of $\widehat{\mathscr{E}}_{eff}(\alpha)$ is similar, plotted curves show *e.g.* that angles associated with the minimum and maximum of the curves depend on the height ratio h_{in}/h.

3.4.3.3 $\widehat{\mathscr{E}}_{eff}$ of molded specimens with arbitrary stacking

For the molded specimens with arbitrary stacking, both the discretisation approach (in Section 3.4.3.1 with step length $l_j = 0.2$ mm) and the geometrical approximation approach (in Section 3.4.3.2) result in the sought $\widehat{\mathscr{E}}_{eff}$ as their difference is less than 0.9 kPa (or $\leq 4.8\%$) for specimen $E_{0.5}^{0.6}$ and less than 0.1 kPa (or $\leq 1.0\%$) for specimen $F_{0.3}$. Hereafter, $\widehat{\mathscr{E}}_{eff}$ obtained with the geometrical approximation are reported for specimens with arbitrary stacked inclusions ($E_{0.5}^{0.6}$ and $F_{0.3}$) since in this case $\widehat{\mathscr{E}}_{eff}$ does not depend on the applied discretisation step length l_j.

3.5 Uni-axial tension testing

3.5.1 Molded specimens without inclusion

Two different stress test methods are used to induce stress σ along the vertical x-axis either with a mechanical press (MP, Section 3.5.1.2) or with precision loading (PL, Section 3.5.1.3). Both methods result in experimental force-elongation curves $\mathscr{F}(\Delta l)$ as their elongation Δl is obtained for different loads $\mathscr{F}$ (PL) or vice-versa (MP) so that both methods can be cross-validated on the same specimens. Specimens are positioned vertically by clamping its end terminations depicted in Fig. 3.3(a). Regardless of the applied stress test, additional geometrical measurements are gathered as outlined in Section 3.5.1.1.

3.5.1.1 Geometrical measurements

Geometrical measurements on 3L specimens with different stacking are illustrated in Fig. 3.15. The length $l_i + \Delta l_i$ of each layer $i = 1 \ldots n$ is measured (ruler with accuracy 1 mm) for different loads $\mathscr{F}$ (or elongations Δl), where l_i ($i = 1 \ldots n$) denotes the initial layer length measured for the unloaded ($\mathscr{F} = 0$ N) but vertically clamped specimen. As each clamped specimen is subjected to its own weight (25.2 ± 2.1 g), $l_i \geq l_i^s$ holds, where l_i^s indicates the layer length of the molded specimen. The sought total elongation Δl of each specimen as a function of $\mathscr{F}$ is then obtained from the measured layer elongations Δl_i. For 1L specimens or ML specimens with parallel ($\|$) stacking (Fig. 3.15(a)), $\Delta l = \Delta l_1$ holds since all layers have equal length regardless of $\mathscr{F}$. For ML specimens with serial ($\perp$) stacking (Fig. 3.15(b)), $\Delta l = \sum_{i=1}^{n} \Delta l_i$ holds as the elongation of each layer depends on its molding composition and associated $(\mathscr{E}_{eff})_i$. For 3L specimens with combined serial and parallel ($\perp\|$) stacking (Fig. 3.15(c)), $\Delta l = \Delta l_1 + \Delta l_2$ holds as parallel stacked layers ($i = 2$ and $i = 3$) have equal lengths for all $\mathscr{F}$.

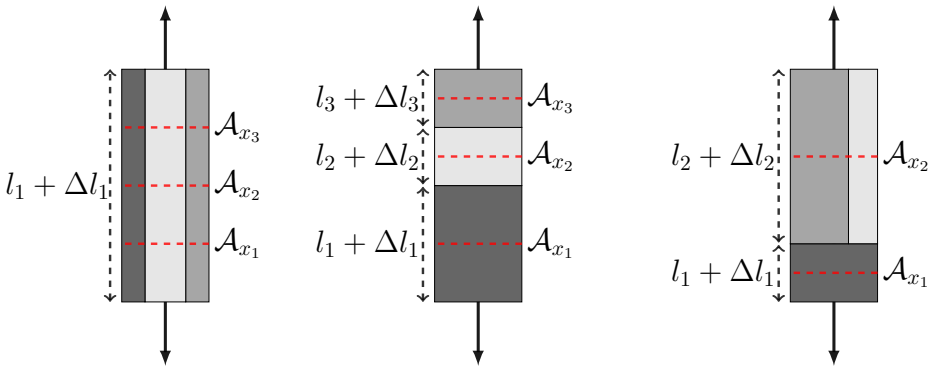

(a) parallel, $\parallel$ (b) serial, $\perp$ (c) combined, $\perp\parallel$

Figure 3.15: Measurement of layer lengths $l_i + \Delta l_i$ and cross-sectional areas $\mathscr{A}_{x.}$ at different positions $x.$ along the test section following an uni-axial force $\mathscr{F}$ (full arrows) on 3L ($n = 3$) specimens with different stacking: a) parallel ($\parallel$) with $l_1 + \Delta l_1 = \ldots = l_n + \Delta l_n$, b) serial ($\perp$), c) combined stacking ($\perp\parallel$) with $l_2 + \Delta l_2 = l_3 + \Delta l_3$.

The specimens cross-sectional area $\mathscr{A}$ perpendicular to the force or vertical x-direction is likely to reduce with $\mathscr{F}$ as schematically depicted in Fig. 3.1. It follows that $\mathscr{A} \leq \mathscr{A}^s$ holds with $\mathscr{A}^s$ the initial cross-sectional area of the unloaded ($\mathscr{F} = 0$ N) but vertically clamped specimen. The sought area $\mathscr{A}$ of each specimen is obtained from cross-sectional areas $\mathscr{A}_{x.}$ (caliper Mitutoyo 500-196-30, accuracy 0.01 mm) measured at two or three different vertical positions $x.$ along its test section subjected to a constant load ($\mathscr{F} \geq 0$ N). For 1L specimens and ML specimens with parallel ($\parallel$) stacking (Fig. 3.15(a)), three area measurements $\mathscr{A}_{x_1}$, $\mathscr{A}_{x_2}$ and $\mathscr{A}_{x_3}$ are taken at 25%, 50% and 75% of the test section with length $l_1 + \Delta l_1$. The sought cross-sectional area $\mathscr{A}$ is then obtained from their mean value,

$$\mathscr{A}^{\parallel} = \frac{\mathscr{A}_{x_1} + \mathscr{A}_{x_2} + \mathscr{A}_{x_3}}{3}, \tag{3.12}$$

so that the measurement accuracy between different positions can be assessed. For serial ($\perp$) stacked ML specimens (Fig. 3.15(b)), the cross-sectional area or each layer ($\mathscr{A}_{x_i}$ with $i = 1 \ldots n$) is measured midway. The sought cross-sectional area $\mathscr{A}$ is then obtained from the weighted arithmetic mean as

$$\mathscr{A}^{\perp} = \frac{\sum_{i=1}^{n} (l_i + \Delta l_i) \mathscr{A}_{x_i}}{l + \Delta l}. \tag{3.13}$$

For 3L specimens with combined serial and parallel ($\perp\parallel$) stacking (Fig. 3.15(c)), two cross-sectional areas $\mathscr{A}_{x_1}$ and $\mathscr{A}_{x_2}$ are measured midway of the serial ($i = 1$) and of the parallel ($i = 2$ or $i = 3$) stacked layers. The sought cross-sectional area $\mathscr{A}$ is thus given as the weighted arithmetic

mean of the serial and one of the parallel layers (taken as $i = 2$) as

$$\mathscr{A}^{\perp\parallel} = \frac{\sum_{i=1}^{2}(l_i + \Delta l_i)\mathscr{A}_{x_i}}{l + \Delta l}. \tag{3.14}$$

3.5.1.2 Mechanical press

An electro-mechanical press (3369, Instron Corp.) with 50 kN force sensor (2530-445/71212, Instron Corp., accuracy 0.2%) is used for uni-axial stress testing of specimens along the parallel x-axis (as depicted in Fig. 3.15) with typical forces $\mathscr{F}$ up to 8 N. The mechanical press (MP) was set for displacement control imposing four maximum elongations Δl of 25, 50, 100 and 150 mm, respectively. The deformation rate was set to 1 mm/s for the 25, 50 and 100 mm elongations and to 2 mm/s for the 150 mm elongation. Force and elongation time series (sampling rate of 10 Hz) were measured during loading of the specimens so that for each specimen four MP datasets are obtained, *i.e.* one for each imposed maximum elongation. No plastic deformation was observed following their unloading (at 5 mm/s).

Due to the relative softness of the tested specimens ($F \leq 8$ N compared to the 50 kN force sensor range), a moving-average filter with variable window size and 1 sample shift is applied to denoise the raw force sensor data in order to enhance the linearity in the force-elongation curves. Resulting smoothed MP force-elongation curves matches well with a linear fit of smoothed MP data as the coefficient of determination yields $R^2 \geq 80$ % with a mean value of 88 % and a standard deviation of 6 %. Raw and smooth MP datasets for maximum elongation $\Delta l = 100$ mm are illustrated in Fig. 3.16 for 2L specimens $\mathrm{II}_{2,\perp}$ and $\mathrm{II}_{3,\perp}$. Overall, the window size in terms of elongation ranges from 0.3 mm up to 6.5 mm (or 2 up to 65 samples), where larger window sizes are used for softer specimen (with lower $\mathscr{E}_{eff}$) as illustrated in Fig. 3.16 for $\mathrm{II}_{2,\perp}$ (window size 6.5 mm or 65 samples, modelled $\mathscr{E}^{\perp,s-ref} = 6.7$ kPa) and $\mathrm{II}_{3,\perp}$ (window size 0.7 mm or 7 samples, modelled $\mathscr{E}^{\perp,s-ref} = 16.9$ kPa). The overall window elongation size corresponds to a mean plus minus standard deviation of 2.1 ± 1.9 mm (or 19 ± 17 samples), which is in accordance with the constant window size of 2.0 mm (or 20 samples) proposed in [40] for 1L specimens resulting in $\mathscr{E}_{eff}^{ref}$. In the following sections, smoothed MP force-elongation curves are considered.

Additional geometrical measurements described in Section 3.5.1.1 are made for each clamped specimen without loading ($\Delta l = 0$ mm) and once each of the maximum elongations is reached. Cross-sectional areas $\mathscr{A}$ of the specimens are then obtained as outlined in Section 3.5.1.1, so that $\mathscr{A}(\mathscr{F})$ contains 5 data points obtained at imposed maximum elongations

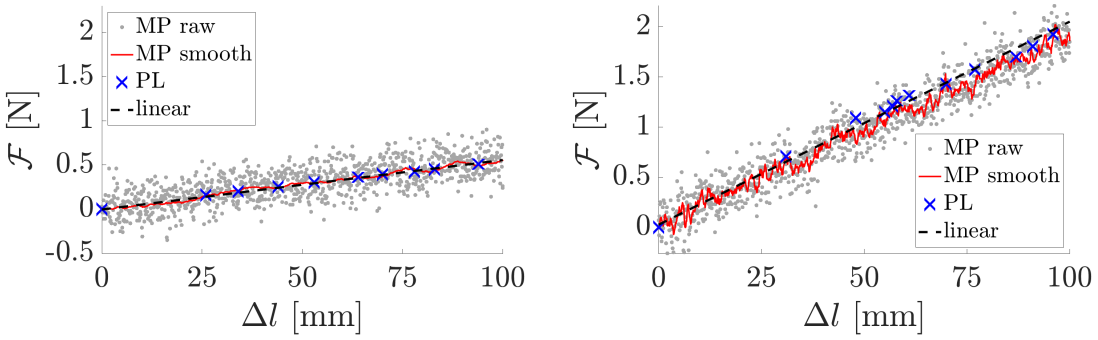

(a) $\mathrm{II}_{2,\perp}$ (b) $\mathrm{II}_{3,\perp}$

Figure 3.16: Linear behavior (dashed line) of measured force-elongation curves $\mathscr{F}(\Delta l)$ with the mechanical press (MP, raw and smooth) for maximum elongation $\Delta l = 100$ mm and with precision loading (PL) for 2L specimens: a) $\mathrm{II}_{2,\perp}$, modelled $\mathscr{E}^{\perp,s-ref} = 6.7$ kPa, MP smooth with 6.5 mm (or 65 samples) window, PL for $m \leq 52$ g, b) $\mathrm{II}_{3,\perp}$, modelled $\mathscr{E}^{\perp,s-ref} = 16.9$ kPa, MP smooth with 0.7 mm (or 7 samples) window, PL for $m \leq 196$ g.

$\Delta l \in \{0, 25, 50, 100, 150\}$ mm. Elongations Δl deduced from geometrical measurements of layer lengths $l_i + \Delta l_i$ as outlined in Section 3.5.1.1, matches the imposed maximum elongations to within 1 mm (or $\leq 4\%$ difference for $\Delta l \geq 25$ mm), which corresponds to the ruler accuracy. It follows that the estimated accuracy of elongations Δl obtained from geometrical measurements yields $\geq 96\%$ for $\Delta l \geq 25$ mm. The accuracy increases with Δl.

3.5.1.3 Precision loading

Uni-axial stress testing (along the parallel x-axis) of a specimen by means of precision loading (PL) is performed by clamping its end terminations so that its upper end is fixed while a weight m is added to the lower end. The weight is incremented with 5 up to 10 g (calibrated scale, Vastar 500G X 0.01G, accuracy 0.01 g). The load force $\mathscr{F}$ for added mass m yields $\mathscr{F} = m \cdot g_0$ with gravitational constant $g_0 = 9.81$ m/s^2. For each weight increment, the specimens elongation Δl is deduced from geometrical measurements of its layer lengths $l_i + \Delta l_i$, as outlined in Section 3.5.1.1, with an estimated accuracy (Section 3.5.1.2) of $\geq 96\%$ for $\Delta l \geq 25$ mm. Depending on the specimen, the assessed total elongation varies between 55 mm and 255 mm, corresponding to a total added weight between 71 g and 416 g. The cross-sectional area $\mathscr{A}$ of tested specimens is measured as outlined in Section 3.5.1.1 whenever the elongation increment due to added weights yields about 20 ± 5 mm so that $\mathscr{A}(\mathscr{F})$ contains between 6 and 18 data points depending on the total elongation. A single PL force-elongation dataset per specimen is gathered without data smoothing as illustrated in Fig. 3.16 for $\mathrm{II}_{2,\perp}$ ($m \leq 52$ g) and

$II_{3,\perp}$ ($m \leq 196$ g). The PL force-elongation curves matches well with a linear PL data fit as the coefficient of determination yields $R^2 \geq 90$ %.

3.5.2 Molded specimens with inclusion

In order to experimentally estimate the linear or low-strain effective Young's moduli $\mathscr{E}_{eff}$ of the 15 molded composite specimens, uni-axial tension tests using precision loading (PL) are performed [14]. Firstly, the tested specimen is placed vertically and fixed from one clamping end. Then, a weight of mass m (Vastar 500G X 0.01G, accuracy 0.01 g) is added to the other clamping end in order to control the force increment. The weight is increased at a single rate for each specimen. Overall, *i.e.* considering all specimens, the weight is incremented with 10.9 ± 6.9 g. Total added weight ranges from 46.8 g to 425.9 g resulting in a total applied loading force $\mathscr{F}$ ranging from 0.5 N to 4.2 N. The applied force $\mathscr{F}$ causes an elongation Δl_s of each equivalent serial stacked layer with initial length l_s. The total elongation $\Delta l = \sum_{s=1}^{k} \Delta l_s$ is then measured at every added weight increment with an accuracy of 0.05 mm where k indicates the number of equivalent serial stacked layers. Total elongation measured for all specimens ranges from 23.0 mm up to 131.0 mm. From these measurements, force-elongation relationship $\mathscr{F}(\Delta l)$ can be obtained. Examples of two force-elongation diagrams for two different specimens $A_{0.0}$ and $A_{0.8}$ are plotted in Fig. 3.17(a). Additionally, the midway cross-sectional area of each equivalent serial stacked layer $\mathscr{A}_{x_s}$ perpendicular to the forcing direction is measured with an accuracy of 0.02 mm as illustrated in Fig. 3.15. For each specimen, cross-sectional areas $\mathscr{A}_{x_s}$ are measured at a constant weight increment amounting to 26.7 ± 15.9 g for all specimens, which corresponds to an elongation increment of 10.6 ± 4.5 mm. The specimen cross-sectional area $\mathscr{A}$ is then calculated from the arithmetic mean of its measured cross-sectional areas weighted by their respective lengths as

$$\mathscr{A} = \frac{\sum_{s=1}^{k} (l_s + \Delta l_s) \mathscr{A}_{x_s}}{l + \Delta l}. \tag{3.15}$$

A quadratic fit (coefficient of determination $R^2 \geq 99\%$) to the area-elongation data $\mathscr{A}(\Delta l)$ is then used in order to have a continuous approximation of the area-elongation relationship $\mathscr{A}^q(\Delta l)$ for each specimen. An example of resulting data points $\mathscr{A}(\Delta l)$ and their continuous fit $\mathscr{A}^q(\Delta l)$ for two different specimens $A_{0.0}$ and $A_{1.0}$ is plotted in Fig. 3.17(b).

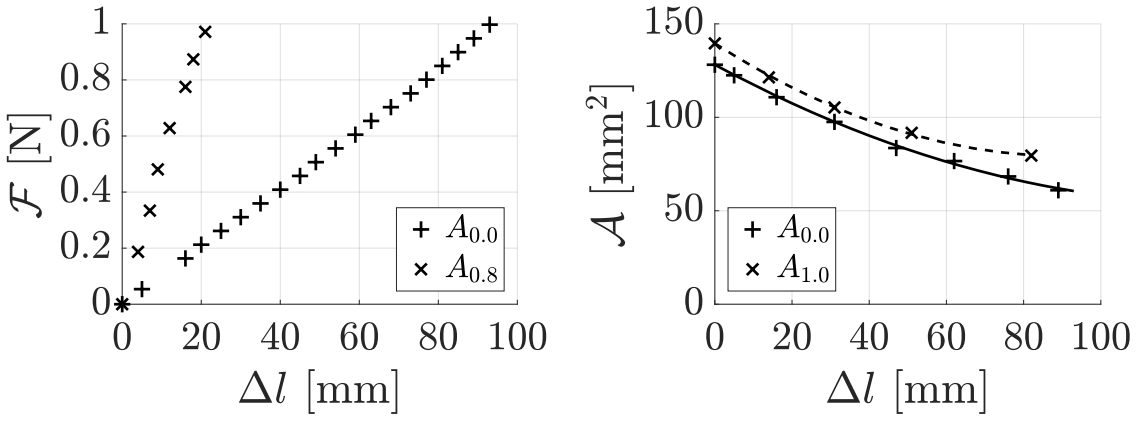

(a) $\mathscr{F}(\Delta l)$ (b) $\mathscr{A}(\Delta l)$

Figure 3.17: Examples of uni-axial tension testing data: a) force-elongation data $\mathscr{F}(\Delta l)$ for specimens $A_{0.0}$ and $A_{0.8}$ with $m \leq 102$ g and $m \leq 231$ g, respectively, b) area-elongation data $\mathscr{A}(\Delta l)$ and quadratic fits $\mathscr{A}^q(\Delta l)$ with $R^2 = 99\%$ (lines) for specimens $A_{0.0}$ and $A_{1.0}$.

3.6 Model validation

3.6.1 Molded specimens without inclusion

Force-elongation curves $\mathscr{F}(\Delta l)$ and geometrical test section characteristics obtained during MP or PL testing allow to obtain experimental stress-strain curves for each tested specimen. As the test sections geometry was shown to vary (*e.g.* cross-sectional area $\mathscr{A}$ in Section 3.5.2), the true stress σ_t and true strain ε_t are assessed. The true stress σ_t is then obtained as in Eq. (3.1) using instantaneous area $\mathscr{A}^q$ (or alternatively $\mathscr{A}^*$) so that

$$\sigma_t = \frac{\mathscr{F}}{\mathscr{A}^q}. \tag{3.16}$$

Similarly, the true strain $\varepsilon_t = \int \frac{\delta l}{l}$ is obtained using instantaneous length l so that

$$\varepsilon_t = \ln\left(\frac{l}{l_0}\right). \tag{3.17}$$

The experimental elastic Young's modulus of each specimen from either MP ($\mathscr{E}_{eff}^{MP}$) or PL ($\mathscr{E}_{eff}^{PL}$) testing is then obtained as the slope of a linear fit to the elastic region in which stress σ_t is proportional to the strain ε_t so that

$$\mathscr{E}_{eff} = \frac{\sigma_t}{\varepsilon_t} \tag{3.18}$$

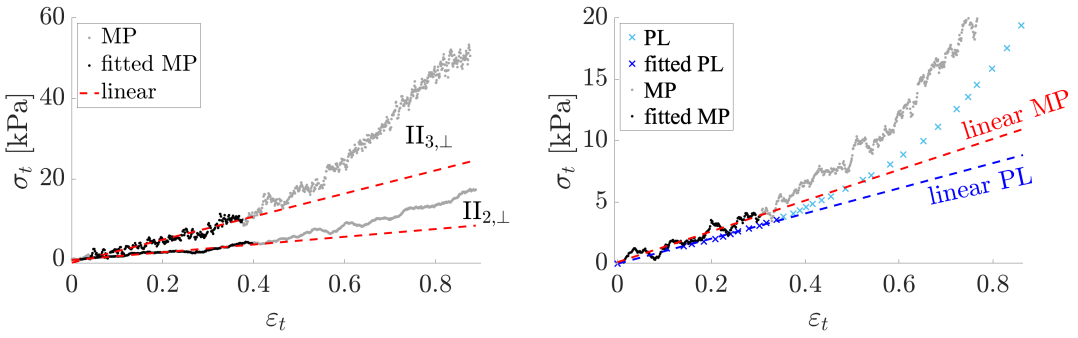

(a) $II_{2,\perp}$ and $II_{3,\perp}$ - MP

(b) $II_{2,\parallel}$ - MP and PL

Figure 3.18: Examples of stress-strain curves $\sigma_t(\varepsilon_t)$ from MP (•) or PL (×) testing, data within the linear elastic region (fitted MP or PL) and linear fit (dashed line) whose slope ($R^2 \geq 90\%$) corresponds to the elastic Young's modulus $\mathscr{E}_{eff}^{MP}$ or $\mathscr{E}_{eff}^{PL}$: a) MP results for specimens $II_{2,\perp}$ and $II_{3,\perp}$, b) MP and PL results for specimen $II_{2,\parallel}$.

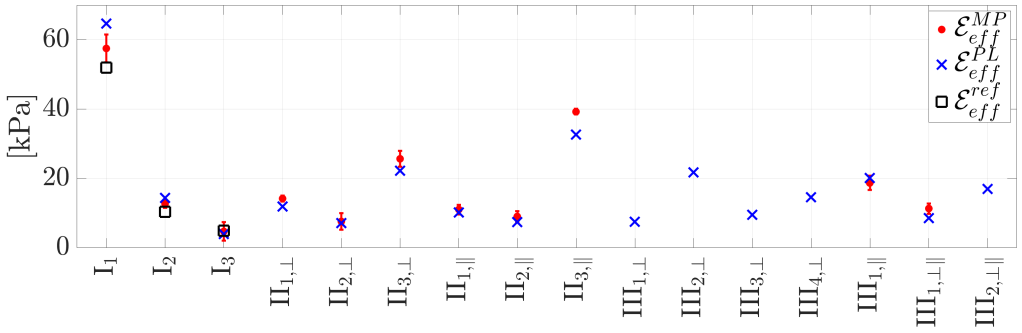

Figure 3.19: Young's moduli $\mathscr{E}_{eff}^{MP}$ (mean (•) and standard deviation (bar)) and $\mathscr{E}_{eff}^{PL}$ (×) for 1L (I.), 2L (II.) and 3L (III.) specimens. $\mathscr{E}_{eff}^{ref}$ from Table 3.1 ([17, 40]) are plotted for I..

in accordance with Hooke's law of linear elastic deformation. The elastic region $0 \leq \varepsilon_t \leq 0.2$ is extended to $\varepsilon_t > 0.2$ as long as the linear fit accuracy R^2 increases until at least $R^2 \geq 90\%$. The mean and standard deviation of the overall upper limit of the linear region yields $\varepsilon_t = 0.3 \pm 0.1$ which corresponds to an elongation of 31 ± 9 mm for PL testing ($R^2 \geq 97\%$) and an elongation of 29 ± 13 mm for MP testing ($R^2 \geq 90\%$). Examples of experimental MP and PL stress-strain curves, their linear elastic regions and associated linear stress-strain data fits are illustrated in Fig. 3.18. Sought slopes $\mathscr{E}_{eff}^{MP}$ and $\mathscr{E}_{eff}^{PL}$ for each of the tested specimen are plotted in Fig. 3.19. For each of the MP tested specimens, the mean and standard deviation (≤ 4.1 kPa) are plotted as four values are obtained, one for each of the imposed maximum elongations $\Delta l \in \{25, 50, 100, 150\}$ mm. For the 1L specimens (I.), literature values $\mathscr{E}_{eff}^{ref}$ reported in Table 3.1 [17, 40] are plotted as well.

Table 3.7: 1L specimen and single layer composition: reference $\mathscr{E}_{eff}^{ref}$ [17, 40] and measured $\mathscr{E}_{eff}^{MP}$ and $\mathscr{E}_{eff}^{PL}$ from MP and PL tests.

Specimen	$\mathscr{E}_{eff}^{ref}$ [kPa]	$\mathscr{E}_{eff}^{MP}$ [kPa]	$\mathscr{E}_{eff}^{PL}$ [kPa]
I_1	52.0	57.5	64.7
I_2	10.4	12.7	14.4
I_3	4.9	4.7	4.0

Values for 1L specimens (I.) $\mathscr{E}_{eff}^{ref}$, $\mathscr{E}_{eff}^{MP}$ and $\mathscr{E}_{eff}^{PL}$ are detailed in Table 3.7. Although reference values $\mathscr{E}_{eff}^{ref}$ are of the same order or magnitude as $\mathscr{E}_{eff}^{MP}$ and $\mathscr{E}_{eff}^{PL}$ for all three specimens, $\mathscr{E}_{eff}^{ref}$ underestimates measured $\mathscr{E}_{eff}^{MP}$ and $\mathscr{E}_{eff}^{PL}$ for I_1 (with 5.5 kPa for MP and 12.7 kPa for PL) and for I_2 (with 2.3 kPa for MP and 4 kPa for PL) whereas all $\mathscr{E}_{eff}^{\cdot}$-values (MP, PL and reference from literature) match to within 1 kPa for I_3. Therefore, model validation for molded ML specimens is assessed using layer values given by $\mathscr{E}_{eff}^{ref}$ (as for the modelled design values of molded ML specimens $\mathscr{E}_{eff}^{s-ref}$ in Table 3.4) and by the measured $\mathscr{E}_{eff}^{MP}$ and $\mathscr{E}_{eff}^{PL}$ for which modelled values are denoted $\mathscr{E}_{eff}^{s-MP}$ and $\mathscr{E}_{eff}^{s-PL}$, respectively. It is further noted that since all 2L (II.) and 3L (III.) specimens are composed of a combination of the composition of the 1L specimens, all measured $\mathscr{E}_{eff}^{MP}$ and $\mathscr{E}_{eff}^{PL}$ are within the range spanned between the softest (I_3) and most rigid (I_1) 1L specimen.

The mean and standard deviation of the overall difference between mean $\mathscr{E}_{eff}^{PL}$ and $\mathscr{E}_{eff}^{MP}$ for all specimens yields -0.8 ± 3.5 kPa. Thus the overall difference is of the same order of magnitude as the standard deviation ≤ 4.1 kPa observed between different MP tests on the same specimen so that both MP and PL tests provide accurate measurements of $\mathscr{E}_{eff}$ for all specimens. Therefore, most of the 3L specimens are subjected only to PL testing as PL testing provides the highest fit accuracy ($R^2 \geq 97\%$) of the linear elastic region with slope $\mathscr{E}_{eff}^{PL}$. Obtained $\mathscr{E}_{eff}^{PL}$ for 2L and 3L specimens with similar compositions match as the difference is limited to 0.4 kPa between $II_{2,\perp}$ and $III_{1,\perp}$ and to -0.4 kPa between $II_{3,\perp}$ and $III_{2,\perp}$. This confirms the model assumption that changing the layer order, in this case due to layer splitting and layer permutation, in ML specimens does not affect the Young's modulus when the overall composition remains similar.

The effective Young's modulus for each of the molded ML specimens is modelled as outlined in Section 3.2 while the stacking composition ratio $\mathscr{B}_{j,j+1}$ between adjacent layers is calculated using the single layer compositions $\mathscr{E}_{eff}^{\cdot}$ associated with 1L specimens summarised in Table 3.7. Thus layer compositions are either taken from literature ($\mathscr{E}_{eff}^{ref}$) as during specimens design (Table 3.4), or obtained from the measured MP ($\mathscr{E}_{eff}^{MP}$) and PL ($\mathscr{E}_{eff}^{PL}$) tests on 1L specimens. The corresponding modelled effective Young's modulus of the homogeneous elastic specimen

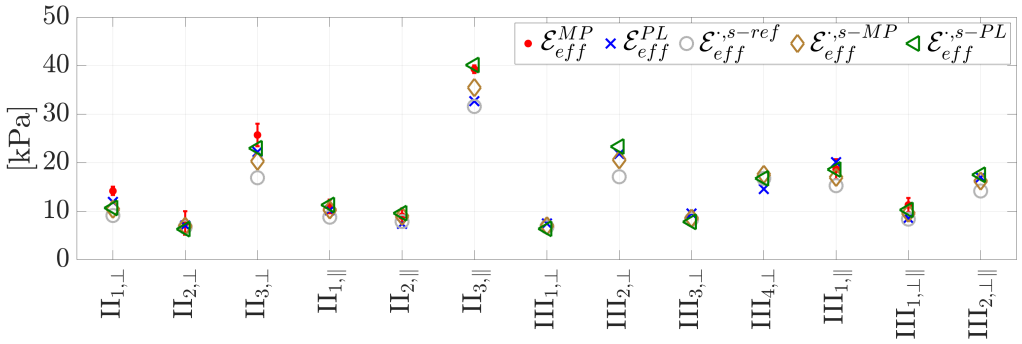

Figure 3.20: Measured and modelled $\mathscr{E}_{eff}$ for 2L (II.) and 3L (III.) specimens.

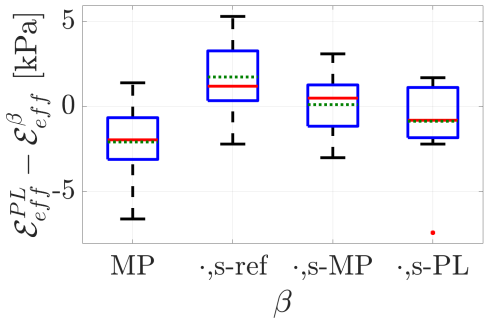

Figure 3.21: Boxplots with median (full line), mean (dotted line), interquartile range between the first and third quartile (box), extrema (whiskers) of the overall difference for ML molded specimens between $\mathscr{E}_{eff}^{PL}$ from PL tests and $\mathscr{E}_{eff}^{\beta}$ set to: a) measured $\mathscr{E}_{eff}^{MP}$ from MP tests, b) modelled $\mathscr{E}_{eff}^{\cdot,s-ref}$, c) modelled $\mathscr{E}_{eff}^{\cdot,s-MP}$, d) modelled $\mathscr{E}_{eff}^{\cdot,s-PL}$.

yields $\mathscr{E}_{eff}^{\cdot,s-ref}$, $\mathscr{E}_{eff}^{\cdot,s-MP}$ and $\mathscr{E}_{eff}^{\cdot,s-PL}$, respectively. Modelled $\mathscr{E}_{eff}^{\cdot,s-ref}$, $\mathscr{E}_{eff}^{\cdot,s-MP}$ and $\mathscr{E}_{eff}^{\cdot,s-PL}$ and measured $\mathscr{E}_{eff}^{MP}$ and $\mathscr{E}_{eff}^{PL}$ for ML specimens (II. and III.) are plotted in Fig. 3.20. Overall measured and modelled values are of the same order of magnitude so that the intended variation – reflecting the impact of stacking orientation, stacking dimension ratios and stacking composition underlying the ML specimens design – is observed for both the measured and modelled $\mathscr{E}_{eff}$.

The repartitions of the differences between the measured $\mathscr{E}_{eff}^{PL}$ for each ML specimen and each of the model values $\mathscr{E}_{eff}^{\cdot,s-ref}$, $\mathscr{E}_{eff}^{\cdot,s-MP}$ and $\mathscr{E}_{eff}^{\cdot,s-PL}$ is assessed by boxplots in Fig. 3.21. As a comparison, also the difference between measured $\mathscr{E}_{eff}^{PL}$ and measured $\mathscr{E}_{eff}^{MP}$ for ML specimens subjected to both PL and MP testing is shown as well. It is noted that model differences and measured differences are of the same order of magnitude so that the model approach is validated. In Fig. 3.20 is seen that $\mathscr{E}_{eff}^{PL}$ is slightly underestimated by $\mathscr{E}_{eff}^{\cdot,s-ref}$, so that the mean (1.7 kPa) and median (1.2 kPa) differences with respect to $\mathscr{E}_{eff}^{\cdot,s-ref}$ are positive. The overall

model accuracy improves for $\mathscr{E}_{eff}^{\cdot,s-MP}$ and for $\mathscr{E}_{eff}^{\cdot,s-PL}$ compared to $\mathscr{E}_{eff}^{\cdot,s-ref}$ as the range spanned between the extrema reduces from $[-2.2\ \ 5.3]$ kPa to within $[-3.0\ \ 3.0]$ kPa for $\mathscr{E}_{eff}^{\cdot,s-MP}$ and even further to within $[-2.2\ \ 1.7]$ kPa for $\mathscr{E}_{eff}^{\cdot,s-PL}$. Consequently, the overall model accuracy in terms of these extrema yields ± 3 kPa for $\mathscr{E}_{eff}^{\cdot,s-MP}$ and ± 2.2 kPa for $\mathscr{E}_{eff}^{\cdot,s-PL}$. Both repartitions of the differences between $\mathscr{E}_{eff}^{PL}$ and either $\mathscr{E}_{eff}^{\cdot,s-MP}$ or $\mathscr{E}_{eff}^{\cdot,s-PL}$ are characterised by a mean and median value near zero (< 1 kPa) and a standard deviation which is less than ± 2.4 kPa, which is the same as the standard deviation obtained for the difference between experimental values $\mathscr{E}_{eff}^{PL}$ and $\mathscr{E}_{eff}^{MP}$. Consequently, the overall model accuracy in terms of the standard deviation yields ± 2.4 kPa. It is noted that for the soft specimen with $\mathscr{E}_{eff}^{PL} \leq 15$ kPa, this accuracy increases to ± 1.5 kPa.

3.6.2 Molded specimens with inclusion

The sought $\mathscr{E}_{eff}$ is obtained by fitting the low-strain region of the stress-strain curves to a linear model whose slope equals $\mathscr{E}_{eff}$. For each specimen, the low-strain region is determined as the range for which R^2 is maximum, where $R^2 \geq 98\%$ expresses the goodness of fitting a linear model to the stress-strain curve with a lower bound at $\varepsilon_t = 0$. For all specimens tested, the mean and standard deviation of the upper bound of the low-strain region is $\varepsilon_t = 0.26 \pm 0.02$, which corresponds to a total elongation of 24.5 ± 1.7 mm. Examples of fitting a linear model to a low-strain region are plotted in Fig. 3.22 for three different specimens. Fig. 3.22(a) shows the different fits, and hence slopes $\mathscr{E}_{eff}$, obtained for two specimens $A_{0.0}$ and $A_{0.6}$, without and with an inclusion, respectively. Fig. 3.22(b) shows similar fits, and hence slopes $\mathscr{E}_{eff}$, obtained for two specimens $A_{0.6}$ and $B_{0.6}$ with the same inclusion ($h_{in}/h = 0.6$ and $l_{in}/l_2 = 1$) but positioned at either the side ($A_{0.6}$) or the centre ($B_{0.6}$) of the superficial layer in $A_{0.0}$.

The model approach outlined in Section 3.4 is next used to predict the low-strain $\widehat{\mathscr{E}}_{eff}$ of each of the 15 molded specimens. Modelled $\widehat{\mathscr{E}}_{eff}$ and measured $\mathscr{E}_{eff}$ values are plotted in Fig. 3.23(a). The difference $\mathscr{E}_{eff} - \widehat{\mathscr{E}}_{eff}$ between measured and modelled values is plotted in Fig. 3.23(b). The absolute value $|\mathscr{E}_{eff} - \widehat{\mathscr{E}}_{eff}|$ for specimens with inclusions corresponds to a model error ranging from 1.0 kPa up to 7.1 kPa, which amounts to 7.4% up to 18.3% of the measured $\mathscr{E}_{eff}$. Overall $\mathscr{E}_{eff} - \widehat{\mathscr{E}}_{eff}$ of molded specimens is characterised by a mean and standard deviation of 2.7 ± 2.7 kPa. Compared to the overall model accuracy of 0.0 ± 2.4 kPa obtained for two and three layer specimens reported in [14], the overall model accuracy for specimens with inclusions is thus shifted due to the non-zero mean to the range from 0.0 kPa up to 5.2 kPa. The positive non-zero mean of 2.7 kPa indicates that the model tends to underestimate measured values. From Fig. 3.23 is seen that the underestimation (with 2.7 kPa up to 7.1 kPa) is associated with specimens of type A and type B for which the influence of the inclusion on the Young's modu-

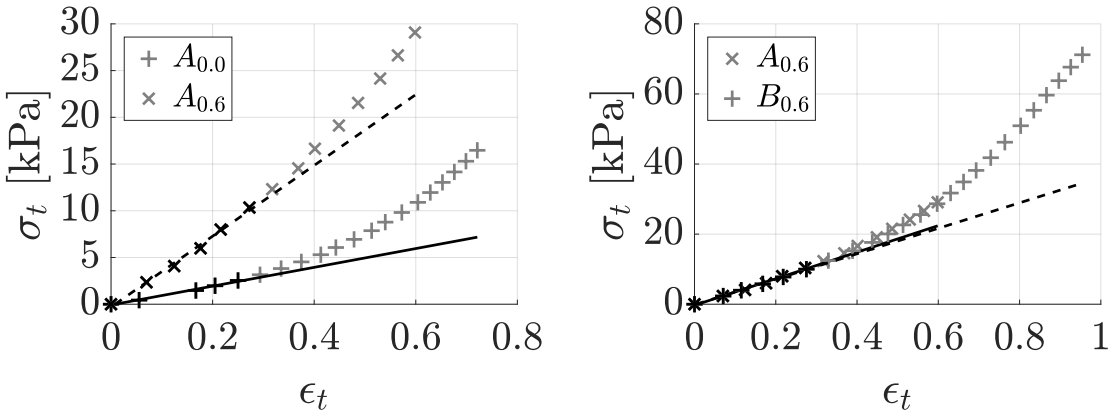

(a) Size (b) Position

Figure 3.22: Experimental stress-strain curves $\sigma_t(\varepsilon_t)$ for three specimens and linear fits (lines) to the low-strain region ($R^2 \geq 98\%$) with slope $\mathscr{E}_{eff}$: a) specimens $A_{0.0}$ and $A_{0.6}$ (low-strain region $\varepsilon_t \leq 0.25$ and $\varepsilon_t \leq 0.27$), b) specimens $A_{0.6}$ and $B_{0.6}$ (low-strain region $\varepsilon_t \leq 0.27$).

lus is most prominent as their measured effective Young's modulus ($\mathscr{E}_{eff} \geq 30.6$ kPa) is at least tripled compared to $\mathscr{E}_{eff} = 10.2$ kPa, measured for the reference specimen without inclusion $A_{0.0}$. Despite this underestimation, the measured $\mathscr{E}_{eff}$ and modelled $\widehat{\mathscr{E}}_{eff}$ values exhibit the same tendencies so that the experimental data validate the model approach for all specimen types (including the ones with arbitrary stacking) and also the model properties discussed in Section 3.4.2 such as:

- Comparing measured $\mathscr{E}_{eff}$ for specimens of type A (inclusion at the side) and type B (inclusion at the centre) confirms that the transverse position of the inclusion within the superficial layer does not affect the effective Young's modulus of the specimen as the difference between $\mathscr{E}_{eff}$ measured for $A_{h_{in}/h}$ and $B_{h_{in}/h}$ is less than 1.6 kPa for all three assessed h_{in}/h ratios (0.1, 0.3, 0.6).
- Comparing measured $\mathscr{E}_{eff}$ for specimens of type A (inclusion with $l_{in}/l_2 = 1$) and type D (inclusion with $l_{in}/l_2 = 0.2$) confirms the influence of the inclusion size (length l_{in}/l_2 and height h_{in}/h ratios) on the modelled $\widehat{\mathscr{E}}_{eff}$ shown in Fig. 3.11 so that in particular the length of the inclusion in the force direction (l_{in}/l_2) affects the effective Young's modulus $\mathscr{E}_{eff}$ for these specimens.
- Comparing measured $\mathscr{E}_{eff}$ for specimens $A_{0.8}$ (type A, inclusion in the superficial layer) and $C_{0.8}$ (type C, inclusion in both the superficial and the muscle layer) confirms that the influence of the inclusion on measured $\mathscr{E}_{eff}$ increases with the Young's modulus ratio $\mathscr{E}^{in}/\mathscr{E}$, which for the molded specimens (Table 3.5) reduces from 74.5 in the superficial layer to 4.6 in the muscle layer.

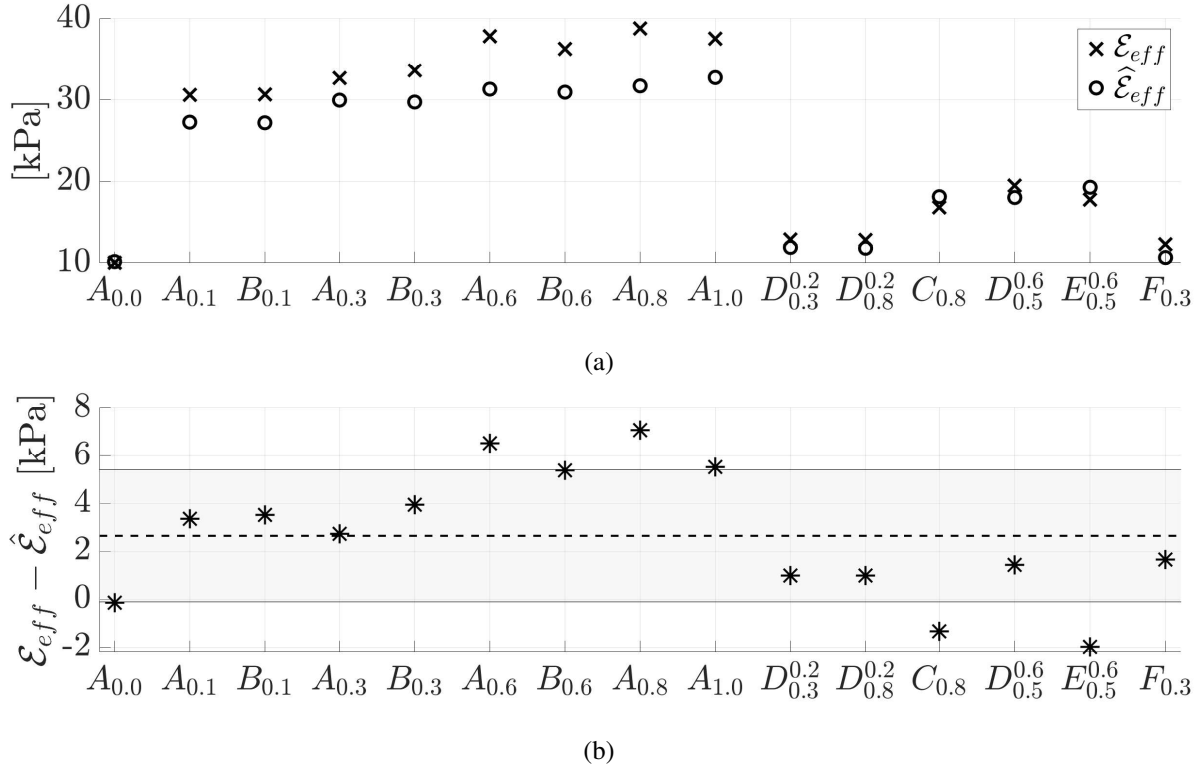

Figure 3.23: Low-strain Young's moduli for molded ML specimens: a) measured $\mathscr{E}_{eff}$ ($\times$) and modelled $\widehat{\mathscr{E}}_{eff}$ ($\circ$). b) difference $\mathscr{E}_{eff} - \widehat{\mathscr{E}}_{eff}$ ($*$) with the overall mean (dashed line) and standard deviation (shaded area).

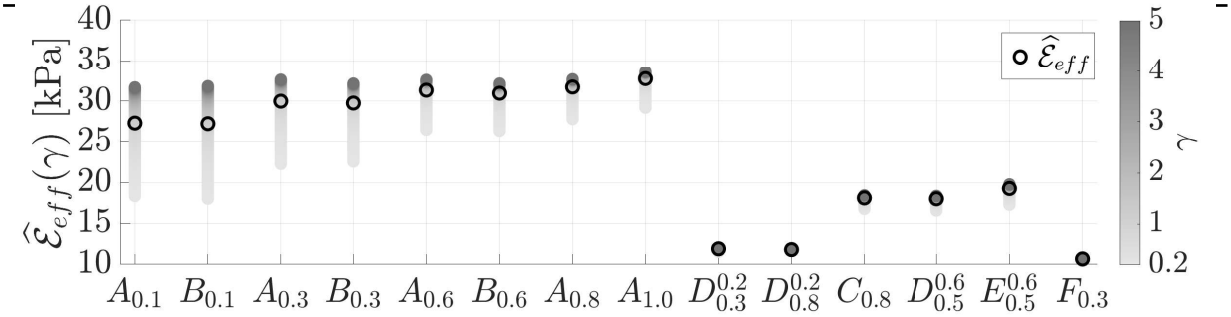

(a) $\widehat{\mathscr{E}}_{eff}(\gamma)$ (gray scale), $\widehat{\mathscr{E}}_{eff}$ for $\gamma = 1$ (∘)

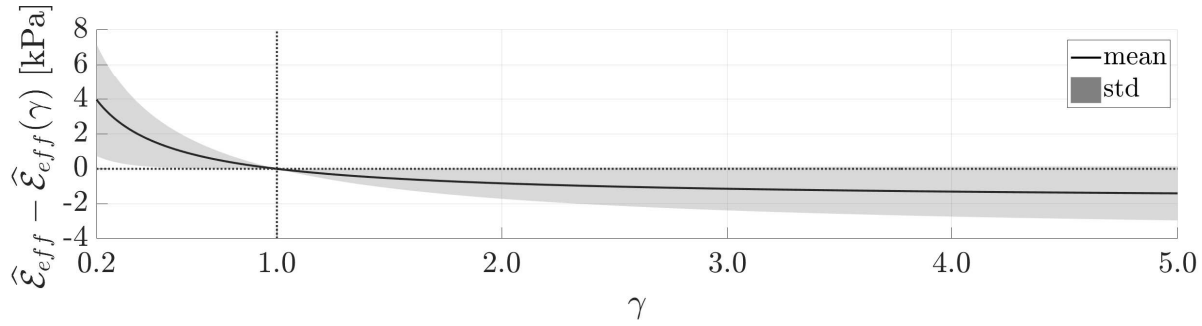

(b) mean and standard deviation of $\widehat{\mathscr{E}}_{eff} - \widehat{\mathscr{E}}_{eff}(\gamma)$

Figure 3.24: Effect of scaling the Young's modulus of the inclusion $\mathscr{E}^{In}$ with a scalar $0.2 \leq \gamma \leq 5$ on modelled $\widehat{\mathscr{E}}_{eff}$ for all 14 ML composite types with inclusion: a) $\widehat{\mathscr{E}}_{eff}(\gamma)$ for increasing $0.2 \leq \gamma \leq 5$ (gray scale) and $\widehat{\mathscr{E}}_{eff}$ for $\gamma = 1$ (∘), b) overall mean (full line) and standard deviation (std, shaded region) of $\widehat{\mathscr{E}}_{eff} - \widehat{\mathscr{E}}_{eff}(\gamma)$. As a reference, dotted lines indicate zero difference (horizontal) and $\gamma = 1$ (vertical).

The influence of the ratio $\mathscr{E}^{In}/\mathscr{E}$ is further explored using the model. The Young's modulus of the inclusion $\mathscr{E}^{In}$, and the Young's modulus ratio $\mathscr{E}^{In}/\mathscr{E}$ of the superficial and muscle layer given in Table 3.5, are scaled as $\gamma\mathscr{E}^{In}$. The scalar γ is varied between 0.2 ($\mathscr{E}^{In}$ divided by 5) and 5 ($\mathscr{E}^{In}$ multiplied by 5) so that unscaled model values $\widehat{\mathscr{E}}_{eff}$ for $\mathscr{E}^{In}$ are obtained for $\gamma = 1$. In particular, the scaled Young's modulus of the inclusion $\gamma\mathscr{E}^{In}$ ranges from 60 kPa up to 1.49 MPa so that the associated Young' modulus ratios $\mathscr{E}^{In}/\mathscr{E}$ for the superficial layer (ratio from 14.9 up to 372) and for the muscle layer (ratio from 2.6 up to 65) containing the inclusion remain greater than 1 (so an inclusion is embedded in a softer layer). Modelled $\widehat{\mathscr{E}}_{eff}(\gamma)$ for all 14 composite types with inclusion are plotted in Fig. 3.24(a). Values $\widehat{\mathscr{E}}_{eff}$ (circles) for $\gamma = 1$ obtained for the molded specimens are indicated as a reference. For each composite type, $\widehat{\mathscr{E}}_{eff}(\gamma)$ increases with γ. Values of $\widehat{\mathscr{E}}_{eff}(\gamma)$ for $\gamma \in \{0.2, 1.0, 5.0\}$ and the relative maximum difference (in %) of $\widehat{\mathscr{E}}_{eff}(\gamma)$

Table 3.8: Influence of scaling inclusions Young's modulus $\mathscr{E}^{In}$ with scalar $\gamma \in \{0.2, 1, 5\}$ on modelled $\widehat{\mathscr{E}}_{eff}$ (in kPa) for all 14 composite types with inclusion and the relative maximum difference $\mathscr{D}$ (in %) with respect to $\widehat{\mathscr{E}}_{eff}$ for $\gamma = 1$.

γ	$A_{0.1}$	$B_{0.1}$	$A_{0.3}$	$B_{0.3}$	$A_{0.6}$	$B_{0.6}$	$A_{0.8}$	$A_{1.0}$	$D_{0.3}^{0.2}$	$D_{0.8}^{0.2}$	$C_{0.8}$	$D_{0.5}^{0.6}$	$E_{0.5}^{0.6}$	$F_{0.3}$
0.2	18.4	18.0	22.3	22.6	26.4	26.3	27.8	29.2	11.6	11.7	16.8	16.6	17.3	10.4
1.0	27.3	27.2	30.0	29.8	31.3	31.0	31.7	32.8	11.9	11.8	18.1	18.0	19.3	10.7
5.0	31.7	31.8	32.6	32.2	32.6	32.2	32.7	33.6	12.0	11.8	18.4	18.4	19.8	10.7
$\mathscr{D}$	49	51	34	32	20	19	15	13	3	1	9	10	13	3

with respect to $\widehat{\mathscr{E}}_{eff}$ for $\gamma = 1$

$$\mathscr{D} = \frac{\widehat{\mathscr{E}}_{eff}(5) - \widehat{\mathscr{E}}_{eff}(0.2)}{\widehat{\mathscr{E}}_{eff}} \tag{3.19}$$

are summarised in Table 3.8. The relative maximum difference $\mathscr{D}$ ranges from 1% up to 51%. As observed in Fig. 3.24(a), the influence of scaling the Young's modulus of the inclusion on $\widehat{\mathscr{E}}_{eff}$ depends on the composite type. The overall (for all composite types) mean and standard deviation (std) of the difference $\widehat{\mathscr{E}}_{eff} - \widehat{\mathscr{E}}_{eff}(\gamma)$ as a function of γ is plotted in Fig. 3.24(b). Both the mean and std become zero at $\gamma = 1$ for which the difference is zero by definition (since $\widehat{\mathscr{E}}_{eff} = \widehat{\mathscr{E}}_{eff}(\gamma = 1)$). As $\widehat{\mathscr{E}}_{eff}(\gamma)$ increases with γ, the overall mean of $\widehat{\mathscr{E}}_{eff} - \widehat{\mathscr{E}}_{eff}(\gamma)$ decreases monotonically as γ increases. Thus, the overall mean difference is positive for $\gamma < 1$ and negative for $\gamma > 1$ since $\widehat{\mathscr{E}}_{eff} > \widehat{\mathscr{E}}_{eff}(\gamma < 1)$ and $\widehat{\mathscr{E}}_{eff} < \widehat{\mathscr{E}}_{eff}(\gamma > 1)$. The rate at which the overall mean difference decreases slows down with γ. The model suggests that, for the assessed composite types, $\widehat{\mathscr{E}}_{eff}$ becomes less sensitive to the exact value of $\mathscr{E}^{In}$ for large $\mathscr{E}^{In}/\mathscr{E}$ ratios. The overall standard deviation of $\widehat{\mathscr{E}}_{eff} - \widehat{\mathscr{E}}_{eff}(\gamma)$ increases with $|\gamma - 1|$, which expresses that the influence of scaling $\mathscr{E}^{In}$ on $\widehat{\mathscr{E}}_{eff}$ differs between composite types.

3.7 Conclusion

In this chapter, the effective low-strain elastic Young's modulus of silicone ML composites is measured on 31 molded bone-shaped specimens using uni-axial stress testing. ML specimens were designed so that the stacking orientation (serial, parallel, combined or arbitrary) and the range of composition and dimension ratios affect the specimens effective elastic Young's modulus $\mathscr{E}_{eff}$. Concretely, the specimens $\mathscr{E}_{eff}$ varies between 4 kPa and 65 kPa, which overlaps the range associated with normal human VF's (up to 60 kPa). The $\mathscr{E}_{eff}$ of six 2L and two 3L specimens is experimentally determined from MP and from PL testing so that both methods are

cross-validated as their difference yields less than 3.5 kPa, which is of the same order of magnitude as the difference (≤ 4.1 kPa) associated with multiple MP testing on the same specimen. More complex ML composite types with at least 4 layers are obtained by embedding a stiffer (298 kPa) inclusion with variable size, position and stacking in the superficial or/and muscle layer of a reference specimen that is obtained from a three-layer vocal fold anatomical representation of the muscle, superficial and epithelium layers. Measured effective Young's moduli of all molded ML composite specimens are compared to modelled values describing equivalent homogenised specimens based on the geometry of its layers, Young's moduli and stacking. For ML specimens consisting solely out of serial and/or parallel stacked layers an analytical model approach is applied, which exploits the hypothesis of homogeneous strain for parallel stacked layers and the hypothesis of homogeneous stress for serial stacked layers. The model approach is extended to specimens for which the inclusion results in arbitrary stacking, first using spatial discretisation along the force direction of the portion with arbitrary stacking and then using area conservation to propose a geometrical approximation for inclined or bent inclusions with arbitrary stacking. Modelled effective Young's moduli are validated against measured values resulting in an overall model accuracy between 0.0 kPa and 5.2 kPa.

The quasi-analytical model proposed in this chapter allows one to explore the influence of its parameters on the predicted effective Young's modulus. Concretely, the influence of the dimensions of an inclusion in the superficial layer and of the influence of scaling the Young's modulus of the inclusion for different ML composite types are discussed. In the first case, the length of the inclusion in the force direction is shown to determine the modelled effective Young's modulus, whereas in the latter case it was found that the rate at which the effective Young's modulus increases with the inclusions slows down, so that eventually for stiff inclusions the exact value of its Young's modulus becomes less important. It is expected, that the proposed model and subsequent model parameter studies are of interest for the *a-priori* characterisation and design of silicone ML composite vocal fold replicas mimicking the complex ML anatomical vocal fold structure without or with inclusion, as in the case of a structural pathology or abnormality.

As this chapter contributes to the mechanical characterisation of multi-layer silicone composites, used to mold silicone vocal fold replicas, the next chapter extends this characterisation by studying non-linear models to accurately provide continuous fits of the stress-strain data.

CHAPTER 4

Modelling and validation of the non-linear elastic stress-strain behaviour of multi-layer silicone composites

---

Based on:

Ahmad, M., Pelorson, X., Guasch, O., Fernández, I. A., & Van Hirtum, A. (2023). Modelling and validation of the non-linear elastic stress-strain behaviour of multi-layer silicone composites. Journal of the Mechanical Behavior of Biomedical Materials, 139, 105690.

4.1 Introduction

As it is well established [52, 53] that biological soft tissues, and thus human VF tissues [4, 6, 34, 54, 55], are characterised by small stresses in response to relatively large strains ε_t, greater than one and thus deformations larger than 100% as shown in Fig. 4.1(a), it is of interest to assess how the stress-strain relationship of silicone ML composites behaves beyond the linear range and how the non-linear behaviour compares to the one typically observed in biological soft tissues. The structural mechanics of the silicone ML composites as well as the pertinence of these composites to represent biological soft tissues (in the context of VF replicas) is further investigated. In the present study, 63 measured stress-strain curves on 40 molded specimens from uni-axial stretching at room temperature described in Chapter 3 are further analysed in order to characterise and model the stress-strain curves for $\varepsilon_t > \varepsilon_l$. We aim at proposing a phenomenological continuous model of the elastic stress-strain curves valid within and beyond the low-strain range. The total strain range of interest is limited to $\varepsilon_t \leq 1.5$. This corresponds to a degree of deformation $\Delta l/l_0$ up to 350% (see Fig. 4.1(a)), or about 10 times the maximum elongation of 35% associated with the overall mean low-strain upper limit $\varepsilon_l = 0.3$. The measured maximum strain $\max(\varepsilon_t)$ depends on the specimen and is limited to $\max(\varepsilon_t) \leq 1.36$. An overview of $\max(\varepsilon_t)$ as a function of $\mathscr{E}_{(eff)}$ is given in Fig. 4.1(b). Respectively, 52 and 25 of the measured stress-strain data curves satisfy $\max(\varepsilon_t) \geq 0.4$ and $\max(\varepsilon_t) \geq 0.77$, which corresponds to an extension of the strain range of about 33% and 156% beyond the upper limit of the low-strain region $\varepsilon_l \approx 0.3$.

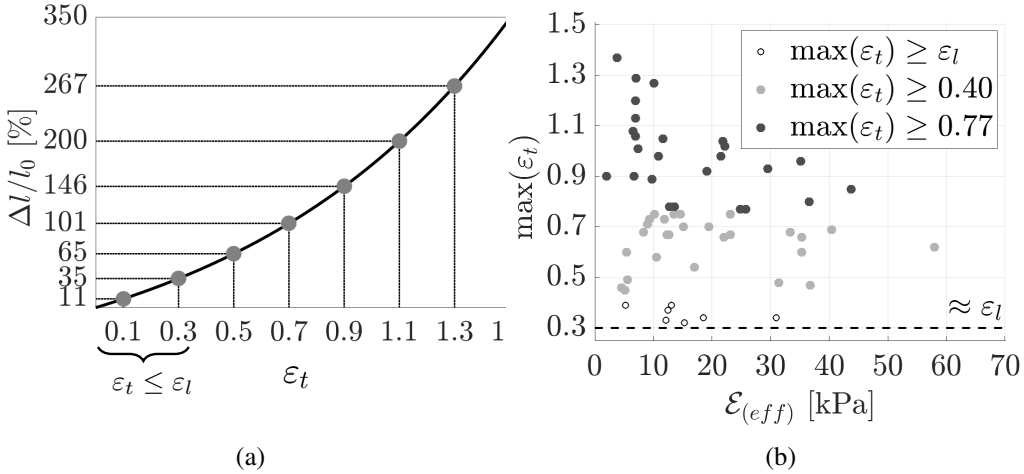

(a) (b)

Figure 4.1: a) Degree of deformation $\Delta l/l_0$ for true strain $0 \leq \varepsilon_t \leq 1.5$. The overall low-strain range $\varepsilon_t \leq \varepsilon_l$ with $\varepsilon_l \approx 0.3$ is indicated. b) Measured maximum strain $\max(\varepsilon_t)$ as a function of low-strain Young's modulus $\mathscr{E}_{(eff)}$. The linear low-strain upper limit $\varepsilon_l \approx 0.3$ is indicated (dashed line).

4.2 Continuous elastic stress-strain relationships and a priori modelled parameter expressions

The typical stress-strain data curve plotted in Fig. 4.2(a) shows that the elastic linear low-strain range $\varepsilon_t \leq \varepsilon_l$, expressed with Hooke's law using the low-strain effective Young's modulus $\mathscr{E}_{(eff)}$ as

$$\sigma_t(\varepsilon_t) = \mathscr{E}_{(eff)}\,\varepsilon_t, \tag{4.1}$$

transitions to a more rapid increase of stress σ_t with strain ε_t indicating elastic non-linear stress-strain behaviour for $\varepsilon > \varepsilon_l$. In accordance with models proposed for soft biological tissues accounting for the rapid non-linear increase of stress with strain for $\varepsilon_t > \varepsilon_l$ [4, 52, 53, 56–58], the following exponential and third order polynomial (cubic) non-linear continuous two-parameter relationships with $\mathscr{C}^1$ continuity are assessed in order to model the measured $\sigma_t(\varepsilon_t)$ curves:

$$\text{exponential}: \sigma_t(\varepsilon_t) = A\,(e^{B\,\varepsilon_t} - 1), \tag{4.2a}$$

$$\text{cubic}: \sigma_t(\varepsilon_t) = a\,\varepsilon_t^3 + b\,\varepsilon_t, \tag{4.2b}$$

with (A,B) and (a,b) their respective two parameter sets. Fig. 4.2 illustrates the linear fit of

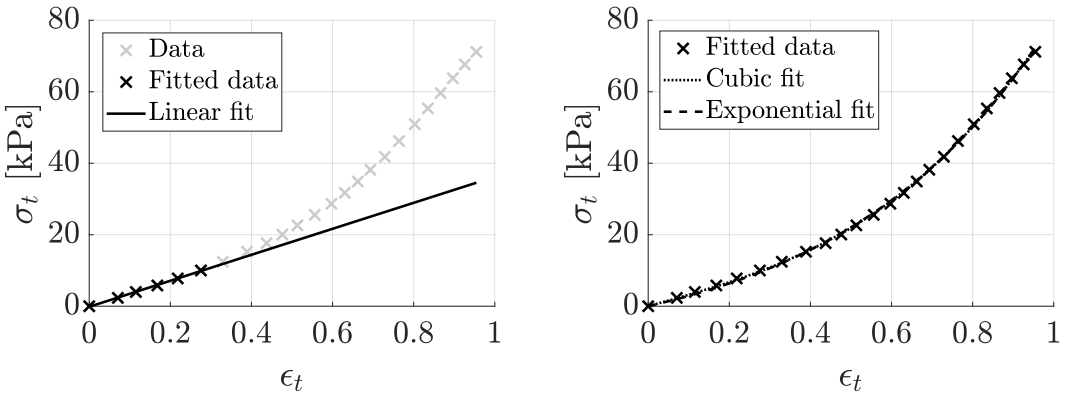

(a) Linear model (b) Non-linear models

Figure 4.2: Experimental stress-strain data curve $\sigma_t(\varepsilon_t)$ (symbols) and stress-strain models (lines) with fit accuracy $R^2 \geq 99.5\%$ for a five-layer ($n = 5$) specimen with combined ($\|\perp$) stacking: a) linear (full line) low-strain ($\varepsilon_t \leq \varepsilon_l$) fit with slope $\mathscr{E}_{eff} = 36$ kPa, b) continuous non-linear cubic (dotted line) and exponential (dashed line) fits.

Eq. (4.1) (in Fig. 4.2(a)) to the low-strain region $\varepsilon_t \leq \varepsilon_l$ and the continuous exponential and cubic fits of Eq. (5.2) (in Fig. 4.2(b)) to a typical stress-strain data set. For each measured stress-strain curve, best fit parameter sets $(\widehat{A},\widehat{B})$ and $(\widehat{a},\widehat{b})$ are estimated by minimising the root mean

square error (rmse),

$$\text{rmse} = \sqrt{\frac{1}{N}\sum_{i=1}^{N}\left[(\widehat{\sigma}_t)_i - (\sigma_t)_i\right]^2} \tag{4.3}$$

between measured σ_t and fitted $\widehat{\sigma}_t$ stresses with N the number of strain data points within the analysis range and i the index of individual data points. The goodness of fit, expressed by the coefficient of determination R^2, yields $R^2 > 99.5\%$ for each continuous model to the measured stress-strain curves, obtained using either MP or PL uni-axial tensile testing. Therefore, both continuous two-parameter relationships can be used to represent the measured stress-strain curves.

4.2.1 Linear low-strain behaviour of continuous stress-strain models

The first order derivatives of Eq. (4.2a) and Eq. (4.2b) with respect to ε_t become

$$\text{exponential}: \frac{d\sigma_t}{d\varepsilon_t} = A\,B\,e^{B\,\varepsilon_t}, \tag{4.4a}$$

$$\text{cubic}: \frac{d\sigma_t}{d\varepsilon_t} = 3\,a\,\varepsilon_t^2 + b. \tag{4.4b}$$

The linear low-strain behaviour for $\varepsilon_t \leq \varepsilon_l$ of the exponential Eq. (4.2a) and cubic Eq. (4.2b) relationship is then obtained from the first order Taylor expansion near $\varepsilon_t \approx 0$ as:

$$\text{exponential}: \sigma_t(\varepsilon_t \approx 0) = A\,B\,\varepsilon_t, \tag{4.5a}$$

$$\text{cubic}: \sigma_t(\varepsilon_t \approx 0) = b\,\varepsilon_t, \tag{4.5b}$$

where it is used that both the exponential and cubic models have no residual stress at zero strain so that $\sigma_t(\varepsilon_t \approx 0) \approx 0$ kPa. Consequently, the elastic low-strain (effective) Young's modulus $\mathscr{E}_{(eff)}$, describing the linear stress-strain behaviour in the low-strain range $\varepsilon_t \leq \varepsilon_l$ (Eq. (4.1)) is expressed in terms of the continuous model fit parameters as:

$$\text{exponential}: \mathscr{E}_{(eff)} = A\,B, \tag{4.6a}$$

$$\text{cubic}: \mathscr{E}_{(eff)} = b. \tag{4.6b}$$

4.2.2 Non-linear behaviour of continuous stress-strain models

Using $A = \mathscr{E}_{(eff)}/B$ (Eq. (4.6a)) and $b = \mathscr{E}_{(eff)}$ (Eq. (4.6b)) and assuming that $\mathscr{E}_{(eff)}$ is a known quantity, the continuous models in Eq. (4.2a) and Eq. (4.2b) can be rewritten depending

on the low-strain linear Young's modulus $\mathscr{E}_{(eff)}$, which yields the two continuous one-parameter relationships

$$\text{exponential}: \sigma_t(\varepsilon_t) = \frac{\mathscr{E}_{(eff)}}{B}\,(e^{B\varepsilon_t} - 1), \tag{4.7a}$$

$$\text{cubic}: \sigma_t(\varepsilon_t) = a\,\varepsilon_t^3 + \mathscr{E}_{(eff)}\,\varepsilon_t, \tag{4.7b}$$

with the unknown parameters B and a (already in Eq. (5.2)) determining the non-linear behaviour in the range $\varepsilon_t > \varepsilon_l$.

From the first order expansion of the non-linear continuous relationships in Eq. (5.2) it follows that the local linear slopes $\mathscr{E}_{NL}$ associated with their linear approximations near any ε_t are expressed as:

$$\text{exponential}: \mathscr{E}_{NL} = \mathscr{E}_{(eff)}\,e^{B\varepsilon_t}, \tag{4.8a}$$

$$\text{cubic}: \mathscr{E}_{NL} = 3\,a\,\varepsilon_t^2 + \mathscr{E}_{(eff)}. \tag{4.8b}$$

At low-strain (for $\varepsilon_t \approx 0$), these expressions reduce to $\mathscr{E}_{NL}(\varepsilon_t \approx 0) \approx \mathscr{E}_{(eff)}$ in accordance with the linear low-strain behaviour described in Section 4.2.1. As both the exponential (Eq. (4.7a)) and cubic (Eq. (4.7b)) relationship fit the measured data for the assessed strain range, estimated stresses are assumed to match. Equating Eq. (4.7a) and Eq. (4.7b) for any matching strain value ε_t^m and making use of Eq. (4.8a) and Eq. (4.8b) results in the following relationship between $\mathscr{E}_{NL}$ and the low-strain Young's modulus $\mathscr{E}_{(eff)}$,

$$\mathscr{E}_{NL}\ln\left(\frac{\mathscr{E}_{NL}}{\mathscr{E}_{(eff)}}\right) + 2\,\mathscr{E}_{(eff)}\ln\left(\frac{\mathscr{E}_{NL}}{\mathscr{E}_{(eff)}}\right) - 3\,\mathscr{E}_{NL} + 3\,\mathscr{E}_{(eff)} = 0. \tag{4.9}$$

The solution $\mathscr{E}_{NL}(\mathscr{E}_{(eff)})$ is accurately approximated as $\mathscr{E}_{NL} = 8.58\,\mathscr{E}_{(eff)}$ ($R^2 = 99.9\%$) as illustrated in Fig. 4.3 for $\mathscr{E}_{(eff)} \in \left[0.1, 350\right]$, which includes the values of interest indicated in Table 3.5. Consequently, the parameter sets (A,B) and (a,b) associated with the local linear behaviour of the non-linear exponential and cubic functions at strain ε_t^m are given in terms of $\mathscr{E}_{(eff)}$ as,

$$\text{exponential}: \quad B = \frac{1}{\varepsilon_t^m}\ln\left(\frac{\mathscr{E}_{NL}}{\mathscr{E}_{(eff)}}\right), \qquad A = \frac{\varepsilon_t^m\,\mathscr{E}_{(eff)}}{\ln\left(\frac{\mathscr{E}_{NL}}{\mathscr{E}_{(eff)}}\right)}, \tag{4.10a}$$

$$\text{cubic}: \quad b = \mathscr{E}_{(eff)}, \qquad a = \frac{\mathscr{E}_{NL} - \mathscr{E}_{(eff)}}{3\,(\varepsilon_t^m)^2}. \tag{4.10b}$$

Using the ratio $\mathscr{E}_{NL}/\mathscr{E}_{(eff)} \approx 8.58$, the two-parameter sets of Eq. (5.2) can be expressed as a function of $\mathscr{E}_{(eff)}$ since

$$\text{exponential}: \quad B \approx 2.15\,\frac{1}{\varepsilon_t^m}, \qquad A \approx 0.47\,\mathscr{E}_{(eff)}\,\varepsilon_t^m, \tag{4.11a}$$

$$\text{cubic}: \quad b \approx \mathscr{E}_{(eff)}, \qquad a \approx 2.53\,\mathscr{E}_{(eff)}\,\frac{1}{(\varepsilon_t^m)^2}. \tag{4.11b}$$

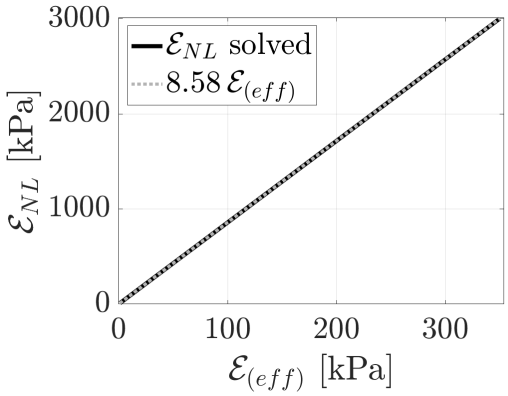

Figure 4.3: Solutions $\mathscr{E}_{NL}$ from Eq. (4.9) as a function of $\mathscr{E}_{(eff)}$ (thick full line) and superimposed linear fit (light dotted line) with $R^2 = 99.9\%$.

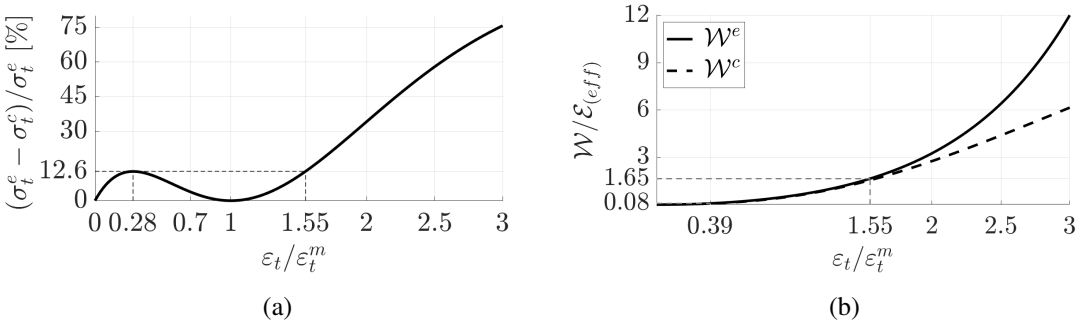

Figure 4.4: For the exponential (superscript e) and cubic (superscript c) relationship: a) relative difference (%) between modelled true stresses σ_t as a function of normalised strain $\varepsilon_t/\varepsilon_t^m$, b) strain energy density function $\mathscr{W}$ normalised by low-strain $Y_{(eff)}$.

These (positive) model parameter approximations respect the low-strain behaviour in Eq. (4.6a) and Eq. (4.6b) as $AB \approx \mathscr{E}_{(eff)}$ and $b \approx \mathscr{E}_{(eff)}$. Beyond the low-strain region, the cubic parameter a and the exponential parameter A are proportional to $\mathscr{E}_{(eff)}$. In addition, the cubic parameter a and exponential parameters (A,B) not only depend on $\mathscr{E}_{(eff)}$, but also on the considered strain ε_t^m at which the cubic and exponential model are imposed to match. For $\varepsilon_t^m = 1$, this gives $B \approx 2.15$, $A/\mathscr{E}_{(eff)} \approx 0.5$ and $a/\mathscr{E}_{(eff)} \approx 2.5$. For $\varepsilon_t^m \neq 1$, the model parameters B, A and a will decrease or increase with respect to their value at $\varepsilon_t^m = 1$, depending on $\varepsilon_t^m < 1$ or $\varepsilon_t^m > 1$, since $B \propto \varepsilon_t^{-1}$, $A \propto \varepsilon_t$ and $a \propto \varepsilon_t^{-2}$.

The relative difference (in percentage) between the modelled true stresses from the exponential (σ_t^e) and cubic (σ_t^c) relationships as a function of the normalised strain $\varepsilon_t/\varepsilon_t^m$ is plotted in Fig. 4.4(a). The difference is zero at $\varepsilon_t/\varepsilon_t^m \in \{0, 1\}$ as for these strains the stresses match. For intermediate stresses $0 \leq \varepsilon_t/\varepsilon_t^m \leq 1$, the difference is less than the maximum of 12.6% associated

with $\varepsilon_t/\varepsilon_t^m = 0.28$. For $\varepsilon_t/\varepsilon_t^m > 1$, the difference increases since σ_t^e (exponential) increases more rapidly than σ_t^c (cubic). Overall, the stress-difference remains less than 12.6% when fulfilling the condition $\varepsilon_t/\varepsilon_t^m \leq 1.55$ and increases thereafter. Thus ε_t^m should be at least 65% of the maximum assessed strain $\max(\varepsilon_t)$ to ensure this accuracy between the curves obtained with the model parameters. For $0.77 \leq \varepsilon_t^m \leq 1.36$, which is reasonable considering the variation of the maximum strain ($\max(\varepsilon_t) \leq 1.36$) in the measured stress-strain curves (see Fig. 4.1(b)), we get using Eq. (4.11) the model parameter ranges $1.58 \leq B \leq 2.79$, $0.36 \leq A/\mathscr{E}_{(eff)} \leq 0.64$, $1.36 \leq a/\mathscr{E}_{(eff)} \leq 4.27$ and $b = \mathscr{E}_{(eff)}$.

Introducing the elongation parameter $\lambda = l/l_0$ so that $\lambda = e^{\varepsilon_t}$ and $\lambda \geq 1$, the strain energy density function expressing the strain energy per unit volume of the deformed material is obtained as the work done by the load

$$\mathscr{W}(\lambda) = \int_1^{\lambda} \frac{\sigma_t(\lambda)}{\lambda^2} d\lambda. \tag{4.12}$$

Inserting the exponential σ_t^e and the cubic σ_t^c stress relationship with parameter values for $\varepsilon_t^m = 1$, $\mathscr{W}$ normalised by the linear low-strain modulus $\mathscr{E}_{(eff)}$ becomes,

$$\text{exponential :} \quad \frac{\mathscr{W}^e(\lambda)}{\mathscr{E}_{eff}} \approx 0.47 \left(\frac{\lambda^{1.15}}{1.15} + \frac{1}{\lambda} - 1.87 \right), \tag{4.13a}$$

$$\text{cubic :} \quad \frac{\mathscr{W}^c(\lambda)}{\mathscr{E}_{eff}} \approx -\frac{1}{\lambda} \Big(2.53 \ln^3(\lambda) + 7.59 \ln^2(\lambda) + 16.18 \ln(\lambda) + 16.18 \Big). \tag{4.13b}$$

$\mathscr{W}^e$ and $\mathscr{W}^c$ are plotted in Fig. 4.4(b) as a function of $\varepsilon_t/\varepsilon_t^m$. As observed, the curves are similar within the range $0 \leq \varepsilon_t/\varepsilon_t^m \leq 1.55$ because the normalised difference $(\mathscr{W}^e - \mathscr{W}^c)/\mathscr{W}^e$ is limited to within 12.6% with a single maximum at $\varepsilon_t/\varepsilon_t^m = 0.39$.

4.3 Results

4.3.1 Parameter values: best fit, best fit approximation and modelled

Parameters obtained by minimising the rmse (Eq. (4.3)) between the continuous exponential ($\widehat{a}$ and $\widehat{b}$) or cubic ($\widehat{A}$ and $\widehat{B}$) fits for $\widehat{\sigma}_t(\varepsilon_t)$ and the measured stress-strain curves $\sigma_t(\varepsilon_t)$ for the complete strain range up to $\max(\varepsilon_t)$ are plotted in Fig. 4.5 as a function of the low-strain Young's modulus $\mathscr{E}_{(eff)}$. As detailed in Section 4.2.2, the best fit accuracy yields $R^2 > 99.5\%$ for each stress-strain data set. Thus, both the exponential and cubic two-parameter relationships provide accurate fits of the measured data sets.

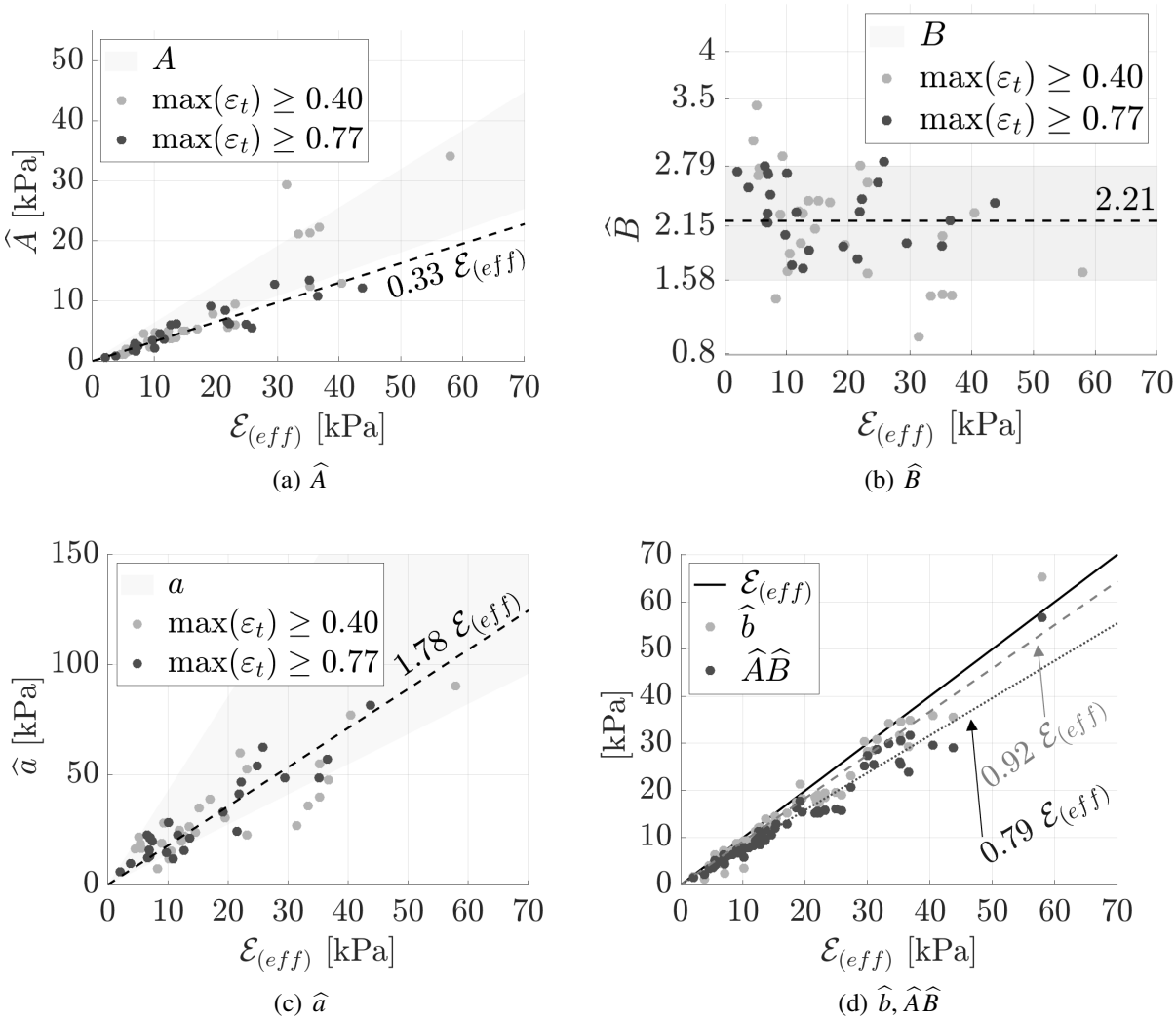

(a) $\widehat{A}$ (b) $\widehat{B}$

(c) $\widehat{a}$ (d) $\widehat{b}, \widehat{A}\widehat{B}$

Figure 4.5: Exponential $(\widehat{A},\widehat{B})$ and cubic $(\widehat{a},\widehat{b})$ best fit ($R^2 > 99.5\%$) parameters to measured stress-strain curves in the range $\varepsilon_t \leq \max(\varepsilon_t)$ as a function of $\mathscr{E}_{(eff)}$: a) $\widehat{A}$ for $\max(\varepsilon_t) \geq \{0.40, 0.77\}$, b) $\widehat{B}$ for $\max(\varepsilon_t) \geq \{0.40, 0.77\}$, c) $\widehat{a}$ for $\max(\varepsilon_t) \geq \{0.40, 0.77\}$ and d) $\widehat{b}$, $\widehat{A}\widehat{B}$ and $\mathscr{E}_{(eff)}$. In a,b,c) shaded regions indicate modelled parameter ranges for $0.77 \leq \varepsilon_t^m \leq 1.36$, dashed lines show fitted parameter approximations for $\max(\varepsilon_t) \geq 0.77$. In d) the identity function (full line) and linear fits (dashed and dotted line) are plotted.

As the rmse-minimisation is a constraint optimisation, resulting estimations of $\widehat{A}$ (Fig. 4.5(a)), $\widehat{B}$ (Fig. 4.5(b)) and $\widehat{a}$ (Fig. 4.5(c)), mainly determining the non-linear stress-strain behaviour for $\varepsilon_t > \varepsilon_l$ with $\varepsilon_l \approx 0.3$, depend on the extent of the strain range $\varepsilon_t \leq \max(\varepsilon_t)$ and thus on $\max(\varepsilon_t)$. Therefore, parameter estimations on data sets with $\max(\varepsilon_t) \geq 0.40$ (light gray dots) and $\max(\varepsilon_t) \geq 0.77$ (dark gray dots) are different. Best fit parameter estimations $\widehat{A}$, $\widehat{B}$ and $\widehat{a}$ for

data sets with $\max(\varepsilon_t) \geq 0.77$ can be approximated (dashed black lines) as :

$$\widehat{A} \approx 0.33\ \mathscr{E}_{(eff)}, \qquad (\text{fit accuracy } R^2 = 84\%), \tag{4.14a}$$

$$\widehat{B} \approx 2.21, \qquad (\text{mean with standard deviation} \pm 0.52), \tag{4.14b}$$

$$\widehat{a} \approx 1.78\ \mathscr{E}_{(eff)}, \qquad (\text{fit accuracy } R^2 = 83\%). \tag{4.14c}$$

In accordance with the modelled parameter expressions (A,B) in Eq. (4.11a) and a in Eq. (4.11b), approximations of best fit parameters $\widehat{A}$ and $\widehat{a}$ depend linearly on the low-strain Young's modulus $\mathscr{E}_{(eff)}$ whereas $\widehat{B}$ is approximately constant. For comparison, modelled parameter ranges for $0.77 \leq \varepsilon_t^m \leq 1.36$ ($1.58 \leq B \leq 2.79,\ 0.36 \leq A/\mathscr{E}_{(eff)} \leq 0.64,\ 1.36 \leq a/\mathscr{E}_{(eff)} \leq 4.27$) are indicated (shaded regions). It is seen that the best fit parameters and their approximations are of the order of magnitude of the modelled parameters.

Following the model expressions in Eq. (4.6), the linear low-strain stress behaviour regardless of $\max(\varepsilon_t)$ is determined by the cubic parameter b (Eq. (4.6a)) or the exponential parameter product AB (Eq. (4.6b)). Therefore, the best fit parameter $\widehat{b}$ (light gray dots), the product $\widehat{A}\widehat{B}$ (dark gray dots) as well as the low-strain Young's modulus $\mathscr{E}_{(eff)}$ (full line, identity function) are plotted as a function of $\mathscr{E}_{(eff)}$ for all data sets in Fig. 4.5(d). It is seen that $\widehat{b}$ and $\widehat{A}\widehat{B}$ can be approximated as

$$\widehat{b} \approx 0.92\ \mathscr{E}_{(eff)}, \qquad (\text{fit accuracy } R^2 = 95\%), \tag{4.15a}$$

$$\widehat{A}\widehat{B} \approx 0.79\ \mathscr{E}_{(eff)}, \qquad (\text{fit accuracy } R^2 = 94\%). \tag{4.15b}$$

As the slopes 0.92 and 0.79 are smaller than one, $\widehat{b}$ and $\widehat{A}\widehat{B}$ underestimate the measured low-strain Young's modulus $\mathscr{E}_{(eff)}$ with 8% and 21% respectively. Note that for the exponential best fit parameters $\widehat{A}$ and $\widehat{B}$ a trade-off can be observed from Fig. 4.5(a) and Fig. 4.5(b) since *e.g.* for $\mathscr{E}_{(eff)} \approx 32$ kPa large values of $\widehat{A}$ are compensated by low values of $\widehat{B}$ and vice-versa. This trade-off between $\widehat{A}$ and $\widehat{B}$ partly explains the slightly reduced performance of the exponential best fit compared to the cubic one within the low-strain region in order to predict $\mathscr{E}_{(eff)}$. The mean and standard deviation between the measured $\mathscr{E}_{(eff)}$ and best fit estimations ($\widehat{b}$ and $\widehat{A}\widehat{B}$) mounts to 3.7 ± 2.8 kPa (exponential) and 1.9 ± 1.8 kPa (cubic). The accuracies mentioned for the measurement (3.5 kPa, see Section 3.6.1) and the model (5.2 kPa, see Section 3.6.2) of the low-strain Young's modulus $\mathscr{E}_{(eff)}$ are of the same order of magnitude so that, in particular, the cubic best fit parameter $\widehat{b}$ to the full strain range provides an estimation of $\mathscr{E}_{(eff)}$. Note that in this case, the linear low-strain domain and hence its upper limit, ε_l, is not quantified.

Three different parameter sets for the cubic and exponential continuous curve fits can be distinguished. Besides the best fit parameters sets (exponential $(\widehat{A},\widehat{B})$ or cubic $(\widehat{a},\widehat{b})$), best fit parameter approximations are obtained combining Eq. (4.14) and Eq. (4.15a) whereas modelled

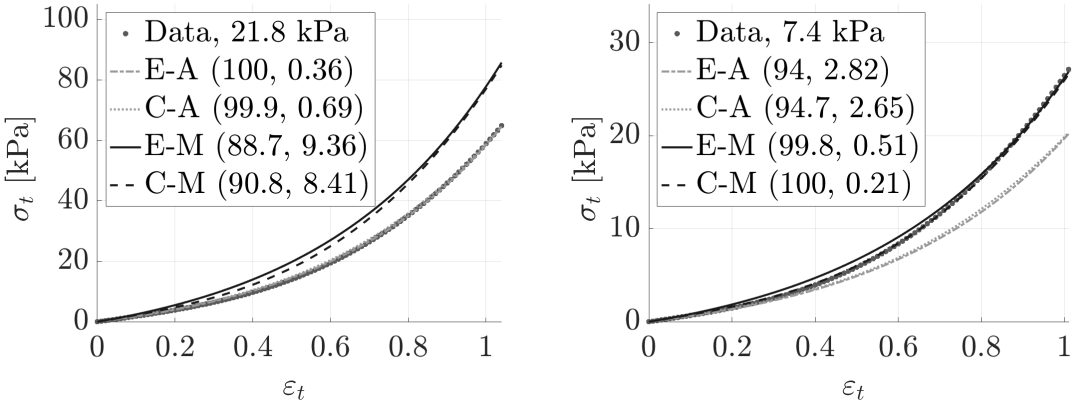

(a) (b)

Figure 4.6: Examples of measured stress-strain data (symbols) and $\mathscr{E}_{eff}$ (in kPa), resulting cubic (C-·) and exponential (E-·) fits with the best fit approximation parameter sets (·-A) and the modelled parameter sets (·-M) for three-layered silicone composites with: a) serial ($\perp$) stacking and b) combined ($\|\perp$) stacking. The fit accuracy (R^2, rmse) with R^2 (in %) and root mean square error rmse (in kPa) is indicated for each fit.

parameters are obtained using Eq. (4.11) at $\varepsilon_t^m = 1$. This value is chosen for convenience since it ensures that $\varepsilon_t/\varepsilon_t^m \leq 1.55$ for each data set (Section 4.2.2 and Fig. 4.4). As the best fit parameter approximations and the modelled parameters depend on the low-strain Young's modulus, the fit accuracy might vary when either measured $\mathscr{E}_{eff}$ or modelled $\widehat{\mathscr{E}}_{eff}$ (as outlined in Chapter 3) effective Young's modulus values for ML silicone composites are used. Examples of cubic (C-·)

Table 4.1: Mean and standard deviation of the accuracy (R^2 in %) of cubic and exponential two-parameter relationships to stress-strain data using either best fit parameters (dark dots in Fig. 4.5), best fit approximated parameters (Eq. (4.14) and Eq. (4.15a)), or modelled parameters at $\varepsilon_t^m = 1$ (Eq. (4.11)) for data sets with $\max(\varepsilon_t) \geq \{\varepsilon_l, 0.40, 0.77\}$.

	Best fit		Approximations		Modelled at $\varepsilon_t^m = 1$	
	Cubic	Exponential	Cubic	Exponential	Cubic	Exponential
$\max(\varepsilon_t) \geq \varepsilon_l$	99.9 ± 0.1	99.9 ± 0.1	98 ± 2^a 95 ± 5^b	98 ± 2^a 94 ± 5^b	92 ± 10^a 91 ± 13^b	87 ± 12^a 87 ± 19^b
$\max(\varepsilon_t) \geq 0.40$	99.8 ± 0.2	99.8 ± 0.1	98 ± 2^a 95 ± 5^b	98 ± 2^a 94 ± 5^b	90 ± 11^a 91 ± 16^b	86 ± 13^a 89 ± 16^b
$\max(\varepsilon_t) \geq 0.77$	99.8 ± 0.2	99.8 ± 0.1	97 ± 3^a 95 ± 4^b	98 ± 3^a 95 ± 4^b	88 ± 12^a 89 ± 16^b	85 ± 14^a 87 ± 18^b

[a] using measured low-strain $\mathscr{E}_{eff}$.
[b] using modelled low-strain $\widehat{\mathscr{E}}_{eff}$.

and exponential (E-·) fits for three-layered specimens with the best fit parameter approximation sets (·-A) and the modelled parameter sets (·-M) are plotted in Fig. 4.6. An overview of the exponential and cubic fit accuracies for the different parameter sets is given in Table 4.1 where the mean and standard deviation of R^2 are reported. Overall, both the cubic and exponential fits exhibit similar tendencies. The overall mean fit performance is at least $R^2 \geq 85\%$ illustrating that all parameter sets can be used to obtain a continuous fit of the measured stress-strain curves. Nevertheless, best fit parameter approximations with the modelled $\widehat{\mathscr{E}}_{eff}$ results in mean R^2 values of at least 94% and a standard deviation of 5% at most. Consequently, these relationships in combination with the model of the low-strain effective Young's modulus outlined in Chapter 3 can be used to obtain an *a priori*, and hence measurement free, characterisation of stress-strain curves up to $\varepsilon_t \leq 1.5$ for the ML silicone composites. Nevertheless, modelled parameter sets can be used as well since the reduced fit performance (expressed by a decrease of the mean and an increase of the standard deviation of R^2) is reasonable considering that, in contrast to the data-based approximations in Eq. (4.14) and Eq. (4.15a), no experimental data are used to obtain Eq. (4.11). Indeed, Eq. (4.11) is obtained using the assumption that cubic and exponential curves provide similar stress estimations when $\varepsilon_t/\varepsilon_t^m \leq 1.55$. This assumption was motivated (Fig. 4.4 in Section 4.2.2) as well as supported by the accuracy ($R^2 > 99.5\%$ in this section) of the cubic and exponential best fits.

4.3.2 High-strain elastic Young's modulus

Fit accuracies reported in Table 4.1 for the continuous exponential and cubic relationships, inspired on stress-strain models proposed for soft biological tissues, suggest that ML silicone composites behave, at least partly, in a similar manner. For soft tissues, the continuous stress-strain behaviour is generally described as consisting of an exponential strain range, which includes the linear low-strain elastic range, followed by a linear elastic high-strain range. Eq. (4.9), for which the solution is plotted in Fig. 4.3, suggests that the high-strain elastic Young's modulus $\mathscr{E}_{NL}$ can be expressed as a linear function of the low-strain elastic Young's modulus $\mathscr{E}_{(eff)}$ with slope 8.58. Since this relationship $\mathscr{E}_{NL} = 8.58\,\mathscr{E}_{(eff)}$ underlies the modelled parameters for which the mean fit accuracy amounts to $R^2 \geq 85\%$, the high-strain elastic Young's modulus is investigated. Concretely, two additional parameters are introduced to characterise the linear high-strain region $\varepsilon_t \geq \varepsilon_t^{NL}$, *i.e.* onset strain ε_t^{NL} and high-strain Young's modulus $\mathscr{E}_{NL}$. In the range $\varepsilon_t \leq \varepsilon_t^{NL}$, the stress is again described using the continuous two-parameter exponential and cubic relationships given in Eq. (5.2). Best fit parameter estimations are again obtained by minimising the rmse given in Eq. (4.3). Overall, it is found that the best fit accuracy is slightly improved, at the cost of two additional parameters, from $R^2 \geq 99.5\%$ to $R^2 \geq 99.6$ % for the cubic and $R^2 \geq 99.7\%$ for the exponential relationship, respectively. An example of best fits with (EO) and without (E) high-strain linear elastic range is plotted in Fig. 4.7. When accounting for a linear high-strain

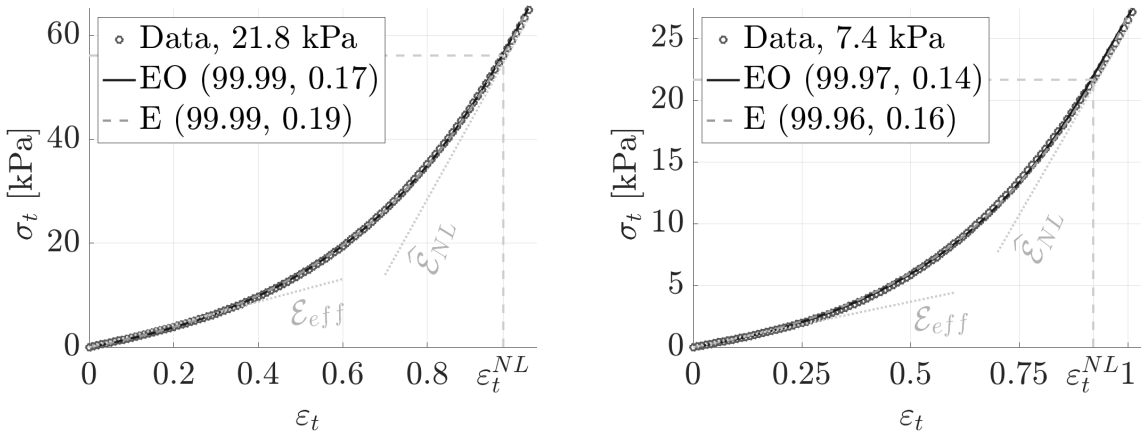

(a) (b)

Figure 4.7: Examples of measured stress-strain data (symbols) and low-strain linear slope $\mathscr{E}_{eff}$ (in kPa) and resulting exponential best fits without (E) and with (EO) linear high strain range with slope $\widehat{\mathscr{E}}_{NL}$ and onset ε_t^{NL} for three-layered silicone composites with: a) serial ($\perp$) stacking, $\mathscr{E}_{eff} = 21.8$ kPa, $\widehat{\mathscr{E}}_{NL} = 145.6$ kPa and $\varepsilon_t^{NL} = 0.98$, b) combined ($\|\perp$) stacking, $\mathscr{E}_{eff} = 7.4$ kPa, $\widehat{\mathscr{E}}_{NL} = 60.1$ kPa and $\varepsilon_t^{NL} = 0.92$. The fit accuracy ($R^2$, rmse) with R^2 (in %) and root mean square error rmse (in kPa) is indicated for each fit.

stress behaviour, expressions in Eq. (4.14) and Eq. (4.15) become, respectively,

$$\widehat{A} \approx 0.40\ \mathscr{E}_{(eff)}, \qquad \text{(fit accuracy } R^2 = 87\%\text{)}, \tag{4.16a}$$

$$\widehat{B} \approx 2.07, \qquad \text{(mean with standard deviation} \pm 0.67\text{)}, \tag{4.16b}$$

$$\widehat{a} \approx 1.60\ \mathscr{E}_{(eff)}, \qquad \text{(fit accuracy } R^2 = 74\%\text{)} \tag{4.16c}$$

and

$$\widehat{b} \approx 0.92\ \mathscr{E}_{(eff)}, \qquad \text{(fit accuracy } R^2 = 98\%\text{)}, \tag{4.17a}$$

$$\widehat{A}\widehat{B} \approx 0.81\ \mathscr{E}_{(eff)}, \qquad \text{(fit accuracy } R^2 = 98\%\text{)}. \tag{4.17b}$$

Thus, the cubic and exponential best fit parameters can again be approximated as a constant or linear function of the low-strain elastic Young's modulus $\mathscr{E}_{(eff)}$. Comparing expressions of $\widehat{b}$ and $\widehat{A}\widehat{B}$ in Eq. (4.15) with those in Eq. (4.17) shows that these parameter approximations, describing the linear low-strain behaviour ($\varepsilon_t \leq \varepsilon_l$), remain similar since the slopes vary 0% or 2.5%, respectively. The change to best fit parameter approximations $\widehat{a}$, $\widehat{A}$ and $\widehat{B}$, determining the non-linear stress-strain behaviour for $\varepsilon_t \leq \varepsilon_t^{NL}$, remains limited, as well as the slopes in Eq. (4.16), which respectively differ in 11%, 18% and 10% from those in Eq. (4.14). Parameters $\widehat{\mathscr{E}}_{NL}$ and ε_t^{NL} determining the linear high-strain behaviour are plotted in Fig. 4.8. From Fig. 4.8(b) it is seen that the ratio between the estimated high-strain and low-strain

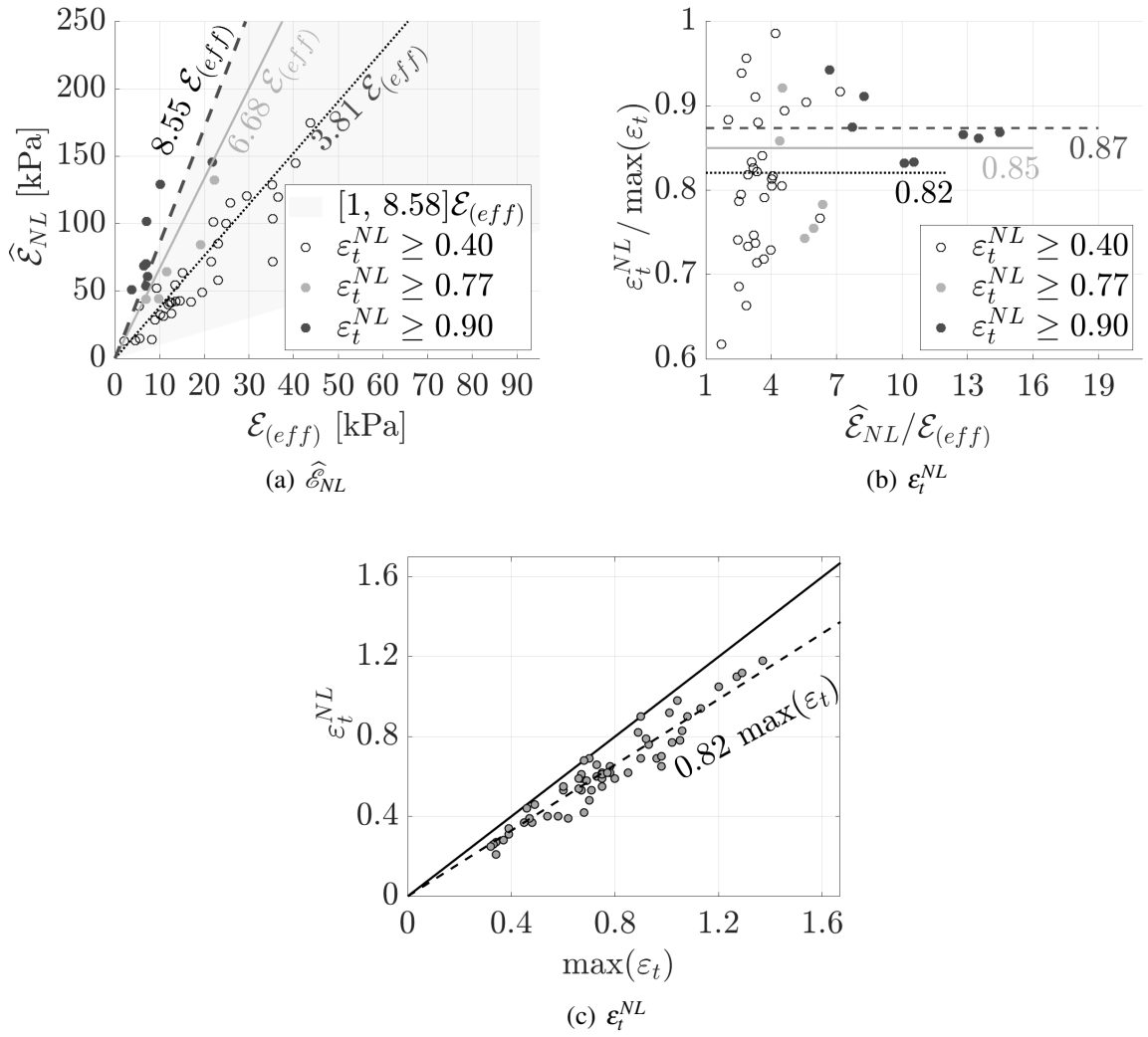

(a) $\widehat{\mathcal{E}}_{NL}$ (b) ε_t^{NL}

(c) ε_t^{NL}

Figure 4.8: Linear high-strain elastic parameters $(\widehat{\mathcal{E}}_{NL}, \varepsilon_t^{NL})$ for $\varepsilon_t^{NL} \geq \{0.40, 0.77, 0.90\}$: a) estimated high-strain Young's modulus $\widehat{\mathcal{E}}_{NL}$ as a function of low-strain Young's modulus $\mathcal{E}_{(eff)}$ with shaded region $[1, 8.58]\,\mathcal{E}_{(eff)}$, linear fits ($R^2 = 87\%$, $R^2 = 88\%$ and $R^2 = 91\%$) are indicated (lines), b) normalised high-strain lower limit $\varepsilon_t^{NL}/\max(\varepsilon_t)$ as a function of the ratio between high-strain and low-strain Young's moduli $\widehat{\mathcal{E}}_{NL}/\mathcal{E}_{(eff)}$, mean values (horizontal lines) are indicated (standard deviation of 10%, 7% and 4%), c) ε_t^{NL} as a function of $\max(\varepsilon_t)$, linear fit (dashed line) ($R^2 = 96\%$) and identity function (full line).

Young's moduli $\widehat{\mathcal{E}}_{NL}/\mathcal{E}_{(eff)}$ is mostly smaller than 5 for $\varepsilon_t^{NL} < 0.77$ and smaller than 7 for $\varepsilon_t^{NL} < 0.90$, whereas the ratio is greater than 7 for $\varepsilon_t^{NL} \geq 0.90$. This implies, as plotted for $\varepsilon_t^{NL} \geq \{0.40, 0.77, 0.90\}$ in Fig. 4.8(a), that the slopes characterising the linear fits ($R^2 = 87\%$, $R^2 = 88\%$ and $R^2 = 91\%$) of $\widehat{\mathcal{E}}_{NL}(\mathcal{E}_{(eff)})$ increase with ε_t^{NL}. For $\varepsilon_t^{NL} \geq 0.9$, the resulting slope of 8.55 ($\widehat{\mathcal{E}}_{NL} = 8.55\,\mathcal{E}_{(eff)}$) is within 1% of the slope of 8.58 (left border of the shaded region

Table 4.2: Mean and standard deviation of the accuracy (R^2 in %) of non-linear cubic and exponential two-parameter and linear two-parameter high-strain relationships to stress-strain data using either best fit parameters, best fit approximated parameters or modelled parameters at $\varepsilon_t^m = \varepsilon_t^{NL}$ and $\varepsilon_t^{NL} = 0.85\max(\varepsilon_t)$ for data sets with $\max(\varepsilon_t) \geq \{\varepsilon_l, 0.40, 0.77, 0.90\}$.

	Best fit		Approximations		Modelled at $\varepsilon_t^m = \varepsilon_t^{NL}$	
	Cubic	Exponential	Cubic	Exponential	Cubic	Exponential
$\max(\varepsilon_t) \geq \varepsilon_l$	99.9 ± 0.1	99.9 ± 0.1	98 ± 2^a 89 ± 13^b	98 ± 2^a 87 ± 17^b	28 ± 37^a 31 ± 36^b	27 ± 36^a 32 ± 36^b
$\max(\varepsilon_t) \geq 0.40$	99.9 ± 0.1	99.9 ± 0.1	98 ± 2^a 92 ± 7^b	98 ± 2^a 91 ± 10^b	32 ± 38^a 39 ± 36^b	31 ± 37^a 37 ± 36^b
$\max(\varepsilon_t) \geq 0.77$	99.9 ± 0.1	99.9 ± 0.1	98 ± 2^a 94 ± 4^b	98 ± 2^a 94 ± 7^b	52 ± 39^a 64 ± 31^b	54 ± 39^a 62 ± 32^b
$\max(\varepsilon_t) \geq 0.90$	99.9 ± 0.1	99.9 ± 0.1	98 ± 2^a 94 ± 5^b	98 ± 2^a 94 ± 7^b	71 ± 33^a 61 ± 37^b	69 ± 33^a 60 ± 37^b

[a] using measured $\mathscr{E}_{eff}$, $\mathscr{E}_{NL}$ and ε_t^{NL}.
[b] using modelled $\widehat{\mathscr{E}}_{eff}$, $\mathscr{E}_{NL}$ and ε_t^{NL}.

in Fig. 4.8(a)) underlying modelled parameters, *i.e.* $\mathscr{E}_{NL} = 8.58\,\mathscr{E}_{(eff)}$ is found as the solution of Eq. (4.9) (see Fig. 4.3). This suggests that although augmenting the number of parameters increases the best fit accuracy, high-strain linear behaviour is only retrieved for $\varepsilon_t^{NL} \geq 0.9$ in which case the high-strain Young's modulus is about 8.55 times the low-strain Young's modulus. From Fig. 4.8(c) it is seen that the onset of the high-strain region is approximated as a linear fit ($R^2 = 96\%$) of $\max(\varepsilon_t)$, namely $\varepsilon_t^{NL} \approx 0.82\max(\varepsilon_t)$, with $\max(\varepsilon_t) \leq 1.36$ for the assessed data sets.

An overview of the exponential and cubic fit accuracies for different parameter sets accounting for a high-strain linear range for $\varepsilon_t \geq \varepsilon_t^{NL}$ is given in Table 4.2 where the mean and standard deviation of R^2 are reported. Comparing these values with those in Table 4.1 shows that best fit accuracies are similar, whereas fits obtained with the approximated parameter sets or the modelled parameter sets are either similar or deteriorate. Consequently, accounting for a linear high-strain range does not significantly improve the fit accuracy. Moreover, using the approximated or modelled parameter results in the most accurate *a priori*, *i.e.* measurement free, stress-strain characterisation of ML silicone composites when a high-strain linear range is not explicitly accounted for. Note that in this case $\widehat{\mathscr{E}}_{NL}$ can still be estimated as $\widehat{\mathscr{E}}_{max}$ denoting the slope of the stress-strain curves near $\max(\varepsilon_t)$ as a linear high-strain region implies a constant slope for $\varepsilon_t \geq \varepsilon_t^{NL}$. The relative difference $\Delta\widehat{\mathscr{E}}_{NL}$ (in percentage) between $\widehat{\mathscr{E}}_{max}$ and $\mathscr{E}_{NL}$ is plotted in Fig. 4.9 for $\max(\varepsilon_t) \geq \{0.4, 0.77, 0.9\}$. It is seen that the mean (7.2%, 3.4% and 0.8%) and standard deviation (12.3%, 8.3% and 7.9%) of $\Delta\widehat{\mathscr{E}}_{NL}$ decreases for increasing $\max(\varepsilon_t)$. This supports the previous observation that a linear high-strain range does not occur for all measured

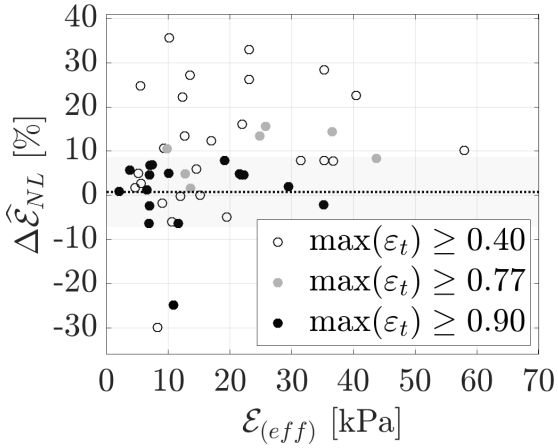

Figure 4.9: Relative difference $\Delta\widehat{\mathscr{E}}_{NL}$ between the linear stress-strain slope $\widehat{\mathscr{E}}_{max}$ estimated near $\max(\varepsilon_t)$ and $\mathscr{E}_{NL}$ near ε_t^{NL} for $\max(\varepsilon_t) \geq \{0.4, 0.77, 0.9\}$. The shaded region indicates the mean (0.8%, dotted line) plus and minus the standard deviation for $\max(\varepsilon_t) \geq 0.9$.

stress-strain curves.

4.4 Conclusion

In agreement with polynomial and exponential stress-strain models for soft biological tissues, best fits (in terms of root mean square error) of two-parameter cubic and exponential relationships are shown to provide an accurate ($R^2 > 99.5\%$) and continuous description of measured low-strain (up to ≈0.3) and subsequent (up to a maximum of 1.36) non-linear stress-strain behaviour of 6 single-layer and 34 ML silicone composites, commonly used to mimic the ML structure of human vocal folds. These composites are characterised by their layer stacking (serial, parallel, combined or arbitrary), measured effective low-strain Young's modulus $\mathscr{E}_{(eff)}$ up to 40 kPa, and some contain a stiff ($\mathscr{E} = 298$ kPa) inclusion as observed in certain structural vocal fold pathologies. Best fit parameter sets, minimising the root mean square error between the fitted and measured data (mean fit accuracy $R^2 \geq 99.8\%$), can be approximated as a constant or linear function of $\mathscr{E}_{(eff)}$ with a very limited accuracy loss regardless of the assessed maximum strain (mean fit accuracy $R^2 \geq 97\%$ with measured $\mathscr{E}_{(eff)}$ and $R^2 \geq 94\%$ with modelled $\mathscr{E}_{(eff)}$). Besides, the best fit parameter sets and resulting approximated best fit parameter sets, modelled parameter sets are considered as well. The modelled parameter sets depend on $\mathscr{E}_{(eff)}$ in the same way as the best fit approximated parameters. Contrary to the best fit parameter sets and subsequent best fit approximated parameters, no data are used to derive the modelled parameter sets so that the found accuracy (mean fit accuracy $R^2 \geq 85\%$

with measured or modelled $\mathscr{E}_{(eff)}$) supports the model approach which uses the assumption that the cubic and exponential relationship match at a strain-value corresponding to at least 64% of the maximum strain. This ensures that both relationships as well as their strain energy density functions agree to within 12.6% for the full strain range. Thus for a matching strain value of 1.0, the cubic and exponential relationships, and hence the modelled two-parameter sets, can be applied for strains up to 1.55, which is about 4.5 times the low-strain limit. Modelled parameter sets can be interpreted in terms of the low-strain elastic Young's modulus $\mathscr{E}_{(eff)}$. In addition, a modelled expression for the high-strain elastic Young's modulus $\mathscr{E}_{NL}$, characterising a linear high-strain stress behaviour, is obtained as $8.58\,\mathscr{E}_{(eff)}$. Consequently, for the sought ML silicone composites, it is is seen that both best fit approximated parameter sets and the modelled parameter sets can be used to characterise the linear and non-linear stress-strain relationship once $\mathscr{E}_{(eff)}$ is known. Moreover, for these composites it is shown that using modelled instead of measured $\mathscr{E}_{(eff)}$ values does not significantly affects the mean fit accuracy. Therefore, combining the previously proposed low-strain Young's modulus model discussed in Chapter 3 with the cubic or exponential stress-strain characterisation and approximated or modelled two-parameter sets as a function of $\mathscr{E}_{(eff)}$ results in an *a priori* stress-strain characterisation. This is of particular benefit to the design of experimental studies of the normal or abnormal vocal fold structure as these studies often rely on ML silicone vocal fold replicas. The assessed maximum strains and deformation degrees are pertinent for normal vocal folds auto-oscillation. In future, it is of interest to further investigate stress-strain curves with strains up to 1.55 or more in order to study the linear high-strain behaviour as well as the proposed non-linear model approach.

Whereas this chapter (and the previous chapter) focused on extensive model validation in terms of layer stacking and composition, the next chapter will focus on using the validated models to predict the stress-strain behaviour of deformable mechanical VFs replicas.

CHAPTER 5

On the elasticity of deformable vocal folds replicas

Based on:

Van Hirtum, A., Ahmad, M., & Pelorson, X. (2023). Uni-axial stress-strain characterisation of silicone composite specimens derived from vocal folds replicas. European Journal of Mechanics - A/Solids, revised.

Van Hirtum, A., Ahmad, M., Chottin, R., & Pelorson, X. (2023). A Composite Analogy to study the Linear Elasticity of a Pressurised Latex Tube with application to a mechanical vocal fold replica. International Journal of Applied Mechanics, revised.

5.1 Introduction

In this chapter, the aim is to contribute to the overall characterisation and prediction of mechanical properties of deformable mechanical VF replicas with constant (first type, silicone molded replicas) as well as with variable (second type, pressurised latex tube replicas) elasticity. A systematic characterisation and a validated analytical model predicting the elasticity of deformable VF replicas is of interest for the (*a-priori*) mechanical characterisation and hence the design of deformable VF replicas.

This is of particular interest for physical studies requiring a systematic variation of the VF elasticity either due to intra- and inter-speaker diversity (voice type, morphology, aging, breathing *etc.* [9]) or due to a structural pathology (scar, nodule, carcinoma, cyst *etc.* [1]). In the long term, results are of potential interest (as a predictive or training tool) for personalised VFs health care.

5.2 Methods: replica-based ML silicone specimens

Bone-shaped ML silicone specimens with serially stacked layers are designed based on the ML composition of the silicone VF replicas (M5, MRI and EPI) described in Section 2.2.1. Specimens are designed as 2L (label II_{M5} for M5-based), 3L (label III_{MRI} for MRI-based) or 4L (label IV_{EPI} for EPI-based) serially stacked composites with layer compositions given in Table 2.2. Consequently, each layer has constant width (15 mm) and constant height (10 mm). The layer lengths l_i on the other hand are set so that for each replica either layer length ratios l_i/l match corresponding layer thickness ratios l_t/L_x (specimens denoted with subscript L) or so that $\mathcal{V}_i/\mathcal{V}_{test}$ matches the corresponding layer volume ratio $\mathcal{V}/\mathcal{V}_{VF}$ (specimens denoted with subscript V). Thus, two different specimens are designed based on the composition of each replica, *i.e.* $\mathrm{II}_{M5,L}$ and $\mathrm{II}_{M5,V}$ for the M5 replica, $\mathrm{III}_{MRI,L}$ and $\mathrm{III}_{MRI,V}$ for the MRI replica and $\mathrm{IV}_{EPI,L}$ and $\mathrm{IV}_{EPI,V}$ for the EPI replica.

The six molded specimens are depicted in Fig. 5.1. Layer lengths (laser transceiver, Panasonic HL-G112-A-C5, wavelength 655 nm, accuracy 8 μm) are indicated (in mm). For convenience, low-strain Young's modulus $\mathscr{E}$ (in kPa) of each layer is given as well (see also Table 2.2).

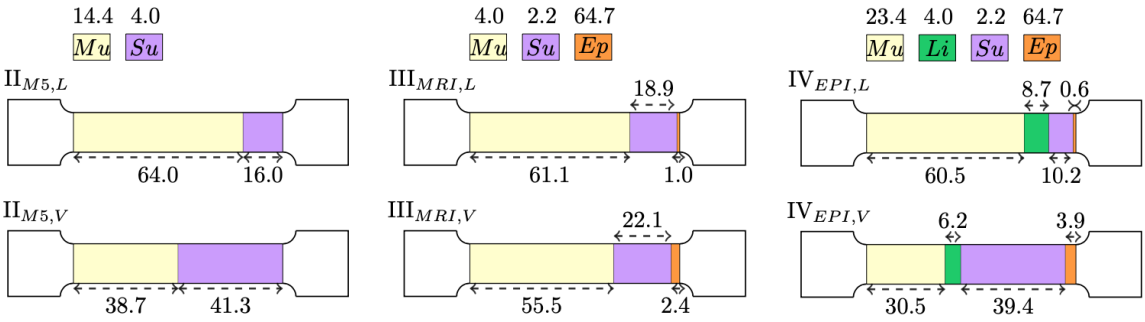

(a) II$_{M5,L}$, II$_{M5,V}$ (b) III$_{MRI,L}$, III$_{MRI,V}$ (c) IV$_{EPI,L}$, IV$_{EPI,V}$

Figure 5.1: Molded length (subscript L) and volume (subscript V) based serial stacked silicone specimens with layer lengths l_i (in mm) following the silicone VF replicas. Each legend specifies layers $\mathscr{E}$ (in kPa) with Muscle-Mu, Ligament-Li, Superficial-Su and Epithelium-E following in Table 2.2 and Fig. 2.2 for: a) M5, b) MRI and c) EPI.

5.2.1 Stress-strain measurements

The stress-strain behaviour of the molded silicone ML specimens is measured at room temperature ($21 \pm 2°$C) from uni-axial stress tests by means of precision loading [14, 59]. Briefly, the force-elongation relationship $\mathscr{F}(\Delta l)$ along the force direction, is measured on vertically placed specimens by fixing the upper clamping end and adding a known weight m (calibrated scale, Vastar 500G X 0.01G, accuracy 0.01 g) to the lower clamping end. The weight is incremented with 2.3 ± 1.9 g. The load force $\mathscr{F}$ for added mass m is $\mathscr{F} = m \cdot g_0$ with gravitational constant $g_0 = 9.81$ m/s^2. For each weight increment, the specimens elongation Δl is obtained as $\Delta l = \sum_{i=1}^{n} \Delta l_i$ with Δl_i the measured elongation of each layer (ruler, accuracy 0.05 mm). Depending on the specimen, the assessed total elongation varies between 44 mm and 198 mm, corresponding to a total added weight between 14.5 g and 125.8 g. Measured force-elongation data are illustrated in Fig. 5.2(a).
The area-elongation relationship $\mathscr{A}(\Delta l)$ for each specimen is obtained from measuring the layers midway cross-sectional area perpendicular to the force $\mathscr{A}_i$ (caliper Vernier, accuracy 0.02 mm). The cross-sectional area $\mathscr{A}$ results from the weighted arithmetic mean. The specimens cross-section area $\mathscr{A}$ is measured whenever the elongation increment yields 12.6 ± 5.2 mm, corresponding to a weight increment of 6.0 ± 5.0 g, so that $\mathscr{A}(\Delta l)$ contains between 5 and 12 data points depending on the total elongation. A quadratic fit (coefficient of determination $R^2 \geq 98\%$) is applied to the measured $\mathscr{A}(\Delta l)$ data for each specimen resulting in a continuous approximation $\mathscr{A}^q(\Delta l)$. Measured area-elongation data $\mathscr{A}(\Delta l)$ and fitted curves $\mathscr{A}^q(\Delta l)$ are illustrated in Fig. 5.2(b).

Experimental true stress-strain curves $\sigma_t(\varepsilon_t)$ are then obtained from the instantaneous

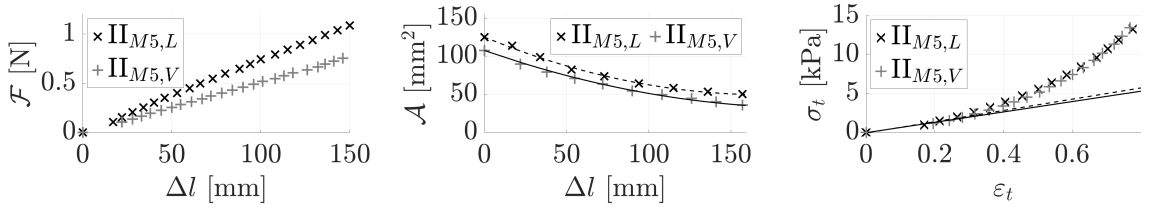

(a) $\mathscr{F}(\Delta l)$ (b) $\mathscr{A}(\Delta l)$ (c) $\sigma_t(\varepsilon_t)$

Figure 5.2: Examples of uni-axial stress tests data for M5-based specimens II$_{M5,L}$ ($\times$) and II$_{M5,V}$ ($+$): a) measured force-elongation data $\mathscr{F}(\Delta l)$, b) measured area-elongation data $\mathscr{A}(\Delta l)$ and quadratic fits $\mathscr{A}^q(\Delta l)$ with $R^2 = 99\%$ (lines) and c) stress-strain curves $\sigma_t(\varepsilon_t)$ with linear fits (lines) to the linear low-strain range $\varepsilon_t \leq 0.32$ with $R^2 > 96\%$ with slope 8.0 kPa (dashed, II$_{M5,L}$) and slope 7.2 kPa (full, II$_{M5,V}$).

force-elongation $\mathscr{F}(\Delta l)$ and area-elongation curves $\mathscr{A}^q(\Delta l)$. Stresses are measured for strains $\varepsilon_t \approx 1.08$ for specimens II$_{M5,\cdot}$, $\varepsilon_t \approx 0.49$ for specimens III$_{MRI,\cdot}$ and $\varepsilon_t \approx 0.44$ for specimens IV$_{EPI,\cdot}$. The effective low-strain elastic Young's modulus $\mathscr{E}_{eff}$ of each ML specimen is then obtained experimentally as the slope of the linear best fit to the strain range up to upper low-strain limit ε_l, *i.e.* the elastic low-strain region $\varepsilon_t \leq \varepsilon_l$, in which the stress σ_t is proportional to the strain ε_t.' in accordance with Hooke's law of linear elastic deformation. The mean and standard deviation of the overall upper limit of the linear low-strain region yields $\varepsilon_l = 0.28 \pm 0.03$ which corresponds to an elongation of 37 ± 7 mm. Examples of experimental stress-strain data $\sigma_t(\varepsilon_t)$ and associated linear fits ($R^2 > 99\%$) to the linear low-strain region $\varepsilon_t \leq \varepsilon_l$ are illustrated in Fig. 5.2(c).

5.2.2 Stress-strain model approach

5.2.2.1 Low-strain model: effective low-strain Young's modulus $\widehat{\mathscr{E}}_{eff}$

Hooke's law of linear elastic deformation (Eq. (5.6)) holds in the low-strain range so that the stress-strain relationship is characterised by the low-strain Young's modulus. As each specimen consists out of n serial stacked layers, Reuss's hypothesis [44] of homogeneous stress can be applied. This implies that the stress σ_t in an equivalent homogeneous composite and the stress $\sigma_{t,i=1\ldots n}$ in each layer is assumed constant so that $\sigma_{t,i=1\ldots n} = \sigma_t$. The effective low-strain Young's modulus of the equivalent homogeneous composite with length $l = \sum_{i=1}^{n} l_i$ is then modelled as

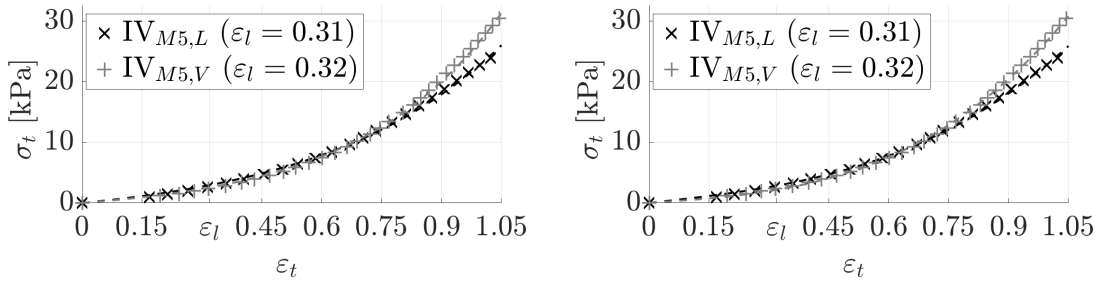

(a) best fits $\sigma_t^e(\varepsilon_t)$ (b) best fits $\sigma_t^c(\varepsilon_t)$

Figure 5.3: Illustration of measured stress-strain data for specimens II$_{M5,L}$ (×) and II$_{M5,V}$ (+) and non-linear continuous best fits (dashed lines) with $R^2 \geq 99.9\%$ and rmse < 0.3 kPa using two-parameter relationships: a) exponential $\sigma_t^e(\varepsilon_t)$, b) cubic $\sigma_t^c(\varepsilon_t)$. Linear strain limit ε_l is indicated.

the harmonic mean of the layers Young's moduli $\mathscr{E}_i$ weighted with their lengths ł$_i$ as

$$\widehat{\mathscr{E}}_{eff} = \frac{\sum_{i=1}^{n} l_i}{\sum_{i=1}^{n} \left(\frac{l_i}{\mathscr{E}_i} \right)}. \tag{5.1}$$

This model approach is validated (accuracy 2.4 kPa) on 15 composite specimens (2L, 3L and 4L) with layer Young's moduli $\mathscr{E}_i \leq 65$ kPa as is the case in this work (Table 2.2) [14, 59].

5.2.2.2 Continuous non-linear stress-strain model for strains up to 1.55

In [60], it was shown that the linear and non-linear stress-strain data $\sigma_t(\varepsilon_t)$ for silicone composites can be approximated for $\varepsilon_t \leq 1.55$ using either an exponential (superscript e) or cubic (superscript c) two-parameter relationship

$$\text{exponential: } \sigma_t^e(\varepsilon_t) = A\,(e^{B\varepsilon_t} - 1), \tag{5.2a}$$

$$\text{cubic: } \sigma_t^c(\varepsilon_t) = a\,\varepsilon_t^3 + b\,\varepsilon_t, \tag{5.2b}$$

with $(A,B)^e$ and $(a,b)^c$ their respective two-parameter sets.

The best fit using these relationships is obtained for parameter sets minimising the root mean square error (rmse in kPa) between the fitted and measured data. For the silicone specimens, depicted in Fig. 5.1, the accuracy associated with the best fits yields $R^2 \geq 99.9\%$ and

rmse < 0.3 kPa. This is illustrated in Fig. 5.3 for specimens $\mathrm{II}_{M5,L}$ and $\mathrm{II}_{M5,V}$ for the exponential $\sigma_t^e(\varepsilon_t)$ (Fig. 5.3(a)) or cubic $\sigma_t^c(\varepsilon_t)$ (Fig. 5.3(b)) relationship.

Besides these best fit parameter sets (suffix -fit), two pairs of generic parameter sets in the strain range $\varepsilon_t \leq 1.55$ are recently proposed in [60]. Generic parameter sets are expressed as a function of the effective low-strain Young's modulus $\mathscr{E}_{eff}$, so that the exponential (superscript e) and the cubic (superscript c) relationships in Eq. (5.2) constitute continuous stress-strain models, comprising the linear low-strain range ($\varepsilon_t \leq \varepsilon_l$ with $\varepsilon_l \approx 0.28$) as well as the non-linear stress-strain range ($\varepsilon_l < \varepsilon_t \leq 1.55$) thereafter. Generic parameter sets were either modelled analytically (suffix -M) or estimated as an overall approximation (suffix -A) of the best fits parameters for stress-strain curves measured on 40 silicone composite specimens. Resulting generic two-parameter sets $(A,B)^e$ and $(a,b)^c$ as a function of the effective low-strain Young's modulus $\mathscr{E}_{eff}$ are thus either expressed analytically (suffix -M) as

$$\text{modelled exponential } (A,B)^e \text{ – E-M: } (\mathscr{E}_{eff}/2.15,\ 2.15)^e, \tag{5.3a}$$

$$\text{modelled cubic } (a,b)^c \text{ – C-M: } (2.53\,\mathscr{E}_{eff},\ \mathscr{E}_{eff})^c \tag{5.3b}$$

or as the overall best fit parameter sets approximation (suffix -A) as

$$\text{approximated exponential } (A,B)^e \text{ – E-A: } (\mathscr{E}_{eff}/3.03,\ 2.21)^e, \tag{5.4a}$$

$$\text{approximated cubic } (a,b)^c \text{ – C-A: } (1.78\,\mathscr{E}_{eff},\ 0.92\,\mathscr{E}_{eff})^c. \tag{5.4b}$$

The accuracy of the exponential and cubic fits with the generic parameter sets is $R^2 \geq 85\%$ for the modelled parameter sets (E-M and C-M) and $R^2 \geq 94\%$ for the best fit parameter approximations (E-A and C-A) [60]. Note that this accuracy holds regardless how the specimens effective low-strain Young's modulus $\mathscr{E}_{eff}$ is obtained, *i.e.* either modelled using Eq. (5.1) (Section 4.2) or measured as the slope of the linear low-strain region (Section 3.5). From Eq. (5.3) follows that modelled generic parameter sets relate to $\mathscr{E}_{eff}$ as $b = \mathscr{E}_{eff}$ and $AB = \mathscr{E}_{eff}$, whereas for the generic best fit approximation parameter sets follows from Eq. (5.4) that $b = 0.92\,\mathscr{E}_{eff}$ and $AB = 0.73\,\mathscr{E}_{eff}$. In addition, a linear fit of the best fit parameter product AB as a function of $\mathscr{E}_{eff}$ resulted in the relationship $AB = 0.79\,\mathscr{E}_{eff}$ [60].

5.2.2.3 High-strain model: effective high-strain Young's modulus $\mathscr{E}_{NL}$

Linear stress-strain behaviour might occur at sufficiently large strains as *e.g.* observed for biological materials [52, 57]. The stress-strain behaviour in a linear high-strain range $\varepsilon_t^{NL} \leq \varepsilon_t \leq 1.55$ is thus again characterised by an effective high-strain Young's modulus $\mathscr{E}_{NL}$ with $\mathscr{E}_{NL} > \mathscr{E}_{eff}$. Consequently, $\mathscr{E}_{NL}$ can be estimated as the slope of the linear fit to the stress-strain curves in the high strain range (suffix -fit). In [60] was shown that for the specimens of interest $\mathscr{E}_{NL}$ is

linearly proportional to $\mathscr{E}_{eff}$. Analytical reasoning showed that the ratio $\mathscr{E}_{NL}/\mathscr{E}_{eff}$ at $\varepsilon_t^{NL} = 1$ yields $\mathscr{E}_{NL}/\mathscr{E}_{eff} = 8.58$. In addition, it is shown that $\mathscr{E}_{NL}/\mathscr{E}_{eff}$ can be expressed analytically as a function of the linear high-strain range onset ε_t^{NL} as the local slope to either the exponential and cubic two-parameter stress-strain relationships, which is modelled as:

$$\text{exponential } (A,B)^e - \text{E-}\cdot\text{:}\ \mathscr{E}_{NL}/\mathscr{E}_{eff} = e^{B\,\varepsilon_t^{NL}}, \tag{5.5a}$$

$$\text{cubic } (a,b)^c - \text{C-}\cdot\text{:}\ \mathscr{E}_{NL}/\mathscr{E}_{eff} = 3\,k\,(\varepsilon_t^{NL})^2 + 1, \tag{5.5b}$$

with generic exponential parameter B either modelled following E-M ($B = 2.15$, Eq. (5.3a)) or approximated E-A ($B = 2.21$, Eq. (5.4a)) and constant $k = a/\mathscr{E}_{eff}$ obtained from generic parameter $a \propto \mathscr{E}_{eff}$, which is modelled following C-M ($k = 2.53$, Eq. (5.3b)) or approximated following E-A ($k = 1.78$, Eq. (5.4b)).

5.3 Results: replica-based ML silicone specimens

5.3.1 Linear low-strain effective Young's modulus $\mathscr{E}_{eff}$

For each of the six composite replica-based specimens depicted in Fig. 5.1, either length-based (subscript L) or volume-based (subscript V), the linear low-strain effective Young's modulus in the range $\varepsilon_t \leq \varepsilon_l$ is measured ($\mathscr{E}_{eff}$) as outlined in Section 3.5 and modelled ($\widehat{\mathscr{E}}_{eff}$) following Eq. (5.6). Measured $\mathscr{E}_{eff}$ (crosses) and modelled $\widehat{\mathscr{E}}_{eff}$ (empty symbols) plotted in Fig. 5.4 are between 3 kPa and 10 kPa. Measured $\mathscr{E}_{eff}$-values are summarised in Table 5.1.

Measured $\mathscr{E}_{eff}$ for MRI-based (around 5.0 kPa) and EPI-based (around 5.4 kPa) are of similar value, whereas higher $\mathscr{E}_{eff}$ are observed for M5-based specimens (around 7.6 kPa).

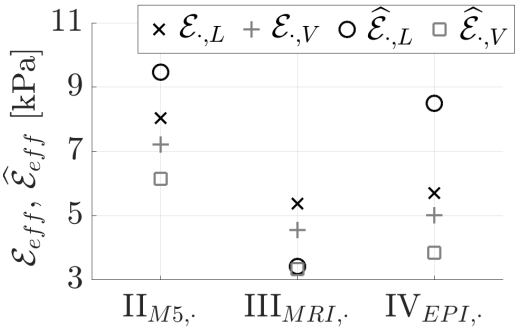

Figure 5.4: Measured $\mathscr{E}_{eff}$ ($\times$, $+$) and modelled $\widehat{\mathscr{E}}_{eff}$ ($\circ$, $\square$) for specimens II$_{M5,\cdot}$, III$_{MRI,\cdot}$ and IV$_{EPI,\cdot}$ using either the thickness ($\cdot$,L) or volume ($\cdot$,V) ratio of silicone VF replicas.

Table 5.1: Measured low-strain Young's moduli $\mathscr{E}_{eff}$.

Specimen	$\mathscr{E}_{eff}$ [kPa] L-based†	V-based‡
$\mathrm{II}_{M5,\cdot}$	8.0	7.2
$\mathrm{III}_{MRI,\cdot}$	5.4	4.5
$\mathrm{IV}_{EPI,\cdot}$	5.7	5.0

† specimens $\mathrm{II}_{M5,L}$, $\mathrm{III}_{MRI,L}$, $\mathrm{IV}_{EPI,L}$.
‡ specimens $\mathrm{II}_{M5,V}$, $\mathrm{III}_{MRI,V}$, $\mathrm{IV}_{EPI,V}$.

Measured $\mathscr{E}_{\cdot,L}$ for length ratio based specimens (subscript L, symbol $\times$ in Fig. 5.4) are up to 0.9 kPa greater than $\mathscr{E}_{\cdot,V}$ observed for volume ratio based specimens (subscript V, $+$ symbol in Fig. 5.4). The absolute difference $|\mathscr{E}_{eff} - \widehat{\mathscr{E}}_{eff}|$ between measured and modelled Young's moduli yields between 1.0 kPa and 2.8 kPa. Except for $\mathrm{III}_{MRI,L}$, the difference is positive for length-based specimens and negative for volume-based specimens. Overall, values and tendencies observed for modelled $\widehat{\mathscr{E}}_{eff}$ agree with those observed for measured $\mathscr{E}_{eff}$.

The impact ($\mathrm{II}_{M5,\cdot}$, $\mathrm{IV}_{EPI,\cdot}$) or lack thereof ($\mathrm{III}_{MRI,\cdot}$) of the imposed ratio (thickness L or volume V) on modelled $\widehat{\mathscr{E}}_{eff}$ is understood considering the harmonic mean in Eq. 5.1. The mean depends on layer lengths l_i and layer Young's moduli $\mathscr{E}_i$ indicated in Fig. 5.1 and in Table 2.2. For all replicas, Y_i is larger in the muscle layer than in the superficial layer so that shortening the muscle layer, corresponding to imposing the volume ratio instead of the length ratio, results in reducing $\widehat{\mathscr{E}}_{eff}$. The decrease is significant for M5-based (3.4 kPa) and EPI-based (4.7 kPa) replicas. For MRI-based specimens the decrease is not significant (0.1 kPa) as the muscle layer is shortened with less than $\leq 15\%$ (or ≤ 5.6 mm) and in addition $\mathscr{E}_i$ of the muscle (4.0 kPa) and superficial (2.2 kPa) layer are of the same order of magnitude.

From the model approach outlined in Section 5.2.2 follows that exponential (E-·) parameter product AB and cubic (C-·) parameter b are proportional to the low-strain Young's modulus $\mathscr{E}_{eff}$. Therefore, the ratios $AB/\mathscr{E}_{eff}$ and $b/\mathscr{E}_{eff}$ are plotted in Fig. 5.5. Overall, ratios associated with best fit parameters (E-fit, C-fit) vary between specimens from 0.6 up to 0.92. The ratios are constant applying either of the generic parameter sets (E-M, C-M and E-A, C-A). The unity value, associated with modelled parameter sets (E-M and C-M) provides an upper limit. Ratios associated with best fit parameter approximations $AB/\mathscr{E}_{eff} = 0.73$ (E-A) and $b/\mathscr{E}_{eff} = 0.92$ (C-A) and best fit parameters are in good agreement given that their absolute difference is limited (1% up to 33%, mean 8%, median 5%).

5.3.2 Non-linear continuous stress-strain model

The exponential and cubic continuous two-parameter relationships with generic modelled parameter sets (··-M) and with generic best fit approximation parameter sets (··-A) are applied to model the non-linear stress-strain behaviour in the range $\varepsilon_t \leq 1.55$. This is illustrated for the cubic model approach with parameters obtained using measured $\mathscr{E}_{eff}$ (Table 5.1) in Fig. 5.6 for specimens $\text{II}_{M5,L}$, $\text{II}_{M5,V}$, $\text{III}_{MRI,V}$ and $\text{IV}_{EPI,V}$. The cubic best fit (C-fit) to the measured data for each specimen is plotted as well. The model accuracy of each curve with respect to the measured data is indicated (R^2 in percentage, rmse in kPa) as is low-strain upper limit ε_l. For specimens $\text{III}_{MRI,V}$ and $\text{IV}_{EPI,V}$, the measured strain range yields up to about twice ε_l since $\varepsilon_t \leq 0.49$. Within this range, both C-M and C-A curves provide accurate estimates of the measured data as rmse ≤ 0.39 kPa and $R^2 \geq 95.6\%$. This is in particular the case for the C-M curves for which the associated accuracies approximate the best fit accuracies ($R^2 \geq 99.9\%$ and rmse ≤ 0.03 kPa). For specimens $\text{II}_{M5,L}$ and $\text{II}_{M5,V}$ the measured strain-range is extended, up to about thrice ε_l

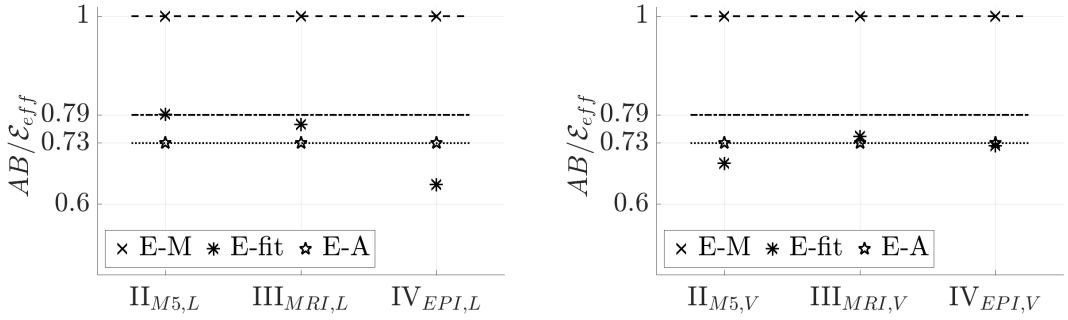

(a) exponential relationship: $AB/\mathscr{E}_{eff}$

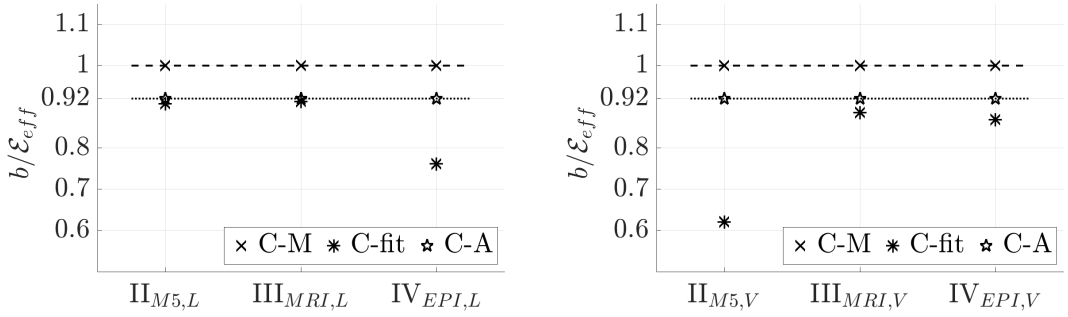

(b) cubic relationship: $b/\mathscr{E}_{eff}$

Figure 5.5: Ratios a) $AB/\mathscr{E}_{eff}$ for the exponential (E-·) relationship and b) $b/\mathscr{E}_{eff}$ for the cubic (C-·) relationship for length-based (left) and volume-based (right) specimens from modelled (··-M, ×, dashed unity line), best fit (··-fit, ₂₇₃₄) and best fit approximation (··-A, , dotted line) parameters. In a) ratio $AB/\mathscr{E}_{eff} = 0.79$ (dash-dotted line) is indicated [60].

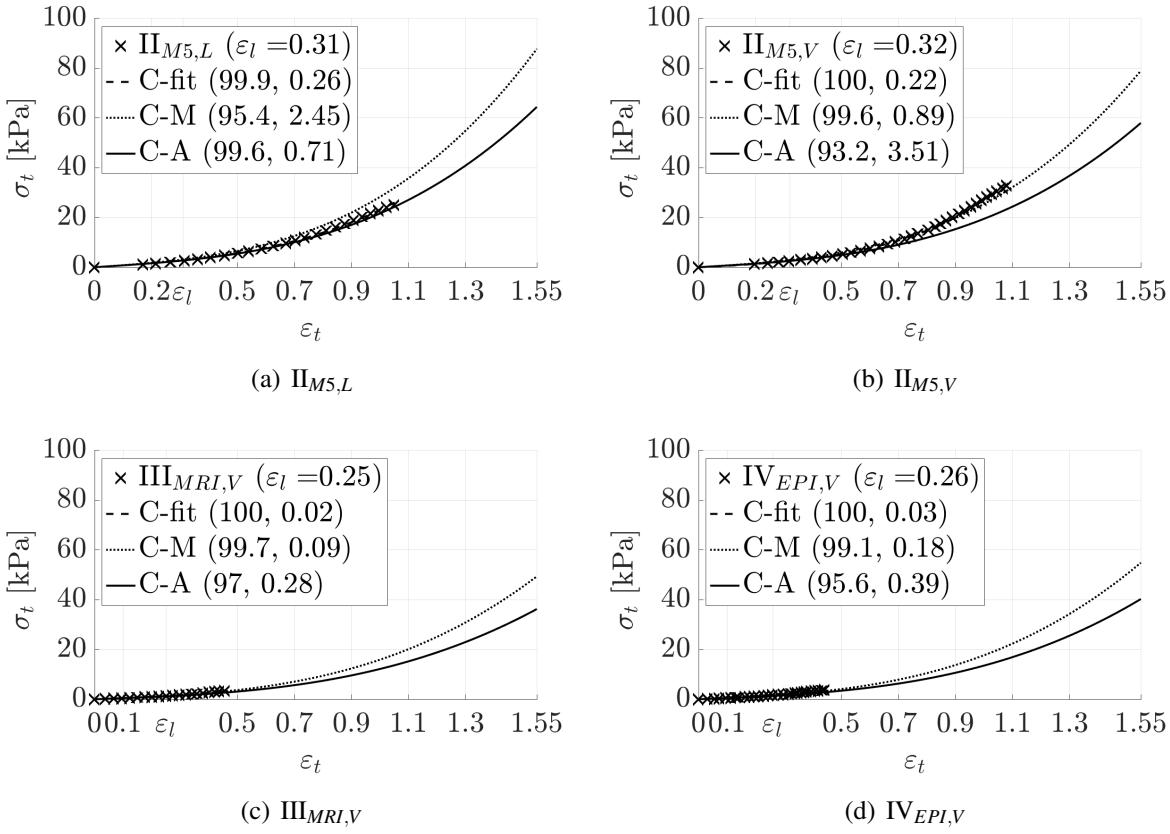

(a) II$_{M5,L}$ (b) II$_{M5,V}$

(c) III$_{MRI,V}$ (d) IV$_{EPI,V}$

Figure 5.6: Illustration of measured ($\times$) stress-strain data $\sigma_t(\varepsilon_t)$ and their cubic best fit (C-fit): a) II$_{M5,L}$, b) II$_{M5,V}$, c) III$_{MRI,V}$ and d) IV$_{EPI,V}$. Modelled cubic curves ($\varepsilon_t \leq 1.55$) with generic modelled (C-M) and best fit approximation (C-A) parameter sets from measured $\mathscr{E}_{eff}$. Data fit accuracies (R^2 in %, rmse in kPa) and low-strain upper limit ε_l are indicated.

since $\varepsilon_t \leq 1.08$. The C-A curve ($R^2 = 99.6\%$ and rmse $= 0.71$ kPa) agrees best with measured data for specimen II$_{M5,L}$ whereas the C-M curve ($R^2 \geq 99.6\%$ and rmse ≤ 0.89 kPa) provides the best estimate for specimen II$_{M5,V}$.

The stress-strain behaviour of the specimens is assessed beyond the measured range considering the modelled continuous non-linear stress-strain behaviour up to $\varepsilon_t \leq 1.55$. Modelled cubic curves using the generic modelled parameter sets (C-M) for the length-based and volume-based specimens are plotted in Fig. 5.7. Parameter sets depend on $\mathscr{E}_{eff}$ summarised in Table 5.1. It follows that modelled curves for specimens with similar low-strain Young's modulus $\mathscr{E}_{eff}$ are in close agreement. This is the case for specimens IV$_{EPI,L}$ and III$_{MRI,L}$ ($\mathscr{E}_{eff}$-difference of 0.3 kPa or 5%) and for specimens IV$_{EPI,V}$ and III$_{MRI,V}$ ($\mathscr{E}_{eff}$-difference of 0.5 kPa or 10%). Modelled stresses increase with $\mathscr{E}_{eff}$ so that stress curves for II$_{M5,\cdot}$ are increased compared to curves for III$_{MRI,\cdot}$ and IV$_{EPI,\cdot}$. For the same reason, stresses associated with length-based specimens are

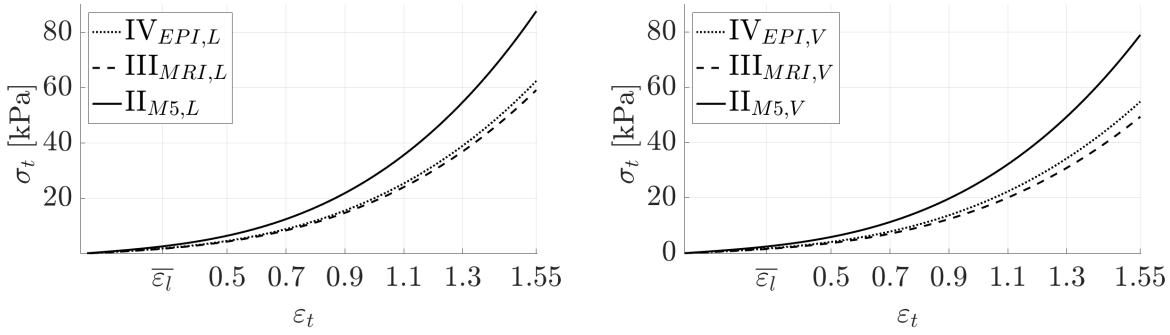

(a) L-based (b) V-based

Figure 5.7: Modelled cubic stress-strain curves $\sigma_t(\varepsilon_t)$ with the generic modelled parameter set (C-M) using measured $\mathscr{E}_{eff}$ for a) length-based specimens (IV$_{EPI,L}$, III$_{MRI,L}$, II$_{M5,L}$), b) volume-based specimens (IV$_{EPI,V}$, III$_{MRI,V}$, II$_{M5,V}$). The mean low-strain upper limit is $\overline{\varepsilon_l} = 0.28$.

increased compared to volume-based specimens.

5.3.3 High-strain effective Young's modulus $\mathscr{E}_{NL}$ and onset strain ε_t^{NL}

The linear high-strain range is characterised by its effective high-strain Young's modulus $\mathscr{E}_{NL}$ and onset strain ε_t^{NL} (Section 4.3.2). For the modelled exponential and cubic curves associated with each specimen, this slope can be estimated from a linear fit to the strain interval $[\varepsilon_t^{NL}\ 1.55]$. The influence of onset strain ε_t^{NL} on the estimated slope and the linear fit accuracy (R^2) is illustrated in Fig. 5.8 for specimen IV$_{EPI,L}$. Linear fits to the interval $[\varepsilon_t^{NL}\ 1.55]$ of modelled exponential curves with generic parameter sets, either modelled (E-M) or obtained as best fit approximation (E-A), are plotted for four onset strain $\varepsilon_t^{NL} \in \{1.00, 1.20, 1.27, 1.35\}$. Linear slope $\mathscr{E}_{NL}$ is indicated for each parameter set whereas the minimum linear fit accuracy R^2 for both parameter sets is given. Regardless of ε_t^{NL}, slope $\mathscr{E}_{NL}$ for curves E-M is 26% greater than those found for curves E-A. From Fig. 5.8 is seen that $\mathscr{E}_{NL}$ and R^2 increase with ε_t^{NL}, *i.e.* when the fit interval is shortened. Concretely, slopes $\mathscr{E}_{NL}$ increase with 30% for both E-M and E-A while minimum accuracy R^2 increases from 97.62% to 99.68%.

A systematic overview of effective high-strain Young's modulus $\mathscr{E}_{NL}$ normalised with effective low-strain Young's modulus $\mathscr{E}_{eff}$ as a function ε_t^{NL} is provided in Fig. 5.9. Plotted high-strain to low-strain effective Young's modulus ratios $\mathscr{E}_{NL}/\mathscr{E}_{eff}$ depend on the applied model (exponential or cubic), and thus also on the applied generic parameter set (modelled -M or best fit approximation -A), but not on the specimen.

The slopes obtained from linear fits to intervals $[\varepsilon_t^{NL}\ 1.55]$ of the modelled cubic and expo-

nential curves, for each of the two generic parameter sets (C-M-fit, C-A-fit, E-M-fit and E-A-fit) as illustrated for the exponential curve in Fig. 5.8, are plotted (symbols) for seven discrete ε_t^{NL}-values between 1 and 1.5. For each value of ε_t^{NL}, the overall minimum linear fit accuracy, which corresponds to values obtained for exponential curves, is indicated between brackets. The minimum fit accuracy $R^2 \geq 97.62\%$ (or $R^2 \geq 98.97\%$ for cubic curves) is sufficiently high to argue that linear fits provide a good approximation of modelled non-linear stress-strain curves in the intervals $[\varepsilon_t^{NL}\ 1.55]$ with $\varepsilon_t^{NL} \geq 1$. Nevertheless, in order to potentially extend the linear range continuously beyond the validated non-linear model range $\varepsilon_t = 1.55$, a fit accuracy of $R^2 \leq 99\%$ seems more appropriate considering the fitted linear high-strain curves in Fig. 5.8, *e.g.* comparing plotted linear approximations for $\varepsilon_t^{NL} = 1$ ($R^2 \geq 97.62\%$) and $\varepsilon_t^{NL} = 1.27$ ($R^2 \geq 99.37\%$).

Fitted slopes $\mathscr{E}_{NL}$ are further compared to the modelled local slopes (at ε_t^{NL}) of the non-

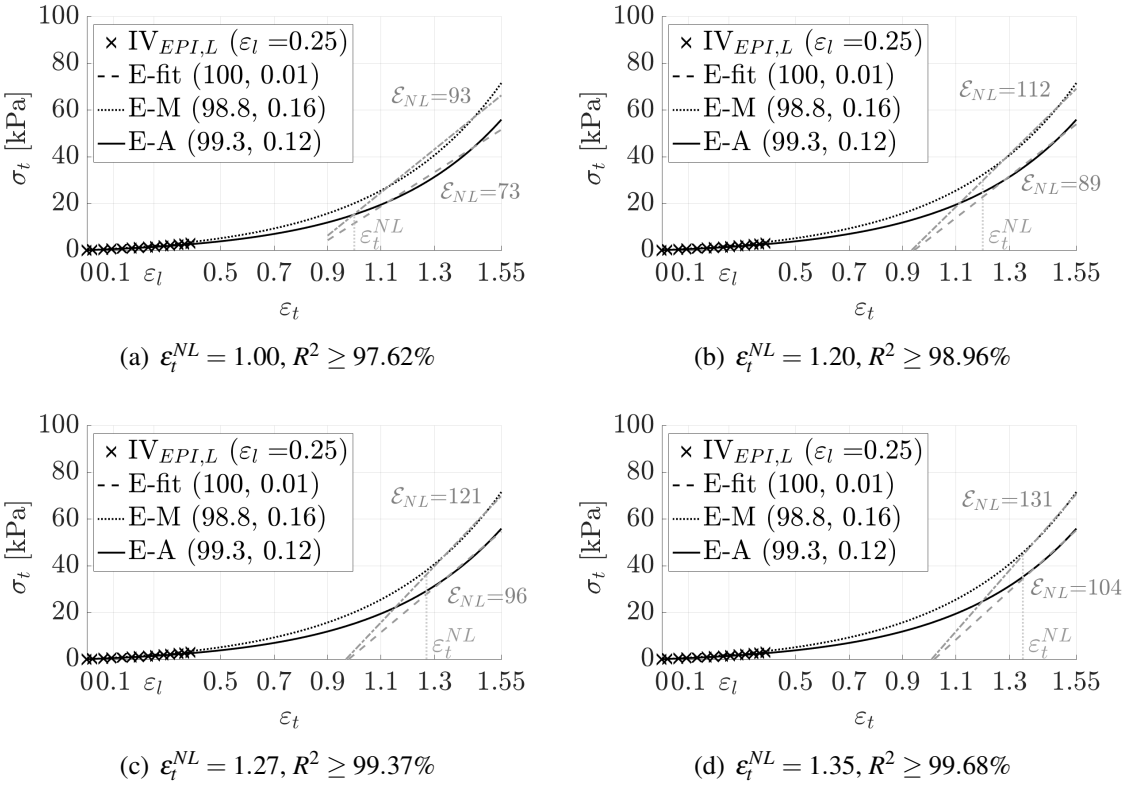

(a) $\varepsilon_t^{NL} = 1.00$, $R^2 \geq 97.62\%$

(b) $\varepsilon_t^{NL} = 1.20$, $R^2 \geq 98.96\%$

(c) $\varepsilon_t^{NL} = 1.27$, $R^2 \geq 99.37\%$

(d) $\varepsilon_t^{NL} = 1.35$, $R^2 \geq 99.68\%$

Figure 5.8: Influence of high strain onset $\varepsilon_t^{NL} \in \{1.00, 1.20, 1.27, 1.35\}$ (subplots) on slope $\mathscr{E}_{NL}$ (in kPa) and accuracy ($\min(R^2)$ in %) of linear fits (gray lines) to intervals $[\varepsilon_t^{NL}\ 1.55]$ of modelled exponential stress-strain curves $\sigma_t(\varepsilon_t)$ using generic modelled (E-M) or best fit approximation (E-A) parameter sets for specimen IV$_{EPI,L}$ ($\mathscr{E}_{eff} = 5.7$ kPa). Measured ($\times$) stress-strain data and their exponential best fit (E-fit) are plotted. Model and fit accuracies (R^2 in %, rmse in kPa) and low-strain limit ε_l are indicated in the legends.

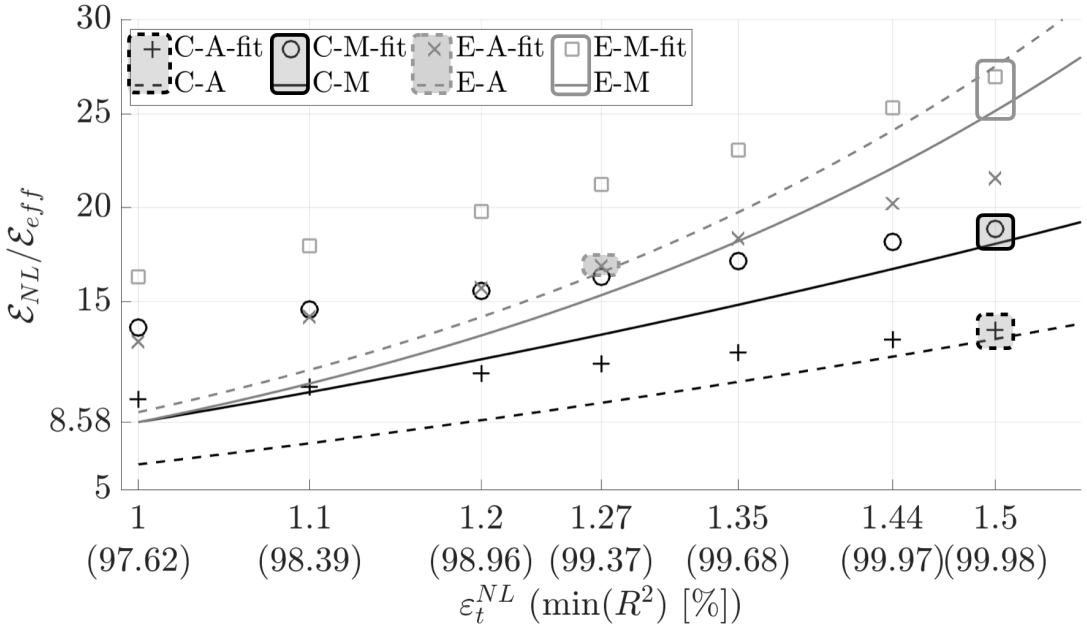

Figure 5.9: High-strain to low-strain effective Young's modulus ratio $\mathcal{E}_{NL}/\mathcal{E}_{eff}(\varepsilon_t^{NL})$ with $\mathcal{E}_{NL}$ obtained for both generic parameter sets (modelled -M and best fit approximation -A) as the slope of linear fits (min(R^2) in %, symbols) to exponential and cubic model curves (C-A-fit, C-M-fit, E-A-fit, E-M-fit) in intervals $[\varepsilon_t^{NL}\ 1.55]$ for $\varepsilon_t^{NL} \in \{1, 1.1, 1.2, 1.27, 1.35, 1.44, 1.5\}$ or modelled local slopes (C-A, C-M, E-A, E-M) from Eq. (5.5) (continuous lines). Reference ratio 8.58, best match between fitted and modelled slopes (frames) and selected values (shaded frames) following the 'first-decimal-criterion' (local and fitted slopes match until the first decimal place) are indicated.

linear models using Eq. (5.5). Normalised local slopes $\mathcal{E}_{NL}/\mathcal{E}_{eff}$ for the exponential and cubic model depend again on the applied generic parameter set (C-M, C-A, E-M and E-A). Local modelled slopes $\mathcal{E}_{NL}/\mathcal{E}_{eff}$ are plotted (lines) as function of ε_t^{NL} in Fig. 5.9. Modelled curves C-M and E-M match at $\varepsilon_t^{NL} = 1$ for which $\mathcal{E}_{NL}/\mathcal{E}_{eff} = 8.58$ confirming the reference ratio indicated in Section 4.3.2). Fitted (symbols) as well as local (lines) $\mathcal{E}_{NL}/\mathcal{E}_{eff}$ increase with ε_t^{NL} in a range which spans from $\mathcal{E}_{NL}/\mathcal{E}_{eff} \approx 8.58$ for $\varepsilon_t^{NL} = 1$ up to about thrice this value ($\mathcal{E}_{NL}/\mathcal{E}_{eff} \approx 25$) at $\varepsilon_t^{NL} = 1.5$. The best matches between the fitted and local slopes $\mathcal{E}_{NL}/\mathcal{E}_e$ are indicated (frames) in Fig. 5.5. For the cubic model, fitted and local slopes correspond until the first decimal place for $\varepsilon_t^{NL} \approx 1.5$ for both generic parameter sets. This results in $\mathcal{E}_{NL}/\mathcal{E}_{eff} \approx 13.2$ holds for the generic best fit approximation parameter set (C-A-fit vs C-A) and $\mathcal{E}_{NL}/\mathcal{E}_{eff} \approx 18.5$ for the generic modelled parameter set (C-M-fit vs C-M). For the exponential model, fitted and local slopes only agree until the first decimal when the generic best fit approximation parameter set (E-A-fit vs E-A) is applied for which $\mathcal{E}_{NL}/\mathcal{E}_{eff} \approx 16.7$ at $\varepsilon_t^{NL} \approx 1.27$. An overview of the high-strain onset ε_t^{NL} and associated normalised high-strain Young's modulus $\mathcal{E}_{NL}/\mathcal{E}_{eff}$ following this criterion is given in Table 5.2. Satisfying this 'first-decimal-criterion', *i.e.* requiring that fitted

Table 5.2: High strain onset ε_t^{NL} and normalised high-strain Young's modulus $\mathscr{E}_{NL}/\mathscr{E}_{eff}$ for which local and fitted slopes match until the first decimal ('first-decimal-criterion').

	$\mathscr{E}_{NL}/\mathscr{E}_{eff}$	ε_t^{NL}
C-A vs C-A-fit	13.2	1.5
C-M vs C-M-fit	18.5	1.5
E-A vs E-A-fit	16.7	1.27
E-M vs E-M-fit	-	-

and modelled local slopes match until the first decimal, ensures that linear fits are a continuous extension of modelled non-linear curves as observed in [52, 53, 57]. From the overview in Table 5.2 is seen that selected $\varepsilon_t^{NL} \geq 1.27$, which ensures a high-strain linear fit accuracy of $R^2 > 99\%$ to the modelled non-linear curves in the high-strain range.

From Table 5.2 is seen that the exponential model approach with generic best fit approximation parameter set (E-A) is associated with the largest, and hence most meaningful, high-strain interval within the range associated with the non-linear model. Moreover, resulting ratios are within the range associated with cubic model approaches (C-M and C-A). Finally, the E-A model resulted in the best overall model accuracy ($R^2 = 98 \pm 3\%$) [60]. Therefore, the E-A model is used to consider high-strain Young's moduli $\mathscr{E}_{NL}$ for all specimens. Resulting $\mathscr{E}_{NL}$ are summarised in Table 5.3.

Table 5.3: High-strain Young's moduli $\mathscr{E}_{NL} \approx 16.7\,\mathscr{E}_{eff}$.

Specimen	$\mathscr{E}_{NL}$ [kPa] L-based†	V-based‡
$\mathrm{II}_{M5,\cdot}$	134	120
$\mathrm{III}_{MRI,\cdot}$	90	75
$\mathrm{IV}_{EPI,\cdot}$	95	84

† specimens $\mathrm{II}_{M5,L}$, $\mathrm{III}_{MRI,L}$, $\mathrm{IV}_{EPI,L}$.
‡ specimens $\mathrm{II}_{M5,V}$, $\mathrm{III}_{MRI,V}$, $\mathrm{IV}_{EPI,V}$.

5.4 Methods: PLT VF

5.4.1 Measured stress-strain curves and low-strain Young's modulus $\mathscr{E}_{eff}$

Increasing (or decreasing) the internal water pressure P_{PLT} expands (or shrinks) the radius of the PLT replica with respect to the posterior-anterior y-axis defined in Section 2.2.2. For each imposed P_{PLT}, a top view image within the x–y plane and a side view image within the y–z plane of the replica are gathered from the camera positions indicated in Fig. 2.3(b). The characteristic lengths $L_x(y)$ (top view) and $L_z(y)$ (side view) correspond to the distances between the replica's edges as indicated in Fig. 5.10. The internal pressure P_{PLT} is systematically increased ($\uparrow$) or decreased ($\downarrow$) between 450 Pa and 6500 Pa with steps of about 100 Pa. Extracted edges for top and side view images as a function of y/L_y (with $L_y = 42$ mm) are illustrated in Fig. 5.11(a) and in Fig. 5.11(b) for increasing P_{PLT}. For each image, and hence imposed P_{PLT}, mean $\overline{L}_x$ (top view) and $\overline{L}_z$ (side view) are quantified for different y/L_y ranges, *i.e.* overall mean ($0 \leq y/L_y \leq 1$ or interval length $\Delta y/L_y = 1$, standard deviation less than 2.5%) or local mean values (standard deviation less than 0.2%) for a 4 mm range (interval $\Delta y/L_y = 0.1$) with centre values 2.4 mm apart at $y/L_y = 0.5$ (centre, $0.45 \leq y/L_y \leq 0.55$), $y/L_y = 0.4$ (towards the water inlet, $0.35 \leq y/L_y \leq 0.45$) or $y/L_y = 0.6$ (away from the water inlet, $0.55 \leq y/L_y \leq 0.65$). Resulting $\overline{L}_x(P_{PLT})$ (top view) and $\overline{L}_z(P_{PLT})$ (side view) and standard deviations (bars) are illustrated in Fig. 5.11. Increasing (or decreasing) P_{PLT} also increases (or decreases) the mean characteristic

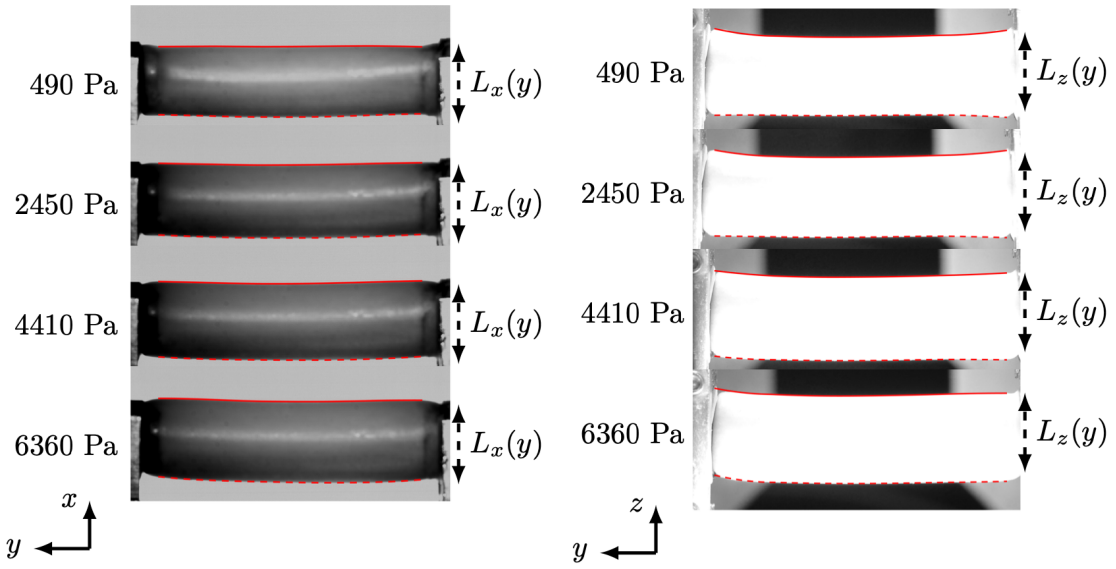

(a) top view (b) side view

Figure 5.10: Illustration of edge detection from PLT replica imaging and extracted $L_x(y)$ (a: top view) and $L_z(y)$ (b: side view) for different P_{PLT} (Pa).

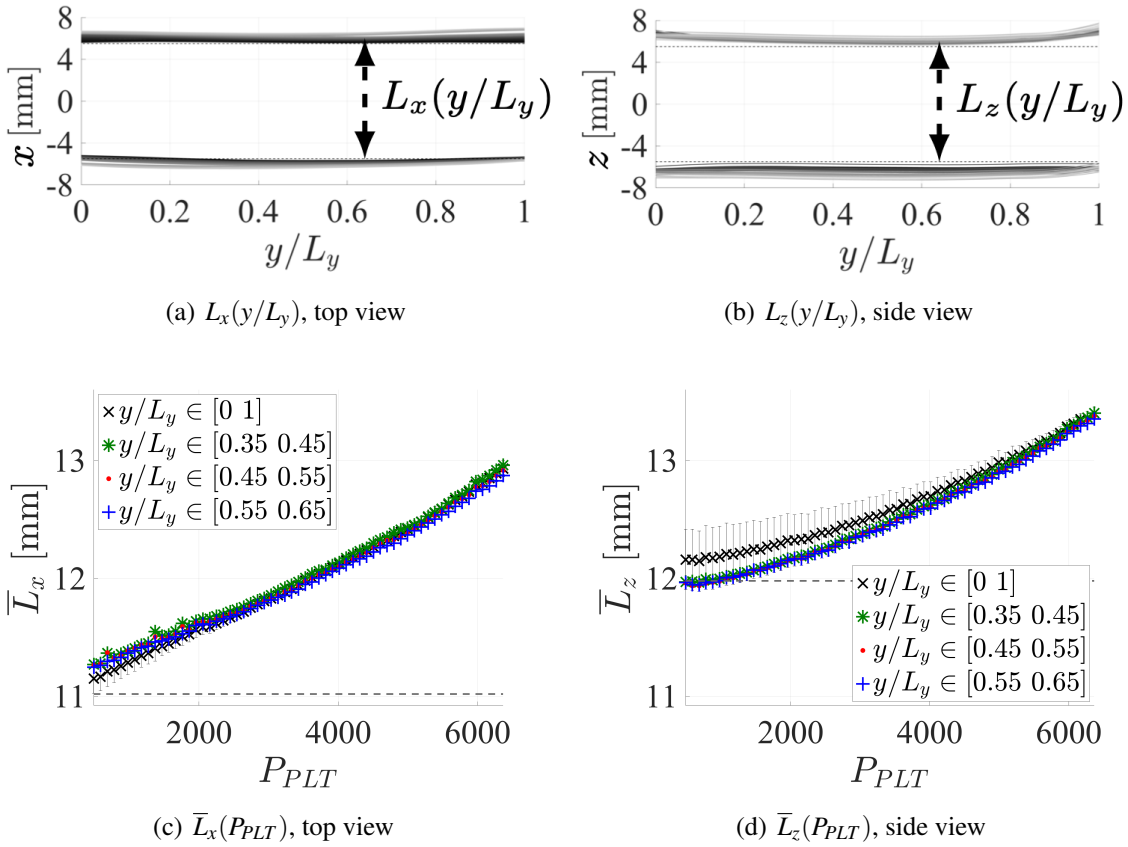

(a) $L_x(y/L_y)$, top view

(b) $L_z(y/L_y)$, side view

(c) $\overline{L}_x(P_{PLT})$, top view

(d) $\overline{L}_z(P_{PLT})$, side view

Figure 5.11: Characteristic lengths characterisation of PLT replica from imaging: a,b) $L_x(y/L_y)$ (top view) and $L_z(y/L_y)$ (side view) for increasing P_{PLT} (lighter in colour) and c,d) mean (symbols) and standard deviation (vertical bars) of $\overline{L}_x(P_{PLT})$ (top view) and $\overline{L}_z(P_{PLT})$ (side view) for 4 y/L_y-ranges. Dashed line indicates reference values for $P_{PLT} = 0$ Pa associated with either the latex tube outer radius of 11.2 mm (in a,c) or the metal support diameter of 12.0 mm (in b,d).

lengths $\overline{L}_z$ (side view) and $\overline{L}_x$ (top view) associated with expansion (or shrinking) of the PLT VF. For each imposed P_{PLT}, $\overline{L}_x$ and $\overline{L}_z$ of different y/L_y-intervals agree to within 0.25 mm and this discrepancy reduces further to within 0.1 mm for the local y/L_y intervals ($\Delta y/L_y = 0.1$ or 4 mm).

The PLT replica can be considered as an inhomogeneous material consisting of both latex and water. Consequently, the relationship between the changing pressure P_{PLT} and the replica's deformation is, as for the silicone composites, governed by an effective Young's modulus $\mathscr{E}_{eff}$ characterising the stress-strain behaviour. The strain ε_t^x (or ε_t^z) along the x (or z) direction from top (or side) view imaging is then obtained from Eq. 3.17 with $l = \overline{L}_x$ (or $l = \overline{L}_z$) at $P_{PLT} \approx 450$ Pa (lowest assessed P_{PLT}) and elongation $\Delta l(P_{PLT}) = \overline{L}_x(P_{PLT}) - l$ (or $\Delta l(P_{PLT}) = \overline{L}_z(P_{PLT}) - l$). The stress σ_t along both radial directions is set by the imposed internal pressure so that $\sigma_t = P_{PLT}$

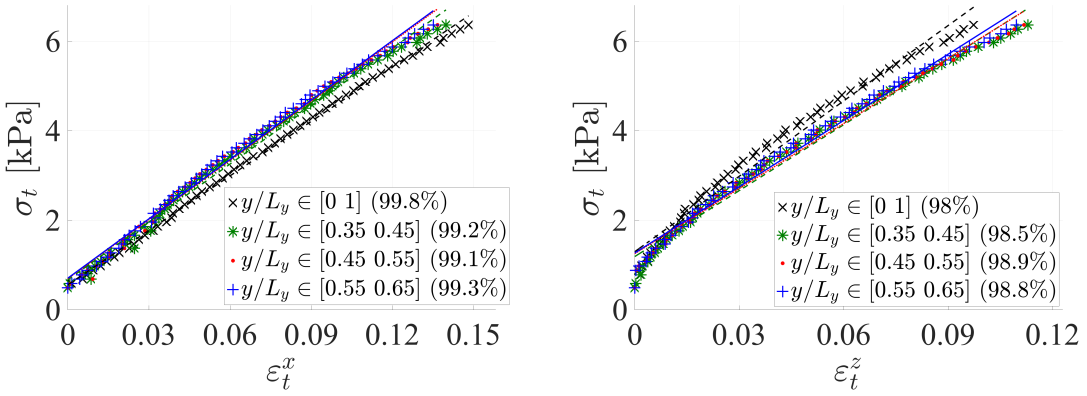

(a) $\sigma_t(\varepsilon_t^x)$, top view () (b) $\sigma_t(\varepsilon_t^z)$, side view

Figure 5.12: Image-based stress-strain curves $\sigma_t(\varepsilon_t)$ (symbols) and their linear fits (lines) for the PLT replica (increasing P_{PLT}, subscript $\uparrow$): a) $\sigma_t(\varepsilon_t^x)_\uparrow$ (top view), b) $\sigma_t(\varepsilon_t^z)_\uparrow$ (side view). Different y/L_y intervals (symbols) used to quantify $\overline{L}_x$ or $\overline{L}_z$ are indicated as well as the fit accuracy (R^2 in percentage).

holds. Resulting stress-strain curves $\sigma_t(\varepsilon_t^x)$ (top view) and $\sigma_t(\varepsilon_t^z)$ (side view) for the PLT replica are plotted in Fig. 5.13. Different curves are obtained as $\varepsilon_t^x(\overline{L}_x)$ and $\varepsilon_t^z(\overline{L}_z)$ depend on the y/L_y interval (indicated in the legend) used to quantify mean values $\overline{L}_x$ and $\overline{L}_z$. Thus, strain ranges $\varepsilon_t^x \leq 0.15$ and $\varepsilon_t^z \leq 0.12$ are observed for stresses σ_t up to 6.5 kPa.

Linear fits (lines) of the stress-strain curves and their accuracies R^2 (in %) are illustrated in Fig. 5.13. For each curve, the fit accuracy yields $R^2 > 98\%$. Therefore, it is reasonable to assume that measured strains are within the elastic low-strain range for both the x and the z direction. The effective elastic low-strain Young's moduli $\mathscr{E}_{eff}^x$ and $\mathscr{E}_{eff}^z$ is then estimated experimentally following Eq. (5.6) as the slope of the linear fit (fit accuracy $R^2 > 98\%$) to the measured $\sigma_t(\varepsilon_t^x)$ and $\sigma_t(\varepsilon_t^z)$, respectively.

5.5 Results: PLT VFs replica

5.5.1 Measured effective low-strain Young's moduli

Linear fits (lines) to the stress-strain curves and their accuracies (coefficient of determination R^2 in %) are illustrated in Fig. 5.13. For each curve, the fit accuracy yields $R^2 > 98\%$. The

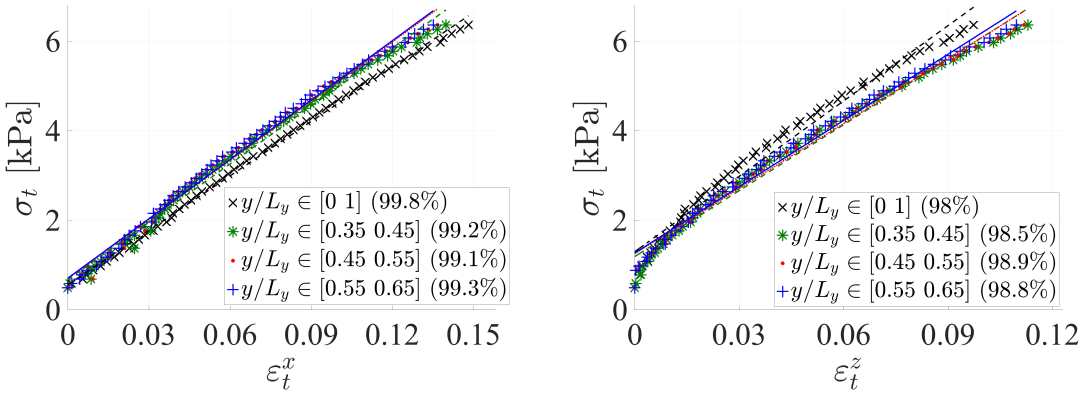

(a) $\sigma_t(\varepsilon_t^x)$, top view (b) $\sigma_t(\varepsilon_t^z)$, side view

Figure 5.13: Image-based stress-strain curves $\sigma_t(\varepsilon_t)$ (symbols) and their linear fits (lines) for the PLT replica (increasing P_{PLT}, subscript $\uparrow$): a) $\sigma_t(\varepsilon_t^x)_\uparrow$ (top view), b) $\sigma_t(\varepsilon_t^z)_\uparrow$ (side view). Different y/L_y intervals (symbols) used to quantify $\overline{L}_x$ or $\overline{L}_z$ are indicated as well as the fit accuracy (R^2 in %).

effective elastic Young's moduli $\mathscr{E}_{eff}^x$ and $\mathscr{E}_{eff}^z$ are then estimated experimentally as the slope of the linear fit to the measured $\sigma_t(\varepsilon_t^x)$ and $\sigma_t(\varepsilon_t^z)$ following Hooke's law of linear elastic deformation [61]

$$\mathscr{E}_{eff}^{x(z)} = \frac{\sigma_t}{\varepsilon_t^{x(z)}}. \tag{5.6}$$

Therefore, it is reasonable to assume that measured strains, up to $\varepsilon_t^x \leq 0.15$ $\varepsilon_t^x \leq 0.12$, are within the linear elastic range [61] for both the x and the z direction.

Measured effective Young's moduli $\mathscr{E}_{eff}^x$ and $\mathscr{E}_{eff}^z$ are plotted in Fig. 5.14. Values obtained for increasing and decreasing internal pressure ($\sigma_t(\varepsilon_t^z)_\uparrow$, $\sigma_t(\varepsilon_t^z)_\downarrow$, $\sigma_t(\varepsilon_t^x)_\uparrow$ and $\sigma_t(\varepsilon_t^x)_\downarrow$) for each of the assessed y/L_y intervals (legend) are shown. For each y/L_y interval, it is seen that the influence of increasing ($\uparrow$) or decreasing ($\downarrow$) the water pressure P_{PLT} is negligible as estimated $\mathscr{E}_{eff}^x$ and $\mathscr{E}_{eff}^z$ are affected with less than 1.5%. This confirms the hypothesis of linear elastic deformation expressed in Eq. 5.6 for the assessed strain range.

The influence of the exact position of the small (4 mm) intervals centred around $y/L_y \in \{0.4, 0.5, 0.6\}$ is limited to less than 2% with respect to the value at $y/L_y = 0.5$. It is noted that both $\mathscr{E}_{eff}^x$ and $\mathscr{E}_{eff}^z$ systematically increase with y/L_y, *i.e.* away from the water inlet. The means and standard deviations for these intervals yield $\mathscr{E}_{eff}^x = 44 \pm 1$ kPa ($\leq 2.3\%$ variation) and $\mathscr{E}_{eff}^z = 49 \pm 1$ kPa ($\leq 2.1\%$ variation). Consequently, $\mathscr{E}_{eff}^z$ is increased with 11% compared to $\mathscr{E}_{eff}^x$. The influence of the boundary conditions at the extremities on $\mathscr{E}_{eff}$ is notable considering

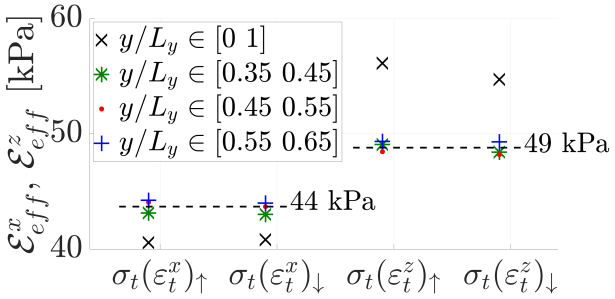

Figure 5.14: Effective elastic Young's modulus $\mathscr{E}^x_{eff}$ (and $\mathscr{E}^z_{eff}$) estimated as the linear slope to curves $\sigma_t(\varepsilon^x_t)_\uparrow$ and $\sigma_t(\varepsilon^x_t)_\downarrow$ (and $\sigma_t(\varepsilon^z_t)_\uparrow$ and $\sigma_t(\varepsilon^z_t)_\downarrow$). Different y/L_y intervals (symbols) used to determine ε^x_t and ε^z_t are indicated. Overall mean values, excluding values for $y/L_y \in [0\ 1]$, for $\sigma_t(\varepsilon^x_t)$ and $\sigma_t(\varepsilon^z_t)$ are indicated (dashed lines).

the whole y-range ($0 \leq y/L_y \leq 1$) as compared to the discussed mean values $\mathscr{E}^x_{eff}$ decreases with 7% (to 41 kPa) and $\mathscr{E}^z_{eff}$ increases with 12% (to 55 kPa). So that the difference between $\mathscr{E}^z_{eff}$ and $\mathscr{E}^x_{eff}$ for the whole y-range is increased to 34% (compared to 11% for the short intervals).

5.5.2 Equivalent multi-layer composite representation

Equivalent multi-layer (ML) composite representations of the deformable portion of the PLT replica are considered. Three different equivalent composite representations are assessed by fitting two (2L), three (3L) or four (4L) layers within the rectangle enveloping the coronal section of the PLT replica without internal stress ($P_{PLT} = 0$ kPa). Assessed representations are illustrated in Fig. 5.15. The rigid non-deformable part (dark-shaded in Fig. 5.15) of the PLT replica, corresponding to the metal support in Fig. 2.3(a), is excluded from the equivalent composite so that its lengths along the transverse (x) and the streamwise (z) direction yield $l = 6.6$ mm and $h = 11.4$ mm, respectively. The deformable portion of the PLT replica (water and latex envelop) is thus represented as a ML material composed of a layer with unknown Young's modulus (question mark in Fig. 5.15) adjacent to one (for the 2L representation), two (for the 3L representation) or three (for the 4L representation) thin latex (natural rubber [40]) outer layers for which Young's modulus $\mathscr{E}_r = 1.1$ MPa and layer thickness 0.2 mm (l_2, h_1 and h_3 in Fig. 5.15). Remaining dimensions yield $h_2 = 11.0$ mm a $l_2 = 6.4$ mm. All layers in the assessed composite representations are stacked either serial ($\perp$) or parallel ($\parallel$) with respect to the force ($\mathscr{F}$) direction, which is either along the transverse ($\mathscr{F}_x$) or streamwise ($\mathscr{F}_z$) direction. For such stacks, the relationship between the effective Young's modulus of the homogenised composite and layer Young's moduli $\mathscr{E}_i$ of the different layers can be expressed analytically [14, 59]. For k serial ($\perp$) stacked layers with respect to the force direction, the effective Young's modulus $\mathscr{E}^{\perp}_{eff}$ of the homogenised composite is obtained as the harmonic mean of the layers Young's moduli $\mathscr{E}_i$ weighted with their lengths in the force direction following the Reuss hypothesis of homogeneous stress [14, 44, 59]. For $\mathscr{F}_x$

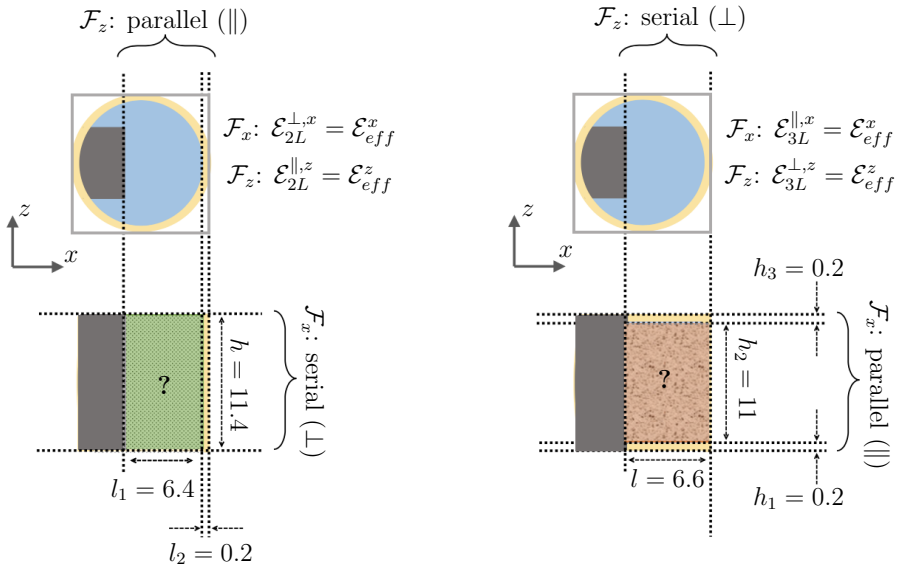

(a) 2L: $\mathcal{E}_{2L}^{x}$ =? and $\mathcal{E}_{2L}^{z}$ =?

(b) 3L: $\mathcal{E}_{3L}^{x}$ =? and $\mathcal{E}_{3L}^{z}$ =?

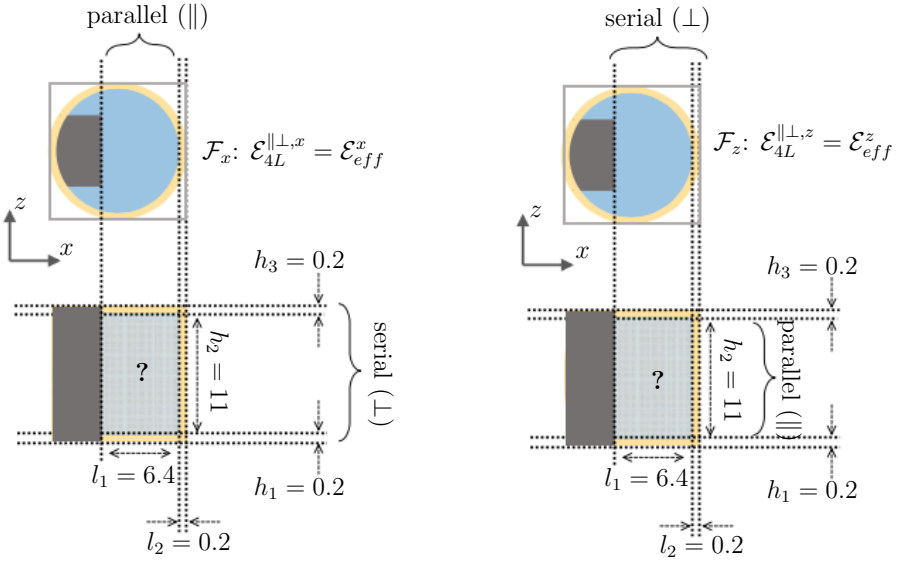

(c) 4L: $\mathcal{E}_{4L}^{x}$ =? (left) and $\mathcal{E}_{4L}^{z}$ =? (right)

Figure 5.15: Coronal (medio-frontal) section (dimensions in mm) of the right deformable PLT VF replica without internal stress ($P_{PLT} = 0$ kPa) (top) and equivalent multi-layer (light-shaded) composite representation (bottom) with effective Young's modulus $\mathcal{E}_{eff}^{x} = 44$ kPa and $\mathcal{E}_{eff}^{z} = 49$ kPa excluding the non-deformable rigid portion (dark-shaded): a) two-layer (2L), b) three-layer (3L), c) four-layer (4L). The mutual layer orientation for a transverse $\mathcal{F}_x$ or streamwise $\mathcal{F}_z$ force is indicated. Young's moduli $\mathcal{E}_{\cdot}^{x}$ =? and $\mathcal{E}_{\cdot}^{z}$ =? of the equivalent inner layer (texture, question mark) are sought. For the latex thin outer layer(s) (light-shaded) $\mathcal{E}_r = 1.1$ MPa holds.

and $\mathscr{F}_z$ this becomes respectively

$$\mathscr{E}_{eff}^{\perp,x} = \frac{\sum_{i=1}^{k} l_i}{\sum_{i=1}^{k} \left(\frac{l_i}{\mathscr{E}_i} \right)} \quad \text{and} \quad \mathscr{E}_{eff}^{\perp,z} = \frac{\sum_{i=1}^{k} h_i}{\sum_{i=1}^{k} \left(\frac{h_i}{\mathscr{E}_i} \right)}. \tag{5.7}$$

with $l = \sum_{i=1}^{k} l_i$, $h = \sum_{i=1}^{k} h_i$. For k parallel ($\|$) stacked layers with respect to the force direction, the effective Young's modulus $\mathscr{E}_{eff}^{\|}$ of the homogenised composite is obtained as the arithmetic mean of the layers Young's moduli $\mathscr{E}_i$ weighted with their heights perpendicular to the force direction following the Voigt hypothesis of homogeneous strain [14, 43, 59]. For $\mathscr{F}_x$ and $\mathscr{F}_z$ this becomes respectively

$$\mathscr{E}_{eff}^{\|,x} = \frac{\sum_{i=1}^{k} h_i \mathscr{E}_i}{\sum_{i=1}^{k} h_i} \quad \text{and} \quad \mathscr{E}_{eff}^{\|,z} = \frac{\sum_{i=1}^{k} l_i \mathscr{E}_i}{\sum_{i=1}^{k} l_i}. \tag{5.8}$$

When layers are stacked both parallel and serial, *i.e.* combined ($\|\perp$), with respect to the force direction, firstly adjacent parallel stacked layers are homogenised using Eq. (5.8) and then the remaining serial stack is homogenised using Eq. (5.7) [14, 59].

Analytical expressions of effective Young's moduli of each homogenised representation are then set to match $\mathscr{E}_{eff}^{x} = 44$ kPa (for $\mathscr{F}_x$) and $\mathscr{E}_{eff}^{z} = 49$ kPa (for $\mathscr{F}_z$) measured for the PLT replica. This way, analytical expressions of the effective Young's modulus of each homogenised composite (2L, 3L or 4L) subjected to a transverse force $\mathscr{F}_x$ (or streamwise force $\mathscr{F}_z$) reduce to first-order linear equations whose unknown is the Young's modulus $\mathscr{E}_{\cdot}^{x}$ (or $\mathscr{E}_{\cdot}^{z}$) of the equivalent inner layer (texture, question mark in Fig. 5.15). As the layers of the 2L representation (Fig. 5.15(a)) are stacked serial for a force along the x-dimension and parallel for a force along the z-dimension, the unknowns $\mathscr{E}_{2L}^{x}$ and $\mathscr{E}_{2L}^{z}$ are expressed as

$$\mathscr{E}_{2L}^{x} = \frac{l_1 \, \alpha_{1,x}}{1 - \frac{l_2}{\mathscr{E}_r} \alpha_{1,x}} \quad \text{and} \quad \mathscr{E}_{2L}^{z} = \frac{\alpha_{1,z}}{l_1} - \frac{l_2 \, \mathscr{E}_r}{l_1} \tag{5.9}$$

with $\alpha_{1,x} = \mathscr{E}_{eff}^{x}/l$, $\alpha_{1,z} = \mathscr{E}_{eff}^{z} l$ and $l = l_1 + l_2$.

Also, the layers of the 3L representation (Fig. 5.15(b)) are stacked parallel for a force along the x-dimension and serial for a force along the z-dimension so that unknowns $\mathscr{E}_{3L}^{x}$ and $\mathscr{E}_{3L}^{z}$ are expressed as

$$\mathscr{E}_{3L}^{x} = \frac{\alpha_{2,x}}{h_2} - \frac{2 h_1 \, \mathscr{E}_r}{h_2} \quad \text{and} \quad \mathscr{E}_{3L}^{z} = \frac{h_2 \, \alpha_{2,z}}{1 - \frac{2 h_1 \, \alpha_{2,z}}{\mathscr{E}_r}} \tag{5.10}$$

with $\alpha_{2,x} = \mathscr{E}_{eff}^{x} h$, $\alpha_{2,z} = \mathscr{E}_{eff}^{z}/h$ and $h = 2h_1 + h_2$ since $h_1 = h_3$.

Table 5.4: Young's modulus $\mathscr{E}_{\cdot}^{x}$ and $\mathscr{E}_{\cdot}^{z}$ of the inner layer of the equivalent 2L ($\mathscr{E}_{2L}^{x}$ and $\mathscr{E}_{2L}^{z}$), 3L ($\mathscr{E}_{3L}^{x}$ and $\mathscr{E}_{3L}^{z}$) and 4L ($\mathscr{E}_{4L}^{x}$ and $\mathscr{E}_{4L}^{z}$) composite representation. Measured effective Young's moduli $\mathscr{E}_{eff}^{x}$ and $\mathscr{E}_{eff}^{z}$ for the PLT replica (Section 5.5.1) and $\mathscr{E}_{r}$ for the outer latex layer(s) (natural rubber [40]) are given.

	$\mathscr{E}_{\cdot}^{x}$ [kPa]	$\mathscr{E}_{\cdot}^{z}$ [kPa]
inner layer, 2L	$\mathscr{E}_{2L}^{x} = 42.7^{\dagger}$	$\mathscr{E}_{2L}^{z} = 15.1$
inner layer, 3L	$\mathscr{E}_{3L}^{x} = 4.1$	$\mathscr{E}_{3L}^{z} = 47.4^{\dagger}$
inner layer, 4L*	$\mathscr{E}_{4L}^{x} = 4.3$	$\mathscr{E}_{4L}^{z} = 14.5$
outer latex, ML	$\mathscr{E}_{r} = 1100$	
homogenised‡, ML	$\mathscr{E}_{eff}^{x} = 44$	$\mathscr{E}_{eff}^{z} = 49$

† general representation ($\mathscr{E}_{r}$-variation), serial ($\perp$) stack.
* design representation (known $\mathscr{E}_{r}$), combined ($\parallel\perp$) stack.
‡ set to match $\mathscr{E}_{eff}^{x}$ and $\mathscr{E}_{eff}^{z}$ measured on the PLT replica.

Additionally, the layers of the 4L representation (Fig. 5.15(c)) are stacked parallel and serial for both force directions so that unknowns $\mathscr{E}_{4L}^{x}$ and $\mathscr{E}_{4L}^{z}$ are obtained combining using expressions in Eq. (5.9) and in Eq. (5.10) as

$$\mathscr{E}_{4L}^{x} = \frac{h}{h_2}\left[\frac{l_1\alpha_{1,x}}{1-\dfrac{l_2}{\mathscr{E}_r}\alpha_{1,x}} - \frac{2h_1\mathscr{E}_r}{h}\right] \quad \text{and} \quad \mathscr{E}_{4L}^{z} = \frac{l}{l_1}\left[\frac{h_2\,\alpha_{2,z}}{1-\dfrac{2h_1\,\alpha_{2,z}}{\mathscr{E}_r}} - \frac{l_2\,\mathscr{E}_r}{l}\right]. \tag{5.11}$$

The values of $\mathscr{E}_{\cdot}^{x}$ and $\mathscr{E}_{\cdot}^{z}$ for 2L ($\mathscr{E}_{2L}^{x}$ and $\mathscr{E}_{2L}^{z}$), 3L ($\mathscr{E}_{3L}^{x}$ and $\mathscr{E}_{3L}^{z}$) and 4L ($\mathscr{E}_{4L}^{x}$ and $\mathscr{E}_{4L}^{z}$) representations are presented in Table 5.4. As a reference, effective Young's moduli $\mathscr{E}_{eff}^{x}$ and $\mathscr{E}_{eff}^{z}$ of the PLT replica are indicated as well.

Resulting $\mathscr{E}_{eff}^{x}$ and $\mathscr{E}_{eff}^{z}$, from measurements on the PLT VF replica (Section 5.5.1), as well as $\mathscr{E}_{\cdot}^{x}$ and $\mathscr{E}_{\cdot}^{z}$ for the equivalent ML composite representations in Table 5.4 are within the range (up to 65 kPa) reported for the anatomical layers of a normal VF of a male adult [3, 4, 6, 7, 34–36], *i.e.* muscle, vocalis ligament, superficial layer and epithelium. Therefore, Young's moduli associated with the homogenised ($\mathscr{E}_{eff}^{x}$ and $\mathscr{E}_{eff}^{z}$) and the inner layer ($\mathscr{E}_{\cdot}^{x}$ and $\mathscr{E}_{\cdot}^{z}$) of the equivalent ML composite representations are also within the range characterising molded silicone ML VF replicas as their composition is chosen in order to mimic the Young's modulus of the different anatomical VF layers [8, 16, 17, 29, 45, 59]. Note, that Young's modulus Y_r of the latex outer layer is out of this range as its value is much greater (factor 17) than 65 kPa corresponding to the upper limit of the range associated with anatomical layers.

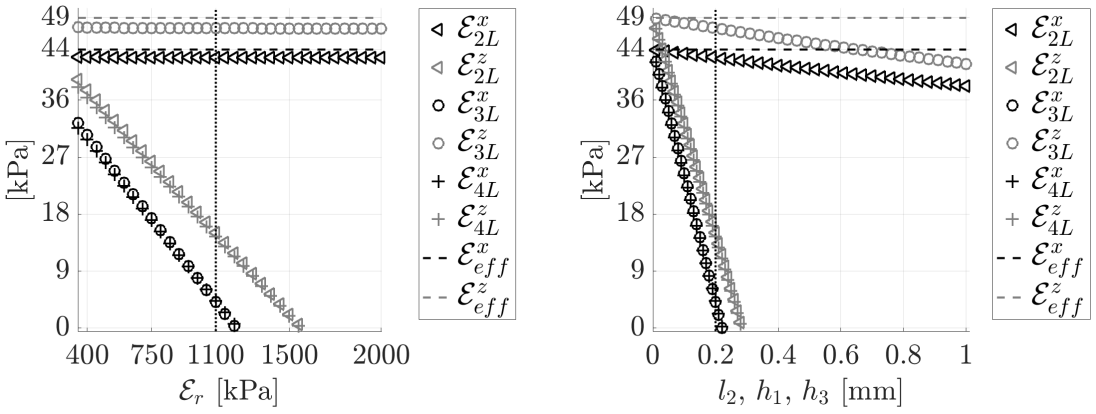

(a) with $l_2 = h_1 = h_3 = 0.2$ mm (b) with $Y_r = 1100$ kPa

Figure 5.16: Influence of outer thin latex layer characteristics on $\mathscr{E}^x_{\cdot}$ (black symbols) and $\mathscr{E}^z_{\cdot}$ (gray symbols) on the equivalent 2L (◁), 3L (○) and 4L (+) composite representations of the PLT replica for which $Y_r = 1100$ kPa and $l_2 = h_1 = h_3 = 0.2$ mm (dotted vertical lines) and homogenised effective Young's moduli $\mathscr{E}^x_{eff} = 44$ kPa and $\mathscr{E}^z_{eff} = 49$ kPa (dashed horizontal lines): a) for variation of Young's modulus Y_r, b) for variation of layer dimension l_2, h_1, h_3.

5.5.3 Influence of outer layer characteristics

From Table 5.4 is seen that for all assessed equivalent ML composite representations of the PLT replica, $\mathscr{E}_r$ associated with the outer latex layer(s) is much larger (factor 20 up to 270) than $\mathscr{E}^x_{\cdot}$ and $\mathscr{E}^z_{\cdot}$ of the inner layer. Since the arithmetic mean for parallel layer stacking (Eq. (5.8)) is more affected by layers with high Young's modulus than to the harmonic mean for serial layer stacking (Eq. (5.7)), serial layer stacks are expected to be some what robust with respect to variations to the outer latex layer dimensions (l_2, h_1, h_3) and its Young's modulus $\mathscr{E}_r$. From Fig. 5.15 is seen that purely serial layer stacking occurs only for the 2L representation in the case of transverse force $\mathscr{F}_x$ ($\mathscr{E}^x_{2L}$, Fig. 5.15(a)) and for the 3L representation in the case of streamwise force $\mathscr{F}_z$ ($\mathscr{E}^z_{3L}$, Fig. 5.15(a)). Consequently, these representations, and thus resulting $\mathscr{E}^x_{2L}$ and $\mathscr{E}^z_{3L}$, are robust with respect to outer latex layer characteristics. This is further illustrated in Fig. 5.16 where $\mathscr{E}^x_{\cdot}$ and $\mathscr{E}^z_{\cdot}$ (from Eq. (5.9), Eq. (5.10) and Eq. (5.11)) are plotted as a function of $\mathscr{E}_r$ (Fig. 5.16(a)) and as a function of outer layer dimension l_2, h_1, h_3 (Fig. 5.16(b)). Values of the experimentally assessed PLT VF replica, *i.e.* $Y_r = 1.1$ MPa and $l_2 = h_1 = h_3 = 0.2$ mm, are indicated (dotted vertical lines). Young's modulus $\mathscr{E}_r$ is varied between 0.4 MPa and 2.0 MPa, which spans a range reported for natural rubber [62, 63] (Piercan Ltd.) and outer layer dimensions (l_2, h_1, h_3) are varied from 0.01 mm up to 1 mm. It is seen that $\mathscr{E}^x_{2L}$ and $\mathscr{E}^z_{3L}$ are indeed least affected (with less than 10 kPa) by variation of the outer layer characteristics ($\mathscr{E}_r$ and l_2, h_1, h_3) as their value remains near $\mathscr{E}^x_{eff}$ and $\mathscr{E}^z_{eff}$ characterising the homogenised composite representations. It follows that the $\mathscr{E}^x_{2L}$ and $\mathscr{E}^z_{3L}$ are robust to changes

of the latex outer layer(s) characteristics. For all other representations, $\mathscr{E}_{.}^{x}$ and $\mathscr{E}_{.}^{z}$ decrease rapidly when Y_r or outer layers dimension (l_2, h_1, h_3) are increased until eventually negative values are reached due to the increase of the second term (with minus sign) on the right-hand side in $\mathscr{E}_{2L}^{z}$ (Eq. (5.9)), $\mathscr{E}_{3L}^{x}$ Eq. (5.10), $\mathscr{E}_{4L}^{x}$ and $\mathscr{E}_{4L}^{z}$ in Eq. (5.11). These representations, such as the 4L representation, are thus limited to the range for which $\mathscr{E}_{.}^{x} > 0$ kPa and $\mathscr{E}_{.}^{z} > 0$ kPa since negative values are not physical and do not allow a comparison with the human VF or other mechanical deformable VF replicas such the molded silicone ML replicas mentioned in Section 5.5.2. For the 4L representation $\mathscr{E}_{4L}^{x} < \mathscr{E}_{4L}^{z}$ (difference ≈ 10 kPa) holds so that the inner layer reflects the imposed anisotropy of the homogenised equivalent composite ($\mathscr{E}_{eff}^{x} < \mathscr{E}_{eff}^{z}$, difference 5 kPa). Furthermore, it is observed in Fig. 5.16 (and in Table 5.4) that $\mathscr{E}_{3L}^{x} \approx \mathscr{E}_{4L}^{x}$ and $\mathscr{E}_{2L}^{z} \approx \mathscr{E}_{4L}^{z}$. This is due to the similar transverse 3L and 4L parallel layer stacks and the similar streamwise 2L and 4L parallel layer stacks (as depicted in Fig. 5.15) whereas the remaining serial stacking part for the 4L representation is, again due to the harmonic mean, only marginally affected by the thin latex outer layer with high $\mathscr{E}_r$. Overall, for $\mathscr{E}_{4L}^{x} > 0$ and $\mathscr{E}_{4L}^{z} > 0$ as for the used PLT replica (Table 5.4), the equivalent 4L composite representation is most elegant since the representation is applied to both the transverse and streamwise force directions and reflects the associated anisotropy ($\mathscr{E}_{4L}^{x} < \mathscr{E}_{4L}^{z}$) observed for the PLT VF replica $\mathscr{E}_{eff}^{x} < \mathscr{E}_{eff}^{z}$. Moreover, since the inner layer of the 4L representation only concerns the water portion of the PLT replica, found $\mathscr{E}_{4L}^{x}$ and $\mathscr{E}_{4L}^{z}$ might be exploited in order to vary the latex outer layers characteristics ($\mathscr{E}_r$ or/and its length) in order to approximate a prescribed effective Young's moduli for the homogenised equivalent 4L composite. This way, the 4L representation might potentially contribute to PLT replica design. On the other hand, representations associated with $\mathscr{E}_{2L}^{x}$ and $\mathscr{E}_{3L}^{z}$ are of interest when latex outer layer characteristics are either not accurately known or out of the working range of the 4L representation ($\mathscr{E}_{4L}^{x} \leq 0$ and $\mathscr{E}_{4L}^{z} \leq 0$).

5.6 Conclusion

In this chapter, the elastic linear low-strain stress-strain behaviour of each molded multi-layer serial stacked composite specimen is characterised by its effective low-strain Young's modulus $\mathscr{E}_{eff}$ which is both modelled and measured at room temperature. The low strain range extends up to 0.28 and measured $\mathscr{E}_{eff}$ range between 4.5 kPa and 8 kPa. This low-strain Young's modulus allows then to model the non-linear stress-strain behaviour (up to 90 kPa) of each specimen for strains up to 1.55 using two-parameter exponential and cubic relationships using generic parameter sets. The modelled $\mathscr{E}_{eff}$-dependence of the generic parameter sets is confirmed for estimated best fit parameters (fit accuracy of $R^2 \geq 99.9\%$). Although that no experimental validation is assessed, it is noted that modelled non-linear stress-strain curves with generic parameter sets are in good agreement with measured data for both M5-based specimens gathered for strains up to 1.08. Next, a 'first-decimal-criterion' is proposed in order to define the strain onset of a linear high-

strain region and its effective high-strain Young's modulus, valid within and potentially beyond the strain range up to 1.55 for which the non-linear model approach was validated in Chapter 4. This criterion requires that at the high-strain onset, local slopes to the non-linear curves and fitted slopes to strains above the high-strain onset match until the first decimal place. The modelled linear high-strain range using this criterion, is thus a continuous continuation of the non-linear stress-strain model. Moreover, this criterion implies that the high-strain linear behaviour is an accurate alternative ($R^2 > 99\%$) for the non-linear stress-strain curves.

Additionally, the effective elastic Young's modulus of the PLT VF replica is measured along the transverse right-left (x) and the streamwise inferior-superior (z) direction. Measured $\mathscr{E}^x_{eff} = 44$ kPa and $\mathscr{E}^z_{eff} = 49$ kPa show an anisotropy of 11% with respect to $\mathscr{E}^x_{eff}$ characterising the main auto-oscillation direction. These values are within the range, up to 65 kPa, reported for anatomical layers of a male adult human VF, which illustrates the relevance of this type of mechanical VF replicas from a mechanical point of view. Next, equivalent 2L, 3L and 4L composite representations are assessed consisting of an inner layer to which one, two or three latex outer layers are added. The effective Young's modulus of the homogenised representation is set to match $\mathscr{E}^x_{eff} = 44$ kPa and $\mathscr{E}^z_{eff} = 49$ kPa observed for the PLT replica and the Young's modulus of the latex outer layer(s) is also known. The unknown Young's moduli $\mathscr{E}^x_{\cdot}$ and $\mathscr{E}^z_{\cdot}$ of the inner layer are then obtained analytically. The assessed 4L representation is most elegant considering both force directions. Associated $\mathscr{E}^x_{4L} = 4.3$ kPa and $\mathscr{E}^z_{4L}$ 14.5 kPa reflect the anisotropy observed for the effective Young's moduli of the PLT replica. It is argued that this representation might be exploited for PLT replica design where the outer latex layer characteristics can be adapted in order to prescribe an overall effective Young's modulus. On the other hand, the transverse 2L ($\mathscr{E}^x_{4L} = 42.7$ kPa) and streamwise 3L ($\mathscr{E}^z_{4L} = 47.4$ kPa) serial stack representations are robust to changes of the outer layer characteristics, so that these representations remain valid in case that outer layer characteristics are not accurately known or changed. Regardless of the applied representation, found Young's moduli for the inner layer are within the range pertinent to human VF layers. This might contribute to the comparison between the Young's moduli associated with the PLT replica and with other types of deformable VF replicas such as molded silicone VF replicas. So far, the comparison between replicas is indirect as it is limited to auto-oscillation features, whereas current results might allow to account directly for the Young's moduli or linear elasticity.

In the next chapter, the validated model to estimate the effective Young's modulus is used to design a newly silicone VF replica without and with an embedded structural inclusion, in order to assess the influence of such structural change on the fluid-structure interaction underlying VFs auto-oscillation.

CHAPTER 6

Experimental study of the influence of structural properties on the fluid-structure interaction

6.1 Introduction

The vocal folds vibration, and hence acoustic source properties of voiced speech sounds, rely on the vocal folds elasticity which is therefore a crucial part of the underlying fluid-structure interaction for healthy as well as pathological conditions. The human vocal folds are an extremely complex structure, and systematically studying the influence of varying structural properties of the human VFs on voice quality is not feasible without invasive muscular stimulation. Therefore, physical studies often rely on simplified mechanical vocal folds replicas. Several VFs pathologies can alter the material properties of the vibratory tissue, e.g., the presence of an inclusion or a scar. In this work, it is aimed to characterise the structural properties of deformable mechanical silicone VFs replicas in order to be able to further systematically investigate and quantify the effect of structural VFs pathologies like inclusions.

6.2 Rectangular silicone VFs replicas

In order to assess the influence of structural properties, *i.e.* the effective Young's modulus, on the fluid-structure interaction of VFs replicas, a replica with simplified geometry inspired by the EPI model introduced in Chapter 2 is built. The newer replica has a rectangular cross-section in the medio-frontal plane. Therefore, each layer has constant thickness $L_z = 10.2$ mm along the inferior-superior direction. The layers are stacked on top of each other in the left-right (x) direction as shown in Fig. 6.1(a). The overall dimensions $L_y = 17.0$ mm along the posterior-anterior direction and $L_x = 8.5$ mm (excluding the backing layer of a thickness $l_t = 4.0$ mm) along the left-right direction rest unchanged from the original design of the EPI replica. The thickness of each layer in the left-right direction, l_t, is designed so that the normalised volume of each layer V_i/V_{VF} corresponds to the appropriate value of the original EPI model, as given in Table 6.1. Each layer thickness l_t and Young's modulus values are indicated as well. The fabrication process of the rectangular VFs replicas follows the same steps used to build the ML

Table 6.1: Design of molded rectangular replica layers: measured Young's modulus $\mathscr{E}$, layer thickness l_t, mixture (Mix) TE (Thinner-Ecoflex) or TD (Thinner-Dragonskin), mass mixing ratio $\mathscr{M}$, and the normalised volumes $\mathscr{V}/\mathscr{V}_{VF}$ of the EPI replica that the design of the rectangular replica is based on.

Layer	$\mathscr{E}$ [kPa]	l_t [mm]	Mix	$\mathscr{M}$ [-]	$\mathscr{V}/\mathscr{V}_{VF}$ [%]
Muscle	23.4	3.2	TE	1:2	38.1
Ligament	4.0	0.7	TE	4:2	7.6
Superficial	2.2	4.3	TE	8:2	50.3
Epithelium	64.7	0.3	TD	1:2	4.0

Table 6.2: Effect of embedding a structural inclusion in the superficial layer of the rectangular VFs replica on its elasticity: measured Young's modulus of the inclusion $\mathscr{E}^{In}$, measured inclusion dimensions l_x, l_y, and l_z, the equivalent length of the inclusion homogenised layer l_{eq} (as defined in Section 3.4.3.1, modelled Young's modulus in the x direction of the inclusion equivalent homogenised layer $\widehat{\mathscr{E}}^x_{eq}$, modelled effective Young's modulus in the x direction of the rectangular replica $\widehat{\mathscr{E}}^x_{eff}$, modelled Young's modulus in the z direction of the inclusion equivalent homogenised layer $\widehat{\mathscr{E}}^z_{eq}$, modelled effective Young's modulus in the z direction of the rectangular replica $\widehat{\mathscr{E}}^z_{eff}$.

Inclusion	$\mathscr{E}^{In}$ [kPa]	l_x [mm]	l_y [mm]	l_z [mm]	l_{eq} [mm]	$\widehat{\mathscr{E}}^x_{eq}$ [kPa]	$\widehat{\mathscr{E}}^x_{eff}$ [kPa]	$\widehat{\mathscr{E}}^z_{eq}$ [kPa]	$\widehat{\mathscr{E}}^z_{eff}$ [kPa]
No inclusion	-	0	0	0	0	-	**3.7**	-	**12.5**
Serial inclusion	298	2	10	4	2	70.4	**6.1**	3.6	**12.9**
Parallel inclusion	298	4	10	2	4	36.3	**15.1**	2.7	**12.8**

silicone specimens, detailed in Chapter 3. Each fold is built layer-by-layer using 3D-printed molds with the appropriate silicone mixture given in Table 6.1. Each molded layer thickness l_t is measured using a laser transceiver (Panasonic HL-G112-A-C5, wavelength 655 nm, accuracy 8 μm). The thickness of all layers molded has an accuracy of $\pm$ 0.3 mm, which falls well within the reported accuracy in Section 3.4.1. Figure 6.1(b) shows an example of two folds of the rectangular VFs replica in their fixation.

6.3 Structural inclusion design

As the presence of a stiffer region somewhere within the vocal fold structure is commonly reported in case of a vocal fold abnormality or pathology [1, 49–51, 64–66], a structural inclusion is embedded in the superficial layer of the rectangular replica as depicted in Fig. 6.2. The inclusion has a fixed length of 10 mm, fixed width of 4 mm, and a fixed thickness of 2 mm. Depending on the stacking of the inclusion with respect to the layers of the replica, the dimensions l_x in the left-right direction and l_z in the inferior-superior direction will change. The length l_y in the posterior-anterior direction remains constant, however. As it is shown in Fig. 6.2, the inclusion is either stacked in serial (Fig. 6.2(a)) or in parallel (Fig. 6.2(d)) with respect to the direction of the layers. Both Fig. 6.2(b) and Fig. 6.2(e) show a side view (medio-sagittal plane) of the rectangular replica (with transparent top layers) to visualise the constant length $l_y = 10$ mm of the inclusion, regardless of which way it is stacked. It is noted that the centre of the inclusion is intersected with the centre of the layers in the medio-sagittal plan, as can be seen from Fig. 6.2(b) and Fig. 6.2(e), so that the inclusion dimensions l_y and l_z are centred within the replica dimensions L_y and L_z. The inclusion, however, is inserted directly on top of the ligament layer, regardless of stacking, so that the inclusion is not centred withing the superficial layer in the left-right direction. Ta-

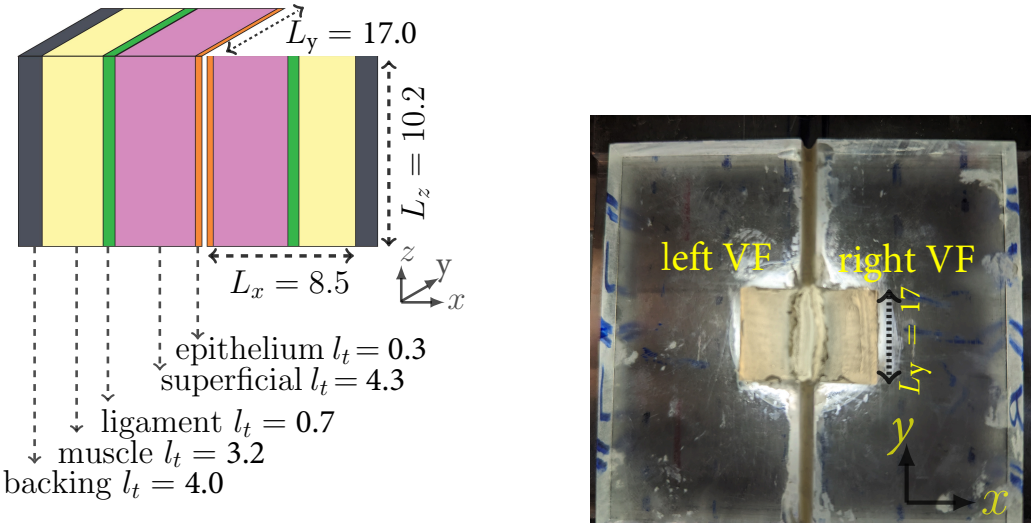

(a) Schema (b) In fixation

Figure 6.1: Rectangular VFs replica: a) overview of the four-layer replica dimensions given in mm, where l_t is a layer thickness and L_x, L_y and L_z are the overall dimensions b) top view (superior-inferior) of two rectangular folds in their acrylic fixation.

ble 6.2 gives the dimensions of the inclusion in the case of either serial or parallel stacking, and as the Young's modulus of the inclusion is known $\mathscr{E}^{In} = 298$ kPa, the effective Young's modulus of the inclusion's equivalent, homogenised layer can be calculated and thus the overall effective Young's modulus of the replica can be calculated as well, for either the left-right direction $\widehat{\mathscr{E}}^x_{eff}$ (assuming the uniaxial forces applied are in the x direction) or the inferior-superior direction $\widehat{\mathscr{E}}^x_{eff}$ (assuming the uniaxial forces applied are in the z direction). In line with the previously validated results, the value of the effective Young's modulus in the x direction $\widehat{\mathscr{E}}^x_{eff}$ is indeed larger for the parallel stacking of the inclusion compared to the serial stacking. Both values are larger than the value of the effective Young's modulus of the replica with no inclusions by factors of 4.1 and 1.7, respectively. Evidently, the values for the effective Young's modulus along the z direction $\widehat{\mathscr{E}}^z_{eff}$ possess less variability, due to the fact that the layers now are considered stacked in parallel, where the low values of the effective Young's modulus of the inclusion's equivalent, homogenised layer $\widehat{\mathscr{E}}^z_{eq}$ tend to be masked in calculating the WAM of each parallel layer. The value of the effective Young's modulus $\mathscr{E}^x_{eff}$ of one rectangular replica (without inclusion) was experimentally validated (using a modified setup as shown in Appendix D) against the model value with a difference of 0.5 kPa, which is in line with the accuracy of the models reported in Chapter 3.

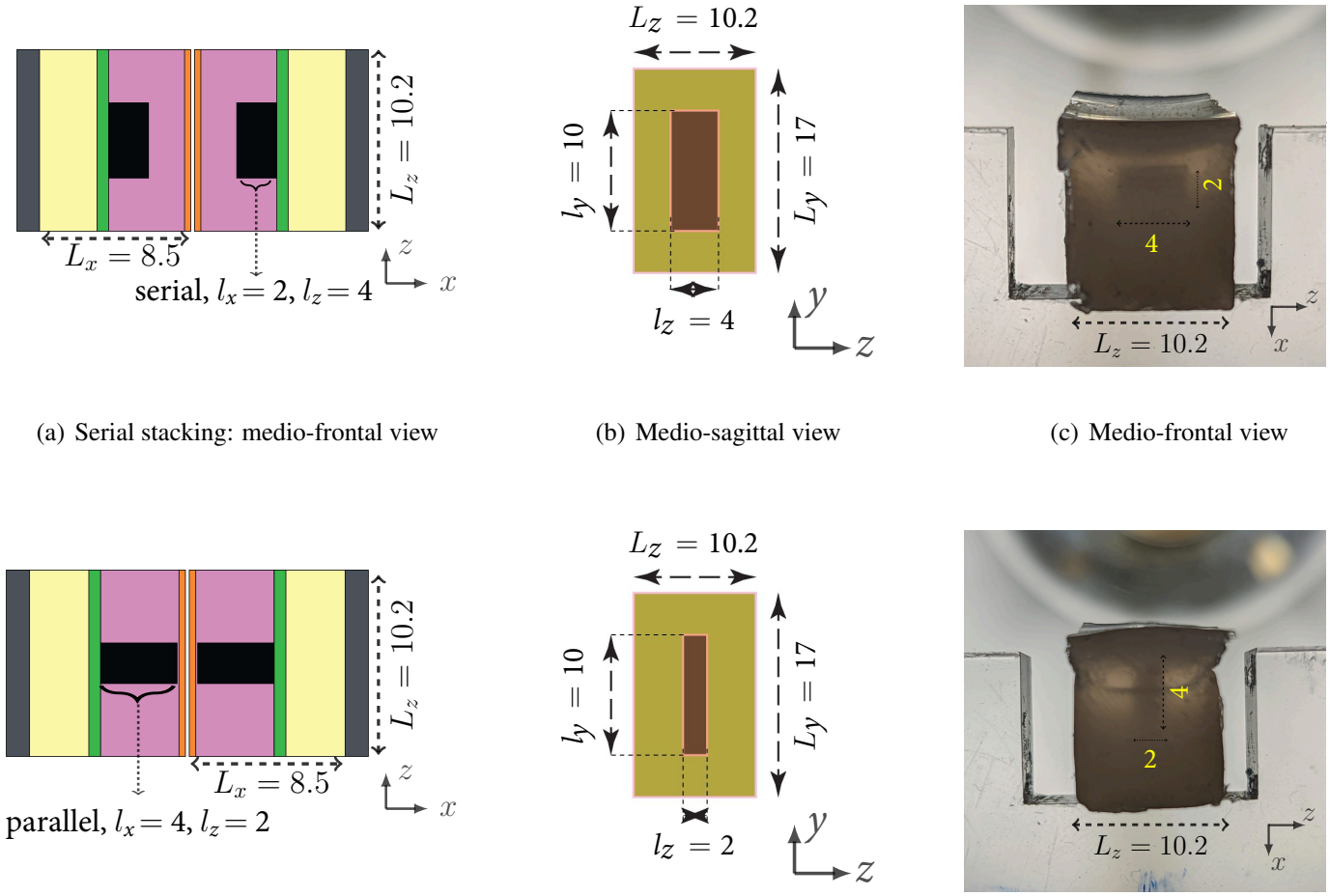

(a) Serial stacking: medio-frontal view

(b) Medio-sagittal view

(c) Medio-frontal view

(d) Parallel stacking: medio-frontal view

(e) Medio-sagittal view

(f) Medio-frontal view

Figure 6.2: Embedded structural inclusion design. The first row shows a serially-stacked inclusion, while the second row shows a parallelly-stacked inclusion: a) and d) medio-frontal view (front view), b) and e) medio-sagittal view (side view), c) and f) medio-frontal view (front view) of a molded replica with serial and parallel inclusion, respectively. Dimensions are in mm. It is noted that the placement of the replica in figures c) and f) are only for illustration, with the replicas rotated with respect to the fixation in order to visualise the inclusion.

6.4 Fluid-structure interaction experiments

6.4.1 Setup

In order to produce a fluid-structure interaction that results in auto-oscillation, VFs replicas are fixed as shown in Fig. 6.1(b). Using silicone adhesive (Sil-Poxy, Smooth-On, Inc., Easton, PA), each fold was fixed to an acrylic mounting plate. All remaining space between the two mounting plates is filled with glue (Pattex) to prevent air leakage. The models are dusted with talcum powder to minimise surface adhesion between the two folds. As illustrated in Fig. 6.3, below the mounting plate, an upstream tube (diameter 25 mm, constant area 491 mm^2, length 130 mm) representing the trachea is then connected to a pressure reservoir (volume $\pm$ 0.22 m^3) representing the lungs, which is supplied by an air compressor (Atlas Copco GA5 FF-300-8, GA15 FF-8). To prevent parasitic acoustic resonances, the reservoir has been filled with acoustic foam. The continuous steady airflow is controlled by a valve (Norgren, 11-818-987). In order to measure upstream pressure $P_u(t)$, a pressure transducer (Endevco 8507C-5, accuracy $\pm$ 5 Pa given in Appendix B.2) is positioned in a pressure tap 35 mm upstream of the replicas. The airflow is gradually increased till vibration was produced in order to detect the onset of oscillation and hence quantify the threshold pressure. Replicas vibration amplitude in the streamwise z-direction z_r is also measured by a laser transceiver (Panasonic HLG112AC5, 655 nm wavelength, accuracy 80 μm) placed 110 mm downstream of the replicas, as shown in Fig. 6.3(a) for setup (a), or using two lasers as shown in Fig. 6.3(b) for setub (b). The lasers are installed at a distances of 95 mm and 155 mm for measuring the right and the left folds, respectively. The position of the lasers can be freely adjusted in both the x and y directions for measuring the inferior-superior (z direction) displacement of any point on the top surface of the VFs replica in the transverse plan. A data acquisition card (National Instruments BNC-2110 input/output card) are used to acquire all signals, and Labview software programs are used to process them with a sample frequency of 10 kHz. Experiments are performed for rectangular replicas introduced in Section 6.2 as well as original silicone replicas introduced in Section 2.2.1. Table 6.3 gives an overview of the measurements recorded and analysed and the replicas used for the upcoming analysis and results sections. For setup (b), only the measurements from the laser (positioned at $z = 95$ mm on top of the right fold of the replicas) will be considered since the results from both lasers (at indicated measured points) are similar due to symmetry.

6.4.2 Auto-oscillation analysis

As upstream pressure $P_u(t)$ drives vocal folds oscillation, its analysis is essential. The onset pressure P_{On}, also known as the threshold pressure, is the minimal upstream pressure $P_u(t)$ necessary to maintain the auto-oscillation of the vocal folds. It corresponds to the offset pressure

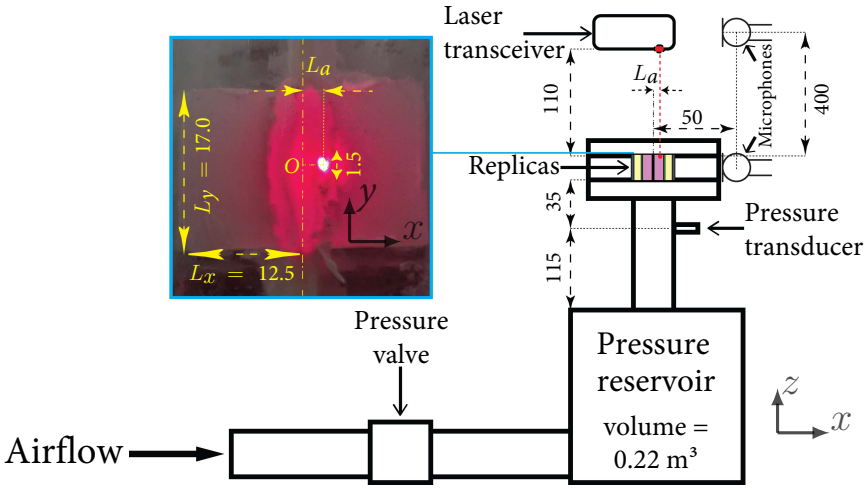

(a) Setup a

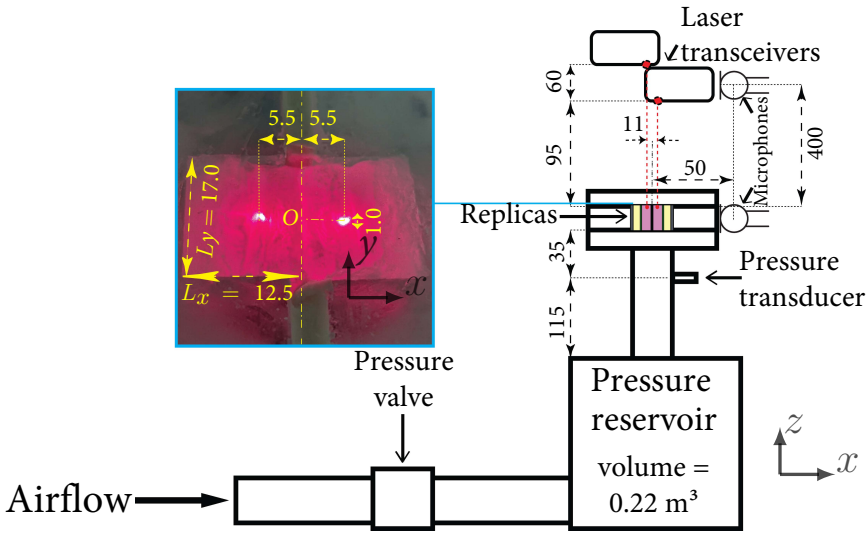

(b) Setup b

Figure 6.3: Overview of the setup (not to scale) used for auto-oscillation experiments. Dimensions given are in mm. Setup (b) is an updated setup (a) with an added second laser transceiver. For setup (a), the distance in the x direction between the laser point and the two folds centre-line $L_a \in \{3.0, 5.0\}$. The laser point has the same y coordinate as the point O, exactly in the centre of the folds, for setup (a), while for setup (b), the position of the laser point $\in \{-6.0, -4.0, -2.0, 0.0, 2.0, 4.0, 6.0\}$ with respect to the point O.

Table 6.3: Vocal folds replicas used and main quantities analysed.

Replica	Setup		Pressure sensor		Laser(s)		Microphone(s)	
	a	b	Recorded	Analysed	Recorded	Analysed	Recorded	Analysed
Rectangular (no inclusion)	✓	—	✓	✓	✓	✓	✓	—
Rectangular (serial inclusion)	✓	—	✓	✓	✓	✓	✓	—
Rectangular (parallel inclusion)	✓	—	✓	✓	✓	✓	✓	—
EPI	—	✓	✓	✓	✓	✓	✓	—
MRI	—	✓	✓	✓	✓	✓	✓	—
M5	—	✓	✓	✓	✓	✓	✓	—

P_{Off}, which is the minimum upstream pressure before oscillation stops. Due to the nonlinearity of the fluid-structure interaction, hysteresis occurs between the threshold pressures, such that P_{On} is greater than P_{Off}.

During experiments, no airflow is provided until measurements start. However, before measurements, the auto-oscillation of the VFs replicas is searched. Airflow is thus provided and is regulated carefully to search for the onset of the oscillation. Once vibration starts, airflow is cut off and the upstream pressure is released to atmospheric pressure. It is noted that the airflow is considered incompressible, laminar, and quasi-steady during oscillations. Measurements then start in order to record the threshold of oscillation in an uninterrupted way as can be seen in Fig. 6.4. As the airflow starts, the upstream pressure P_u starts to increase, and the VFs replicas will start to oscillate as its value reaches the threshold pressure P_{On}, as shown in the left zoomed-in view in Fig. 6.4. The replicas are left to vibrate for at least 20 s to make sure the self-sustained oscillations reach a steady-state as shown in the middle zoomed-in view. After, the airflow is cut, therefore the upstream pressure P_u starts to decrease and the VFs replicas oscillations cease at the offset pressure P_{Off}, as shown in the right zoomed-in view. Fig. 6.5 shows an example of an upstream pressure P_u signal time series (left) and spectrogram (right) for a rectangular replica with a serial inclusion. In Fig. 6.5(a), the measured upstream pressure as well as its mean value $\overline{Pu}$ (in black) are plotted. The extracted values for comparison between replicas, the onset P_{On} and offset P_{Off} pressures, are plotted as well. The value of the mean peak to peak amplitude of oscillations $\overline{P_{pp}}$ is calculated and shown in the figure. It is noted that the standard deviation is less than 5% on average. For every measured pressure or displacement signal, fundamental frequency is calculated. The extracted fundamental frequency is found to be exactly the same between pressure and displacement signals. From Fig. 6.5(b), it can be seen that the fundamental frequency through the time of oscillations $f_0(t)$ is almost constant, with the frequency at the onset f_{On} and offset f_{Off} of oscillations slightly differs from the steady-state oscillation mean frequency $\overline{f_0}$. Both f_{On} and f_{Off} are extracted as well as $\overline{f_0}$ (with a standard deviation less than 5%). As can be seen on both the left and right figures, there are temporary vibrations that start

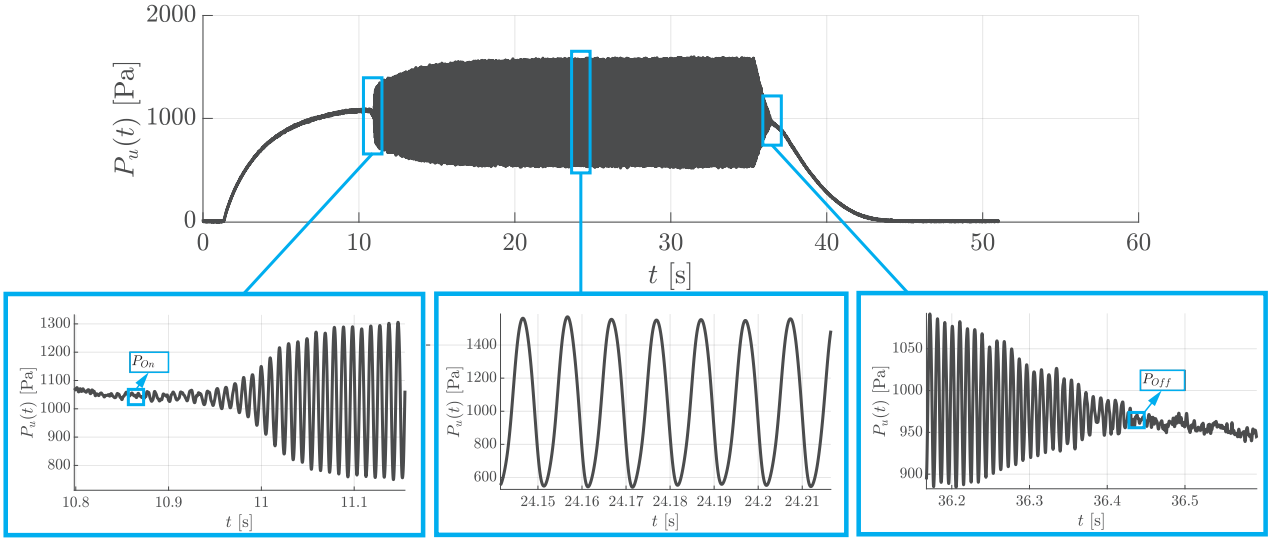

Figure 6.4: Time series of the measured upstream pressure $P_u(t)$ signal for a rectangular replica with a parallel inclusion. The pressure values at oscillation onset P_{On} and offset P_{Off} are indicated (square). A zoomed-in view of $P_u(t)$ around oscillation onset (left), steady-state oscillation (centre), and oscillation offset (right) is presented for clarification.

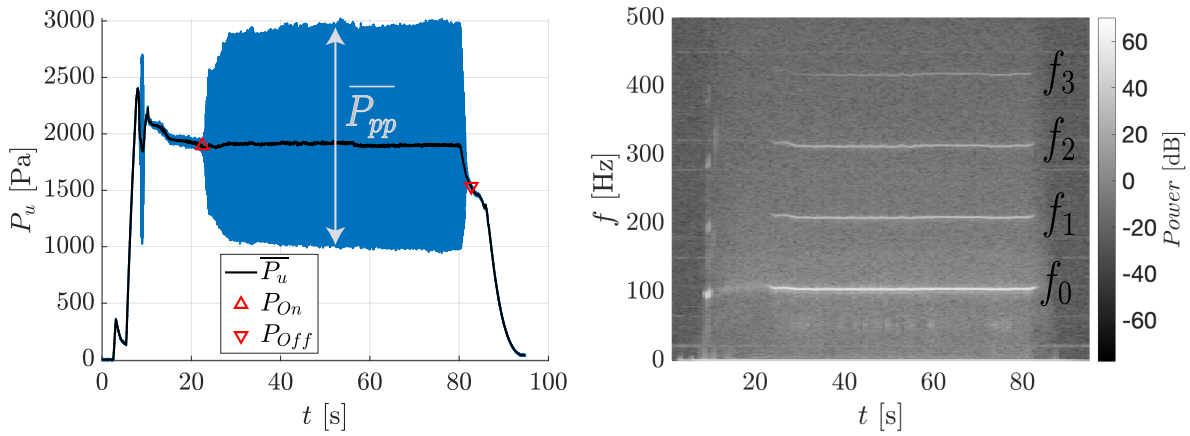

(a) Time series

(b) Spectrogram

Figure 6.5: The pressure signal from the auto-oscillation of a rectangular replica with a serial inclusion: a) time series $P_u(t)$ with the values at onset P_{On} and offset P_{Off} of oscillation detected and plotted (upward and downward pointing triangles, respectively) as well as the peak to peak amplitude mean value during oscillations $\overline{P_{pp}}$ (arrow). The mean pressure $\overline{P_u(t)}$ is also plotted. b) a spectrogram of the pressure signal showing the fundamental frequency f_0 and the first three harmonics (f_1, f_2, and f_3) as well.

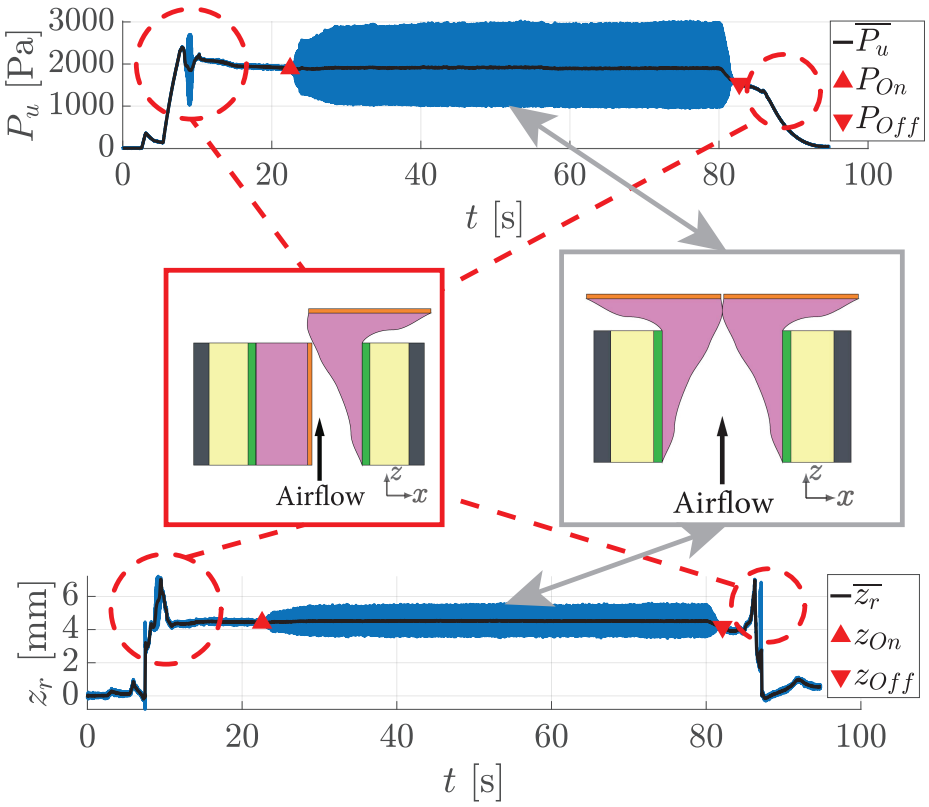

Figure 6.6: Overview of the manner how the rectangular replicas deform due to airflow, with the epithelium layer being rotated 90°, where vibrations circled around show a semi-open replica compared to the steady-state part where the replica is fully open. Both the pressure $P_u(t)$ (top) and displacement $z_r(t)$ (bottom) time series are presented. The associated onset and offset values are plotted (upward and downward pointing triangles, respectively) as well.

and cease very quickly before the steady-state oscillations. This occasionally happens with some rectangular replicas. In Fig. 6.6, the time signals of both the measured upstream pressure $P_u(t)$ and the displacement $z_r(t)$ are shown for a rectangular replica. As can be observed from the pressure signal, and more prominently from the displacement signal, an abrupt change in amplitude accompanied with temporary vibrations occurs due to the fact that the last layer (epithelium) of rectangular replicas being rotated 90° by the airflow. For steady-state oscillations, the last layer of each fold rotate before both start self-oscillating. Occasionally, one fold has its last layer fully rotated before the other, hence the sudden change in both $P_u(t)$ and $z_r(t)$ as well as the occurrence of temporary vibrations. The onset of steady-state oscillations is determined when both folds vibrate, and the offset is determined when the oscillations of both folds cease, as can be seen in Fig. 6.6. For the rectangular replicas, the distance, along the y axis, between the laser measured point and the point O, situated at the centre of the replicas, is fixed. The laser measured point is at the centre of the replica, as was shown in Fig. 6.3(a). For the EPI, M5, and MRI models, more than one point, along the y axis, were measured for different experiments. The distances of the laser measured points range from 6 mm away from the centre of the replica (point O) in the negative y direction to 6 mm in the positive y direction, with a step of 2 mm. For comparison between the displacement measurements of different points, the displacement mean value during oscillations $\overline{z_r}$ is calculated.

6.4.3 Results

For the rectangular replicas tested, the presence of an embedded structural inclusion does indeed affect the fluid-structure interaction, as shown in Table 6.4. Starting with the fundamental frequency of oscillation during the time the replica vibrates $f_0(t)$, the frequency does increase for the case of an embedded serial or parallel inclusion compared to the value of the oscillations frequency for the rectangular replica with no inclusion embedded. Although the mean value of the fundamental frequency during oscillations $_0$ for the case with a parallel inclusion increases by slightly more than 1%, it increases by more than 6% for the case of an embedded serial inclusion. The fundamental frequency at oscillations onset f_{On} and offset f_{Off} increase as well. It is noted though that f_{On} for the case of a serial inclusion is less than f_{Off}. Secondly, both the upstream pressure at the onset of oscillation P_{On} and at the offset P_{Off} increase for the case of an embedded serial inclusion compared to the case of a rectangular replica with no inclusion, with an increase of 35% and 16%, respectively. The peak to peak amplitude mean value during oscillations $\overline{P_{pp}}$ also increases by 79%. However, for the case of a parallel inclusion, it is observed that the pressure values for onset P_{On}, offset P_{Off}, as well as the peak to peak amplitude $\overline{P_{pp}}$ are lower than the case of a serial inclusion and also decrease compared to the case of no inclusion. This is most probably due to the fact that the replicas with an embedded parallel inclusion can get easily damaged during fluid-structure interaction experiments compared to replicas with no embedded inclusions and also compared to replicas with a parallel inclusion embedded.

Table 6.4: Results of main quantities analysed: upstream pressure $P_u(t)$, inferior-superior displacement of the top surface of the replicas $z_r(t)$, and the fundamental frequency of oscillation during the fluid-structure interaction experiments $f_0(t)$. Subscripts On and Off denote oscillations onset and offset values, subscript pp denotes a peak to peak amplitude, and the over-line denotes a mean value during the time of oscillations.

Replica	$P_u(t)$ [Pa]			$z_r(t)$ [mm]			$f_0(t)$ [Hz]		
	P_{On}	P_{Off}	$\overline{P_{pp}}$	z_{On}	z_{Off}	$\overline{z_{pp}}$	f_{On}	f_{Off}	$\overline{f_0}$
Rectangular (no inclusion)	1187	1004	1393	5.3	5.2	1.6	97	97	96
Rectangular (serial inclusion)	1599	1160	2493	3.8	3.7	1.8	99	105	102
Rectangular (parallel inclusion)	1040	954	1095	1.0	0.9	1.1	103	99	97
EPI	378	278	700	0.3	0.2	0.5	78	78	76
MRI	692	556	617	1.8	1.6	0.6	83	82	82
M5	1241	984	2290	1.5	1.2	2.4	105	94	91

This is mainly due to the manner how the replicas oscillate, where the last layer (epithelium) rotates upward by a 90° angle before the replica starts vibrating. For the case of an embedded parallel inclusion, it is more difficult for the replica to have its epithelium layer rotated without the superficial layer (containing the inclusion) separating from the ligament layer that precedes it. This is more evident when observing the displacement signals, where at both onset z_{On} and offset z_{Off} the inferior-superior displacement decrease for the case of the parallel inclusion compared to the values for the replica with no inclusion by 81% and 83%, respectively. For the case of an embedded serial inclusion, both z_{On} and z_{Off} decrease, but the decrease is by 28% and 29%, respectively. As all replicas had to have their last layer rotated before vibration, replicas with parallel inclusions were damaged by having their superficial layer partly separated from the preceding ligament layer, compared to the other two cases where the superficial layer stretches, although at a lower value for the case of a serial inclusion compared to the case of a rectangular replica with no inclusion embedded. It is observed also that the the peak to peak amplitude $\overline{P_{pp}}$ decreases for the case of embedding a parallel inclusion by 32%, where it increases by 13% for the case of a serial inclusion.

The investigated parameters are indeed of higher values compared to the measured values for the EPI VFs replica model, which the rectangular replica design is inspired from. Table 6.4 also shows the extracted parameters for both the M5 and MRI VFs replica models. It is noted that the hysteresis between onset and offset values are observed for the extracted quantities.

Table 6.5 shows different values of the displacement mean value during oscillations $\overline{z_r}$ for the EPI, M5, and MRI replicas. As the setup (b) shown in Fig. 6.3(b) allows for a precise laser point positioning (with a 0.01 mm accuracy), seven different positions for measuring the displacement

Table 6.5: Displacement mean value during oscillations $\overline{z_r}$ of the EPI, M5, and MRI VFs replicas models for different laser point positions along the y axis with respect to the point O at the centre of the replica.

	Distance to the point O along y [mm]						
Replica	-6	-4	-2	0	2	4	6
EPI	0.19	0.26	0.27	0.30	0.26	0.26	0.18
M5	1.54	1.63	1.67	1.71	1.55	1.41	1.35
MRI	2.51	2.54	2.17	1.38	1.25	0.94	0.60

of the top surface of the replicas $z_r(t)$ are chosen, from near the posterior edge with a distance of 6 mm from the centre point O up to 6 mm from the centre, near the anterior edge of the replica. For the EPI and M5 models, $\overline{z_r}$ is indeed maximum at the centre point (with a distance of 0 mm from point O) and it decreases as it the measuring point move away from the centre reaching the edges. However, due to the triangular shape of the MRI VFs replica model, it is observed that the maximum value of the displacement amplitude is not at the centre of the replica, but near the posterior edge.

6.5 Conclusion

Silicone VFs replicas with a simplified rectangular cross-section are proposed. The design of theses replicas are inspired from the layers of the EPI model. The effect of an embedded structural inclusion on the auto-oscillation of these rectangular vocal fold replicas is investigated experimentally. The spectral characteristics of the oscillations (fundamental frequency) and upstream threshold pressures (oscillation onset and offset) as well as the inferior-superior displacement of the top surface of the replicas are assessed. Clearly, the characteristics of the vocal folds replica auto-oscillation are altered. Both the oscillation threshold pressures and fundamental frequency increase for the case of an embedded serial inclusion, while the displacement amplitude at oscillations onset and offset decreases. These observed findings (increase in threshold pressure and fundamental frequency) correspond well to those reported in clinical research on vocal folds structural pathologies (vocal folds scarring as an example). The case of a parallel inclusion is more challenging to quantify, with the current replica design, the effect of the embedded inclusion on the fluid-structure interaction.

CHAPTER 7

Conclusion and perspectives

In the context of physical investigations on vocal folds auto-oscillation presented in the first chapter, using silicone artificial vocal folds replicas introduced in the second chapter, this research has aimed to investigate the effect of structural inclusion on the elasticity and vibration behaviour of artificial vocal fold replicas. Through the development and validation of models for predicting the elasticity of silicone multi-layer composites, as well as the analysis of fluid-structure interaction experiments, we were able to gain a better understanding of how structural inclusions affect these properties. Overall, this thesis aimed to make four main contributions that can be concluded as follows:

In the third chapter, the focus was on validating a model for estimating the effective Young's modulus of silicone multi-layer composites with different stacking conditions and in the case of a structural inclusion presence. The model could successfully account for an arbitrary-shaped inclusion of any size embedded somewhere within a single or multiple layers. The specimens effective Young's modulus varied between 4 kPa and 65 kPa, which overlaps the range associated with normal human vocal folds' (up to 60 kPa). An in-house developed test bench was developed and measurements from the new method and a standard mechanical press method were cross-validated as their difference yields less than 3.5 kPa, which is of the same order of magnitude as the difference ($\leq$ 4.1 kPa) associated with multiple mechanical press testing on the same specimen. Modelled effective Young's moduli were validated against measured values resulting in an overall model accuracy between 0.0 kPa and 5.2 kPa.

In the fourth chapter, the model validation was extended and two models of two parameters were proposed that accounted for the non-linear stress-strain behavior of the silicone multi-layer composites. In agreement with polynomial and exponential stress-strain models for soft biological tissues, best fits (in terms of root mean square error) of two-parameter cubic and exponential relationships were shown to provide an accurate ($R^2 > 99.5\%$) and continuous description of measured low-strain (up to $\approx$0.3) and subsequent (up to a maximum of 1.36) non-linear stress-strain behaviour of six single-layer and thirty four multi-layer silicone composites. Modelled parameter sets could also be interpreted in terms of the low-strain elastic Young's modulus. In addition, a modelled expression for the high-strain elastic Young's modulus $\mathscr{E}_{NL}$, characterising a linear high-strain stress behaviour, was obtained as $8.58\,\mathscr{E}_{(eff)}$. Consequently, for the sought multi-layer silicone composites, it was seen that both best fit approximated parameter sets and the

modelled parameter sets can be used to characterise the linear and non-linear stress-strain relationship once $\mathscr{E}_{(eff)}$ is known. Moreover, for these composites it was shown that using modelled instead of measured values does not significantly affects the mean fit accuracy. Therefore, combining the previously proposed low-strain Young's modulus model discussed in the third chapter with the cubic or exponential stress-strain characterisation and approximated or modelled two-parameter sets as a function of $\mathscr{E}_{(eff)}$ resulted in an *a priori* stress-strain characterisation. In order to characterise and design silicone multi-layer composite vocal folds replicas that mimic the intricate anatomical vocal fold structure without or with inclusion, as in the case of a structural pathology or abnormality, the proposed model and subsequent model parameter studies are anticipated to be useful.

In the fifth chapter, the validated models were applied to molded multi-layer serial stacked composite specimens based on the layers of three silicone vocal folds replicas: M5, MRI, and EPI. Additionally, the effective elastic Young's modulus of the pressurised latex tube vocal folds replica was measured along the transverse right-left (x) and the streamwise inferior-superior (z) direction. Measured $\mathscr{E}^{x}_{eff} = 44$ kPa and $\mathscr{E}^{z}_{eff} = 49$ kPa showed an anisotropy of 11% with respect to $\mathscr{E}^{x}_{eff}$ characterising the main auto-oscillation direction. These values are within the range, up to 65 kPa, reported for anatomical layers of a male adult human vocal folds, which illustrates the relevance of this type of mechanical vocal folds replicas from a mechanical point of view. Next, equivalent two-layer, three-layer and four-layer composite representations were assessed consisting of an inner layer to which one, two or three latex outer layers are added. Regardless of the applied representation, found Young's moduli for the inner layer were within the range pertinent to human vocal fold layers. This might contribute to the comparison between the Young's moduli associated with the pressurised latex tube replica and with other types of deformable vocal folds replicas such as molded silicone replicas.

Finally, in the sixth chapter, an experimental study on the fluid-structure interaction of a newly designed and built artificial vocal folds replicas was presented. The aim of the study is to determine the influence of an embedded structural inclusion on the auto-oscillation of silicone vocal folds replicas with simplified geometries that were influenced by the EPI model in relation to the change in elasticity quantified by the effective Young's modulus. The spectral characteristics of the oscillations (fundamental frequency) and upstream threshold pressures (oscillation onset and offset) as well as the displacement of the top surface of the replica due to vibrations were evaluated. Evidently, the artificial vocal folds' natural auto-oscillation properties had changed. Both the fundamental frequency and the oscillation threshold pressures were observed to increase, while the displacement underlying the vibration amplitude was decreased. While the case of a parallel inclusion the parameters extracted were not in line with their counterparts from the case of a serial inclusion, the auto-oscillation was altered nonetheless compared to the case of a rectangular artificial replica with no inclusion.

Overall, the research findings has shown that the presence of a structural inclusion could significantly affect the behaviour of silicon multi-layer composites. The specific type and size of

the inclusion, as well as the location and orientation of the inclusion within the composite, can all have a major influence on its elasticity and hence the fluid-structure interaction behaviour.

In terms of future research, there are several directions that could build upon the findings of this study. One potential direction is to investigate the effect of structural inclusion on the vibration behavior of other types of vocal fold replicas, such as those with different geometries like the M5, MRI, and EPI models, or those made from different materials like the pressurised latex tube replica. This could help to identify the optimal design and material parameters for improving the performance of artificial vocal fold replicas and potentially lead to the development of novel vocal rehabilitation technologies.

Another direction for future research is to study the effect of structural inclusion on the acoustic properties of the vocal folds, such as the pitch and intensity of the sound produced during phonation. This could help to understand how structural inclusion affects the production of different vowel and consonant sounds and could potentially be used to improve the performance of vocal fold prosthetics or enhance the abilities of singers and other vocal performers.

Finally, further research could focus on the potential applications of predicting the elasticity (for linear or non-linear stress-strain behaviour) of artificial vocal fold replicas, such as improving the durability and performance of vocal fold prosthetics or developing novel vocal rehabilitation technologies. By better understanding the effect of structural abnormalities on the elasticity and vibration behaviour of artificial vocal fold replicas, we can identify new ways to improve the performance of these devices and potentially enhance the communication abilities of individuals with vocal impairments.

Bibliography

1. Rosen, C. & Simpson, C. *Operative techniques in laryngology* 3–8 (Springer-Verlag, 2008) (cit. on pp. 1, 2, 5, 27, 68, 95).
2. O'Shaughnessy, D. *Speech Communication Human and Machine* 1–547 (Addison-Wesley Publishing Company, 1987) (cit. on p. 1).
3. Hirano, M., Kurita, S. & Nakashima, T. in (eds Bless, D. & J.H., A.) 22–43 (College-Hill Press, 1983) (cit. on pp. 1, 6–8, 26, 88).
4. Alipour, F. & Titze, I. Elastic models of vocal fold tissues. *Journal of the Acoustical Society of America* **90,** 1326–1331 (1991) (cit. on pp. 1, 6, 8, 26, 52, 53, 88).
5. Berke, G. & Gerratt, B. Laryngeal biomechanics: an overview of mucosal wave mechanics. *Journal of Voice* **7,** 123–128 (1993) (cit. on p. 1).
6. Min, Y., Titze, I. & Alipour, F. Stress-Strain response of the human vocal ligament. *Annals of Otology, Rhinology Laryngology* **104,** 563–569 (1995) (cit. on pp. 1, 6, 8, 26, 52, 88).
7. Chan, R., Fu, M., Young, L. & Tirunagari, N. Relative contributions of collagen and elastin to elasticity of the vocal fold under tension. *Annals of Biomedical Engineering* **35,** 1471–1483 (2007) (cit. on pp. 1, 6, 8, 26, 88).
8. Murray, P. & Thomson, S. Vibratory responses of synthetic, self-oscillating vocal fold models. *Journal of the Acoustical Society of America* **132,** 3428–3438 (2012) (cit. on pp. 1, 6–8, 16, 26, 88).
9. Riede, T. & Brown, C. Body size, vocal fold length, and fundamental frequency: implications for mammal vocal communication. *Nova Acta Leopoldina NF 111* **380,** 295–314 (2013) (cit. on pp. 1, 2, 7, 68).
10. Mobashir, M., Mohamed, A., Quriba, A., Anany, A. & Hassan, E. Linear measurements of vocal folds and laryngeal dimensions in freshly excised human larynges. *Journal of Voice* **32,** 525–529 (2018) (cit. on pp. 1, 6, 7).
11. Alexander, N., Wang, K. Y., Jiang, K., Ongkasuwan, J. & Lincoln, C. Volumetric analysis of the vocal folds using computed tomography: effects of age, height, and gender. *Laryngoscope* **131,** E240–E247 (2021) (cit. on pp. 1, 7).
12. Hirano, M. *Clinical examination of voice* 1–100 (Springer-Verlag, 1981) (cit. on p. 2).
13. Bouvet, A., Pelorson, X. & Van Hirtum, A. Influence of water spraying on an oscillating channel. *Journal of Fluids and Structures* **93,** 1–20 (2020) (cit. on pp. 2, 8, 9).

14. Ahmad, M., Bouvet, A., Pelorson, X. & Van Hirtum, A. Modelling and validation of the elasticity parameters of multi-layer specimens pertinent to silicone vocal fold replicas. *International Journal of Mechanical Sciences* **208,** 106685 (2021) (cit. on pp. 2, 8, 26, 29, 40, 45, 69, 71, 85, 87).

15. Luizard, P. & Pelorson, X. Threshold of oscillation of a vocal folds replica with unilateral surface growths. *Journal of the Acoustical Society of America* **141,** 3050–3058 (2017) (cit. on pp. 1, 9).

16. Tokuda, I. & Shimamura, R. Effect of level difference between left and right vocal folds on phonation: Physical experiment and theoretical study. *Journal of the Acoustical Society of America* **142,** 482–492 (2017) (cit. on pp. 1, 6–8, 12, 26, 27, 88).

17. Bouvet, A., Tokuda, I., Pelorson, X. & Van Hirtum, A. Influence of level difference due to vocal folds angular asymmetry on auto-oscillating replicas. *Journal of the Acoustical Society of America* **147,** 1136–1145 (2020) (cit. on pp. 1, 6–8, 12, 16, 24, 26, 27, 42, 43, 88).

18. Lucero, J., Pelorson, X. & Van Hirtum, A. Phonation threshold pressure at large asymmetries of the vocal folds. *Biomedical Signal Processing and Control* **62,** 102105 (2020) (cit. on pp. 1, 6).

19. Tembrock, G. *Akustische Kommunikation bei Säugetieren. Die Stimmen der Säugetiere und ihre Bedeutung* (Jan. 1996) (cit. on p. 5).

20. Zhang, Z. Mechanics of human voice production and control. *The Journal of the Acoustical Society of America* **140,** 2614–2635. eprint: `https://doi.org/10.1121/1.4964509` (2016) (cit. on p. 5).

21. Harrington, J. & Cassidy, S. *Techniques in speech acoustics* English (Kluwer Academic, 1999) (cit. on p. 5).

22. Mittal, R., Erath, B. & Plesniak, M. Fluid dynamics of human phonation and speech. *Annual Review of Fluid Mechanics* **45,** 437–467 (2013) (cit. on pp. 5, 6).

23. Van den Berg, J., Zantema, J. & Doornenbal, J. On the air resistance and the Bernoulli effect of the human larynx. *Journal of the Acoustical Society of America* **29,** 626–631 (1957) (cit. on p. 6).

24. Deverge, M. *et al.* Influence of collision on the flow through in-vitro rigid models of the vocal folds. *Journal of the Acoustical Society of America* **114,** 1–9 (2003) (cit. on p. 6).

25. Titze, I. The physics of small-amplitude oscillation of the vocal folds. *Journal of the Acoustical Society of America* **83,** 1536–1552 (1988) (cit. on p. 6).

26. Scherer, R. *et al.* Intraglottal pressure profiles for a symmetric and oblique glottis with a divergence angle of 10 degrees. *Journal of the Acoustical Society of America* **109,** 1616–1630 (2001) (cit. on pp. 6, 7).

27. Ruty, N., Pelorson, X., Van Hirtum, A., Lopez, I. & Hirschberg, A. An in-vitro setup to test the relevance and the accuracy of low-order models of the vocal folds. *Journal of the Acoustical Society of America* **121,** 479–490 (2007) (cit. on p. 6).

28. Drechsel, J. & Thomson, S. Influence of supraglottal structures on the glottal jet exiting a two-layer synthetic, self-oscillating vocal fold model. *Journal of the Acoustical Society of America* **123,** 4434–4445 (2008) (cit. on p. 6).

29. Pickup, B. & Thomson, S. Flow-induced vibratory response of idealized versus magnetic resonance imaging-based synthetic vocal fold models. *Journal of the Acoustical Society of America* **128,** 124–129 (2010) (cit. on pp. 6–8, 26, 88).

30. Cisonni, J., Van Hirtum, A., Pelorson, X. & Lucero, J. The influence of geometrical and mechanical input parameters on theoretical models of phonation. *Acta Acustica* **97,** 291–302 (2011) (cit. on p. 6).

31. Van Hirtum, A. & Pelorson, X. High-speed imaging to study an auto-oscillating vocal fold replica for different initial conditions. *International Journal of Applied Mechanics* **9** (2017) (cit. on pp. 6, 9).

32. Hirano, M. Morphological structure of the vocal cord as a vibrator and its variations. *Folia Phoniatr* **26,** 89–94 (1974) (cit. on p. 6).

33. Story, B. & Titze, I. Voice simulation with a body-cover model of the vocal folds. *Journal of the Acoustical Society of America* **97,** 1249–1260 (1995) (cit. on p. 6).

34. Miri, A. Mechanical characterization of vocal fold tissue: a review study. *Journal of Voice* **28,** 657–666 (2014) (cit. on pp. 6, 8, 26, 52, 88).

35. Zhang, Z., Samajder, H. & Long, J. Biaxial mechanical properties of human vocal fold cover under fold elongation. *Journal of the Acoustical Society of America* **29,** EL356 (2017) (cit. on pp. 6, 8, 26, 88).

36. Chhetri, D., Zhang, Z. & Neubauer, J. Measurement of Young's modulus of vocal folds by indentation. *Journal of Voice* **25,** 1–7 (2011) (cit. on pp. 6, 8, 26, 88).

37. Lucero, J., Van Hirtum, A., Ruty, N., Cisonni, J. & Pelorson, X. Validation of theoretical models of phonation threshold pressure with data from a vocal fold mechanical replica. *Journal of the Acoustical Society of America* **125,** 632–635 (2009) (cit. on p. 6).

38. Plant, R., Freed, G. & Plant, R. Direct measurement of onset and offset phonation threshold pressure in normal subjects. *Journal of the Acoustical Society of America* **116,** 3640–3646 (2004) (cit. on pp. 6, 7).

39. Titze, I. Vocal fold mass is not a useful quantify for describing F_0 in vocalization. *Journal of Speech, Language, and Hearing Research* **54,** 520–522 (2011) (cit. on p. 7).

40. Bouvet, A. *Experimental and theoretical contribution to the analysis and the modelling of the vocal folds vibration* PhD thesis (Grenoble Alpes University, France, 2019), 1–195 (cit. on pp. 7–9, 16, 24, 29, 38, 42, 43, 85, 88, 117).

41. Smith, S. & Thomson, S. Effect of inferior surface angle on the self-oscillation of a computational vocal fold model. *Journal of the Acoustical Society of America* **131,** 4062–4075 (2012) (cit. on p. 8).

42. Cisonni, J., Van Hirtum, A., Luo, X. & Pelorson, X. Experimental validation of quasi-one-dimensional and two-dimensional steady glottal flow models. *Medical Biological Engineering Computing* **48,** 903–910 (2010) (cit. on p. 9).

43. Voigt, W. Ueber die Beziehung zwischen den beiden Elasticitätsconstanten isotroper Körper. *Annals of Physics* **274,** 573–587 (1889) (cit. on pp. 13, 87).

44. Reuss, A. Berechnung der Fließgrenze von Mischkristallen auf Grund der Plastizitätsbedingung für Einkristalle. *ZAMM* **9,** 49–58 (1929) (cit. on pp. 14, 70, 85).

45. Murray, P. & Thomson, S. Synthetic, multi-layer, self-oscillating vocal fold model fabrication. *Journal of Visualized Experiments* **58,** e3498 (2011) (cit. on pp. 26, 88).

46. Shimamura, R. & Tokuda, I. T. Experimental study on level difference between left and right vocal folds. *Acoustical Science and Technology* **38,** 264–267 (2017) (cit. on p. 26).

47. Bouvet, A., Tokuda, I., Pelorson, X. & Van Hirtum, A. Imaging of auto-oscillating vocal folds replicas with left-right level difference due to angular asymmetry. *Biomedical Signal Processing and Control* **63,** 1–12 (2021) (cit. on pp. 26, 27).

48. Van Hirtum, A., Bouvet, A., Tokuda, I. & Pelorson, X. Dynamic vibration mode decomposition of auto-oscillating vocal fold replicas without and with vertical tilting. *Journal of Sound and Vibration* **In press,** 1–11 (2021) (cit. on pp. 26, 27).

49. Hansen, J. K. & Thibeault, S. L. Current Understanding and Review of the Literature: Vocal Fold Scarring. *Journal of Voice* **20,** 110–120 (Apr. 2006) (cit. on pp. 27, 95).

50. Friedrich, G. *et al.* Vocal fold scars: current concepts and future directions. Consensus report of the Phonosurgery Committee of the European Laryngological Society. *European Archives of Oto-Rhino-Laryngology* **270,** 2491–2507 (2013) (cit. on pp. 27, 95).

51. Mattei, A. *et al.* Cell therapy and scarred vocal folds. *Eur Ann Otorhinolaryngol Head Neck Dis* **134,** 339–349 (2017) (cit. on pp. 27, 95).

52. Fung, Y. Elasticity of soft tissues in simple elongation. *American Journal of Physiology* **213,** 1605–1624 (1967) (cit. on pp. 52, 53, 72, 80).

53. Fung, Y. *Biomechanics* (Springer, 2010) (cit. on pp. 52, 53, 80).

54. Zhang, K., Siegmund, T. & Chan, R. A constitutive model of the human vocal fold cover for fundamental frequency regulation. *Journal of the Acoustical Society of America* **119,** 1050–1062 (2006) (cit. on p. 52).

55. Alipour, F. & Vigmostad, S. Measurement of vocal folds elastic properties for continuous modeling. *Journal of Voice* **26,** 816e21–816e29 (2012) (cit. on p. 52).

56. Demiray, H. A note on the elasticity of soft biological tissues. *Journal of Biomechanics* **5,** 309–311 (1972) (cit. on p. 53).

57. Tanaka, M. L., Weisenbach, C. A., Carl Miller, M. & Kuxhaus, L. A continuous method to compute model parameters for soft biological materials. *Journal of Biomechanical Engineering* **133,** 1–7 (2011) (cit. on pp. 53, 72, 80).

58. Burks, G., De Vita, R. & Leonessa, A. Characterization of the continuous elastic parameters of porcine vocal folds. *Journal of Voice* **34** (2020) (cit. on p. 53).

59. Ahmad, M., Pelorson, X., Fernández, I., Guasch, O. & Van Hirtum, A. Low-strain effective Young's modulus model and validation for multi-layer vocal fold based silicone specimens with inclusions. *Journal of Applied Physics* **131,** 1–12 (2022) (cit. on pp. 69, 71, 85, 87, 88).

60. Ahmad, M., Pelorson, X., Guasch, O., Fernández, A. & Van Hirtum, A. Modelling and validation of the non-linear elastic stress–strain behaviour of multi-layer silicone composites. *Journal of the Mechanical Behavior of Biomedical Materials* **139,** 105690 (2023) (cit. on pp. 71, 72, 75, 80).

61. Strobl, G. R. *The physics of polymers: Concepts for understanding their structures and behavior* (Springer, 2011) (cit. on p. 84).

62. Department, C. U. E. *Materials data book* 41 (Cambridge University Press, 2003) (cit. on p. 89).

63. Strobl, G. *The Physics of Polymers* 511 (Springer, 2007) (cit. on p. 89).

64. Thibeault, S. L., Gray, S. D., Bless, D. M., Chan, R. W. & Ford, C. N. Histologic and Rheologic Characterization of Vocal Fold Scarring. *Journal of Voice* **16,** 96–104 (2002) (cit. on p. 95).

65. Rousseau, B. *et al.* Characterization of Vocal Fold Scarring in a Canine Model. *The Laryngoscope* **113,** 620–627 (cit. on p. 95).

66. Hirano, S. *et al.* Prevention of Vocal Fold Scarring by Topical Injection of Hepatocyte Growth Factor in a Rabbit Model. *The Laryngoscope* **114,** 548–556 (cit. on p. 95).

APPENDIX A

Axes and planes

In order to describe the point of view of the different figures, the medical planes and axes used, illustrated in Figure A.1, are:

Medical planes:

- Medio-frontal or coronal plane,
- Transverse or horizontal plane,
- Medio-sagittal or longitudinal plane.

Axes:

- Posterior - anterior,
- Inferior - superior,
- Right - left.

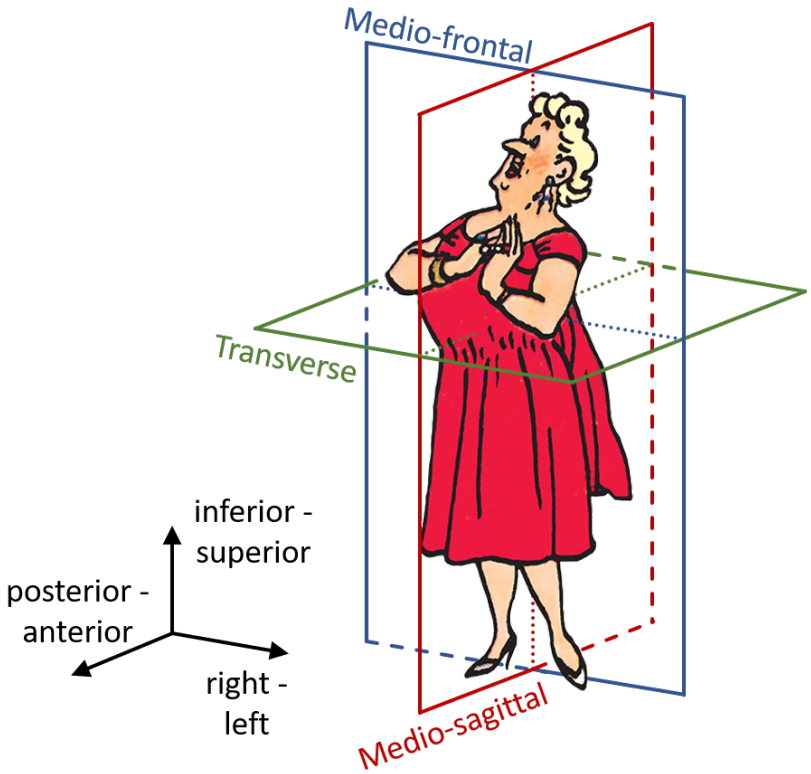

Figure A.1: Illustration of the different planes and axes used [40].

APPENDIX B

Sensors calibration

B.1 Scale calibration

A digital scale (Vastar 500G X 0.01G) shown in Fig. B.1(a) is used to weigh the silicone mixtures used in building silicone VFs replicas and silicone specimens used in validating Young's modulus estimation model. It is also used in measuring the weights added in the PL experiments. The scale is calibrated by measuring the weights of calibrated masses shown in Fig. B.1(b) between 1 g and 20 g with a step of 1 g, between 20 g and 100 g with a step of 10 g, and between 100 g and 200 g with a step of 20 g, where the first range [1:20] g covers the range of the weight of silicon mixtures used in building the replicas (mean = 9.1 g, std. = 2.7 g) as well as the loads added in PL experiments ($m \leq 20\ g$). Fig. B.2(a) shows the calibration curve obtained for this scale for the first range, where a linear model is fitted. Fig. B.2(b) shows the fitting residuals, where they are close to the scale accuracy (0.01 g) for almost all points. In addition, Fig. B.2(c) and Fig. B.2(d) show the calibration curve with the linear fit and the fitting residuals for the bigger range [1:200] g. Linear fits have an $R^2 > 99\ \%$.

(a) Vastar scale (b) Calibrated mass

Figure B.1: (a) The digital scale weighing a calibrated mass (50 g). (b) Calibrated masses used for the scale calibration and adding weights during PL experiments.

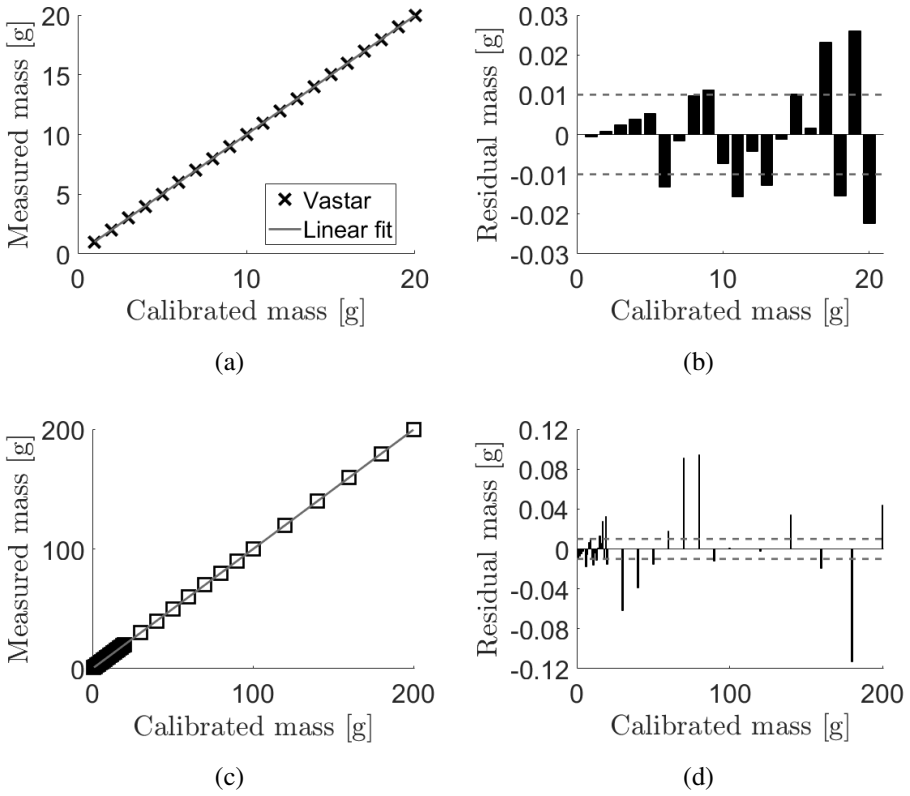

Figure B.2: (a) Calibration curve obtained for the scale for a range of [1:20] g with a linear model fitted to the measurements ($R^2 > 99$ %). (b) Fitting residuals (in bars) compared to the scale accuracy (in dashed lines) for the range up to 20 g. (c) Calibration curve for a bigger range [1:200] g with a linear fit ($R^2 > 99$ %). (d) Fitting residuals for the range up to 200 g.

B.2 Pressure sensor calibration

The piezoresistive pressure transducer 8507C-5 are utilized for measuring pressure. These sensors are calibrated with respect to a liquid column manometer Kimo MG80 (accuracy 5 Pa). Flows in a tube of uniform cross-section (25 mm in diameter) with a constriction at its end are measured to obtain pressures greater than atmospheric pressure. The uniform cross-section includes a wall pressure tab (diameter 0.4 mm). Fig. B.3 depicts the calibration curve with a sensibility of 672.6 Pa/V ($R^2 > 99\%$).

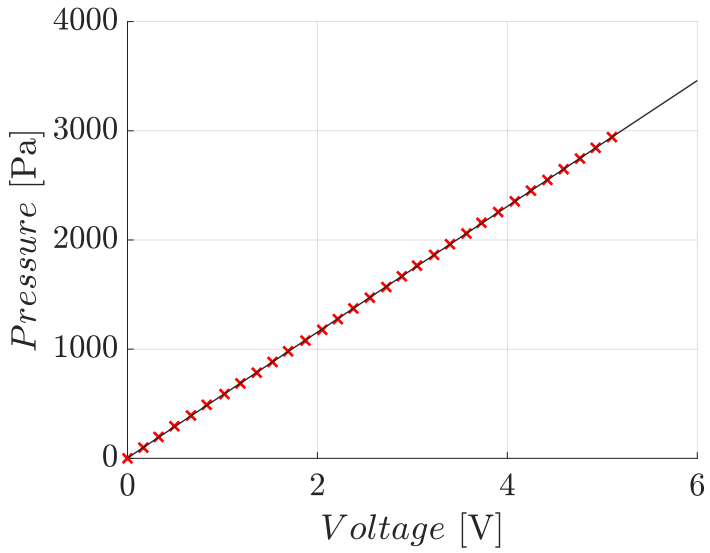

Figure B.3: Calibration curve obtained for the pressure sensor for a range of [0:2942] Pa with a linear model fitted to the measurements ($R^2 > 99$ %).

APPENDIX C

Silicone molding

C.1 Molding of bone-shaped silicone specimens

Silicone molded bone-shaped specimens are used for tensile testing. In the production of the silicone multi layer specimens, we utilise 3D-printed molds to achieve the desired shape and dimensions of the specimen, given in Fig. C.1. The molds were designed and then printed using a high-resolution 3D printer (Stratasys ABS-P430) with a resolution of 0.33 mm.

To begin the molding process, we first prepared the 3D-printed molds by cleaning them to remove any excess residue or contaminants. Next, we mixed the different silicones according to the desired mixture, ensuring that the proper ratio was used.

Once the silicones were mixed, they were then placed in a vacuum chamber to remove any trapped air and ensure a smooth surface on the finished specimens. It is then poured into the 3D-printed molds, taking care to avoid introducing any air bubbles.

After the silicone mixture had cured, the molds were carefully removed to reveal the finished specimens.

An example of the measurements performed with either MP or PL are presented for either one-layer specimens in Fig. C.3, two-layer specimens in Fig. C.4, or three-layer specimens as in Fig. C.3.

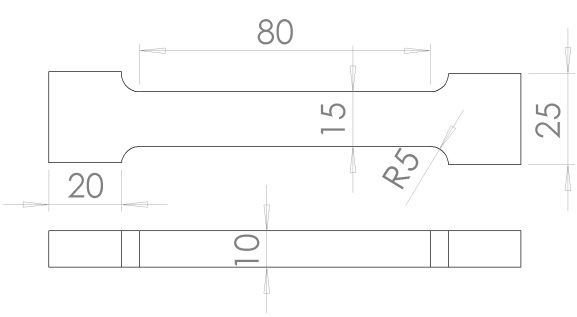

(a) Specimen dimension

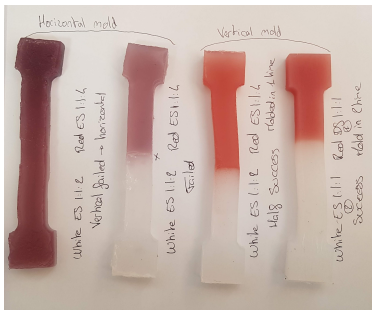

(b) Specimen trials

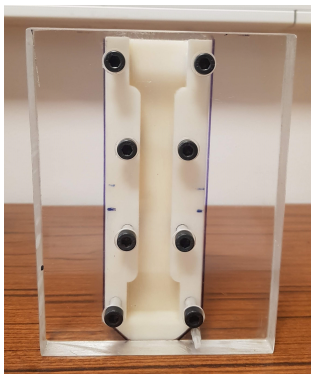

(c) Vertical mold

(d) Horizontal mold

(e) Laser vertical mold

Figure C.1: 3D-printed molds and specimens moldings.

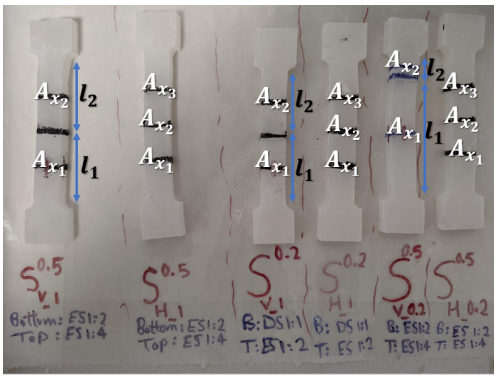

(a) 2-layer specimens

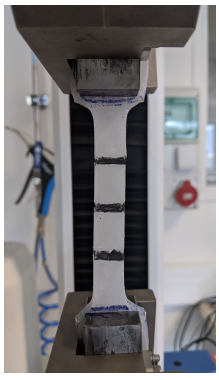

(b) MP

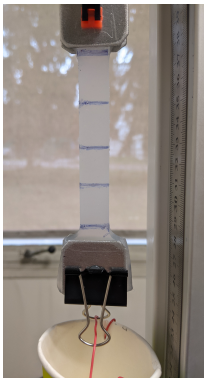

(c) PL

Figure C.2: Example of molded specimens, during tensile test using either MP or PL.

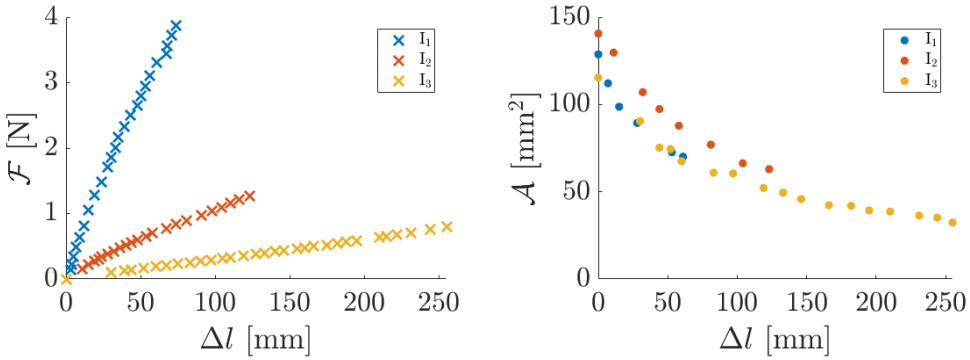

(a) Force-elongation (b) Cross-section area

Figure C.3: a,b) PL .

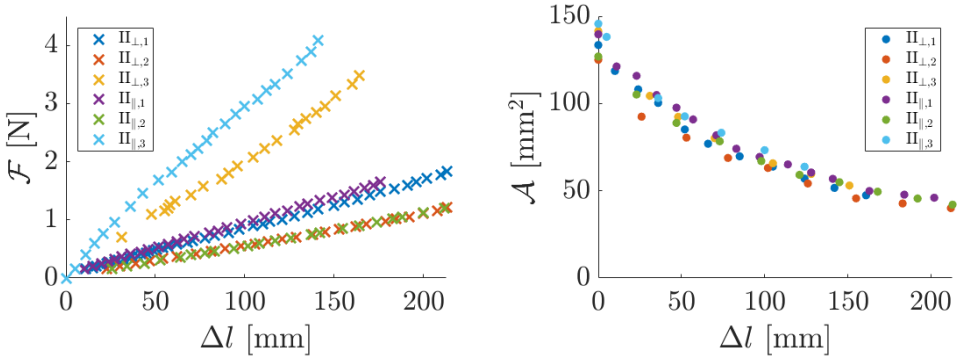

(a) Force-elongation (b) Cross-section area

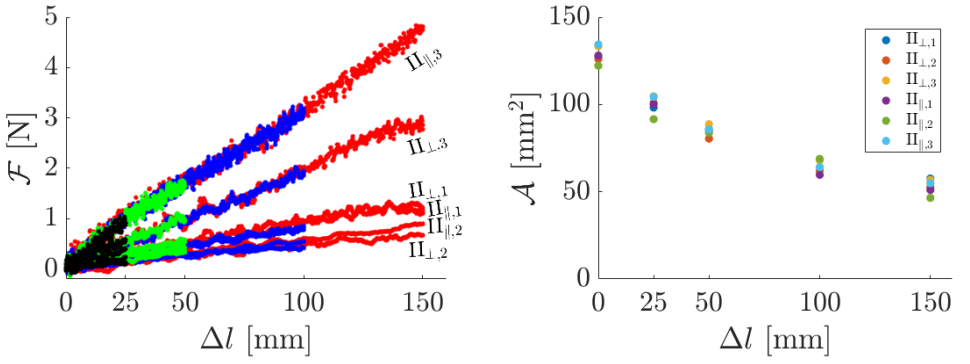

(c) Force-elongation (d) Cross-section area

Figure C.4: a,b) PL and c,d) MP

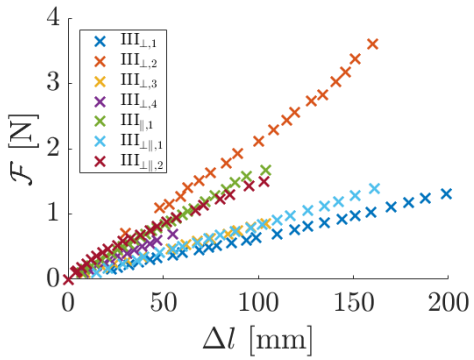

(a) Force-elongation

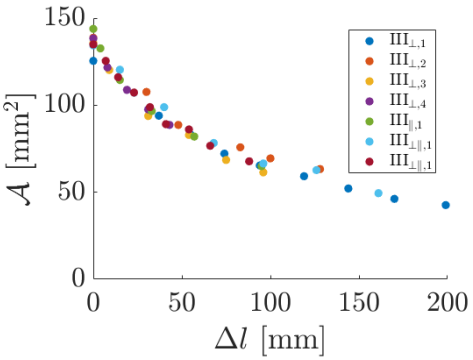

(b) Cross-section area

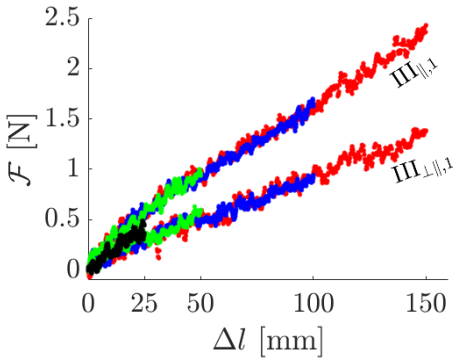

(c) Force-elongation

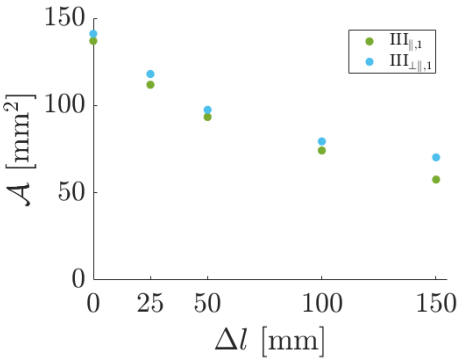

(d) Cross-section area

Figure C.5: a,b) PL and c,d) MP

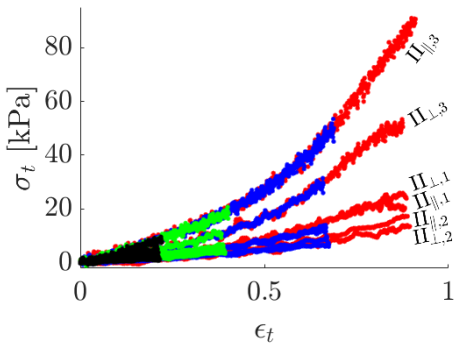

(a) Stress-strain behaviour 2L

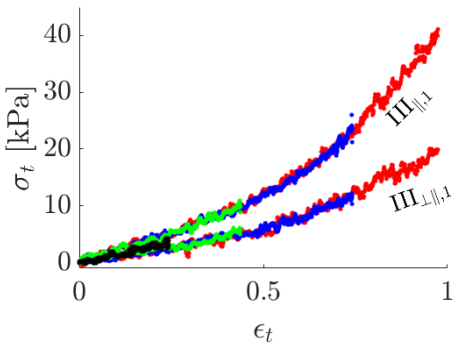

(b) Stress-strain behaviour 3L

Figure C.6: MP

APPENDIX D

Effective Young's modulus of rectangular replicas

As introduced in Chapter 6, new silicone replicas with a rectangular cross section were built. In order to measure the effective Young's modulus of these rectangular silicone vocal folds replica, a modified precision loading (PL) setup is developed in order to account for the smaller replica size compared to the previously tested specimens, as well as to have the ability to measure smaller elongation steps due to smaller applied uni-axial forces.

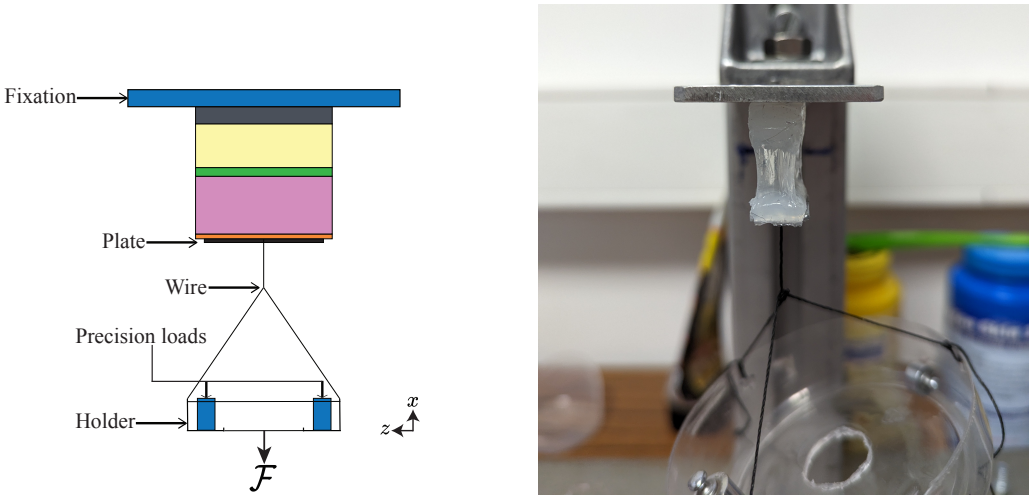

(a) Modified setup overview (b) Replica under loading

Figure D.1: Modified PL setup.

D.1 Modified PL setup and protocol

Figure D.1 shows the new modified setup. The setup consist of a rigid steel plate (Young's modulus of 210 GPa) to which the rectangular silicon replica is fixed with a superglue. A light and thin steel plate (mass of 0.1 g, thickness of 0.3 mm) is then glued to the other surface of the

Table D.1: Effect of embedding a structural inclusion in the superficial layer of the rectangular VFs replica on its elasticity: measured Young's modulus of the inclusion $\mathscr{E}^{In}$, measured inclusion dimensions l_x, l_y, and l_z, the equivalent length of the inclusion homogenised layer l_{eq} (as defined in Section 3.4.3.1, experimental Young's modulus in the x direction of the rectangular replica $\mathscr{E}^x_{eff}$, modelled effective Young's modulus in the x direction of the rectangular replica $\widehat{\mathscr{E}}^x_{eff}$, modelled Young's modulus in the z direction of the rectangular replica $\mathscr{E}^z_{eff}$, modelled effective Young's modulus in the z direction of the rectangular replica $\widehat{\mathscr{E}}^z_{eff}$.

Inclusion	$\mathscr{E}^{In}$ [kPa]	l_x [mm]	l_y [mm]	l_z [mm]	l_{eq} [mm]	$\mathscr{E}^x_{eff}$ [kPa]	$\widehat{\mathscr{E}}^x_{eff}$ [kPa]	$\mathscr{E}^z_{eff}$ [kPa]	$\widehat{\mathscr{E}}^z_{eff}$ [kPa]
No inclusion	-	0	0	0	0	**1.4**	**3.7**	**31.2**	**29.2**
Serial inclusion	298	2	10	4	2	**2.4**	**6.1**	**29.0**	**29.5**
Parallel inclusion	298	4	10	2	4	**5.5**	**15.1**	**30.8**	**29.4**

replica, this plate is connected to a holder to add precision loads, and is cut from the middle to allow a laser transceiver beam (Panasonic HLG112AC5, 655 nm wavelength, accuracy 80 μm) placed 130 mm below the replica. The elongation Δl is measured either from the readings of the laser or with using a vernier caliper (accuracy 0.02 mm), while the applied uni-axial force $\mathscr{F}$ is calculated from the added precision loads m (Vastar 500G X 0.01G, accuracy 0.01 g).

D.2 Measurement and results

To be able to estimate the low-strain effective Young's moduli $\mathscr{E}_{eff}$ of the three rectangular replicas, both the force-elongation data as well as the area-elongation data calculated from volume conservation of the replica under deformation are used to calculate stress-strain $\sigma_t(\varepsilon_t)$ curves as detailed in Chapter 3. Regarding to the force-elongation data, total added weights are up to 260 g, with elongations up to 22 mm, as can be seen in Figure D.2. As for the stress-strain curves, the low-strain ranges is chosen when $\varepsilon_t \approx 0.3$ as validated before, where the resulting goodness of fitting a linear model $R^2 \geq 90\%$. The stress-strain curves for the three rectangular silicone replicas are given in Figure D.3. The resulting experimental effective Young's moduli $\mathscr{E}_{eff}$, as well as the modelled values, can be found in Table D.1. For modelled moduli, the backing layer is not taken into account for values calculated for the x direction, while it is taken into account for estimating the moduli values for the z direction.

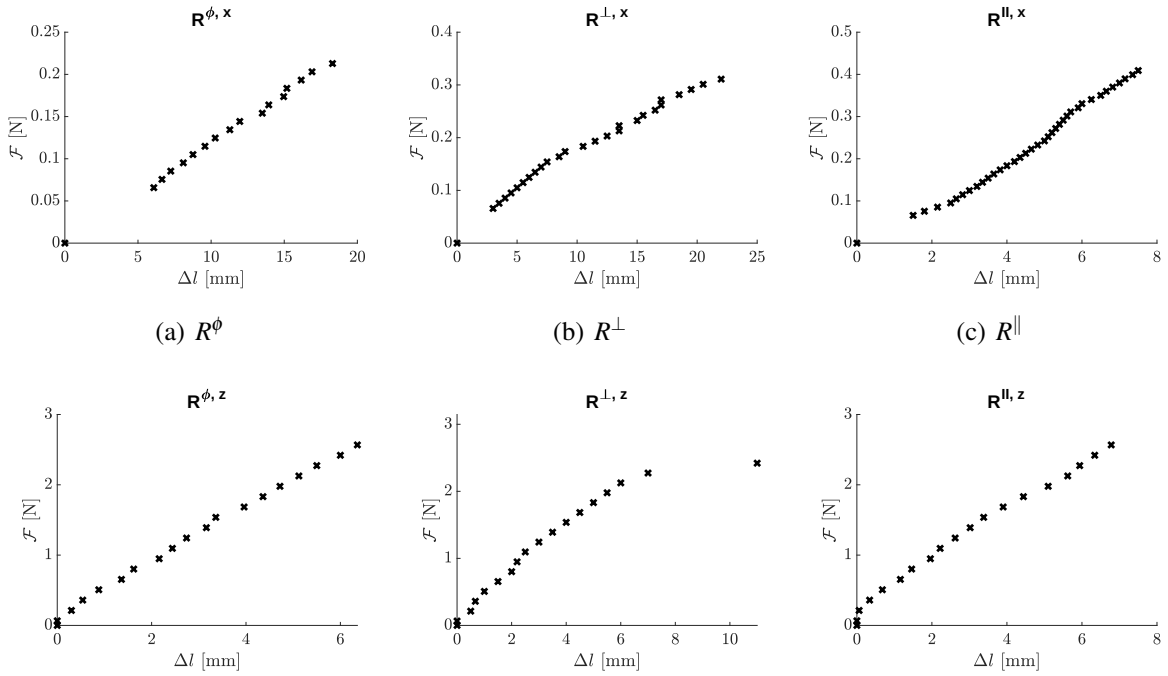

(a) R^{ϕ} (b) $R^{\perp}$ (c) $R^{\parallel}$

(d) R^{ϕ} (e) $R^{\perp}$ (f) $R^{\parallel}$

Figure D.2: Force-elongation data $\mathscr{F}(\Delta l)$ for three rectangular replicas configurations: without an inclusion R^{ϕ} (a, d), with a serial $R^{\perp}$ (b, e), or with a parallel inclusion $R^{\parallel}$ (c, f), where the forcing is applied either in the x (a, b, c) or in the z direction (d, e, f).

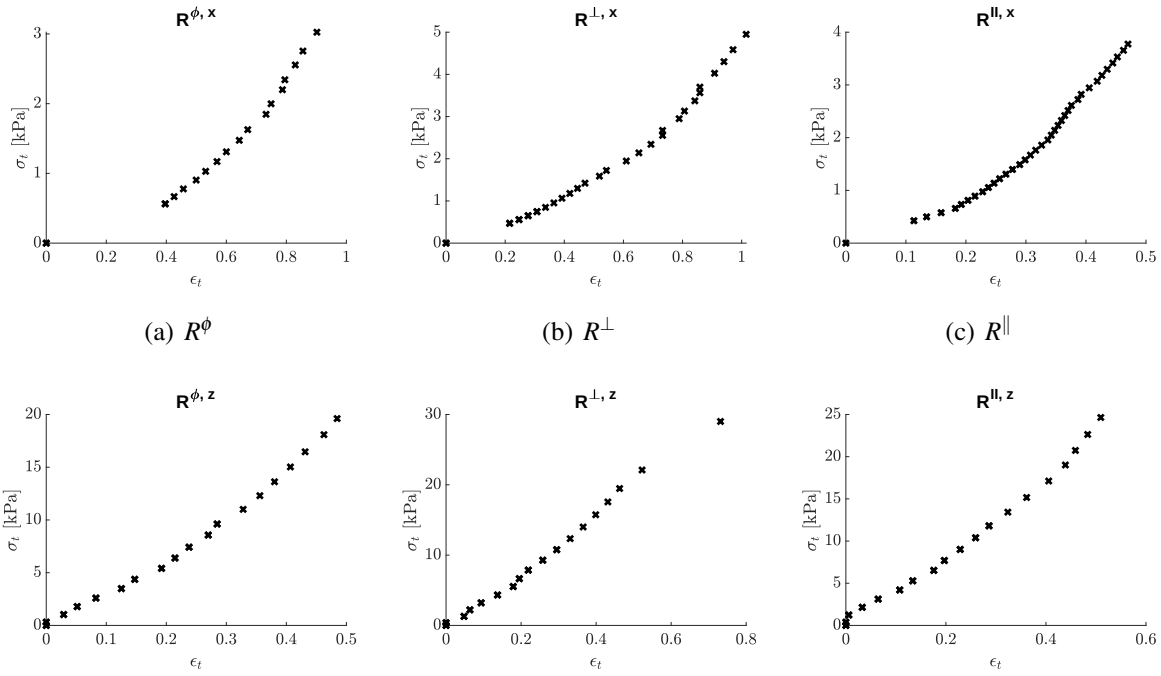

(a) R^{ϕ} (b) $R^{\perp}$ (c) $R^{\parallel}$

(d) R^{ϕ} (e) $R^{\perp}$ (f) $R^{\parallel}$

Figure D.3: Experimental stress-strain curves $\sigma_t(\varepsilon_t)$ for the three rectangular replicas configurations: without an inclusion R^{ϕ} (a, d), with a serial $R^{\perp}$ (b, e), or with a parallel inclusion $R^{\parallel}$ (c, f), where the uni-axial forcing is applied either in the x (a, b, c) or in the z direction (d, e, f).

Résumé —

L'interaction fluide-structure entre le flux d'air pulmonaire et les tissus multicouches déformables des cordes vocales entraîne une auto-oscillation soutenue. Cette thèse vise à apporter trois contributions à la recherche sur l'auto-oscillation des cordes vocales. Tout d'abord, proposer et valider un modèle analytique pour le module d'Young effectif des composites silicone multicouches connaissant la rigidité et la géométrie de ses couches. Le modèle doit également prendre en compte les inclusions de forme arbitraire de toute taille incorporées dans des couches individuelles ou multiples. Deuxièmement, caractériser le comportement contrainte-déformation des composites silicone multicouches avec des relations à deux paramètres pour tenir compte de la gamme de déformation non linéaire. Des expressions analytiques du module d'Young linéaire à forte déformation et du début de déformation linéaire à forte déformation sont également formulées. Troisièmement, une étude expérimentale de l'influence d'une inclusion structurelle sur l'auto-oscillation des cordes vocales est réalisée. L'influence des paramètres structurels de répliques de cordes vocales normales et anormales sur la vibration est quantifiée. En effet, une telle contribution est particulièrement importante à long terme pour les expériences physiques (utilisant des répliques moulées déformables à base de silicone) présentant une variation systématique de l'élasticité simulant soit la variabilité intra et inter-speaker, soit une pathologie structurelle. **Mots clés :** Élasticité, Relations contraintes-déformations non linéaires, Interaction fluide-structure, Mesures expérimentales in-Vitro, Modelisation théorique, Parole

Abstract —

The fluid-structure interaction between lung airflow and deformable multi-layer vocal folds tissues results in sustained auto-oscillation. This thesis intends to make three contributions to vocal fold auto-oscillation research. Firstly, propose and validate an analytical model for the effective Young's modulus of multi-layer silicone composites knowing its layers' stiffness and geometry. The model must also account for arbitrary-shaped inclusions of any size embedded in single or multiple layers. Secondly, characterising the stress-strain behaviour of multi-layer silicone composites with two-parameter relationships to account for non-linear strain range. Analytical expressions of the linear high-strain Young's modulus and the linear high-strain onset are also formulated. Thirdly, an experimental study of the influence of a structural inclusion on vocal folds auto-oscillation is performed. The influence of the structural parameters of normal and abnormal vocal folds replicas on vibration is quantified. Indeed, such a contribution is of particular importance in the long term for physical experiments (using deformable silicone-based molded replicas) featuring systematic elasticity variation simulating either intra- and inter-speaker variability or structural pathology. **Keywords:** Elasticity, Nonlinear stress strain relations, Fluid-structure interaction, In-Vitro experimental measurements, Theoretical modeling, Speech